STUDIES OF HYDRODYNAMICS AND FLUCTUATIONS IN SANDPILES

A THESIS SUBMITTED FOR THE DEGREE OF
DOCTOR OF PHILOSOPHY (SCIENCE)
IN PHYSICS (THEORETICAL)

by
ANIRBAN MUKHERJEE

Department of Physics
University of Calcutta

2023

In loving memory of my mother
Mitali Mukherjee
(1966 - 2015)

ACKNOWLEDGEMENTS

First and foremost, I would like to express my deepest appreciation to my supervisor, Prof. Punyabrata Pradhan, for introducing me to the beautiful world of sandpiles. I am deeply indebted for his constant guidance, patience, and surely for the constructive criticisms.

I am thankful to my thesis committee members, Prof. Sakuntala Chatterjee, and Prof. Priya Mahadevan, for their questions, suggestions, and encouragement during the seminars. I acknowledge the financial support of the Department of Science and Technology, India [Fellowship No. DST/INSPIRE Fellowship/2017/IF170275], as well as the S. N. Bose National Centre for Basic Sciences for providing the subsistence allowance during the extension period of one year. Additionally, I acknowledge the Thematic Unit of Excellence on Computational Materials Science and the Cray Supercomputing Facility of the Technical Research Centre (TRC) at S. N. Bose National Centre for Basic Sciences, funded by the Department of Science and Technology, India, for computational facilities.

Special thanks to Prof. Sobhan Kumar Sounda from my undergraduate college RKMRC, Narendrapur, who passionately taught us many topics beyond the syllabus in Physics. I am also grateful to my professors during my post-graduation at RKMVU, Belur, namely Bobby Ezhuthachan, Abhijit Bandyopadhyay, Parthasarathi Majumdar, and Somendra Mohan Bhattacharjee. They have taught me a lot about physics and have stood by me during my most difficult times. In this regard, I also want to express my gratitude to the monk and mathematician, Mahan Maharaj.

I am grateful to Sanjoy da, Deblina di, Abhijit da, and Bijoy da from the Computer Services Cell of our centre for providing immediate support whenever needed. Thanks should also go to Gurudas da, Amit da, Ananya di, and others from the Library, where I spent a lot of time during the last year of my tenure, for their service. Additionally, I would like to acknowledge the academic section for helping me with official matters several times. I take this opportunity to thank all the staff, including the cleaners and gardeners, who make our centre a livable and beautiful place for research.

Now, here comes the most difficult part – acknowledging my friends and colleagues. I believe it would be better if I stick to a timeline. Firstly, from my college days, I would like to thank my friends Sanjib, Debraj, Souparna, and Subhajit. Many thanks to all of my Belur batchmates, particularly Raunaq, Nobu, Somnath, Aritra, Sreetama, Arkajyoti, Suman, and Sourav, who literally became my family after the demise of my mother and supported me

to survive during that time. Without them, I might not be here today. I'd also like to thank Dinu, Suchetan, Somnath, Ritam, and Sayak for our numerous adda sessions at Maidan.

I would like to extend my sincere thanks to my group members and my colleagues Arghya da, Sayani di, Lalu da, Dhiraj da, Tanmoy, Deepsikha, Animesh and Rupayan not only for being great academic colleagues but also for being soulful friends at the same time.

Although my stay at the SN Bose hostel was short due to the pandemic, I want to express my gratitude to Atul, Neeraj, Ananda, Sumanti, Anwesha, Sasthi, Dipanjan, Kaushik, Anupam, Kanchan, Manodip, Dhrubajyoti, Ardhendu, Saurav Kanth, my batchmates Koustuv, Arundhuti, Amrit, Purushottam, Arka, Vishal, Sayantan, Didhiti, Bihalan, and my wonderful seniors Shauri di, Monalisa di, Subhasis da, Rahul da, Anulekha di, Poonam di, Rakesh da, Sumanta da and Alik da (Gurudev) for making my stay great. I also extend my heartfelt thanks to all the colleagues, or the "*Devils of Dungeon*" of my first-floor bay.

I would like to give a special mention to Ankan, Shantanu, Gurudev, and Rituparna for being my go-to guys. With them, I also thank Anirbnan Goswami, Susmita, Shovon, and Sayan for our amazing tours in the hills. For a very short but memorable time, I would like to thank Shibendu and Ramesh.

I must not forget to mention Priyanka, Swarnali, Samrat da, and Suvam Shukla, with whom I had the opportunity to work as a representative in the Student's Advisory Committee (SAC), which was undemocratically revoked during the pandemic. Establishing an official and democratic Student's Body should be our utmost priority, and I encourage my juniors to strive to build one.

I would like to express my deepest love to my wife Rituparna for making my life romantic since 2018.

Apart from academics, I also have a political life, and it would be unforgivable not to mention my comrades, Ratul da, Munmun di, Soumya, Biswajit da, Biswajit Mama, Shubhadeep da, Gargi di, Trishnika, Satyabrata and many others who helped shape my worldview and taught me to dream for a better world. I am also grateful to Sumita di, who unconditionally gave me shelter in the early days of Covid, and Gita di for cooking amazing food for me.

Finally, I wish to end with a thank you to my mother, who is no longer here to read this.

ABSTRACT

Sandpiles are threshold-activated interacting-particle systems, which are driven far from equilibrium, break time-reversal symmetry and cannot be described by the Boltzmann-Gibbs distribution. They were proposed nearly three decades ago as a mechanism to dynamically generate long-range spatial and temporal correlations in systems found in nature. Indeed, unlike the equilibrium systems near criticality, which is achieved at particular values of control parameters, these systems remain critical apparently without the need for any tuning of parameters and are ubiquitous in nature, e.g., current fluctuations in resistors, stability in large-scale ecological systems, intensity fluctuations in solar flares, and electrical activities in the brain, among others. Many of them remain on the verge of criticality in the time domain, as the temporal fluctuations exhibit long-range correlations in the form of $1/f^{\psi}$ power spectrum (simply known as "$1/f$" noise) with $0 < \psi < 2$. These particular phenomena were thought of as the consequence of *self-organized criticality* - the theoretical concept, which was developed by Bak, Tang, and Wisenfeld (BTW) and was the primary motivation behind introducing sandpile models. However, due to the time-reversible symmetry breaking and thus the violation of detailed balance, the steady-state weights of microscopic configurations are a-priori unknown and a good theoretical understanding of sandpiles, especially their dynamical properties, is still lacking.

In this thesis, we explore the time-dependent properties of a broad class of conserved stochastic sandpiles by developing a theoretical framework for calculating various time-dependent correlations involving current and mass, as well as the associated power spectra. We studied several variants of one-dimensional sandpiles: (i) the conserved *Manna sandpiles* with a two-particle and one-particle transfer rules, (ii) the *model of activated random walkers*, and (iii) the *Oslo ricepile model*. One usually categorizes the first three models as members of the so-called "Manna (universality) class" due to the stochasticity in the particle transfer rule and the presence of a single conserved quantity. For this class of models, we show that, in the thermodynamic limit, the variance of the cumulative bond current up to time T grows subdiffusively as $T^{1/2-\mu}$ with the exponent $\mu \geq 0$ depending on the density regimes considered; similarly, the power spectra of current and mass at low frequency f vary as $f^{1/2+\mu}$ and $f^{-3/2+\mu}$, respectively. Our theory predicts that, far from criticality, $\mu = 0$ and near criticality, $\mu = (\beta+1)/2\nu_{\perp}z > 0$ with β, $\nu_{\perp}$ and z being the order parameter, correlation length, and dynamic exponents, respectively. Notably, the values of the exponent μ estimated for all three variants of the Manna sandpiles are different; it worth mentioning here that, in

the Manna variant with one particle transfer, the exponent $\mu = 0$ is zero throughout. The anomalous suppression of near-critical fluctuations signifies a "dynamic hyperuniformity", characterized by a set of fluctuation relations, in which current, mass and tagged-particle displacement fluctuations are shown to have a precise quantitative relationship. In particular, the relation between the self-diffusion coefficient $\mathcal{D}_s(\rho)$, the activity, and density, explains a previous simulation observation [Eur. Phys. J. B **72**, 441 (2009)] that, near criticality, the self-diffusion coefficient in the Manna sandpile has the same scaling behaviour as the activity itself.

Furthermore, in the Oslo model, the critical height for threshold activity is defined as stochastic instead of the particle transfer rule, and it also involves two conserved quantities: density and centre of mass. As a result, the fluctuation properties in this model become quite different from those of the others. We find that the variance of the cumulative bond current up to time T grows subdiffusively as T^{α}, with $\alpha \approx 1/3$ near criticality. Correspondingly, the power spectra of current and mass at low frequencies f vary as $f^{\psi_{\mathcal{J}}}$ and $f^{-\psi_M}$, with $\psi_{\mathcal{J}} \approx 2/3$ and $\psi_M \approx 4/3$. Unlike the Manna sandpiles, the fluctuations away from criticality are further suppressed with values of $\psi_{\mathcal{J}} = 3/2$ and $\psi_M = 1/2$ which were obtained theoretically. Our study demonstrates that the additional conserved quantity manifests itself through the appearance of hyperuniformity near criticality and even stronger (in fact, the strongest possible) hyperuniformity away from criticality. However, the relation between the self-diffusion coefficient, activity, and density in the Oslo model remains the same as in the Manna model with the two-particle transfer rule, despite having a *vanishing* total current fluctuation in the system.

PUBLICATIONS

PAPERS TO BE INCLUDED IN THE PH.D. THESIS

1. "*Dynamic correlations in the conserved Manna sandpile* ", Anirban Mukherjee and Punyabrata Pradhan, Phys. Rev. E **107**, 024109 (2023).

2. "*Hydrodynamics and current fluctuations in the conserved Oslo ricepile model*", **Anirban Mukherjee**, Dhiraj Tapader, Animesh Hazra, Subhrangshu Sekhar Manna and Punyabrata Pradhan, manuscript to be submitted.

3. "*Hydrodynamics and dynamical fluctuations in the model of activated random walkers*", **Anirban Mukherjee**, Animesh Hazra, Sayani Chatterjee and Punyabrata Pradhan, manuscript to be submitted.

4. "*Dynamic fluctuations in the Manna model with one-particle transfer rule*", **Anirban Mukherjee** and Punyabrata Pradhan, manuscript to be submitted.

OTHER PUBLICATIONS

1. "*Exact dynamic correlations in mass transport processes*", Animesh Hazra, **Anirban Mukherjee** and Punyabrata Pradhan, manuscript to be submitted.

CONTENTS

LIST OF FIGURES

Figure 5.6 *Left panel:* Comparison of bond current fluctuation $\langle \mathcal{Q}^2(T) \rangle$ for $T \gg 1$ and $\sigma^2_{M_l}(\bar{\rho})$ is plotted as a function of relative density $\Delta = \bar{\rho} - \rho_c$. Simulation data for current fluctuation is shown in a solid violet line for $L = 1000$. Corresponding simulation data for $\sigma^2(M_l)$ is shown in a dashed green line for $L = 1000$ and $l = 500$, which shows excellent agreement with the bond current fluctuation, confirming our theoretical prediction of Eq. (5.79). *Right panel:* Scaled mass fluctuation, $\sigma^2_{M_l}(\bar{\rho})/l$, as a function of subsystem size, l, is plotted. Simulation data for $\bar{\rho} = 4$ (violet line), 2 (green line), and 1.74 (blue line) are shown for $L = 5000$, whereas $\bar{\rho} = 1.735$ (orange line) and 1.734 (red line) are plotted for $L = 10000$. Away from criticality, it indicates l^{-1} decay of the scaled fluctuation of maximal hyperuniformity as given in Eq. (5.78). Near criticality, the decay becomes much slower, approximately $l^{-0.6}$, as obtained from simulations, indicating hyperuniform fluctuations. 152

Figure 5.7 The power spectrum of the subsystem mass is plotted against frequency. *Left panel:* Simulation data of the power spectrum for subsystem size $l = 500$ and system size $L = 1000$ are plotted for density values away from criticality, namely $\bar{\rho} = 2$ (red), 3 (blue), and 4 (green) as solid lines. The corresponding theoretical lines, obtained using Eq. (5.80), are plotted for densities $\bar{\rho} = 2$ (dot-dot-dashed line), $\bar{\rho} = 3$ (dot-dashed line), and $\bar{\rho} = 4$ (dotted line), confirming that away from criticality, the mass power spectrum decays as $f^{-1/2}$ at low frequency in accordance with our analytical prediction given in Eq. (5.81). *Right panel:* The same data, obtained from simulation for system size $L = 5000$ and subsystem size $l = 2500$, are plotted for near-critical density values $\bar{\rho} = 1.7344$ (green line), 1.736 (blue line) and 1.738 (red line). As the density approaches the critical value, the decay of the power spectrum tends to a power law of $f^{-4/3}$ in the low frequency regime, as shown by the guiding line indicating the hyperuniformity of the system. 154

LIST OF TABLES

1

INTRODUCTION

Equilibrium thermodynamics was pioneered several centuries ago by Sadi Carnot, Lord Kelvin, and Rudolf Clausius with a systematic theoretical formulation of heat, mechanical work, entropy, etc. This classic branch of physics deals with the macroscopic laws of reversible processes. Later on, near the end of the 19^{th} and the beginning of the 20^{th} century, James Maxwell, Ludwig Boltzmann, J. Willard Gibbs, Max Planck, and Satyendra Nath Bose developed the theory of statistical mechanics, which, for the first time, connected the microscopic laws of physics (involving Newtonian dynamics) to the macroscopic thermodynamic laws. Indeed, according to the celebrated Boltzmann–Gibbs theory, the statistical description of an equilibrium system, which is kept in contact with a heat bath having temperature T, can be characterized by a probability $P(C)$ of finding the system in a certain microscopic configuration C,

$$P(C) = \frac{1}{Z} \exp\left[-\frac{E(C)}{k_B T}\right], \tag{1.1}$$

where $E(C)$ is the internal energy of the configuration C, Z is the partition function, and k_B is the Boltzmann constant. The purpose of equilibrium statistical mechanics is to derive the macroscopic properties/laws (equations of states, phase diagrams, various fluctuation properties, static fluctuation-response relations, and so on) by starting with the fundamental equation (1.1). The Boltzmann-Gibbs formula as in Eq.(1.1) has the advantage of not being dependent on the details of the dynamical trajectories of microscopic constituents and the precise nature of the coupling of the system to the heat bath; the only requirement is that, the coupling is "weak" with respect to the energy scale of the system.

Notably, the equilibrium processes or the reversible transformations that occur at an infinitesimally slow (quasi-static) rate - much slower compared to the equilibration rate, are just the limiting case of the more general nonequilibrium (or irreversible) processes, which are abundantly observed in nature. Indeed, unlike the equilibrium processes, nonequilibrium processes, such as various biological processes and matter or particle flow in the presence of a bulk or boundary drive, are usually characterized by rapid changes in matter. For ex-

ample, when a system is connected to more than one heat bath, with unequal temperatures, one would expect heat flow to occur from the higher temperature to the lower one. Perhaps the closest counterpart to the equilibrium state in such a situation is a nonequilibrium steady state, which the system approaches after a sufficiently long time. Even in this simplest of nonequilibrium settings, the probability of a microscopic configuration C is *a-priori* not known and one would like to ask,

$$P_{noneq}(C) = ? \tag{1.2}$$

In fact, there is no general answer to the above question yet. This is because the steady-state measure $P_{noneq}(C)$ of a system driven far from equilibrium must be determined from the explicit knowledge of the microscopic dynamical rules governing the system as well as the heat baths.

In the past, several formulations, especially the original one by Onsager and Machlup (discussed later), were developed to describe linear irreversible processes, mostly based on the "near-equilibrium" phenomenological laws connecting forces and currents in a system [1–4]. These near-equilibrium "linear-response" theories start with the premise that the changes or responses in a system are linear with respect to the external perturbations, which drive the system *slightly* away from an equilibrium state. Of course, such a formulation is appropriate when the strength of the perturbations is only small. Later, a microscopic dynamical formulation of the so-called *linear-response theory* was put forward by Green and Kubo [5–8], where a set of fluctuation-response relations or the "fluctuation-dissipation theorem" (originally discovered by Johnson and Nyquist) can be derived from the underlying microscopic dynamical laws (classical or quantum mechanical) of motion. In this way, one can relate various transport coefficients, which characterize the response of a system to an external perturbation, to the microscopic time-dependent correlation functions calculated in equilibrium (e.g., the conductivity is related to the equilibrium current fluctuation). Indeed, this approach is successful because the averages of relevant observables, required to calculate the transport coefficients, are, in fact, calculated in equilibrium. This stems from the assumption that the nonequilibrium steady-state locally gives rise to an equilibrium state ("local equilibrium hypothesis"), conforming to the local thermodynamic variables (temperature and pressure, etc.). However, in the absence of explicit knowledge of the nonequilibrium steady state in driven systems, the Green-Kubo linear-response theory cannot be straightforwardly extended to the calculation of transport coefficients for driven systems in general.

In this scenario, to develop a general nonequilibrium theory, it is imperative that one considers driven systems on a case-by-case basis, revisits the basic principles of symmetries and conservation laws, and then attempts to calculate the transport coefficients, and importantly their precise relationship to the corresponding dynamic correlations in the

unperturbed nonequilibrium steady states. Interestingly, recently a hydrodynamic theory - called *macroscopic fluctuation theory*, albeit applicable for a particular class of models with a "gradient property" [9, 10], has been developed by generalizing the Onsager-Machlup near-equilibrium theory to systems out of equilibrium. Indeed, the basic ingredients of the theory are only transport coefficients. Despite the expectation that the macroscopic fluctuation theory may be applicable to a much broader class of systems, called "driven diffusive systems", rigorous proofs are only available for the models having a product measure [11] and thus having vanishing spatial correlations. Of course, developing a fluctuating hydrodynamic formalism for interacting-particle systems that are diffusive yet have nontrivial spatio-temporal correlations, would be quite interesting. Indeed, starting with a microscopic dynamical approach to analytically calculate the transport coefficients in systems with nonzero spatial correlations remains a challenge. In this thesis, we have made some theoretical progress in analytically calculating dynamical correlation functions a broad class of nonequilibrium interacting-particle systems - conserved stochastic sandpiles. Indeed, sandpiles present unique challenges, as obtaining the microscopic steady-state measures are difficult to obtain and often are not explicitly known. Despite these obstacles, we believe to have advanced our theoretical understanding of the large-scale hydrodynamic properties of various sandpile models and characterized their time-dependent properties concerning current and mass fluctuations and the associated power spectra.

Before delving into a more detailed discussion of the problem and related concepts, it is essential to grasp the concept of nonequilibrium steady states and explore what is known about the *dynamical characterization* of equilibrium or near-equilibrium systems. By doing so, we can establish a foundation for our research and contextualize the significance of our findings in the broader field of nonequilibrium phenomena.

1.1 MARKOV PROCESSES

The goal of statistical mechanics is to understand the macroscopic behaviour of observable systems based on their underlying microscopic dynamics, such as Newtonian mechanics or quantum mechanics. However, dealing with many-body systems presents extreme challenges due to the immense number of variables involved. In addition, Newtonian or quantum dynamics pose another hurdle due to limited understanding of the properties of the time-evolution operator involved. To address this, various simpler realizations of dynamical rules, such that involving stochastic processes, and related techniques, have been developed; one of which is the modelling of many-particle systems through stochastic Markovian dynamics [12, 13]. Stochastic processes provide a framework to model the interactions among observable particles probabilistically, effectively capturing the effects of noise in the system.

Indeed, even in the deterministic dynamical framework (such as the Newtonian one), noise can arise due to the lack of information for several (fast) degrees of freedom, and the slow variables (e.g., conserved densities) could be thought of as essentially evolving through a random or stochastic process only.

Stochastic techniques have contributed to a more diverse range of models and come alongside powerful computational methods. Among the essential types of stochastic processes are Markov processes, which possess no memory. This means that the system's time evolution depends solely on its present state and not its history. These evolutions are familiar to us, as they are represented by first-order differential equations commonly used in mechanics to describe the autonomous evolution of a state, such as positions and momenta. However, Markov processes introduce randomness to these descriptions, making the updates partially stochastic rather than fully deterministic. As a result, they give rise to a unique set of probability distributions for possible trajectories.

A discrete-time stochastic process can be described as a sequence defined over a state space, denoted as K. The set of possible paths for this process is represented as Ω, comprising elements $\omega = (x_0, x_1, \ldots, x_n, \ldots)$, where the state at time n, denoted as x_n, belongs to the state space K. To fully characterize the stochastic process, two key components are considered:

(I) The initial distribution or the law, denoted as μ, which governs the probabilities of obtaining different initial states, represented by x_0.

(II) The updating rules or conditional probabilities that determine the likelihood of transitioning to a state x_n given that the process was in state x_{n-1} at the time $n-1$.

A stochastic process is classified as Markovian if the update rule to reach state x_n solely depends on the preceding state x_{n-1} and does not rely on any historical information before time $n-1$.

If the state space K is finite, the update rules aforementioned can be expressed through transition probabilities from a state x to another state y denoted by non-negative numbers $p(x,y)$, which satisfy the normalization condition $\sum_y p(x,y) = 1$. These transition probabilities, represented by elements of the transition matrix P, define the specific Markov process. When a Markov process starts with the initial distribution μ and evolves with a transition matrix P, the probability of a trajectory $(a_0, a_1, \ldots, a_n) \in K^{n+1}$ can be defined as

$$Prob_\mu \left[x_0 = a_0, x_1 = a_1, \ldots, x_{n-1} = a_{n-1}, x_n = a_n\right] = \mu(a_0) \cdot p(a_0, a_1) p(a_1, a_2) \ldots p(a_{n-1}, a_n). \tag{1.3}$$

μ_n is called the probability distribution of state configurations at the time n, given as

$$\mu_n(x) = \mathbf{Prob}_\mu \left[x_n = x\right] = \sum_{a \in K} \mu_{n-1}(a) p(a, x). \tag{1.4}$$

The difference equation of the above probability at two time steps now can be written using the above equation as

$$\mu_n(x) - \mu_{n-1}(x) = \sum_{a \in K} \left[\mu_{n-1}(a) p(a,x) - \mu_{n-1}(x) p(x,a) \right], \tag{1.5}$$

which is called the master equation of Markov chains.

The most significant aspect that describes the long-term evolution of a process is the stationary distribution, denoted as ρ. It can be defined as an invariant state of the transition matrix operator P. The stationary distribution implies that $\mu_n(x) = \rho(x)$ for any value of n when n is greater than a certain cutoff point. This condition changes Eq. (1.5) as

$$0 = \sum_{a \in K} \left[\rho(a) p(a,x) - \rho(x) p(x,a) \right], \tag{1.6}$$

which we call the stationarity condition of Markov processes. Equilibrium is a special stationary distribution that implies $\rho(a)p(a,x) = \rho(x)p(x,a)$, also known as the detailed balance condition. Otherwise, the stationary states that satisfy Eq.(1.6) are known as nonequilibrium steady states, particularly in which we are interested.

An example of a stationary distribution is the equilibrium Gibbs-Boltzmann distribution, which provides the distribution of a state a, denoted by $\mu(a)$, in terms of the energy function of that state, $E(a)$. It can be expressed as $\mu(a) = \mathcal{Z}^{-1} \exp\{-E(a)/kT\}$, where $\mathcal{Z}$ is the partition function, and T is the temperature of the reservoir [14]. When using this distribution, the detailed balance condition is modified to

$$\exp\left\{-\frac{E(a)}{kT}\right\} p(a,x) = \exp\left\{-\frac{E(x)}{kT}\right\} p(x,a). \tag{1.7}$$

So, if the system jumps from a state a to another state a' after receiving some energy ϵ from the heat bath at temperature T, we can write the above detail balance condition as

$$p_\epsilon(a,a') = \exp\left\{-\frac{\epsilon}{kT}\right\} p_{-\epsilon}(a',a). \tag{1.8}$$

One of the implications of having such a relationship among transition rates is that a process can be considered an equilibrium process if the probability of any given trajectory is the same as the probability of that trajectory being reversed in time. On the other hand, if this condition is not met, the process is classified as nonequilibrium [15].

One of the important questions one could ask is about the fluctuation properties of the observables generated by the stochasticity of Markov processes. For example, there are many instances of Markov systems that can be driven towards nonequilibrium steady states by external forces, such as boundary-driven *symmetric simple exclusion processes* (SSEP) or *sym-*

metric zero-range processes (ZRP). Additionally, there are systems, such as *asymmetric simple exclusion processes* (ASEP) and sandpiles, which inherently violate the detailed balance and remain in nonequilibrium stationary states. Before delving into a discussion about sandpiles, which are the main focus of this thesis, we will first explore some known results in the context of exclusion and zero-range processes.

Furthermore, it is essential to consider that the models mentioned above involve many-body interacting particle systems. As a result, a (underdamped-)Langevin dynamics approach is not suitable for characterizing the states of these processes or systems. Instead, hydrodynamical descriptions are commonly employed to address such problems. In these descriptions, the state of the systems is characterized by coarse-grained density observables at each spatial point, and the evolution of the conserved dynamics is governed by continuity equations.

1.2 ONSAGER-MACHLUP THEORY

The dynamic characterization of of a state slightly (or, linearly) perturbed from an equilibrium one is developed mainly by Lars Onsager through a series of works in first half of 20^{th} century [1, 2, 4]. Let us first describe the path integral method to calculate the action or Onsager-Machlup functional for a single particle in a nonequilibrium steady state by balancing between an external force and thermal fluctuations. The dynamical equation of the position x of the particle can be written as [16]

$$\frac{\partial x}{\partial t} = f(x) + g(x)\eta(t), \tag{1.9}$$

where

$$f(x) = -\Gamma(x)\frac{\partial \mathcal{H}}{\partial x} + f_1(x); \tag{1.10}$$

$\Gamma(x)\partial\mathcal{H}/\partial x$ is the force term that is pushing the particle towards equilibrium, $f_1(x)$ is space-dependent external force and η is Gaussian white noise. The probability of a path $x_0 = x(t_0)$, $x_1 = x(t_1)$, ..., $x_{n-1} = x(t_{n-1})$ and $x_n = x(t_n)$ traversed by the particle at different discrete time $t_0 < t_1 < \ldots t_{n-1} < t_n$, starting from an initial position x_0 at the time t_0 is given by

$$P\left(x_n, t_n; \ldots; x_1, t_1 | x_0, t_0\right) = \left\langle \delta(x_n - \phi(t_n; x_{n-1}, t_{n-1})) \ldots \delta(x_1 - \phi(t_1; x_0, t_0)) \right\rangle, \tag{1.11}$$

where the average is taken w.r.t. noise and $\phi(t_i; x_0, t_0)$ is the solution of Eq.(1.9) at t_i. Since, the noise η is Gaussian white noise, Eq.(1.11) can further be written as

$$P\left(x_n, t_n; \ldots; x_1, t_1 | x_0, t_0\right) = \prod_{i=1}^{n} \left\langle \delta(x_i - \phi(t_i; x_{i-1}, t_{i-1})) \right\rangle . \tag{1.12}$$

Due to the assumption of the Markov property of the noise, $\langle \delta(x_i - \phi(t_i; x_{i-1}, t_{i-1})) \rangle$ has a simple interpretation as the probability of observing the particle at position x_i at time t_i, given that it was at x_{i-1} at the previous time t_{i-1}. Consequently, the probability of finding a particle at x_f at time t_f, given that it was at position x_0 at time t_0, can be expressed in terms of a path integral by integrating over all the intermediate positions of the particle as

$$P(x_f, t_f; x_0, t_0) = \int dx_{n-1} \ldots \int dx_1 \left\langle \delta(x_f - \phi(t_f; x_{n-1}, t_{n-1})) \right\rangle \times \ldots \times \left\langle \delta(x_1 - \phi(t_1; x_0, t_0)) \right\rangle . \tag{1.13}$$

The above path integral can be written using the difference variable $h(x_i, x_{i-1})$ that can be obtained by discretization of Eq.(1.9) as

$$h(x_i, x_{i-1}) = \frac{x_i - x_{i-1} - \Delta t f_i}{g_i} - \int_{t_{i-1}}^{t_i} dt' \eta(t'), \tag{1.14}$$

where using the property of delta functions we can write $\delta\left(x_i - \phi(t_i)\right)$ as

$$\delta[h(x_i, x_{i-1})] = \left| \frac{\partial h}{\partial x_i} \right|^{-1}_{x_i = \phi(t_i)} \delta\left(x_i - \phi(t_i)\right) . \tag{1.15}$$

Now the probability $P(x_i, t_i; x_{i-1}, t_{i-1})$ can be written in terms of h [16] as

$$P(x_i, t_i; x_{i-1}, t_{i-1}) = \left| \frac{\partial h(x_i, x_{i-1})}{\partial x_i} \right| \left\langle \delta\left[h(x_i, x_{i-1})\right] \right\rangle , \tag{1.16}$$

with

$$\frac{\partial h(x_i, x_{i-1})}{\partial x_i} = \frac{1}{g_i} \left[1 - \alpha \Delta t f_i' - \alpha \frac{g_i'}{g_i} \left[x_i - x_{i-1} - \Delta t f_i \right] \right] , \tag{1.17}$$

where $\alpha = 0$ and 1 represents Ito and Stratonovich calculus respectively. Finally, using Eq.(1.16) one could write the probability $P(x_f, t_f; x_0, t_0)$ as

$$\begin{aligned} P(x_f, t_f; x_0, t_0) = \int \frac{dx_1}{\sqrt{2\pi \Delta t g_1}} \ldots \int \frac{dx_{n-1}}{\sqrt{2\pi \Delta t g_{n-1}}} \frac{dx_n}{\sqrt{2\pi \Delta t g_n}} \\ \times \exp\left\{ - \sum_i \frac{\Delta t}{2 g_i^2} \left(\frac{x_i - x_{i-1}}{\Delta t} - f_i + \alpha g_i' g_i \right)^2 - \sum_i \alpha \Delta t f_i' \right\} , \end{aligned} \tag{1.18}$$

and in the continuum limit by taking $n \to \infty$ and $\Delta t \to 0$ the probability could be written as an action principle,

$$P(x_f, t_f; x_0, t_0) = \int_{x_0}^{x_f} \mathcal{D}x e^{-\mathcal{S}}, \tag{1.19}$$

where $\mathcal{D}x = \prod_{i=1}^{n} dx_i / \sqrt{2\pi\Delta t g_i}$ and the Onsager-Machlup action $\mathcal{S}$ is given by [16]

$$\mathcal{S} = \int_{t_0}^{t_f} dt \left[\frac{1}{2g(x)^2} \left(\partial_t x - f(x) + \alpha g(x) g'(x) \right)^2 + \alpha f'(x) \right]. \tag{1.20}$$

The action $\mathcal{S}$ is also considered as the entropy function in the nonequilibrium states.

Since the unperturbed state of the system is described by the equilibrium Boltzmann-Gibbs measure, one can calculate the strength of the noise $g(x)$ using the fluctuation-dissipation theorem and can also justify the assumption of Gaussian white noise property. Moreover, this formalism can be extended to fields or systems with infinite degrees of freedom. A brief review of this concept is provided below.

Onsager-Machlup theory [4] actually allows one to perform the variational formalism to solve nonlinear Langevin type equations. Let us consider coupled dynamic Langevin-type equations of motion for the coarse-grained field variables, $\psi^\alpha(x,t)$ as

$$\frac{\partial \psi^\alpha(x,t)}{\partial t} = F^\alpha[\psi](x,t) + \zeta^\alpha(x,t). \tag{1.21}$$

$F^\alpha[\psi]$ are the systematic forces that contain both irreversible relaxation terms such as Eq.(1.28) and reversible mode couplings between ψ fields. The noise ζ^α is defined as follows:

$$\langle \zeta^\alpha(x,t) \zeta^\beta(x',t') \rangle = 2L^\alpha \delta(x-x') \delta(t-t') \delta^{\alpha\beta}, \tag{1.22}$$

where L^α is an operator. For example, for a conserved quantity ψ^α, it takes the form $L^\alpha = -D^\alpha \nabla^2$, which describes diffusive relaxation. Basically, the property of noise encompasses everything that we need to know, and its distribution function can be written as

$$\mathcal{W}[\zeta] \propto \exp\left[-\frac{1}{4} \int d^d x \int dt \sum_\alpha \zeta^\alpha(x,t) \left((L^\alpha)^{-1} \zeta^\alpha(x,t) \right) \right]. \tag{1.23}$$

Eq.(1.21) is crucial to tell us that how the noise is related to the relaxation process of the system, and by replacing $\zeta^\alpha[\psi] = \partial\psi^\alpha/\partial t - F^\alpha[\psi]$ in Eq.(1.23) we obtain the probability distribution $P[\psi]$ for the set of variables ψ^α and using the variable transformation,

$$\mathcal{W}[\zeta]\mathcal{D}[\zeta] = \mathcal{P}[\psi]\mathcal{D}[\psi] \propto e^{-\mathcal{G}[\psi]}\mathcal{D}[\psi] \tag{1.24}$$

one can obtain the Onsager-Machlup functional $\mathcal{G}[\psi]$ as

$$\mathcal{G}[\psi] = \frac{1}{4}\int d^d x \int dt \sum_\alpha \left(\frac{\partial \psi^\alpha}{\partial t} - F^\alpha[\psi](x,t)\right) \times \left[(L^\alpha)^{-1}\left(\frac{\partial \psi^\alpha}{\partial t} - F^\alpha[\psi](x,t)\right)\right]. \quad (1.25)$$

This functional actually gives us the probability of space-time trajectories traversed by the system during the relaxation process and thus potentially solves the desired dynamic correlation functions.

However, the generalization of this procedure to nonequilibrium processes lies in the identification of the operator L^α or the noise strength. In equilibrium, the fluctuation-dissipation theorems, such as the Einstein relation, actually solve the issue. For nonequilibrium processes, we will now discuss the mathematical framework of Markov processes and large deviation theory, which allows one to properly understand the generalization of the Onsager-Machlup functional that has been done for nonequilibrium diffusive processes in the framework of MFT.

1.3 DYNAMIC CRITICAL PHENOMENA

The Onsager-Machlup action derived in Eq. (1.19) for a single particle or the action functional for fields given in Eq. (1.25) give a probability of a particular trajectory. The corresponding equilibrium free energy functional can be derived from the path probabilities in the slow or *quasi-static* driving limit of the system.

Many of a system's properties exhibit singular behaviour when it reaches a critical phase transition, such as the gas-liquid critical point, where the density difference between liquid and gas disappears, or the Curie point of a ferromagnet, where spontaneous magnetization disappears. The equal-time correlation functions determine static properties in classical statistical mechanics. Critical singularities in time, on the other hand, occur in dynamic properties such as multi-time correlation functions, responses to time-dependent perturbations, and transport coefficients and for this purpose, the theory of dynamical critical phenomena has been used to compute such correlation functions [17].

In this thesis, we focus solely on the dynamical theory with a conserved order parameter, known as Model B, which includes systems like the Ising model with Kawasaki dynamics. In Model B, the total magnetization is conserved, and the dynamics follow the detailed balance condition. We base our discussion on the framework presented in Ref. [18].

In Model B, any deviation from thermal equilibrium should relax back to it. The evolution of the order parameter $S(x,t)$ follows a continuity equation, which can be expressed as follows:

$$\frac{\partial S(x,t)}{\partial t} + \nabla \cdot \vec{J}(x,t) = 0, \tag{1.26}$$

$$\vec{J}(x,t) = -D\nabla \frac{\delta \mathcal{H}[S]}{\delta S(x,t)} + \vec{\eta}(x,t), \tag{1.27}$$

where the strength of the noise follows a fluctuation-dissipation theorem to drive the perturbed state back to thermal equilibrium. So, the corresponding stochastic equation of motion can be written by combining Eqs.(1.26) and (1.27) as

$$\frac{\partial S(x,t)}{\partial t} = D\nabla^2 \frac{\delta \mathcal{H}[S]}{\delta S(x,t)} + \zeta(x,t), \tag{1.28}$$

where $\zeta = -\nabla \cdot \vec{\eta}(x,t)$. Upon inserting the Landau-Ginzburg-Wilson Hamiltonian,

$$\mathcal{H}[S] = \int d^d x \left[\frac{r}{2} S(x)^2 + \frac{1}{2} \left[\Delta S(x) \right]^2 + \frac{u}{4!} S(x)^4 - h(x) S(x) \right], \tag{1.29}$$

into Eq. (1.28) and performing the Gaussian approximation of the Hamiltonian, it becomes possible to calculate the temporal correlations and the corresponding transport coefficients. This approach allows us to study the dynamic behaviour of the system and gain insight into its nonequilibrium properties.

1.3.1 *Static characterization of stationary states - density large deviation function*

As mentioned earlier, the instantaneous state of a many-body system can be characterized by some local coarse-grained density. Regardless of whether the system is in an equilibrium state or a nonequilibrium steady state, the probability $P_v(n)$ of finding n particles inside a subvolume v, centred around position $\vec{r}$, can be expressed in terms of a large deviation rate function $a_{\vec{r}}(n/v)$ [14] as

$$P_v(n) \simeq \exp\left[-v a_{\vec{r}} \left(\frac{n}{v} \right) \right]. \tag{1.30}$$

The shape of $a_{\vec{r}}$ is strictly convex and has a minimum at the average density $\bar{\rho}$. Using the distribution $P_v(n)$, we can also derive the distribution of a density profile by incorporating the idea of *spatial additivity*, where we divide the total volume L^d, which is the volume of a d-dimensional box with length scale L, into smaller parts of length scale l and assume

the statistical independence of these $n = L^d/l^d$ boxes. For large enough L and l such that $l/L \ll 1$ we may write the probability of having a state $(\rho_1, \rho_2, \ldots, \rho_n)$ as

$$\textbf{Prob}\left[(\rho_1, \rho_2, \ldots, \rho_n)\right] \simeq \exp\left[-L^d \mathcal{F}\left(\rho_1, \rho_2, \ldots, \rho_n\right)\right], \tag{1.31}$$

where $\mathcal{F}$ is a large deviation function, which can be obtained from $a_{\vec{r}}$ [14]. In the continuum limit, as $L \to \infty$ and $l \to \infty$ with $l \ll L$, and by defining $\vec{r} = L\vec{x}$, Eq. (1.32) can be generalized to

$$\textbf{Prob}\left[\{\rho(\vec{x})\}\right] \simeq \exp\left[-L^d \mathcal{F}\left(\rho(\vec{x})\right)\right]. \tag{1.32}$$

For equilibrium systems, it can be shown that the rate function of subvolume density distribution $a_{\vec{r}}(\rho)$ and $\mathcal{F}(\rho(\vec{x}))$ is and can be written in terms of free energy functional $f(\rho)$ as

$$a_{\vec{r}}(\rho) = a(\rho) = \frac{f(\rho) - f(\bar{\rho}) - (\rho - \bar{\rho}) f'(\bar{\rho})}{kT} \tag{1.33}$$

$$\mathcal{F}(\rho(\vec{x})) = \frac{1}{kT} \int d\vec{x}\left[f(\rho(\vec{x})) - f(\bar{\rho})\right], \tag{1.34}$$

where $f(\rho)$ can be calculated by taking the logarithm of the grand canonical partition function. SSEP is one of the stochastic equilibrium systems, where the above results are applicable.

On the other hand, for nonequilibrium systems, the large deviation functions $\mathcal{F}(\rho(\vec{x}))$ can be very complicated. For example, the density large deviation function of a one-dimensional SSEP [19] connected with two density reservoirs of different densities ρ_a and ρ_b at both sides is given by

$$\begin{aligned} \lim_{L\to\infty} \frac{\log P_L\left[\{\rho(x)\}\right]}{L} &= -\mathcal{F}\left[\{\rho\}\right] \\ \mathcal{F}\left[\{\rho\}\right] &= \int_0^1 dx \left\{\rho(x) \log \frac{\rho(x)}{F(x)} + (1-\rho(x)) \log \frac{(1-\rho(x))}{(1-F(x))} + \log \frac{F'(x)}{\rho_b - \rho_a}\right\}, \end{aligned} \tag{1.35}$$

where $F(x)$ is an auxiliary function that can be obtained from the solution of

$$\rho(x) = F(x) + \frac{F(x)(1-F(x))F''(x)}{F'(x)^2}, \tag{1.36}$$

with the boundary conditions $F(0) = \rho_a$ and $F(1) = \rho_b$. The existence of the auxiliary function makes the large deviation function *non-local*, leading to the emergence of long-range density correlations in this simple $1d$ model. Additionally, in the case of the asymmetric

exclusion process (ASEP) in $1d$, along with this non-locality, the large deviation function of density becomes non-convex near the phase transition [20, 21].

Next, we will discuss the dynamic large deviation function, which holds significance due to the temporal asymmetry of relaxations in nonequilibrium steady states.

1.3.2 *Dynamic characterization of nonequilibrium steady states - current large deviation function*

In this thesis, we only consider systems with particle conservation dynamics. Consequently, the evolution of the local mass should be described in terms of the microscopic continuity equation,

$$\frac{d}{dt}m_i(t) = \mathcal{J}_{i-1}(t) - \mathcal{J}_i(t), \tag{1.37}$$

Here, $m_i(t)$ represents the local mass, and $\mathcal{J}_i$ is the instantaneous current across a bond $(i, i+1)$ of a lattice. Whenever the system transitions from a state $\mathcal{C}'$ to $\mathcal{C}$, it generates some current across different bonds. Now, if we define a quantity called the integrated bond current $\mathcal{Q}_i(t)$ or the net cumulative current across the bond $(i, i+1)$ within a time interval $[0, t]$, its statistical properties will depend on the path on which the system evolved within this temporal interval. In other words, $\mathbf{Prob}(Q_i(t) = Q)$ will depend on different trajectories starting from an initial state up to time t.

It can be shown that if the dynamics has finite relaxation time, in the long time limit the distribution of cumulative current can be written in terms of a large deviation function $\mathcal{G}$ [14] as

$$\mathbf{Prob}\left(\frac{Q(t)}{t} = j\right) \simeq \exp\left[-t\mathcal{G}(j)\right], \tag{1.38}$$

we dropped the spatial index i as the probability would not depend on the position, as well as not on the initial condition of the system. In most studies, rather than directly calculating the probability $\mathbf{Prob}(Q_t)$, the focus is on its cumulative generating function $\mu(\lambda)$. This function is defined in the large time limit as

$$\langle \exp\left[\lambda Q_t\right] \rangle \simeq \exp\left[\mu(\lambda)t\right], \tag{1.39}$$

where $\langle \cdot \rangle$ denotes the trajectory average. $\mu(\lambda)$ is related to the large deviation function $\mathcal{G}(j)$ via a Legendre transformation,

$$\mu(\lambda) = \max_j \left[\lambda j - \mathcal{G}(j)\right]. \tag{1.40}$$

The cumulant generating function $\mu(\lambda)$ is the largest eigenvalue of an exponentially tilted or conditioned Markov generator [22, 23]. However, determining this eigenvalue can be challenging for most systems. Only for a few systems, particularly those with a known steady-state measure, such as SSEP, can this eigenvalue be found, at least perturbatively [24]. Using $\mu(\lambda)$, we can obtain the cumulants of the current $\langle Q_t^k \rangle_c = \langle Q_t^k \rangle - \langle Q_t \rangle^k$, from the following definition,

$$\lim_{t\to\infty} \frac{\langle Q_t^k \rangle_c}{t} = \left. \frac{d^k \mu(\lambda)}{d\lambda^k} \right|_{\lambda=0}. \tag{1.41}$$

The cumulants of $\langle Q_t^k \rangle_c$ provide us not only with the complete statistics of Q_t, but also, as we shall see later, the relevant transport coefficients that govern the hydrodynamic fluctuations of the system.

Interestingly, similar to the *spatial additivity* principle in the context of the static large deviation function, a related additivity principle has been postulated to calculate the moment generating function of the current [25] in stochastic systems governed by some diffusive dynamics. In this regard, let us first define two transport coefficients, bulk diffusivity D and mobility χ, which are required to describe this additivity principle. For a large system size L, it can be observed that the entire distribution of fluctuations in Q_t depends solely on two macroscopic parameters, namely D and χ. Assuming that for $\rho_a = \rho + \Delta\rho$ and $\rho_b = \rho$ with $\Delta\rho$ being small, we know that in the steady state, Fick's law holds, which relates the average current to the bulk diffusivity as

$$\lim_{t\to\infty} \frac{\langle Q_t \rangle}{t} = D(\rho)\frac{\Delta\rho}{L}. \tag{1.42}$$

Furthermore, assuming $\rho_a = \rho_b = \rho$ (resulting in $\langle Q_t \rangle = 0$), and for large t, the variance of current can be written as

$$\lim_{t\to\infty} \frac{\langle Q_t^2 \rangle}{t} = \frac{2\chi(\rho)}{L}. \tag{1.43}$$

In Ref. [25], it has been demonstrated in one dimension that for a large system of size L connected with two reservoirs ρ_a and ρ_b at both ends, where $|\rho_a - \rho_b|$ is finite, dividing the system into n number of small subsystems of size l in such a way that $l \gg 1$ and $L \gg 1$ but $l/L \ll 1$, allows the large deviation function $\mathcal{G}_L(j, \rho_a, \rho_b)$ for the entire system to be expressed as

$$\mathcal{G}_L(j, \rho_a, \rho_b) \simeq \min_{\rho_1,\cdots,\rho_{n-1}} \left\{ \sum_{i=0}^{n-1} \mathcal{G}_{L/n}(j, \rho_i, \rho_{i+1}) \right\}. \tag{1.44}$$

In this expression $\mathcal{G}_{L/n}(j, \rho_i, \rho_{i+1})$ corresponds to the large deviation function for each of the small subsystems. Minimization of $\rho_1, \ldots, \rho_{n-1}$ accounts for the different configurations of the subsystems to obtain the large deviation function for the entire system. If the density profile of the subsystem is smooth enough and monotonic, in the large n limit, we can assume that $\mathcal{G}_{L/n}(j, \rho_i, \rho_{i+1})$ would simply be

$$\mathcal{G}_{L/n}(j, \rho_i, \rho_{i+1}) \simeq \frac{\left[j - \{D(\rho_i)\,(\rho_i - \rho_{i+1})\,/l\}\right]^2}{4\chi(\rho_i)/l}. \tag{1.45}$$

Taking $n \to \infty$ but keeping $l = L/n$ large enough, so that Eqs.(1.42) and (1.43) are still valid, we can write Eq.(1.44) using Eq.(1.45) as

$$\mathcal{G}_L(j, \rho_a, \rho_b) \simeq \frac{1}{L} \min_{\{\rho(x)\}} \frac{\left[jL + D(\rho)\rho'(x)\right]^2}{4\chi(x)}. \tag{1.46}$$

Now, the problem of finding the dynamic large deviation function of current reduces to an optimization problem, and it has been shown [25, 26] that the optimal density profile to sustain certain current j is given by,

$$\rho'(x)^2 = \frac{(Lj)^2\left[1 + 4K\chi(\rho(x))\right]}{D^2(\rho(x)}, \tag{1.47}$$

where K can be fixed from the boundary condition $\rho(0) = \rho_a$ and $\rho(1) = \rho_b$. In simulation, this additivity principle has been tested quite rigorously [27, 28].

Although the derivation of Eq. (1.46) was originally proposed for driven diffusive systems; the same equation remains valid in diffusive systems with periodic boundary conditions. In a homogeneous diffusive system with ring geometry, the steady-state profile is flat. However, the optimal profile transforms into a travelling wave form to maintain a certain value of j above some threshold [29–33]. Such transitions are termed as *dynamic phase transitions*.

But still all of these analyses are practical only for those systems for which the first two cumulants of current fluctuation are known, finding which is a difficult task in itself for stochastic systems for which steady-state measures are not known, such as sandpiles which are the main object of study in this thesis.

1.4 MACROSCOPIC FLUCTUATION THEORY

Recently, there has been notable progress in the study of nonequilibrium diffusive systems through a general approach called macroscopic fluctuation theory (MFT) [9, 11, 14]. MFT has proven effective in dealing with far-from-equilibrium processes and surpassing the limitations of near-equilibrium linear approximations. This framework draws heavily from re-

search on stochastic interacting particle systems and large deviation theory. However, this framework has only been successfully applied to stochastic systems where the steady-state measures are known, enabling the calculation of steady-state temporal correlation functions, which form a crucial component of this theory.

The *macroscopic fluctuating theory* (MFT) has been developed over the last couple of decades to describe diffusive systems characterized by continuum density fields that evolve through a Langevin equation. These systems may locally conserve or not conserve the field. It can be understood as an encapsulating framework that generalizes the large-scale hydrodynamic behavior generated by various Markov processes, regardless of whether they satisfy the detailed balance condition or not.

MFT has three main ingredients [9, 34]:

(I) At the macroscopic level, the system must be described by coarse grained local density $\rho(x,\tau)$ and local currents $j(x,\tau)$ and they should be related by the continuity equation,

$$\partial_\tau \rho + \partial_x j(t) = 0, \tag{1.48}$$

where x and τ are defined in the diffusive limit.

(II) The macroscopic behaviour of the system should be diffusive, and the existence of gradient property in the microscopic evolution of local conserved quantities is required. Correspondingly, the macroscopic diffusive current on average should follow Fick's law.

(III) The instantaneous microscopic current should be divided into a diffusive and fluctuating part, and importantly, the temporal correlation of the fluctuating part needs to be short-ranged compared to the hydrodynamic time scaled of the system under study.

Upon satisfying all three conditions, MFT provides a Langevin-type equation [11] for the evolution of a hydrodynamic system with an infinite number of degrees of freedom, which can be written as

$$\frac{\partial}{\partial \tau}\rho = -\frac{\partial}{\partial x}\left[j^{(d)}(x,\tau) + \eta(x,\tau)\right] = -\frac{\partial}{\partial x} j, \tag{1.49}$$

where the diffusive current $j^{(d)} = -D(\rho)\frac{\partial}{\partial x}\rho$ is the diffusive current and the noise η is defined as

$$\langle \eta(x,\tau)\eta(x',\tau')\rangle = \frac{2\chi(\rho)}{L}\delta(x-x')\delta(\tau-\tau'). \tag{1.50}$$

The two transport coefficients, D and χ, appearing in the above equations are the same as defined in Eqs. (1.42) and (1.43). But the transport coefficients D and χ are not arbitrary. In

fact, in the steady state the existence of local equilibrium implies that they satisfy the local Einstein relation

$$\frac{\chi(\rho)}{D(\rho)} = \frac{1}{f''(\rho)}, \tag{1.51}$$

where $f(\rho)$ is the equilibrium free energy per unit volume. Using the idea of spatial additivity, one could show that the second derivative $f(\rho)$ is related to the intensive subsystem mass fluctuation $\sigma^2(\rho)$ as $\sigma^2(\rho) = 1/f''(\rho)$[35–38]. Using this relation, one can actually check the validity of the local Einstein relation and, consequently, the validity of MFT in the corresponding "equilibrium" or "periodic boundary" version of the nonequilibrium system under discussion. As a matter of fact, it has been shown in Ref.[35–38] that the periodic boundary version of the nonequilibrium processes does not need to satisfy the detailed balance condition. In other words, the microscopic configurations do not need to describe the Gibbs-Boltzmann measure in the periodic boundary case.

Using the Langevin description given above, one can immediately write the probability distribution of the macroscopic space-time volume of the system (without knowing what the actual microscopic dynamics is) within a temporal interval $[0, \tau]$ as

$$\textbf{Prob}\left[\{\rho(x,\tau), j(x,\tau)\}; \tau \in [\tau_1, \tau_2]\right] \simeq \exp\left[-L\int_{\tau_1}^{\tau_2} d\tau \int_0^1 dx \frac{(j + D(\rho)\partial_x\rho)^2}{4\chi(\rho)}\right]. \tag{1.52}$$

Knowing the path probability of the system immediately generalizes both the static and dynamic large-deviation functions of density and current that we discussed earlier. For example, to obtain the probability of observing a density profile $\rho(x,\tau)$ currently at τ, one needs to maximize the probability $\textbf{Prob}\left(\rho(x,\tau'), j(x,\tau'); \tau' \in [-\infty, \tau]\right)$ over infinite history with the constraint of continuity (Eq. (1.48)), which leads us to write the density large deviation function for large L as

$$\mathcal{F}\{\rho(x)\} = \min_{\{\rho,j\}} \int_{-\infty}^{\tau} d\tau' \int_0^1 dx \exp\left[-L\int_{\tau_1}^{\tau_2} d\tau \int_0^1 dx \frac{(j + D(\rho)\partial_x\rho)^2}{4\chi(\rho)}\right]. \tag{1.53}$$

Consequently, it can be shown [9, 11] that, $\mathcal{F}\{\rho(x)\}$ satisfy the following *Hamilton-Jacobi* equation,

$$\int_0^1 dx \left[\frac{\partial}{\partial x}\left(\frac{\delta\mathcal{F}}{\delta\rho}\right)\right]^2 \chi(\rho) - \int_0^1 dx \left(\frac{\delta\mathcal{F}}{\delta\rho}\right)\frac{\partial j^{(d)}}{\partial x} = 0. \tag{1.54}$$

The conserved Manna sandpile on a periodic boundary is one of the examples in which the above-mentioned density large deviation function can be calculated in a coarse-grained limit, shown to be related to subsystem mass fluctuation or compressibility [38].

One of the dynamical quantities that can be studied using the MFT is the net particle current, or the total number of particles flowing across the system for an interval $[0, \tau_H]$ as

$$q(\tau_H) = \frac{1}{\tau_H} \int_0^1 dx \int_0^{\tau_H} j(x, \tau) d\tau, \tag{1.55}$$

whose statistics obey a large deviation principle $P(q) \simeq \exp(-\tau_H L \Phi(j))$ [39] and has been studied extensively in the past [40–44] for various diffusive systems, both with boundary driven and periodic boundary conditions. Either the cumulant generating function of q can be written with the distribution of trajectories $\mathbf{Prob}\,(\rho(x,\tau), j(x,\tau))$; and by imposing the continuity equation as a constraint, the optimization problem reduces to solving two Hamiltonian equations, which leads to the expression of the cumulant generating function of the current. Alternatively, one may use the idea of the additivity principle [25] with some constraints on the transport coefficients D and χ. This reduces the optimization problem to a saddle point approximation, which can be solved using the Lagrangian method, directly leading to the expression of $\Phi(j)$.

The framework of MFT, gives us a set of rules to calculate the large deviation functions, all of these calculations are only applicable to those systems where the transport coefficients D and χ are known. Although bulk diffusivity can be identified (not derived) from the diffusive limit of the local microscopic density evolution equation, it is very difficult to find the mobility χ, which can only be obtained from the fluctuations of the microscopic current in the nonequilibrium steady states. Similarly to equilibrium systems, where mobility has the meaning of a proportionality constant between an external drive and the resulting drift current, MFT also prescribes an operational *linear response method* in the nonequilibrium steady states to calculate mobility by suitably biasing the microscopic Markov process rates [9, 11], which we now discuss briefly.

In a one-dimensional periodic boundary lattice (since we need to calculate mobility in the corresponding local equilibrium of the process), we can apply a small force $\vec{F} = F\hat{x}$ is the positive direction of the x axis, in such a way that it should be coupled with the mass transfer rates $c_{i\to j}$ from site i to j. The biased mass transfer rates can now be written as

$$c^F_{i\to j} = c_{i\to j}\psi(\Delta e_i), \tag{1.56}$$

where $\psi(\Delta e_i)$ is a positive function of $\Delta e_i = \Delta m_{i\to j}(\vec{F}\cdot\delta\vec{x}_{ij})$. Δe_i is the additional cost of moving the mass Δm from site i to j and $\delta\vec{x}_{i\to j} = (j-i)a\vec{x}$ is the displacement vector, where

a is the lattice constant. In the limit $|F| \to 0$, we should have $\psi(\Delta e) = 1$. Thus, we can write the Taylor expansion of $\psi(\Delta e)$ as for

$$\psi(\Delta e_i) \simeq 1 + \left[\frac{d\psi(\Delta e)}{d\Delta e}\right]_{\Delta e=0} \Delta e_i = 1 + \frac{1}{2}\Delta m_{i\to j}(\vec{F}\cdot\delta\vec{x}_{ij}) \simeq \exp\left[\frac{\Delta e_i}{2}\right]. \tag{1.57}$$

The definition of $\psi(\Delta e_i)$ in the exponential form, given in the above equation, introduces an equilibrium-like detailed balance condition in the ratio of the probability of forward and reverse movement of the mass with respect to the direction of the force.

Biasing the system in the above-mentioned manner generates a drift part in the hydrodynamic current j along with the diffusive current $j^{(d)}$ as

$$j = -D(\rho)\frac{\partial\rho}{\partial x} + \chi(\rho)\tilde{F}, \tag{1.58}$$

where the force F needs to be rescaled as $F = \tilde{F}/L$ to balance the diffusive current. In this way, one can identify the mobility χ from the hydrodynamic equation. However, the crucial assumption underlying this analysis is the validity of linear response in the nonequilibrium steady state, which inherently violates time-reversal symmetry, and consequently the detailed balance condition. These two conditions are the main requirements to prove a linear response theory in equilibrium systems. Therefore, it becomes important to calculate the current fluctuations using the dynamic equations, which not only directly provide us with the mobility but also verify the applicability of linear response in the nonequilibrium steady states.

1.5 Self organized criticality, $1/f$ noise, and sandpiles

In systems displaying critical phenomena in equilibrium, precise parameter tuning is necessary to reach the critical state. For instance, in the Ising model, achieving a phase transition requires fine-tuning the temperature and external magnetic field to their respective critical values. If the system is initially prepared with values of temperature and magnetic field far from their critical points, the response to external perturbations will not exhibit any critical behaviour. It is generally reasonable to assume that critical phenomena can only be triggered when all relevant parameters are precisely tuned to specific values in most systems that undergo phase transitions.

In 1987, Bak, Tang, and Wiesenfeld (BTW) introduced the concept of "self-organized criticality" (SOC) [45] to explain the origin of spatio-temporal scale invariance in natural systems [46, 47]. The unique aspect of SOC is that it does not require precise fine-tuning of any control parameters to reach a critical state. Instead, the system inherently organizes itself to a critical state through internal mechanisms. In this scenario, the critical state acts as an

attractor in the configuration space of microstates, resulting from the threshold-activated dynamics within the system and the cascading avalanches that follow when a perturbation is triggered.

The primary motivation for the BTW model [45, 48] was to capture the long-range temporal correlations that are ubiquitous in nature [49]. These correlations often manifest as the so-called "$1/f$" or flicker noise, characterized by low-frequency power spectra with a power-law form $1/f^{\psi}$, where $0 < \psi < 2$, spanning a wide range of frequencies f. The occurrence of $1/f$ noise has been observed in various seemingly unrelated systems.

For example, considering ecology on a large scale as a system with many degrees of freedom, forest fires can be seen as active phenomena that can dramatically alter ecology. It has been observed that the size and frequency of the regions affected by fires follow power laws [50].

Another example is the temporal correlation between neural activities in the brain [51, 52], which serves as a mechanism of cognition. The Integrate and Fire model [53, 54] is a fundamental mathematical model in neuroscience, representing neurons as electrical circuits. The model integrates the incoming synaptic currents, leading to a gradual increase in membrane potential over time. Once the membrane potential crosses a threshold, the neuron fires an action potential. Due to its non-linearity, the model exhibits long-range temporal correlation among synaptic firings.

Among other examples are solar flares [55, 56], stock market fluctuations [57], water flow in rivers [49], and resistance fluctuations in conductors [58]. For more details, see the reviews [46, 59]. Despite its widespread occurrence, a general theory that explains the relative abundance of $1/f$ noise in nature remains elusive.

1.5.1 *Experiments with actual sandpiles*

After introducing sandpile models, a natural question arose: Does a real pile of sand or any other granular material exhibit self-organized criticality (SOC)? This question was addressed by Jaeger et al. in an experiment [60] that involved a pile of granular materials (glass beads and aluminium oxide grains) driven in a slowly rotating drum, causing avalanches of grains to flow down the slope of the pile. The researchers measured the outflux of grains (i.e., particle current at the boundary) over time and calculated the power spectrum of the corresponding time signal by monitoring the change in capacitance, which is related to the particle flow rate through a parallel plate capacitor.

The observed power spectrum showed a broadened peak with a subsequent $1/f^3$ decay for large frequencies. The peak in the power spectrum represented the average interval between two successive avalanches, and the large-frequency power-law decay was mainly due

to short-time correlations in the particle currents. In other words, the characteristic $1/f^{\psi}$ behaviour, with $0 \leq \psi < 2$, as seen in real sandpile models, was not observed in this experiment with real granular materials.

As it is reasonable to assume that the geometrical shapes of the sand particles could introduce inertial effects in the experiment, leading to a reduction in the long-range temporal correlations present in the system, another experiment was conducted in the Norwegian city of Oslo, using rice grains [61]. The rod-like structure of the rice grains introduced sufficient anisotropy into the system to minimize inertial effects. In this experiment, self-organized criticality (SOC) was observed in the avalanche statistics, where the avalanche sizes followed a power-law distribution, suggesting events occurring at all length scales and indicating criticality. This experiment highlighted the fact that SOC is not universal for all threshold-activated systems, and that the specific geometry and anisotropy of the system play a significant role.

1.5.2 *Different models*

Sandpiles are spatially extended and threshold-activated systems in which dynamical activities spread through cascades of toppling events (initiated when a local threshold is crossed), resulting in "avalanche"-like dynamical activities and long-ranged correlations in the systems. In these models, in most cases, detailed balance or time-reversal symmetry is broken. As a result, the probability of the steady-state configurations cannot be described by the Gibbs-Boltzmann distributions, and generally, the exact measures of the corresponding nonequilibrium steady states, generated by these systems are unknown. They were envisaged as model systems driven by slow addition of "energy", or grains, with local energy conservation in bulk and dissipation at the boundary. Due to an intriguing interplay between drive and dissipation, the system evolves, apparently without fine-tuning of any parameters, towards a nonequilibrium steady state characterized through avalanches at all scales, i.e., a scale-invariant critical state with power-law distributions concerning various observables. Several sandpile models have been extensively studied in the past. Some of these models are described below.

The BTW model. Bak, Tang, and Wisenfeld (BTW) introduced sandpiles as representative models that illustrate "self-organized criticality" (SOC), which offers a general mechanism for long-range correlations in natural systems, including $1/f$ noise [45, 48]. The BTW model is specifically defined on a two-dimensional square lattice. At each site (x, y) and at a time t, there exists a height variable $h(x, y, t)$ that represents the number of grains at that site.

When $h(x,y,t) \geq h_c = 2d$ (where $d = 2$ for two dimensions), an excess of $2d$ grains topples, distributing one grain to each of the neighbouring sites in two dimension as follows:

$$\begin{aligned} h(x,y,t+1) &= h(x,y,t) - 4, \\ h(x \pm 1,y,t+1) &= h(x \pm 1,y,t) + 1, \\ h(x,y \pm 1,t+1) &= h(x,y \pm 1,t) + 1. \end{aligned} \tag{1.59}$$

The model updates all sites simultaneously and dissipation is considered through the boundaries, where $h(x,y,t) = 0$ is maintained for all time t at the edges. In particular, the total number of grains remains conserved within the bulk, since grains are only dissipated at the boundary.

The Manna model. Another stochastic variant of the sandpile called the Manna model [62] can be defined similarly. In contrast to BTW, here the threshold height h_c does not depend on the dimension of the model, it is simply $h_c = 2$ for all dimensions. Upon toppling, it vacates the toppled site with unit rate by distributing each particle of the toppled site independently with probability $1/2d$ to the nearest neighbours. In the original definition of this model, all sites are updated parallelly and dissipation is considered through the boundaries, where $h(x,y,t) = 0$ is maintained for all time t at the edges. In this thesis, we particularly study the *conserved* or *fixed energy* variant of this model, introduced by Dickman *et al.* [63].

The Oslo ricepile model. Motivated by the Oslo ricepile experiment, discussed in Sec. 1.5.1, where the phenomenon of *self-organized criticality* was observed, Christensen *et al.* introduced a theoretical model [64] called the Oslo model. The main objective of this model was to reproduce the scaling laws observed in the actual experiment. In the Oslo model, a 1-dimensional lattice contains n_i elongated particles at each site i. These particles topple deterministically to 2 nearest neighbours at a unit rate [65]. The critical height n_c associated with each site is determined stochastically and can be either 2 or 3, with equal probability. Whenever a site's particle count n_i exceeds or equals the critical height n_c, the site becomes unstable, leading to two particles moving deterministically to their nearest neighbours in opposite directions. Following the toppling of an active site, the critical height of that site is reset stochastically.

Model of activated random walkers. Motivated by the Manna sandpile model, a *random walk* version of a stochastic sandpile has also been proposed, known as *activated random walk* (ARW) [66]. In the 1-dimensional lattice, a site i can contain n_i particles, where $n_i \geq 0$. The particles can be in either an active or a sleepy state. The active particles hop randomly to the nearest neighbours with a unit rate. Upon coming in contact with an active particle, a sleeping particle becomes active. An active particle becomes inactive or sleepy at a rate λ. Depending on the sleeping rate and global density ρ, the system can be in an active state for $\rho \geq \rho_c$ or in a sleeping state for $\rho < \rho_c$ with no active particles present, where ρ_c is a function of λ. The calculation of the steady-state measure is the main motivation for studying this

simplified model [66] of stochastic sandpiles. In particular, it has been possible to calculate ρ_c exactly in the completely asymmetric version of this model [67].

Fixed energy or conserved version of sandpile models. To gain a more detailed understanding of self-organized criticality using the tools available for known equilibrium critical phenomena, sandpile models with periodic boundary conditions have been proposed, known as conserved or "fixed energy" sandpiles [68]. In these variants, there is no dissipation of energy, and the total number of grains (or total energy) remains conserved. This conservation property allows the system to reach a critical state by tuning the global density. In this scenario, when the mass density exceeds a certain threshold, the system achieves a stable state with continuous activity, known as the active phase [69]. On the other hand, when the global density of conserved quantity, is small, the system tends to relax and settle into a frozen configuration, indicating the absorbing phase. These nonequilibrium phase transitions are known as active absorbing phase transitions [70].

However, whether the critical state of such a system is equivalent to the SOC version of the same model is still a subject of debate. For example, in the case of the BTW model, the critical density below which activity goes to zero globally for the fixed energy model is different from its SOC version, as studied by Fey et al. [71]. On the other hand, for stochastic systems such as the Manna sandpile and the Oslo ricepile model, it is assumed that both types of criticality are the same, as observed in studies by Dickman *et al.* and Grassberger *et al.* [65, 72].

In this thesis, our main focus is the study of the dynamic correlations of current and mass, particularly in the *fixed energy* version of stochastic sandpile models, where the criticality of the fixed energy version and self-organized criticality (SOC) version are believed to be the same.

Numerous studies of sandpiles have been performed, and significant progress has been made in characterizing the static and dynamic properties of both critical and off-critical states of the systems. However, apart from some exact [73–76] and mathematically rigorous [71, 77, 78] results, the majority of the studies have been carried out using simulations [63, 68, 79] and phenomenological field-theoretical descriptions [80–82]. This is primarily due to the fact that the steady-state measure of a driven interacting-particle system such as sandpiles is in most cases a-priori unknown and, as a result, analytic calculations, beginning with a microscopic dynamical description, prove to be quite challenging [81, 83, 84].

Perhaps not surprisingly, despite the fact that an explanation of $1/f$ noise was the main motivation for BTW's introduction of sandpile models, a good theoretical understanding of their time-dependent properties, particularly the exact hydrodynamics and the related transport coefficients governing the large-scale relaxations, remains lacking [72, 85–88].

1.5.3 *Do sandpiles actually possess* $1/f$ *power spectra?*

Historically, the time-dependent properties of sandpiles have been studied in terms of power spectra of dynamical activity, such as instantaneous toppling events in systems [89, 90]. Studies in the original slowly driven version of BTW sandpile reported the $1/f^{\psi}$ power law behaviour of the power spectrum for the activity, with the exponent $\psi < 2$ [45], although their claim was refuted as several simulation studies later found the exponent $\psi = 2$ [89, 91]. Subsequently, a more careful scaling analysis of simulation data, however, revealed non-trivial power spectra with the exponent $\psi < 2$ [90]. They also provided a clear argument, when one can expect $\psi < 2$ in the time series analysis of $V(t)$ or local toppling events at a time t. An avalanche is defined as a connected sequence of non-zero values of $V(t)$. If the average size (i.e. the total number of topplings) of such avalanches of duration T scales as $s(T) \sim T^{\gamma_{st}}$ and the dynamics is self-similar, then the average shape of the avalanche $V(T,t)$ T should follow $V(T,t) = T^{\gamma_{st}-1} f_{shape}(t/T)$, where f_{shape} is a scaling function [90]. Considering the correlation function $C(\theta,s) = \int dt V(t,s)V(t+\theta,s)$ of avalanches of a given size s, averaged over all such avalanches, one can define the power spectrum by simply taking the Fourier transform of this quantity as $P(f,s) = \int_0^{\infty} d\theta C(\theta,s) \cos f\theta \simeq s^2 g_P(f^{\gamma_{st}} s)$, where $g_P(x)$ is another scaling function. Finally, $P(f) = \int ds D(s) P(f,s) = f^{-\gamma_{st}(3-\tau)} \int^{s^* f^{\gamma_{st}}} x^{2-\tau} g_P(x) dx$, where $D(s) \sim s^{-\tau}$ is the size distribution of the avalanche and s^* is the upper cut-off of the avalanche size. By demanding the convergence of $P(f)$, $\psi = \gamma_{st}(3-\tau)$ can finally be obtained. Now, as can be seen, ψ is crucially dependent on the expression of the scaling function $g_P(x)$. Kertesz and Kiss [89] obtained $\psi = 2$ assuming $g_P(x) \propto 1/(1+x^{2/\gamma_{st}})$. Jensen et al. also yield $\psi = 2$ [91] by assuming $g_p(x) \propto (1-\cos x^{1/\gamma_{st}})/x^{2/\gamma_{st}}$. Therefore, the resolution of this problem can only be achieved through the derivation of the shape function f_{shape} of the avalanche pulses, which remains pending to date. In Ref. [90], the authors obtained this function numerically and found that the original BTW model in two dimensions and the Manna model in one, two and three dimensions exhibit a power spectrum of the form $f^{-\psi}$ with $\psi < 2$.

1.5.4 *Theoretical analysis of* $1/f$ *spectra in sandpiles*

On the theoretical front, a dynamic renormalization group analysis of phenomenological field-theoretical equations describing a "running" sandpile (driven with a finite grain addition rate) allowed an analytical calculation of exponents ψ[92], involving activity and output current, where $1/f$ type noise was observed, with $\psi = -1$; quite interestingly, temporal correlations in the long-time regime were found to be *anti-correlated*, with $\psi = -1 < 0$. In Ref.[92] Hwa and Kardar claimed that 1/f noise could appear in the system if individual avalanches created at different space points are allowed to overlap and develop nontrivial

correlations in the process. This scenario is only possible if the system is driven at a fixed rate, rather than the slow driving limit proposed in SOC theory. They considered one-dimensional critical slope-type sandpiles (toppling condition depends on slope threshold value), where grains are added at a site i with a probability $p = J_{in}/L$ that changes the local height $h(i,t)$ by 1 as $h(i,t+1) = h(i,t)+1$, with J_{in} as average deposition rate and system size L [87, 92]. Local topplings occur only when the local slope $h(i,t) - h(i+1,t) > \Delta$ crosses a certain threshold value Δ, which triggers a transfer of mass n_f from site i to $i+1$ as

$$\begin{aligned} h(i,t+1) &= h(i,t) - n_f, \\ h(i+1,t+1) &= h(i+1,t) + n_f; \end{aligned} \tag{1.60}$$

in simulation $n_f = 2$ and $\Delta = 8$. The left boundary is closed, that is, $h(0,t) = h(1,t)$ and the right boundary dissipates grains, that is, $h(L+1,t) = 0$. Two quantities studied are the power spectrum $S_J(f) \sim J^{\psi_J}$ of the instantaneous current or the outflux at the boundary site $J(t)$ and $S_E(f) \sim f^{-\psi_E}$, the power spectrum of the total number of topplings $E(t)$ that occur in time t. They proposed a continuum drift-diffusion equation for the height variable $h(\vec{x},t)$ based on symmetries and conserved quantities of the system as

$$\frac{\partial h(\vec{x},t)}{\partial t} = D_{\|}\partial_{\|}^2 h + D_{\perp}\partial_{\perp}^2 h - \frac{\lambda}{2}\partial_{\|}(h^2) + \eta(\vec{x},t), \tag{1.61}$$

where $\vec{x}\perp$ and $\vec{x}\parallel$ are defined using the transport direction vector $\hat{n}$ as $\vec{x}\parallel = (\vec{x}\cdot\hat{n})\hat{n}$ and $\vec{x}\perp = \vec{x} - \vec{x}_{\|}$. Noise η in d dimensions defined as

$$\left\langle \eta(\vec{x},t)\eta(\vec{x'},t') \right\rangle = 2\Gamma\delta^d(\vec{x}-\vec{x'})\delta(t-t'), \tag{1.62}$$

and physically indicates the random addition of grains. Although it is not clear whether quadratic terms in h should be allowed or not, as they can break the translation symmetry in h, it has been shown that it is possible to generate such terms in the hydrodynamic equation using symmetry arguments [93]. The dynamic renormalization group analysis of Eq. (1.61) shows that by suitably rescaling length and time variables as $x_{\|} \to bx_{\|}$, $\vec{x}_{\perp} \to b^{\zeta}\vec{x}_{\perp}$, and $t \to b^z t$, the variable h scales as $h \to b^{\chi}h$. This rescaling provides us with the critical exponents χ, ζ, and z. Furthermore, using the dimensional arguments, one can obtain the dynamical correlation of current and energy as $C_J(t) = \langle J(t)J(0)\rangle - \langle J(t)\rangle\langle J(0)\rangle \sim t^{[4\chi+(d-1)\zeta]/z}$ and $C_E(t) = \langle E(t)E(0)\rangle - \langle E(t)\rangle\langle J(0)\rangle \sim t^{[4\chi+(d-1)\zeta+1]/z}$ and the corresponding power spectra $S_J(f) \sim f^{-\psi_J}$ with $\psi_J = 1/z$ and $S_E(f) \sim f^{-\psi_E}$ with $\psi_E = 2/z$. In two dimensions, with the dynamical exponent $z = 6/5$, one finally obtains the numerical values of ψ_J and ψ_E as ≈ 0.83 and ≈ 1.67 respectively, demonstrating the $1/f$ noise spectrum. *Despite a successful theoretical derivation of $1/f$ noise (up to the validity of field-theoretic arguments),*

their framework cannot capture the dynamical instabilities, i.e., the intermittent bursts of activity, which are the signature of sandpiles.

Hwa and Kardar's result could well be the earliest signature of *"dynamic hyperuniformity"* in sandpiles. Recently, this particular aspect of dynamic hyperuniformity, i.e., hyperuniformity in the temporal domain, was also analysed in a variant of the slowly-driven sandpiles, called the Oslo ricepile [94]. Similar low-frequency behaviour of the activity power spectrum with $\psi = -1$ (i.e., anti-correlated) was observed in Ref. [95] for a directed deterministic sandpile on a ladder with a finite driving rate; in the slow-driving limit though, Maslov *et al.* [96] previously showed the model to exhibit $1/f^{\psi}$ power spectrum, with $\psi = 1$, for the total mass fluctuation. In a slightly different study [97] of a driven sandpile, albeit on a periodic domain, the power-spectrum of activity had been found to be $1/f^{\psi}$ with $\psi = 1$. In a conserved deterministic lattice gas in two dimensions [98], subsystem mass fluctuation was found to exhibit the power spectrum $S_M(f) \sim f^{-\psi_M}$, where $\psi = 1.5$ away from criticality and $\psi \approx 1.8$ near criticality.

1.5.5 *Singularity in hydrodynamic transport equations*

Actually, in a variant of the two-state sandpile model, Carlson et al. [99–101] first argued that the hydrodynamics of the sandpile models should be governed by a nonlinear diffusion equation with a *singular bulk diffusion coefficient*. Their argument can be summarized in a simple two-state one-dimensional lattice model on periodic boundary conditions, where a site can either be vacant or contain just a single particle. The dynamics is governed by the hopping of particles with unit rate to the nearest *vacant sites* (unlike SSEP, these do not necessarily have to be the nearest neighbours). This dynamics satisfies the detailed balance condition with w.r.t. the Bernoulli product measure where a site can be either occupied with probability ρ or vacant with probability $1-\rho$, with ρ being the conserved global density, $\rho = N/L$. The local microscopic current across a bond $(i, i+1)$ can then simply be written in terms of a r point correlation function [87], $\mathcal{A}^r(i) = \langle \prod_{r'=1}^{r} \eta_{i+r'-r} \rangle$ (which is the probability of having consecutive r numbers of sites to be occupied to the left of site i) as

$$J(i, i+1) = \sum_r \left[\mathcal{A}^r(i) - \mathcal{A}^r(i+r) \right], \tag{1.63}$$

which satisfy the following local continuity equation,

$$\frac{\partial \langle \eta_i \rangle}{\partial t} = J(i-1, i) - J(i, i+1). \tag{1.64}$$

In the hydrodynamic limit, $i \to x = i/L$ and $t \to \tau = t/L^2$, the above continuity equation takes the form of a nonlinear diffusion equation [87], given by

$$\frac{\partial \rho}{\partial \tau} = \frac{\partial}{\partial x}\left[D(\rho)\frac{\partial \rho}{\partial x}\right], \tag{1.65}$$

where bulk-diffusivity has the singular form $D(\rho) = \frac{1+\rho}{(1-\rho)^3}$. This result can suitably be generalized to open boundaries as well. Though it is nice to derive the transport coefficients from microscopic dynamics, it is very difficult to obtain them for interacting particle systems, which violate detailed balance and consequently the time-reversal symmetry. Particularly in the case of sandpile models, where in most of the time, the stationary steady-state measure is a-priori unknown.

All the sandpile models, such as the deterministic BTW model and the stochastic Manna sandpile, Oslo ricepile, and ARW model described in Sec.1.5.2, are examples of interacting particle systems. Recently, a new hydrodynamic theory has been proposed in Ref.[38, 102], based on local equilibrium assumptions for the 'fixed energy' stochastic sandpile models. This theory allows us to identify the bulk diffusivity in these systems, which exhibits a singular behaviour near criticality. In a variant of Manna sandpile [63], it has been shown that the hydrodynamic density evolution equation follows Eq.(1.65), where $D(\rho) \sim 1/(\rho - \rho_c)^{1-\beta}$, with β defined by $a(\rho) \sim (\rho - \rho_c)^{\beta}$ and $\beta < 1$. This relation tells us how the activity $a(\rho)$ or order parameter scales with density near the active absorbing phase transition. Here, ρ_c is the critical density, and the activity goes to zero when the global density becomes less than critical density, $\rho < \rho_c$, while the system stays in an active state with $a(\rho) \neq 0$ when $\rho \geq \rho_c$. Moreover, using the biasing technique given by the Macroscopic fluctuation theory, the mobility $\chi(\rho)$ has been identified as the activity $a(\rho)$ itself. Ref.[38] has nicely verified the equilibrium-like Einstein relation given in Eq.(1.51). In Ref.[102], this hydrodynamic theory has been further developed to characterize the near-critical large-scale density relaxation in conserved Manna sandpile and found that near criticality, the width of the density perturbation grows anomalously with time as t^{ω}, where $\omega = 1/(\beta + 1)$.

1.5.6 *Residence time distribution*

The residence time of a tagged particle in a sandpile is an interesting time-dependent property to study. Since the particle transports in the sandpiles are governed by active site toppling events, the dynamic properties of the sandpiles are expected to be related to the residence time of a tagged particle inside the system. Residence time is measured as the time interval between the insertion and exit of a tagged particle. Surprisingly, the residence-time distribution is independent of the avalanche exponents, despite being influenced by local

toppling activities and capable of displaying power-law tails. However, these distributions are not universal because they can vary depending on the particle addition details and toppling (or particle-transfer) rules within the systems. Dhar and Pradhan [103–105] extensively studied this quantity and derived the distribution time analytically in the Oslo model.

In the Oslo ricepile experiment [61], the distribution of the residence time T of a tagged particle $P(T, L)$ was measured for the size of the system L. In the actual experiment, it was observed that the distribution actually follows a power law of $T^{-\gamma}$ where $\gamma \approx 2.4$ was observed. The mean residence time was found to scale with the size of the system, L as $\langle T \rangle \sim L^{\nu}$ with $\nu \approx 1.5$. Motivated by this experiment, Christensen et al. proposed the Oslo ricepile model [64] and it was argued later in Ref.[106], that the power law distribution should be dominated by those tagged particles that spend a long time in the system as they are buried deep in the pile by the dynamics. Thus, it can be shown that the residence time is related to the height fluctuation of the sandpile. In fact, it was found that the trapping time is related to the height fluctuation, and the residence time T_{res} has an exponential cutoff $T_{res} \sim \exp(\kappa L^3)$ [105] and the mean residence time $\langle T_{res} \rangle \sim L^2$. The cumulative distribution of residence time was found to be $\textbf{Prob.}(T \geq t) \sim L^{\omega} / \left[t \left\{ \ln(t/L^{\omega}) \right\}^{\delta} \right]$, where ω and δ are model-dependent exponents that appeared as logarithmic corrections. Thus, it gives $P(T, L) \sim T^{-2}$, that is, $\gamma = 2$, and the discrepancy with the observed value in simulation can be accounted for by the neglected logarithmic corrections.

Due to the anisotropy, present in the sandpile models, one can write the space-dependent diffusion equation for the probability distribution of a tagged particle as

$$\frac{\partial P(x,t)}{\partial t} = \frac{1}{2} \nabla^2 \left[\mathcal{D}_s(x) P(x,t) \right], \tag{1.66}$$

where $\mathcal{D}_s(x)$ is the self diffusion coefficient and proportional to the average number of toppling at position x. The initial condition can be specified as $P(x, t = 0) = r(x)$ where $r(x)$ is the addition rate at site x [107]. da Cunha et al. [84] also studied the self diffusion coefficient in the context of stochastic sandpile model and found its scaling property same as activity near the criticality. But, as we shall see later, this quantity can be calculated exactly from the simple argument of random walkers and can be obtained exactly in the steady state as the activity divided by the global density [108].

1.5.7 *Hyperuniformity*

Another fascinating aspect of sandpiles that has only recently been discovered is that the critical state of the sandpiles can be *hyperuniform* [65, 109, 110], meaning that the static fluctuations of subsystem mass scale with subsystem size in an anomalously slow manner [111,

112]. For a system in d dimensions, one can characterize particle number (M_l) fluctuations in a region of volume $v = l^d$ by

$$\sigma^2(\rho) = \frac{\sigma^2(M_l)}{l^d} = \frac{\langle M_l^2 \rangle - \langle M_l \rangle^2}{l^d} \propto l^{-\lambda}. \tag{1.67}$$

The exponent λ can vary between 0 and 1. A value of $\lambda = 0$ corresponds to a completely random state of the system, such as $\sigma^2(M_l) \sim l^d$ following the central limit theorem. On the other hand, a value of $\lambda = 1$ corresponds to $\sigma^2(M_l) \sim l^{d-1}$, representing fluctuations of particle numbers in a subvolume of a completely crystalline state of matter. Any value of λ that meets $0 < \lambda < 1$ denotes hyperuniform fluctuations of particle number or hyperuniformity. As discussed in Ref. [111], hyperuniform states typically exhibit long-range negative spatial correlations of density, which has also been reported for stochastic sandpile models near criticality [65, 109, 110]. This is contrary to what is known in equilibrium critical states, where one would usually expect positive long-range and divergent fluctuations.

However, we currently have limited knowledge of hyperuniform states of matter, and one can only speculate as to how such a state emerges dynamically in the first place [113]. In fact, except for a few exact results concerning static properties of the hyperuniform state [114, 115], there has been little theoretical progress in this direction, and a systematic approach to identifying the precise microscopic dynamical origin of anomalous fluctuations remains elusive. In this scenario, a closer examination of the underlying dynamical mechanism that results in such a state is desirable.

In this thesis, we address the above issues in the context of conserved stochastic sandpiles and specifically focus on a continuous-time variant of the celebrated Manna sandpile [62, 63], activated random walk (ARW) [66], Oslo ricepile model [65] that has drawn a lot of attention in the past. Moreover, our results concerning the dynamical observables have also been presented for a single particle transfer Manna model, which happens to satisfy the detailed balance condition. Stochastic sandpiles are a paradigm for systems, exhibiting a nonequilibrium *absorbing phase transition* from a dynamically active state to an absorbing one having no activities, upon tuning the global density. As we have already mentioned, through several simulation studies in the recent past, it is known that the critical state of the stochastic sandpiles is indeed hyperuniform [65, 109]. In addition, in recent studies, it has been shown that the (near-)critical state of stochastic sandpiles, particularly in the Manna model, is characterized by singular transport coefficients such as bulk diffusivity, leading to anomalous relaxation and particle transport in the system [38, 102].

As a next step, one may ask the long-standing question *'how could one calculate the dynamic correlations in sandpile models using this framework?'* In this thesis, we have tried to answer this question and have obtained some beautiful results, which only highlight the richness of

sandpile models. In the next section, we will give a brief review of the results obtained in this thesis.

1.6 PLAN OF THE THESIS

In this thesis, we study four variants of stochastic sandpile models, namely, the conserved version of the *Manna sandpile* with two-particle transfer (Chapter 2) and one-particle transfer (Chapter 3), the model of *activated random walkers* (ARW, Chapter 4), and the *Oslo ricepile model* (Chapter 5), in one dimension with periodic boundary conditions. The main observables of interest in our study are the current in the system and the mass. While the total mass is conserved due to the periodic boundary conditions of the system, the mass of a subsystem is a fluctuating quantity. This fluctuation of mass in the subsystem is governed by a microscopic continuity equation, which relates the fluctuation of mass to the current. We present the proof of an equilibrium-like Einstein relation that quantitatively connects these two fluctuation relations. This relation allows us to write the fluctuation properties of the subsystem mass, which is a static quantity, to the fluctuation properties of the current, which is a dynamic quantity.

To obtain this result, we have developed a theoretical framework to calculate the dynamic correlations of both mass and current. Using these correlation functions, we computed the fluctuation properties of the spacetime-integrated current and demonstrated the subtlety of its convergence in the infinite volume limit.

By carefully taking the proper limit, we prove that the intensive spacetime-integrated current fluctuation is indeed identical to the macroscopic transport coefficient known as mobility. This mobility relates an external bias to the corresponding drift current in the system. In a sense, we have established a Green-Kubo-like relation in nonequilibrium steady states.

The chapter-wise main results are as follows.

(1) *Chapter 2*

We theoretically investigate the time-dependent correlations for current and mass in the (quasi-)steady state of the one-dimensional conserved Manna sandpile. We begin with a microscopic dynamical description of the model and then introduce a new, albeit approximate, closure scheme that allows us to analytically calculate the time-dependent correlation functions for current and mass, as well as the corresponding power spectra. We establish a direct quantitative relationship between various static and dynamic fluctuation properties in terms of the density-dependent activity - the system's "order parameter", and its derivative.

In sec.2.2.2, we present our calculation method, where we introduce an approximate truncation scheme, helping us to calculate the dynamic correlations. Then in sec.2.2.3,

we study the dynamic properties of bond current fluctuations. We show that, in the thermodynamic limit, with system size $L \to \infty$ and density $\bar{\rho}$ fixed, the variance of the local (bond) current $\mathcal{Q}(T)$ up to time T grows subdiffusively with time. That is, we have $\langle \mathcal{Q}^2(T) \rangle \sim T^{\alpha}$, where, away from criticality (in the time regime $T \ll L^2$), the exponent $\alpha = 1/2$, and near criticality (in the regime $T \ll L^z$), the current fluctuation is further suppressed with the exponent $\alpha = 1/2 - \mu$, where $\mu = (\beta + 1)/2\nu_\perp z > 0$, and β, $\nu_\perp$, and z are the activity, correlation-length, and dynamic exponents, respectively. Thus, the anomalous suppression of the current fluctuation near criticality serves as the *dynamic precursor* to the hyperuniform state formed at the critical point.

In sec.2.2.4.1, we calculated the corresponding power spectrum. We then proceed to calculate the variance of the cumulative subsystem (i.e., space-time integrated) current and elucidate its relationship with the particle mobility in sec.2.2.4.3. We find that the time-dependent (two-point) correlation function for the instantaneous current is long-ranged (power-law) and negative, resulting in the low-frequency behavior of the corresponding power spectrum $S_{\mathcal{J}}(f) \sim f^{\psi_{\mathcal{J}}}$, which vanishes at low frequency, where $\psi_{\mathcal{J}} = 1/2$ away from criticality (strictly speaking, in the time regime $1/L^2 \ll f \ll 1$ for finite L) and $\psi_{\mathcal{J}} = 1/2 + \mu$ near criticality (in the time regime $1/L^z \ll f \ll 1$).

In sec. 2.2.6, we show that the power spectrum $S_M(f)$ for subsystem-mass fluctuation, on the other hand, diverges $S_M(f) \sim f^{-\psi_M}$ at low frequency, where $\psi_M = 3/2$ away from criticality ($1/L^2 \ll f \ll 1$) and $\psi_M = 3/2 - \mu$ near criticality ($1/L^z \ll f \ll 1$). However, these two exponents are not independent and are connected by a scaling relation $\psi_M = 2 - \psi_{\mathcal{J}}$.

We study the self-diffusion coefficient of tagged particles in sec. 2.2.5. We theoretically show that the self-diffusion coefficient $\mathcal{D}_s(\bar{\rho})$ is identically equal to the ratio, $a(\bar{\rho})/\bar{\rho}$, of the activity to the global number density of the system, i.e., $\mathcal{D}_s(\bar{\rho}) = a(\bar{\rho})/\bar{\rho}$, a fluctuation relation that connects the (scaled) fluctuation of the displacement of the tagged particles to the density-dependent activity. This relation immediately explains a previous simulation observation of Ref. [84] that, upon approaching criticality, the self-diffusion coefficient in the conserved Manna sandpile vanishes in the same fashion as the activity.

Furthermore, we derive the equilibrium-like fluctuation relation, also known as the Einstein relation, which connects the scaled fluctuation of the subsystem mass, denoted as $\sigma^2(\bar{\rho}) = \langle M_l^2 \rangle - \langle M_l \rangle^2$ (where M_l represents the mass in a subsystem of size l), with the scaled fluctuation of the subsystem current. This relation involves the density-dependent bulk diffusion coefficient $D(\bar{\rho})$ and is expressed as $\sigma^2(\bar{\rho}) = \sigma_{\mathcal{Q}}^2(\bar{\rho})/2D(\bar{\rho})$.

Finally, in Sec. 2.2.7, we studied the driven hydrodynamics of the Manna sandpile, which was earlier developed in [38]. We showed that the intensive spacetime-integrated current

fluctuation is indeed exactly equal to the mobility, which serves as the proportionality constant between the external drive and the drift current.

(2) *Chapter 3*

In this chapter, we focus on investigating the time-dependent correlations for current and mass in the steady state of the Manna sandpile with a one-particle transfer rule. The microscopic configurations of this model satisfy the detailed balance condition in the active state of the system. As a result, we found that the fluctuation properties of this system remain the same both near- and far-from-criticality. Consequently, dynamic hyperuniformity does not emerge near criticality in this model. In sec.3.3.2, we show that $\langle \mathcal{Q}^2(T) \rangle$ follows a power law with an exponent of $1/2$. Next, in sec. 3.3.3, we demonstrate that the current power spectrum $S_{\mathcal{J}}(f)$ at a low frequency decays as $f^{\psi_{\mathcal{J}}}$, with $\psi_{\mathcal{J}} = 1/2$ as f approaches the *zero* frequency.

We compute the variance of the cumulative subsystem current at sec. 3.3.4, which corresponds to the integration of current over space and time, and examine its connection with particle mobility in sec. 3.4 by studying the driven hydrodynamic of this model. Then, we analyze the power spectrum of the subsystem mass fluctuation in Section 3.3.6. $S_M(f)$ exhibits a divergence at low frequencies, following a power law $f^{-\psi_M}$, where $\psi_M = 3/2$. ψ_M and $\psi_{\mathcal{J}}$ are related by equation $\psi_M = 2 - \psi_{\mathcal{J}}$, as in the previous model. The values of the exponents are the same near-criticality as they are away from criticality.

In section 3.3.5, we studied the mean square displacements of tagged particles in the steady state, which provide insight into the self-diffusion coefficient of individual particles. We confirm that the self-diffusion coefficient, denoted $\mathcal{D}_s(\bar{\rho})$, is equal to the ratio of activity to the global number density of the system, specifically $\mathcal{D}_s(\bar{\rho}) = a(\bar{\rho})/2\bar{\rho}$.

(3) *Chapter 4*

In Sec. 4.2.1, we explore the hydrodynamic equation of density relaxation in the ARW model, which captures the large-scale relaxation properties of this model. We also identify the operator-level expression for the microscopic diffusive current. Importantly, the detailed balance is broken in this model, both in the active and in the absorbing states. In the subsequent section, Sec. 4.2.2.2, we derive the expression of $\langle \mathcal{Q}^2(T) \rangle$, which exhibits a growth behaviour of T^{α}, where $\alpha = 1/2$ away from criticality and $\alpha \approx 1.4$ near criticality. The near-critical exponent has been obtained from simulations. The decrease in the growth exponent α indicates the emergence of dynamic hyperuniformity near criticality.

In Sec. 4.2.3 and 4.2.6, we conducted a study of the power spectra $S_{\mathcal{J}}(f)$ and $S_M(f)$, respectively. For the current power spectrum, we found that the corresponding exponent is $\psi_{\mathcal{J}} = 1/2 + \mu$, where we derived $\mu = 0$ away from criticality and obtained $\mu \approx 0.1$ near criticality from simulation. Furthermore, we observed that ψ_M satisfies the relation

$\psi_M = 2 - \psi_{\mathcal{J}}$. Similarly to our investigation in previous models, we also studied the space-time integrated current in Sec. 4.2.4 and described its relationship with mobility using the driven hydrodynamics formalism in Sec. 4.3.

In Sec. 4.2.5, we proved that the self-diffusivity of the activated random walker model (ARW) is given by the ratio of the active particle density to the global density of the system. The expression for self-diffusivity is $\mathcal{D}_s(\bar{\rho}) = u(\bar{\rho})/2(1+\lambda)\bar{\rho}$, where $u(\bar{\rho})$ represents the global active particle density. Compared to the previous two models, the definition of $\mathcal{D}_s(\bar{\rho})$ in the ARW model includes the active particle density instead of the active site density. This difference results in a distinct hydrodynamic structure of the model compared to the model in Chap. 2, although the gradient property is still present in the microscopic equation.

(4) *Chapter 5*

In this chapter, we study the Oslo model and the fundamental structure of fluctuations of the Oslo model is very different from those we studied in the earlier chapters, is the addition of centre of mass conservation by the microscopic dynamics along with the density conservation in this model. The introduction of two conserved quantities generates maximal dynamic hyperuniformity.

In Sec. 5.2.1, we analyze the fluctuation of the time-integrated current, finding it to follow a power law behaviour as $\langle \mathcal{Q}^2(T) \rangle \sim T^{\alpha}$. Near criticality, from simulations, we determine $\alpha \approx 1/3$. Conversely, away from criticality, we observe a nice power-law decay when plotting the relative current fluctuation $\lim_{T\to\infty} \langle \mathcal{Q}^2(T) \rangle - \langle \mathcal{Q}^2(T) \rangle$ as a function of time, which decays as $T^{-1/2}$ in line with the theoretical derivation. Both near and away from criticality, after the initial growth of dynamic current fluctuation, it eventually saturates at a value dependent on the global density. Remarkably, away from criticality, this saturation value is approached much faster than near criticality, suggesting that away from criticality, current fluctuations exhibit more hyperuniformity compared to near-critical fluctuations.

In Sec. 5.2.2.2 and 5.2.4, we investigate the current and mass power spectra. From both theoretical analysis and simulations, we find $\psi_{\mathcal{J}} = 3/2$ and $\psi_M = 1/2$. However, near criticality, the simulations suggest different values of $2/3$ and $4/3$ for $\psi_{\mathcal{J}}$ and ψ_M, respectively. These results indicate a considerably more suppression of fluctuations away from criticality than near criticality, with fluctuations being more strongly suppressed away from criticality.

In Sec. 5.2.3, we present the calculation of the tagged particle diffusion coefficient, denoted as $\mathcal{D}_s = a(\bar{\rho})/\bar{\rho}$, which interestingly turns out to be the same as the one we found in the Manna model with a two-particle transfer rule. This result holds true both far

and near criticality of the system. The presence of similar diffusive motion for a tagged particle is an intriguing feature that we discovered in the Oslo model, as well as in the three earlier models.

2

THE MANNA SANDPILE WITH TWO PARTICLE TRANSFER RULE

2.1 INTRODUCTION

The stochastic two-state sandpile model was introduced by S. Manna in [62]. The original model was studied on a two-dimensional square lattice with open boundary conditions, where each site can only be occupied with either 0 or 1 particle, and the threshold height is set to $z_c = 2$. The system is updated in parallel by toppling the sites that have a particle number greater than or equal to z_c, with the toppled particles randomly distributed to the nearest neighbours. In this model, the cluster size (s) probability distribution $D(s, L)$ and the probability distribution of avalanche time t, $D(t, L)$ follow power law and satisfy the following the scaling relation(s) for a system of size L as

$$D(s, L) = L^{\beta_s} f_1\left(\frac{s}{L^{\nu_s}}\right), \tag{2.1}$$

$$D(t, L) = L^{\beta_t} f_2\left(\frac{t}{L^{\nu_t}}\right), \tag{2.2}$$

where the expected behaviour of the scaling functions f_1 and f_2 are given by $f_1(x) \sim x^{-\tau+1}$ and $f_2(x) \sim x^{-y+1}$ for $0 \ll x \ll 1$. τ and y are the cluster size exponent and the avalanche lifetime exponent, and are related to the exponents β_s, β_t and ν_s, ν_t as $\tau = (\beta_s + \nu_s)/\nu_s$, $y = (\beta_t + \nu_t)/\nu_t$. Critical exponents were found to be $\beta_s \approx 0.82$, $\nu_s \approx 2.75$ and $\beta_t \approx 0.78$, $\nu_t \approx 1.55$ [62].

In this chapter, we study a specific variant of the Manna sandpile model, introduced by Dickman et al., on a one-dimensional periodic boundary condition. We refer to this model as the *one-dimensional fixed-energy stochastic sandpile*. They studied the model with continuous-time dynamics with the same threshold height z_c as in the original model. Each active site updated with unit rate where exactly two particles leave the site and distributed among two nearest neighbours randomly. The fixed energy model was particularly introduced to characterize the active-absorbing phase transition in the sandpile model with global density as the tuning parameter. Above a critical density, $\rho_c \approx 0.94885$ the system stays in an active

state with a finite amount of active site density for an infinitely long time. On the contrary, below the critical density the system is in the absorbing state with activity or active site density as *zero*. Near the critical density, the activity ($a(\rho)$) follows a power law [63],

$$a(\Delta) = L^{-\beta/\nu_\perp}\mathcal{R}(\Delta L^{1/\nu_\perp}), \tag{2.3}$$

where $\Delta = \rho - \rho_c$ is the relative density from criticality and the critical exponents were found to be $\beta \approx 0.42$, $\nu_\perp \approx 1.81$. The autocorrelation function $C(t)$ of activity increases with system size near criticality as L^z, where z is the dynamical exponent of value $z \approx 1.61$.

In particular, an important time-dependent property, the diffusion of a tagged particle, has been studied in this model by da Cunha et al. [84], where the self-diffusion coefficient, $\mathcal{D}_s$, was reported proportional to activity near criticality in the steady state, which we calculated exactly in sec.2.2.5 and obtained the relation among self-diffusivity, activity and density as $\mathcal{D}_s = a(\bar{\rho})/\bar{\rho}$, where $\bar{\rho}$ is the global-conserved density.

Recently, a hydrodynamic theory of density relaxation in the fixed energy model was developed [38, 102], where the bulk diffusivity $D(\bar{\rho})$ has been identified as $D(\bar{\rho}) \sim \Delta^{\beta-1}$ which is singular as $\bar{\rho}$ approaches the critical density ρ_c and the mobility χ was found to be equal to the activity itself. In this chapter, we further develop the fluctuating hydrodynamics of this theory and calculate the dynamical properties of current and mass fluctuations, which have been shown to be related via an equilibrium-like Einstein relation in sec.A.2.5.

2.2 DYNAMIC CORRELATIONS IN THE STEADY STATE

2.2.1 *Model and definitions*

We consider the continuous-time variant [63] of the conserved ("fixed energy") Manna sandpile [62] on a ring of L sites. Any site i, with $i = 0, 1, \ldots, L-1$, can have $m_i \geq 0$ number of particles, with $m_i = 0, 1, \ldots, N$; the total number of particles

$$N = \sum_{i=0}^{L-1} m_i, \tag{2.4}$$

remains *conserved*; in this paper we throughout denote the global density as $\bar{\rho} = N/L$. The dynamical rules are as following: An *active* site - a site with $m_i > 1$ - topples with rate 1 by randomly, and independently, transferring each of the two particles to one of its nearest neighbours.

The sytem violates detailed balance and eventually reaches a nonequilibrium (quasi-)steady state, which is not described by the familiar equilibrium Boltzmann-Gibbs distribution and whose probability measure is apriori unknown. The steady state of the system is usually

charactarized through a global order parameter, called the activity $a(\bar{\rho})$, defined as the density of active sites,

$$a(\bar{\rho}) = \frac{\langle N_a \rangle}{L}, \tag{2.5}$$

where N_a is the total number of active sites in the system and $\langle . \rangle$ denotes the steady-state average. Interestingly the system has a nontrivial spatio-temporal structure and, upon tuning the global density $\bar{\rho}$, undergoes an absorbing phase transition. That is, above a critical density ρ_c, there are dynamical activities in the system, but, below the critical density, the dynamical activities in the steady state cease and consequently there are no movements of particles in the system. The absorbing phase transition in the conserved Manna sandpile has been intesively studied in the past and can be charactarized by the following critical exponents - the order-parameter exponent β, the correlation-length exponent $\nu_\perp$ and the dynamic exponent z: Up on approaching criticality from above, we have the following scaling behavior of activity $a(\Delta) \sim \Delta^\beta$, correlation length $\xi \sim \Delta^{-\nu_\perp}$, and the relaxation time $\tau_r \sim L^z$ where relative density $\Delta = \bar{\rho} - \rho_c > 0$ and we use the critical density $\rho_c \approx 0.94885$, as estimated in Ref. [63], throughout our paper.

One can write update rules in an infinitesimal time-interval between time t and $t + \mathrm{d}t$ as given below,

$$m_i(t + \mathrm{d}t) = \begin{cases} m_i(t) + 1 & \frac{1}{2}\hat{a}_{i+1}\,\mathrm{d}t \\ m_i(t) + 1 & \frac{1}{2}\hat{a}_{i-1}\,\mathrm{d}t \\ m_i(t) + 2 & \frac{1}{4}\hat{a}_{i+1}\,\mathrm{d}t \\ m_i(t) + 2 & \frac{1}{4}\hat{a}_{i-1}\,\mathrm{d}t \\ m_i(t) - 2 & \hat{a}_i\,\mathrm{d}t \\ m_i(t) & [1 - \Sigma\,\mathrm{d}t], \end{cases} \tag{2.6}$$

where $\Sigma = (3/4)(\hat{a}_{i+1} + \hat{a}_{i-1}) + \hat{a}_i$; here $\hat{a}_i$ is an indicator function with $\hat{a}_i = 1$ if the site is active and $\hat{a}_i = 0$ otherwise. Using the above update rules eq.(2.6), we can write the time evolution equation of the first moment of local mass as

$$\frac{\mathrm{d}}{\mathrm{d}t}\langle m_i(t) \rangle = [\langle \hat{a}_{i-1}(t) - 2\hat{a}_i(t) + \hat{a}_{i+1}(t) \rangle]\,. \tag{2.7}$$

Denoting the local density $\rho_i(t) = \langle m_i(t) \rangle$, we can alternatively write the above equation as

$$\frac{\mathrm{d}}{\mathrm{d}t}\rho_i(t) = \sum_k \Delta_{i,k} a_k(t) \tag{2.8}$$

where $\Delta_{i,k}$ is the discrete Laplacian and $a_k(t) = \langle \hat{a}_k \rangle (t)$ is the average instantaneous activity. On the large spatio-temporal scales and by taking the diffusive scaling limit $i \to x = i/L$ and $t \to \tau = t/L^2$, we can write the hydrodynamic time-evolution equation for the local density field $\rho(x, \tau)$ as in eq.(2.8) [38, 102],

$$\frac{\partial \rho(x,\tau)}{\partial \tau} = \frac{\partial^2 a(\rho)}{\partial x^2} \equiv \frac{\partial}{\partial x}\left(D(\rho) \frac{\partial \rho}{\partial x} \right), \tag{2.9}$$

where $D(\rho)$ is the density-dependent bulk-diffusion coefficient. It has been previously demonstrated in Ref. [38, 102], the bulk-diffusion coefficient can be written in terms of the derivative of the activity $a(\rho)$ wrt density ρ,

$$D(\rho) = \frac{da(\rho)}{d\rho} \equiv a'(\rho). \tag{2.10}$$

Indeed the relaxation processes occuring on a large (coarse-grained) scale are primarily governed by the bulk-diffusion coefficient - the fact that we later use to introduce a truncation scheme [see eq.(2.26)] for analytically calculating various time-dependendent correlation functions, which would not have been possible otherwise in a system with nontrivial correlations as in sandpiles. Notably, one can recast the density evolution equation (2.8) in a microscopic form of the continuity equation,

$$\frac{\mathrm{d}}{\mathrm{d}t}\rho_i(t) = \langle \mathcal{J}_i(t) - \mathcal{J}_{i+1}(t) \rangle \,, \tag{2.11}$$

where the microscopic instantaneous current $\mathcal{J}_i(t)$ is defined as the number of particles crossing a bond $(i, i+1)$ in an infinitesimal time interval $(t, t + \mathrm{d}t)$. It is useful to define a related observable - the cumulative, or time-integrated, bond current $\mathcal{Q}_i(t)$ upto time t, which is used to calculate various other correlation functions, such as that involving mass and activity, and is easily measured in simulations. At the microscopic level, the time-integrated current $\mathcal{Q}_i(t)$ is defined as the total number of particles transferred accross i^{th} bond, connecting the nearest-neighbour pair of sites $(i, i+1)$, during a time interval $[0, t]$. That is, the time-integrated current accross the i^{th} bond during an infinitesimal time interval $[t, t + \mathrm{d}t]$ is simply $\mathcal{J}_i(t)\,\mathrm{d}t$ with

$$\mathcal{J}_i(t) = \lim_{\Delta t \to 0} \frac{(\mathcal{Q}_i(t + \Delta t) - \mathcal{Q}_i(t))}{\Delta t} \equiv \frac{d\mathcal{Q}_i(t)}{\mathrm{d}t}, \tag{2.12}$$

and

$$\mathcal{Q}_i(T) = \int_0^T \mathrm{d}t\, \mathcal{J}_i(t). \tag{2.13}$$

On the average level, we therefore have

$$\langle \mathcal{J}_i(t) \rangle = \left\langle \frac{d\mathcal{Q}_i(t)}{\mathrm{d}t} \right\rangle = \frac{d\,\langle \mathcal{Q}_i(t) \rangle}{\mathrm{d}t}. \tag{2.14}$$

We now decompose the instantaneous current into two parts - a diffusive component $\mathcal{J}_i^{(d)}(t)$ and a fluctuating component $\mathcal{J}_i^{(fl)}(t)$,

$$\mathcal{J}_i(t) = \mathcal{J}_i^{(d)}(t) + \mathcal{J}_i^{(fl)}(t), \tag{2.15}$$

where, motivated by eq.(2.7), we identify the diffusive current as

$$\mathcal{J}_i^{(d)}(t) = \hat{a}_i(t) - \hat{a}_{i+1}(t). \tag{2.16}$$

Indeed, as we see later, in that case only the diffusive-current component possesses long-ranged temporal correlations, varying slowly in time as a power law, and the fluctuating component on the other hand is simply a delta-correlated one, explaining the motivation behind the above decomposition. Note that, due to the fact $\langle \mathcal{J}_i \rangle = \left\langle \mathcal{J}_i^{(d)} \right\rangle = \langle \hat{a}_i \rangle - \langle \hat{a}_{i+1} \rangle$, we must have $\left\langle \mathcal{J}_i^{(fl)} \right\rangle = 0$. Indeed the fluctuating current component can be related to the (conserve) noise term in an appropriately coarse-grained fluctuating hydrodynamic theory, which can be then used to study the large-scale fluctuation properties of the system [9, 116].

In the following sections, we study the fluctuation properties of various compenents of currents, instantaneous and the fluctuating one as decomposed in eq.2.16. Throughout the paper, we use the following notation for correlation function $C_r^{AB}(t,t')$ involving any two local observables $A_i(t)$ and $B_j(t')$ with $t \geq t'$,

$$C^{AB}_{r=|i-j|}(t,t') = \left\langle A_i(t) B_j(t') \right\rangle - \left\langle A_i(t) \right\rangle \left\langle B_j(t') \right\rangle, \tag{2.17}$$

where $r = |j-i|$ is the relative distance. Further, we denote the spatial Fourier transform of the correlation function $C_r^{AB}(t,t')$ as

$$\tilde{C}_q^{AB}(t,t') = \sum_{r=0}^{L-1} C_r^{AB}(t,t') e^{iqr}, \tag{2.18}$$

where $q = 2\pi k/L$ and $k = 0, 1, \ldots, L-1$ and the inverse Fourier transform as

$$C_r^{AB}(t,t') = \frac{1}{L} \sum_q \tilde{C}_q^{AB}(t,t') e^{-iqr}. \tag{2.19}$$

By introducing a truncation scheme as discussed below, we can theoretically compute the statistics of different combinations of various local currents $\mathcal{J}_i$, $\mathcal{J}_i^{(d)}$, $\mathcal{J}_i^{(fl)}$ as well as mass m_i, essentially in terms of the following two correlation functions - $\langle \mathcal{Q}_i(t)\mathcal{Q}_j(t')\rangle$ and $\langle m_i(t)\mathcal{Q}_j(t')\rangle$.

2.2.2 *Theory*

For the conserved Manna sandpile, we write the stochastic update equation of the integrated current $\mathcal{Q}_i(t)$ in an infinitesimal time (continuous) interval $[t, t+\mathrm{d}t]$,

$$\mathcal{Q}_i(t+\mathrm{d}t) = \begin{cases} \textbf{\textit{events}} & \textbf{\textit{probabilities}} \\ \mathcal{Q}_i(t)+1 & \frac{1}{2}\hat{a}_i(t)\,\mathrm{d}t \\ \mathcal{Q}_i(t)+2 & \frac{1}{4}\hat{a}_i(t)\,\mathrm{d}t \\ \mathcal{Q}_i(t)-1 & \frac{1}{2}\hat{a}_{i+1}(t)\,\mathrm{d}t \\ \mathcal{Q}_i(t)-2 & \frac{1}{4}\hat{a}_{i+1}(t)\,\mathrm{d}t \\ \mathcal{Q}_i(t) & 1-\Sigma\,\mathrm{d}t \end{cases} \tag{2.20}$$

where $\Sigma = (\hat{a}_i(t) - \hat{a}_{i+1}(t))$. Using the above update rules, the time-evolution equation for the first moment of the time-integrated current $\mathcal{Q}_i(t)$ can be written as

$$\frac{\mathrm{d}}{\mathrm{d}t}\langle \mathcal{Q}_i(t)\rangle = \langle \hat{a}_i(t)\rangle - \langle \hat{a}_{i+1}(t)\rangle\,. \tag{2.21}$$

Similarly, using eq.(2.20), we find the time-evolution equation for the second moment $\langle \mathcal{Q}_i(t)\mathcal{Q}_{i+r}(t')\rangle = C_r^{\mathcal{Q}\mathcal{Q}}(t,t')$ of the integrated current at two different times t and t', for $t > t'$, as given below (see appendix A.3.1 for details),

$$\frac{\mathrm{d}}{\mathrm{d}t}C_r^{\mathcal{Q}\mathcal{Q}}(t,t') = \Big(C_r^{\hat{a}\mathcal{Q}}(t,t') - C_{r-1}^{\hat{a}\mathcal{Q}}(t,t')\Big). \tag{2.22}$$

The above equation, which is central to our study, is however difficult to solve exactly due to an infinite hierarchy of correlation functions involved and so we employ below an approximation scheme.

We note that the evolution of space and time dependendent activity-current correlation function $C_r^{\hat{a}\mathcal{Q}}(t,t')$ appearing in eq.(2.22) contains higher-order correlation functions, involving activity, current and some other observables. The calculations of the higher-order correlations would eventually result in a rapidly growing complexity in the hierarchy of correlation

functions, which do not constitute a closed set of equations. More specifically, one can start with the infinitesimal time update equation for $\hat{a}_i$ itself,

$$\hat{a}_i(t+\mathrm{d}t) = \begin{cases} \textit{events} & \textit{probabilities} \\ \hat{a}_i(t)+1 & \frac{1}{2}\hat{a}_{i+1}(t)\hat{p}_i(t)\delta_{m_i,1}\,\mathrm{d}t \\ \hat{a}_i(t)+1 & \frac{1}{2}\hat{a}_{i-1}(t)\hat{p}_i(t)\delta_{m_i,1}\,\mathrm{d}t \\ \hat{a}_i(t)+1 & \frac{1}{4}\hat{a}_{i+1}(t)\hat{p}_i(t)\,\mathrm{d}t \\ \hat{a}_i(t)+1 & \frac{1}{4}\hat{a}_{i-1}(t)\hat{p}_i(t)\,\mathrm{d}t \\ \hat{a}_i(t)-1 & \hat{a}_i(t)(\delta_{m_i,2}+\delta_{m_i,3})\,\mathrm{d}t \\ \hat{a}_i(t) & 1-\Sigma\,\mathrm{d}t\,, \end{cases} \tag{2.23}$$

where $\hat{p}_i(t) = (1-\hat{a}_i(t))$ and $\Sigma = (\hat{p}_i(t)/2)(\delta_{m_i,1}+1/2)[\hat{a}_{i+1}+\hat{a}_{i-1}] + \hat{a}_i(\delta_{m_i,2}+\delta_{m_i,3})$. From this update equation, for $t > t'$, we can write the evolution equation for $C_r^{a\mathcal{Q}}(t,t')$ as

$$\frac{\mathrm{d}}{\mathrm{d}t}C_r^{a\mathcal{Q}}(t,t') \equiv \frac{\mathrm{d}}{\mathrm{d}t}\left\langle \hat{a}_0(t)\mathcal{Q}_r(t')\right\rangle_c = \left\langle \left\{\frac{\mathrm{d}}{\mathrm{d}t}\hat{a}_0(t)\right\}\mathcal{Q}_r(t')\right\rangle_c, \tag{2.24}$$

where the observable inside the curly bracket evolves according to the equation,

$$\begin{aligned} &\frac{\mathrm{d}}{\mathrm{d}t}\hat{a}_0(t) = -\hat{a}_0(t)(\delta_{m_0,2}+\delta_{m_0,3}) + \\ &[\hat{p}_0(t)(\hat{a}_1(t)+\hat{a}_{L-1}(t))]\left(\frac{1}{2}\delta_{m_0,1}+\frac{1}{4}\right). \end{aligned} \tag{2.25}$$

Clearly, to solve for $C_r^{a\mathcal{Q}}(t,t')$, one needs to calculate the correlation functions $\langle\delta_{m_0,2}\hat{a}_0(t)\mathcal{Q}_r(t')\rangle$ and $\langle\delta_{m_0,1}\hat{a}_0(t)\hat{a}_1(t)\mathcal{Q}_r(t')\rangle$, which would in turn involve another set of even higher-order correlation functions; of course, in this way, one generates an infinite hierarchy of equations, which is difficult to handle.

We bypass the difficulty by employing the following approximation scheme, which in fact truncates the otherwise infinite hierarchy. To this end, we approximate the local diffusive current, which is the gradient of the instantaneous local activity and written as

$$\mathcal{J}_i^{(d)}(t) = [\hat{a}_i(t)-\hat{a}_{i+1}(t)] \equiv D(\bar{\rho})[m_i(t)-m_{i+1}(t)], \tag{2.26}$$

where the bulk-diffusion coefficient is given by $D(\bar{\rho}) = a'(\bar{\rho})$ as in eq.(2.10) and can be treated as a constant. Essentially, we have assumed in the above truncation scheme that fluctuations around the global density $\bar{\rho}$ are small and the local current (the gradient of activity) relaxes diffusively via the gradient of local mass. As demonstrated later, this approximation captures

relevant correlations quite well on the large (hydrodynamic) time scales. More specifically, to compute correlations between any observable $A(t)$ (e.g., current or mass) and the current observable $\mathcal{J}_i^{(d)}(t)$, we replace the diffusive-current observable $\mathcal{J}_i^{(d)}(t)$ by its truncated form as given in the rhs of eq(2.26), to obtain the following equality (approximate),

$$\langle A(t)\mathcal{J}_i^{(d)}(t')\rangle \simeq a'(\bar{\rho})\left\langle A(t)\{m_i(t') - m_{i+1}(t')\}\right\rangle. \tag{2.27}$$

Now we can proceed further by first rewriting eq.(2.22) as

$$\frac{\mathrm{d}}{\mathrm{d}t}C_r^{\mathcal{Q}\mathcal{Q}}(t,t') = a'(\bar{\rho})\Big(C_r^{m\mathcal{Q}}(t,t') - C_{r-1}^{m\mathcal{Q}}(t,t')\Big), \tag{2.28}$$

and then expressing the time-evolution equation for the mass-current correlations $C_r^{m\mathcal{Q}}(t,t') = \langle m_i(t)\,\mathcal{Q}_{i+r}(t')\rangle - \langle m_i(t)\rangle\langle \mathcal{Q}_{i+r}(t')\rangle$ as

$$\frac{\mathrm{d}}{\mathrm{d}t}C_r^{m\mathcal{Q}}(t,t') \simeq a'(\bar{\rho})\sum_k \Delta_{r,k}C_k^{m\mathcal{Q}}(t,t'), \tag{2.29}$$

where have used eq.(2.26) in the intermediate steps (see appendix sec. A.3.2). It is worth noting that, in eq.(2.26) or in eqs.(2.28) and (2.29), the activity appears simply as a global density-dependent constant prefactor $a(\bar{\rho})$ and thus we obtain a closed set of equations, involving only mass and current correlations; equations (2.28) and (2.29) can be solved, albeit in terms of the activity $a(\bar{\rho})$, which however remains undetermined in our theory. Interestingly, it was previously possible to exactly calculate the dynamic correlation functions in simple exclusion processes [116] because, in that case, one already gets a closed set of equations for mass and current correlations and, furthermore, because the steady-state measure is a product one, allowing one to calculate various static (time-independent) quantities, which enter into the expression of the current and mass fluctuations. Without an explicit knowledge of the steady state measure [117], the Manna sandpile, on the other hand, is nontrivial due to the nonzero spatial correlations present in the system, making explicit calculations of the static quantities, such as the density-dependent activity, quite difficult. Nevertheless, as shown below, by extending the formalism developed in the context of simple exclusion processes [116], one can calculate various dynamic correlations in terms of activity and obtain fluctuation relations, which precisely quantify the underlying relationship between dynamic and static fluctuations in the system.

At this stage, it is useful to introduce the Fourier representation of the respective correlation functions as given in eq.(2.18), and we can then write eqs.(2.28) and (2.29) in the respective Fourier modes,

$$\frac{\mathrm{d}}{\mathrm{d}t}\tilde{C}_q^{\mathcal{Q}\mathcal{Q}}(t,t') = a'(\bar{\rho})\tilde{C}_q^{m\mathcal{Q}}(t,t')\left[1 - e^{iq}\right], \tag{2.30}$$

and

$$\frac{\mathrm{d}}{\mathrm{d}t}\tilde{C}_q^{m\mathcal{Q}}(t,t') = -a'(\bar{\rho})\lambda_q \tilde{C}_q^{m\mathcal{Q}}(t,t'), \tag{2.31}$$

where

$$\lambda_q = 2[1-\cos q]. \tag{2.32}$$

Now, eqs.(2.30) and (2.31), can be integrated to have

$$\begin{aligned}\tilde{C}_q^{\mathcal{Q}\mathcal{Q}}(t,t') = &\int_{t'}^{t} \mathrm{d}t''\, a'(\bar{\rho})\tilde{C}_q^{m\mathcal{Q}}(t'',t')\left[1-e^{iq}\right] \\ &+\tilde{C}_q^{\mathcal{Q}\mathcal{Q}}(t',t'),\end{aligned} \tag{2.33}$$

and

$$\tilde{C}_q^{m\mathcal{Q}}(t,t') = e^{-a'(\bar{\rho})\lambda_q(t-t')}\tilde{C}_q^{m\mathcal{Q}}(t',t'). \tag{2.34}$$

respectively. However, to fully solve for the unequal-time correlation functions $\tilde{C}_q^{\mathcal{Q}\mathcal{Q}}(t,t')$ and $\tilde{C}_q^{m\mathcal{Q}}(t,t')$, we need to calculate their respective equal-time counterparts as well. First we obtain the evolution equation for the equal-time mass-current correlation function $C_r^{m\mathcal{Q}}(t',t')$ and, then writing $C_r^{m\mathcal{Q}}(t',t')$ in the Fourier space (using eq.(A.40); see appendix A.3.4 for details), we get

$$\frac{\mathrm{d}}{\mathrm{d}t'}\tilde{C}_q^{m\mathcal{Q}}(t',t') = -a'(\bar{\rho})\lambda_q \tilde{C}_q^{m\mathcal{Q}}(t',t') + \tilde{f}_q(t'), \tag{2.35}$$

where the Fourier transform of the source term $\tilde{f}_q(t')$ in the steady state is given by

$$\tilde{f}_q = \tilde{C}_q^{m\hat{a}}\left(1-e^{-iq}\right) - 2a(\bar{\rho})\left(1-e^{-iq}\right)\left[1+\frac{\lambda_q}{4}\right]. \tag{2.36}$$

Now eq.(2.35) can be directly integrated to obtain

$$\tilde{C}_q^{m\mathcal{Q}}(t',t') = \int_0^{t'} \mathrm{d}t''\, e^{-a'(\bar{\rho})\lambda_q(t'-t'')}\tilde{f}_q(t''), \tag{2.37}$$

substituting which into eq.(2.34), we get the unequal-time mass-current correlation function in terms of $\tilde{f}_q$,

$$\tilde{C}_q^{m\mathcal{Q}}(t,t') = \int_0^{t'} \mathrm{d}t''\, e^{-a'(\bar{\rho})\lambda_q(t-t'')}\tilde{f}_q(t''). \tag{2.38}$$

To calculate the above correlation, we need to calculate the activity-mass correlation as in eq.(2.36). Importantly, as shown below, we can calculate the static (time-independent) activity-mass correlation function exactly in the steady state (see appendix A.3.5). Using the steady-state condition $dC_r^{mm}(t,t)/dt = 0$, we obtain

$$\frac{\mathrm{d}}{\mathrm{d}t}C_r^{mm}(t,t) = \sum_k 2\left\langle m_0 \Delta_{rk}\hat{a}_k\right\rangle_c + B_r = 0, \tag{2.39}$$

where B_r is the source term having the form,

$$B_r(\bar{\rho}) = 7a(\bar{\rho})\delta_{0,r} - 4a(\bar{\rho})(\delta_{0,r+1}+\delta_{0,r-1}) + \frac{a(\bar{\rho})}{2}(\delta_{0,r+2}+\delta_{0,r-2}). \tag{2.40}$$

Equation (2.39) can be solved by employing a generating function,

$$G(z) = \sum_{r=0}^{\infty} C_r^{m\hat{a}} z^r, \tag{2.41}$$

for the equal-time mass-activity correlation; see appendix.(A.3.5). Here we directly provide the solution of the generating function in terms of the static density-dependent activity,

$$G(z) = \frac{3a(\bar{\rho})}{2} - \frac{a(\bar{\rho})}{4}z, \tag{2.42}$$

implying the mass-activity static correlation to be

$$C_r^{m\hat{a}} = \begin{cases} \frac{3a(\bar{\rho})}{2} & \text{for } r = 0, \\ -\frac{a(\bar{\rho})}{4} & \text{for } |r| = 1, \\ 0 & \text{otherwise,} \end{cases} \tag{2.43}$$

which is in fact exact. Then, by writing Fourier transform of the above equation, we have

$$\tilde{C}_q^{m\hat{a}} = a(\bar{\rho}) + \frac{a(\bar{\rho})}{4}\lambda_q, \tag{2.44}$$

and substituting the above in eq.(2.36), we straightforwardly obtain

$$\tilde{f}_q = -a(\bar{\rho})\Big(1 - e^{-iq}\Big)\left(1 + \frac{\lambda_q}{4}\right). \tag{2.45}$$

2.2.3 *Time-integrated current fluctuation*

In this section, we calculate the time-integrated bond-current fluctuation, by using the theory developed in the previous section. To this end, we substitute eq.(2.45) into eq.(2.38) and get an explicit solution the first term on the rhs of eq.(2.33). Similarly, we can calculate the second term on the rhs of eq.(2.33) as given below,

$$C_r^{\mathcal{Q}\mathcal{Q}}(t,t) \simeq \int_0^t \mathrm{d}t'\, \Gamma_r(t') + \frac{1}{L}\int_0^t \mathrm{d}t'\, a'(\bar{\rho}) \sum_{q=0}^{L-1} \tilde{C}_q^{m\mathcal{Q}}(t',t')\Big[1 - e^{iq}\Big](2 - \lambda_{qr}), \tag{2.46}$$

where $\lambda_{qr} = 2[1 - \cos(qr)]$; see appendix sec A.3.3 for details. Here the quantity $\Gamma_r(t)$ is the strength of the steady-state correlation function for the fluctuating current $\Big\langle \mathcal{J}_0^{(fl)}(t)\mathcal{J}_r^{(fl)}(t')\Big\rangle = \Gamma_r(t)\delta(t-t')$ as derived later in eq.(2.62). Since we are interested only in the steady-state properties, the strength Γ_r is replaced by its steady-state value,

$$\Gamma_r(\bar{\rho}) = 3a(\bar{\rho})\delta_{0,r} - \frac{a(\bar{\rho})}{2}(\delta_{0,r+1} + \delta_{0,r-1}), \tag{2.47}$$

which depends on global density $\bar{\rho}$, through the density-dependent activity $a(\bar{\rho})$; for the detail calculation of the strength Γ_r, see section 2.2.4.1. Now the Fourier transform of eq.(2.46) leads to the second term of rhs of eq.(2.33). By using the inverse Fourier transform of eq.(2.33), we finally obtain the desired space- and time-dependent current correlation function in the steady-state,

$$\begin{aligned} C_r^{\mathcal{Q}\mathcal{Q}}(t,t') =& t'\Gamma_r - a'(\bar{\rho})a(\bar{\rho})\frac{1}{L}\sum_q \int_0^{t'} \mathrm{d}t'' \int_0^{t''} \mathrm{d}t'''\, e^{-a'(\bar{\rho})\lambda_q(t''-t''')}\lambda_q\left(1 + \frac{\lambda_q}{4}\right)(2 - \lambda_{qr}) \\ & - a'(\bar{\rho})a(\bar{\rho})\frac{1}{L}\sum_q \int_{t'}^{t} \mathrm{d}t'' \int_0^{t'} \mathrm{d}t'''\, e^{-a'(\bar{\rho})\lambda_q(t''-t''')}\lambda_q\left(1 + \frac{\lambda_q}{4}\right)e^{-iqr}. \end{aligned} \tag{2.48}$$

The asymptotic behavior of the above equation can be straightforwardly obtained as given below (see appendix A.2.1 for details),

$$\big\langle \mathcal{Q}^2(T)\big\rangle \simeq \begin{cases} \frac{2a(\bar{\rho})}{\sqrt{\pi a'(\bar{\rho})}} T^{\frac{1}{2}} & \text{for } 1 \ll T \ll L^2, \\ \frac{2a(\bar{\rho})}{L} T & \text{for } T \gg L^2. \end{cases} \tag{2.49}$$

In simulation, we verify a special case of eq.(2.48) by putting $r = 0$ and $t = t' \equiv T$, i.e., the time-integrated bond current fluctuation $\langle \mathcal{Q}^2(T) \rangle \equiv C_0^{\mathcal{Q}\mathcal{Q}}(T,T)$ (here average current $\langle \mathcal{Q}(T) \rangle = 0$ for the steady-state measurement). In fig.2.1, we plot $\langle Q^2(T) \rangle$, obtained from simulation (plotted in solid lines), for various densities $\bar{\rho} = 2.0$ (red), $\bar{\rho} = 1.5$ (blue), $\bar{\rho} = 1.2$ (green), $\bar{\rho} = 1.0$ (purple), $\bar{\rho} = 0.97$ (orange) as a function of T. The arrow accross the solid lines in the fig.2.1 signifies the increasing order of global density $\bar{\rho}$.

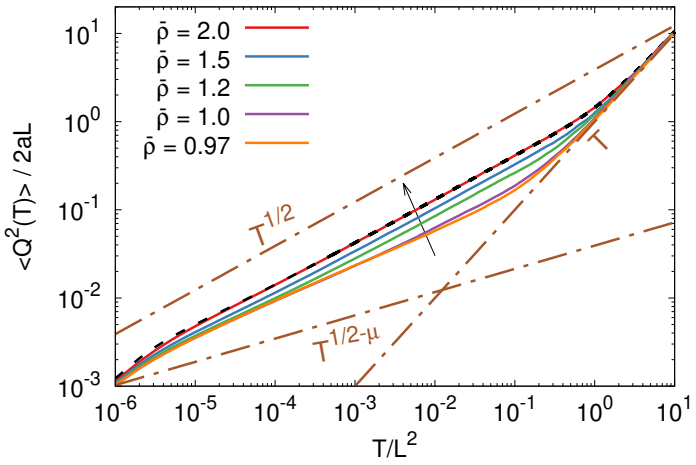

Figure 2.1: Scaled fluctuations of cumulative (time-integrated) bond-current up to time T, obtained from simulations (solid lines), is plotted as a function of scaled time T/L^2 for different densities $\bar{\rho} = 2.0$ (red), $\bar{\rho} = 1.5$ (blue), $\bar{\rho} = 1.2$ (green), $\bar{\rho} = 1.0$ (purple), $\bar{\rho} = 0.97$ (orange), and for system size $L = 1000$, where the arrow accross the solid lines denotes the increasing order of $\bar{\rho}$; theory as in eq.(2.48) with $r = 0$, $t = t' = T$ (black dashed line) is in an excellent agreement with simulation for $\bar{\rho} = 2.0$. Three guiding dot-dashed lines signify the initial-time subdiffusive growth $\langle Q^2(T) \rangle \sim T^{1/2}$ [as in the first part of eq.(2.49)] and the late-time diffusive growth $\langle Q^2(T) \rangle \sim T$ [as in the second part of eq.(2.49)] away from criticality, and the initial-time anomalously suppressed subdiffusive growth $\langle Q^2(T) \rangle \sim T^{1/2-\mu}$ [as in eq.(2.51)] near criticality.

Indeed the dynamical behaviors as predicted by the asymptotics in eq.(2.49) are different in two different time regimes: On smaller initial time scales $1 \ll T \ll L^2$, the time-integrated current grows sub-diffusively as $T^{1/2}$ and, on larger (hydrodynamic) time scales $T \gg L^2$, grows linearly as T. We compare the simulation result with that obtained from our theory eq.(2.48) with $r = 0$ and $t = t' = T$, for $\bar{\rho} = 2.0$ (black dashed line) and for system size $L = 1000$; one can see an excellent agreement between simulation and theory.

As mentioned previously, our theory is expected to be valid at hydrodynamic times ($T \gg L^z$) and the small-time ($T \ll L^z$) behavior of current fluctuation, especially near criticality, is not quite well captured by eq.2.48). However the small-time behavior near criticality can still be obtained qualitatively by using the following standard scaling analysis. Indeed, first resorting to a simple dimensional analysis, we can see that the activity scales as $a(\Delta) \sim \Delta^{\beta} \sim T^{-\beta/\nu_{\perp} z}$, where the relative density $\Delta = \bar{\rho} - \rho_c \ll 1$ and we use the following scaling

relations: correlation length $\xi \sim T^{1/z}$ the relative density $\Delta \sim \xi^{-1/\nu_\perp} \sim T^{-1/\nu_\perp z}$, with z being the dynamic exponent. Thus, by writing $a(\Delta)/\sqrt{a'(\Delta)} \sim T^{-\mu}$, we straightforwardly have, in the initial-time regime $1 \ll T \ll L^z$, the scaling behavior of the current fluctuation $\left\langle \mathcal{Q}^2(T) \right\rangle \sim (a/\sqrt{a'})T^{1/2} \sim T^{\alpha}$, where the exponents

$$\alpha = \frac{1}{2} - \mu \tag{2.50}$$

and

$$\mu = \frac{\beta + 1}{2\nu_\perp z}. \tag{2.51}$$

More precisely, near criticality we expect the following scaling form for the time-integrated bond-current fluctuation to hold,

$$\left\langle \mathcal{Q}^2(T) \right\rangle \simeq L^{\alpha z} \mathcal{G}\left(\Delta L^{1/\nu_\perp}, \frac{T}{L^z}\right) = T^{\alpha} \mathcal{F}\left(\Delta L^{1/\nu_\perp}, \frac{T}{L^z}\right), \tag{2.52}$$

where $\mathcal{G}$ and $\mathcal{F}$ are two scaling functions. To determine the exponent α in eq.(2.52) from simulations, we take density value such that $\Delta L^{1/\nu_\perp} \to 0$ and then we plot in Fig. 2.2 the scaled variance of time-integrated bond current $T^{-\alpha} \left\langle \mathcal{Q}^2(T) \right\rangle$ as a function of the scaled time T/L^z for rather quite smaller system sizes $L = 100$ (solid magenta line), $L = 200$ (green dashed line) and $L = 500$ (blue dotted line), respectively and for $\bar{\rho} = 0.95$. We get a reasonably good scaling collapse of simulation data, with the exponent estimated to be $\alpha \approx 0.297$; our theoretical prediction of the exponent $\alpha \approx 0.26$, computed from scaling relations eqs.(2.50) and (2.51) by using $\beta \approx 0.42$, $z \approx 1.66$ and $\nu_\perp \approx 1.81$ [63], slightly underestimates that obtained from simulation though.

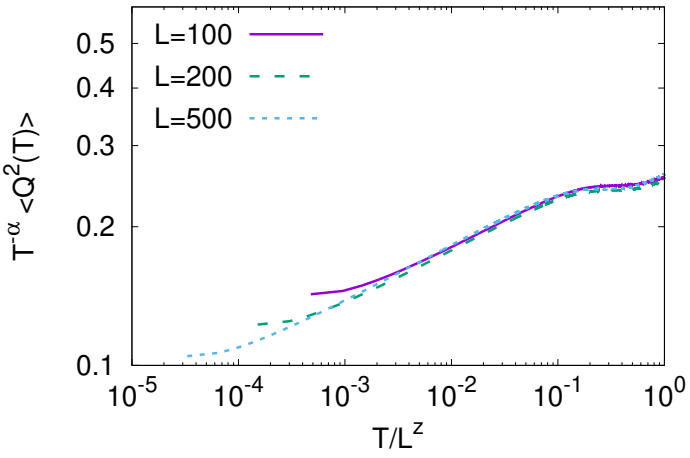

Figure 2.2: The scaled variance $T^{-\alpha}\left\langle \mathcal{Q}^2(T)\right\rangle$ of time-integrated bond current $\mathcal{Q}(T)$ up to time T, obtained from simulations, is plotted as a function of scaled time T/L^z for system size $L = 100$ (solid magenta line), $L = 200$ (green dashed line) and $L = 500$ (blue dotted line) and for (near-critical) density $\bar{\rho} = 0.95$, where, to achieve the scaling collapse, we use $\alpha \approx 0.297$ and $z \approx 1.66$. The value of $\alpha \approx 0.297$ obtained from simulations is not far from $\alpha \approx 0.26$ obtained from theory as in eqs.(2.50) and (2.51) with $\beta \approx 0.42$, $\nu_\perp \approx 1.81$ [63].

The variance of time-integrated bond current is known to grow subdiffusively in the initial-time regime in diffusive systems, such as symmetric simple exclusion processes [116, 118]. Now, away from criticality, the relaxation processes in sandpiles are diffusive [38, 102] and, therefore not surprisingly, the current fluctuation exhibits a subdiffusive growth, as derived in the first part of eq.(2.49). Near-critical relaxation processes in the Manna sandpile, on the other hand, are anomalous and we observe nontrivial scaling behavior. When compared to a normal diffusive system, the Manna sandpile near criticality exhibits strong suppression of current fluctuations and much slower subdiffusive growth of temporal fluctuations due to the lack of local activity, as described in eq.(2.52); we call it a "dynamic hyperuniformity", which is quite analogous to hyperuniformity studied in the spatial domain [109, 111] and is reminiscent of that identified in the context of temporal statistics of avalanches in a particular version sandpile, called the Oslo ricepile [94]. Of course, the dynamic hyperuniformity, or the anomalously subdiffusive growth of temporal fluctuations, can be equivalently characterized in terms of the current and mass power spectra, or the respective dynamic correlation functions, as discussed in the following sections.

2.2.4 *Current fluctuation and its power spectrum*

2.2.4.1 *Instantaneous current*

In this section, we calculate in the steady-state the time-dependent (unequal-time) current-current correlation function $C_r^{\mathcal{J}\mathcal{J}}(t) \equiv C_r^{\mathcal{J}\mathcal{J}}(t, t' = 0)$ of the instantaneous bond current by taking time derivative of time-integrated bond current correlation as given below,

$$C_r^{\mathcal{J}\mathcal{J}}(t) = \left[\frac{\mathrm{d}}{\mathrm{d}t}\frac{\mathrm{d}}{\mathrm{d}t'}C_r^{\mathcal{Q}\mathcal{Q}}(t, t')\right]_{t'=0}, \tag{2.53}$$

where $t \geq t'$. Now, after differentiating eq.(2.48), we can write the time-dependent current correlation as

$$C_r^{\mathcal{J}\mathcal{J}}(t) = \Gamma_r \delta(t) - a'(\bar{\rho})a(\bar{\rho})\left[\frac{1}{L}\sum_q e^{-a'(\bar{\rho})\lambda_q t}\lambda_q\left(1 + \frac{\lambda_q}{4}\right)e^{-\mathrm{i}qr}\right], \tag{2.54}$$

where Γ_r is the strength of the fluctuating current $\mathcal{J}^{fl}(t)$ and calculated below (see eq.(2.62)). We note that, as $\lambda_q \geq 0$ for any q, the current correlation function is *negative* $C_r^{\mathcal{J}\mathcal{J}}(t) < 0$ for any $t > 0$. Moreover, provided that we first take the infinite-system-size limit $L \to \infty$, the time-integrated bond current correlation function $C_0^{\mathcal{J}\mathcal{J}}(t)$ over a large time interval $[-T, T]$ decays as a function of time T as given below,

$$\int_{-T}^{T} C_0^{\mathcal{J}\mathcal{J}}(t)\,\mathrm{d}t \simeq \frac{a(\bar{\rho})}{\sqrt{\pi a'(\bar{\rho})}}T^{-\frac{1}{2}}. \tag{2.55}$$

Finally, by taking the limit $T \to \infty$, we obtain the following identity,

$$\int_{-\infty}^{\infty} C_0^{\mathcal{J}\mathcal{J}}(t)\,\mathrm{d}t = 0; \tag{2.56}$$

see appendix A.2.2 for details. Indeed, the above result is a direct consequence of the negative current correlation present in the system and explains why the time-integrated bond current fluctuation, as derived in eq.(2.49), grows subdiffusively in the initial-time regime, $1 \ll t \ll L^2$. The asymptotic form of the time-dependent instantaneous current correlation function, for $t > 0$, in the thermodynamic limit can be written as

$$C_0^{\mathcal{J}\mathcal{J}}(t) \simeq -\frac{a(\bar{\rho})}{4\sqrt{\pi a'(\bar{\rho})}}t^{-\frac{3}{2}}, \tag{2.57}$$

where the density dependendent term $a(\bar{\rho})/\sqrt{a'(\bar{\rho})}$ in the prefactor is the same as that in eq.(2.49) (see appendix A.2.2). Again, by employing the dimensional scaling argument used

in the previous section to derive eq.(2.51), we obtain a modified power-law decay of the instantaneous current correlation near criticality,

$$C_0^{\mathcal{J}\mathcal{J}}(t) \sim -t^{-\left(\frac{3}{2}+\mu\right)}. \tag{2.58}$$

Clearly the decay is faster than that away from criticality. As discussed previously, the faster decay of the near-critical current correlation function is due to the fact that the activity is very small in the vicinity of criticality, thus resulting in the anomalous suppression of fluctuations. Indeed the suppressed fluctuation is charactarized by the exponent $\mu > 0$, whereas $\mu = 0$ signifies the subdiffusive growth of the time-integrated current, expected in a normal diffusive systems.

2.2.4.2 *Fluctuating current*

Now we discuss the dynamic properties of the fluctuating part $\mathcal{J}_i^{(fl)}(t)$ in the instantaneous bond current, which has already been defined in eq.(2.15) and whose strength appears in the actual current correlation functions (e.g., see eqs.(2.55) and (2.53)). Here we derive the general space and time dependence of the correlation function $C_r^{\mathcal{J}^{(fl)}\mathcal{J}^{(fl)}}(t,t')$ of the fluctuating current $\mathcal{J}_i^{(fl)}(t)$, by using the relation [obtained from the definition in eq.(2.15)],

$$C_r^{\mathcal{J}^{(fl)}\mathcal{J}^{(fl)}}(t,0) = C_r^{\mathcal{J}\mathcal{J}}(t,0) - C_r^{\mathcal{J}\mathcal{J}^{(d)}}(t,0) - C_r^{\mathcal{J}^{(d)}\mathcal{J}}(t,0) + C_r^{\mathcal{J}^{(d)}\mathcal{J}^{(d)}}(t,0), \tag{2.59}$$

and a second relation

$$C_r^{\mathcal{J}\mathcal{J}^{(d)}}(t,0) \equiv \frac{\mathrm{d}}{\mathrm{d}t} C_r^{\mathcal{Q}\mathcal{J}^{(d)}}(t,0) = C_r^{\mathcal{J}^{(d)}\mathcal{J}^{(d)}}(t,0). \tag{2.60}$$

We see that the second and the fourth terms of eq.(2.59) cancel each other. Again, by using the following relation, for $t > t'$,

$$C_r^{\mathcal{J}^{(d)}\mathcal{J}}(t,t') = \frac{\mathrm{d}}{\mathrm{d}t'} C_r^{\mathcal{J}^{(d)}\mathcal{Q}}(t,t') = \frac{\mathrm{d}}{\mathrm{d}t'}\frac{\mathrm{d}}{\mathrm{d}t} C_r^{\mathcal{Q}\mathcal{Q}}(t,t'), \tag{2.61}$$

in eq.(2.59) along with $t' = 0$, we finally have the time-dependent correlation function for the fluctuating current,

$$C_r^{\mathcal{J}^{(fl)}\mathcal{J}^{(fl)}}(t,t'=0) \equiv C_r^{\mathcal{J}^{(fl)}\mathcal{J}^{(fl)}}(t) = \delta(t)\Gamma_r(\bar{\rho}), \tag{2.62}$$

where $\Gamma_r(\bar{\rho})$ is the density-dependendent strength of the fluctuating current $\mathcal{J}^{(fl)}$.

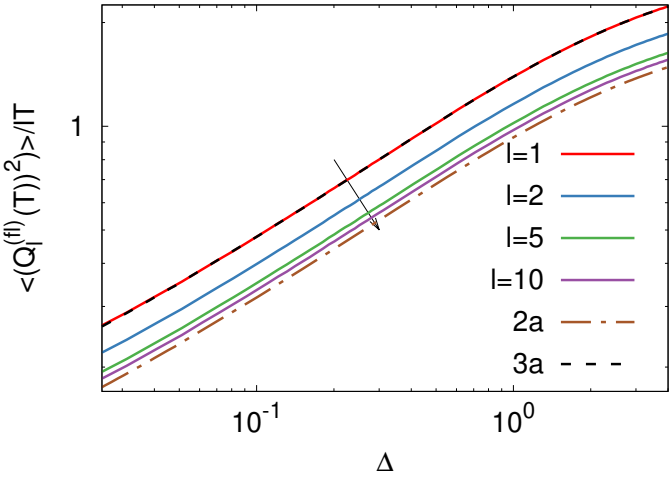

(a)

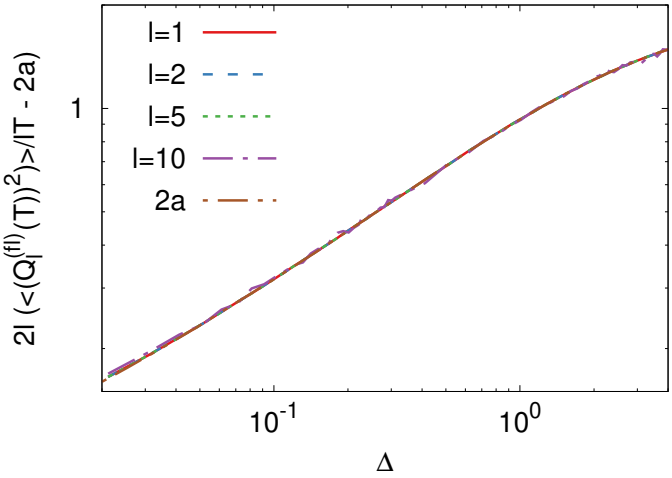

(b)

Figure 2.3: *Top panel:* The scaled variance $\langle [\mathcal{Q}_l^{(fl)}(T)]^2 \rangle / lT$ of space-time-integrated fluctuating current $\mathcal{Q}_l^{(fl)}(T)$ up to time T [as defined in eq.(2.65)], obtained from simulations, is plotted as a function of relative density Δ for different subsystem sizes $l = 1$ (solid red line), $l = 2$ (solid blue line), $l = 5$ (solid green line), $l = 10$ (solid purple line) and the arrow accross the solid line denotes the increasing order of the subsystem size l; we have used system size $L = 1000$ and final time $T = 1000$. The theoretical prediction as in eq.(2.66) with $l = 1$ (black dashed line) is in an excellent agreement with the corresponding simulation; also, one can see that the variance for large l converges quite rapidly to the theoretically predicted value $2a(\bar{\rho})$ [i.e., eq.(2.66) for $l \gg 1$] (brown dot-dashed line). *Bottom panel:* A scaling collapse of the scaled variance of space-time-integrated fluctuating current minus the asymptotic value $2a(\bar{\rho})$ for different subsystem sizes is observed, when plotted as a function of relative density Δ, and it is in excellent agreement with theory in eq.(2.66).

The analytical expression of the strength Γ_r as given in eq.(2.47) has some interesting properties, which are due to the two-particle transfer rule in the Manna sandpile and are noticeably different from that in the variant of sandpile with one-particle transfer [119] and

symmetric simple exclusion processes studied in Ref. [116]. As in the simple exclusion processes, the strength Γ_r for the sandpile with one-particle transfer rule can be shown to be simply delta correlated in space, i.e., $\Gamma_r = 2a(\bar{\rho})\delta_{r,0}$ [120]; this is because both the models have a steady-state with a product measure and therefore do not have any spatial correlations. But, in the case of the Manna sandpile, there are nonzero spatial correlations, leading to the spatially correlated fluctuating current, i.e., $\Gamma_r \neq 0$ for $r \neq 0$, as shown in eq.(2.47). Indeed, as our calculation shows (for details, see appendix sec. A.3.3), eq.(2.47) is exact in the case of Manna sandpile and we have

$$\Gamma_0 = 3a(\bar{\rho}), \tag{2.63}$$

being the strength of the fluctuating current $\mathcal{J}_i^{(fl)}$ accross a single bond $(i, i+1)$. Moreover, we find that there exsists a sum-rule

$$\sum_r \Gamma_r = 2a(\bar{\rho}), \tag{2.64}$$

which, as shown later in eq.(2.72), is directly related to the scaled space-time integrated current fluctuations and therefore related to another transport coefficient, called the mobility, or equivalently, the conductivity, defined as the ratio between average current and an externally applied small biasing force [9, 38]. It has been derived in Ref.[38] that the conductivity in the Manna sandpile is nothing but the density-dependent activity $a(\bar{\rho})$ itself. Remarkably, as shown in the next section, here we show that one can indeed relate the conductivity directly to the current fluctuation in the system.

To verify eq.(2.62) in simulation, let us first define a cumulative (space-time integrated) fluctuating current across a subsystem of size l and up to time T,

$$\mathcal{Q}_l^{(fl)}(T) = \int_0^T \mathrm{d}t \sum_{i=0}^{l-1} \mathcal{J}_i^{(fl)}(t). \tag{2.65}$$

Then, using eqs. (2.47) and(2.62) and after some algebraic manipulations, we obtain, for $l < L$, a fluctuation relation, which immediately connects the scaled current fluctuation and the density-dependent activity,

$$\frac{1}{lT}\left\langle \left(\mathcal{Q}_l^{(fl)}(T)\right)^2 \right\rangle = 2a(\bar{\rho})\left(1 + \frac{1}{2l}\right). \tag{2.66}$$

In fig.2.3a, we plot the lhs of eq.(2.66) as a function of the relative density $\Delta = \bar{\rho} - \rho_c$ for different subsystem sizes $l = 1$ (solid red line), $l = 2$ (solid blue line), $l = 5$ (solid green line), $l = 10$ (solid purple line); we take system size $L = 1000$ and final time $T = 100$. The arrow accross the solid lines denotes an increasing order of the subsystem size l.

Note that the variance of subsystem fluctuating current for subsystem size $l = 1$ is actually the strength Γ_0 of the fluctuating bond current; the corresponding analytical result $\Gamma_0 = 3a(\bar{\rho})$ (dashed black line) as in eq.(2.63) shows an excellent agreement with simulations. For comparison, in the same fig.2.3a, we also plot $2a(\Delta)$ as a function of Δ (the brown dot-dashed line), to demonstrate that, as subsystem size l increases, the scaled variance (lhs of eq.(2.66)) indeed converges towards $2a(\bar{\rho})$, as predicted in eq.(2.66). To show this convergence more quantitatively, in fig. 2.3b we plot the scaled quantity $2l\left[\left\langle \left(\mathcal{Q}_l^{(fl)}\right)^2 \right\rangle - 2a\right]$ for various subsystem sizes $l = 1$ (red solid line), $l = 2$ (blue dashed line), $l = 5$ (green dotted line) and $l = 10$ (purple dot-dashed line); we see that all the curves collapse excellently onto each other and the collasped master curve match excellently with the analytically predicted value $2a(\Delta)$ derived in eq.(2.66).

2.2.4.3 *Space-time integrated current*

In this section we calculate the steady-state variance $\left\langle \bar{Q}^2(l,T) \right\rangle - \left\langle \bar{Q}(l,T) \right\rangle^2$ of the cumulative (space-time integrated) actual particle current $\bar{Q}(l,T) = \sum_{i=0}^{l-1} \mathcal{Q}_i(T)$ across a subsystem of size l and up to time T, which can be written as

$$\begin{aligned} &\left\langle \bar{Q}^2(l,T) \right\rangle - \left\langle \bar{Q}(l,T) \right\rangle^2 = \left\langle \bar{Q}^2(l,T) \right\rangle \\ &= lC_0^{\mathcal{Q}\mathcal{Q}}(T,T) + \sum_{r=1}^{l-1} 2(l-r) C_r^{\mathcal{Q}\mathcal{Q}}(T,T), \end{aligned} \tag{2.67}$$

where we have used the fact that the average steady-state current is zero, i.e., $\left\langle \bar{Q}(l,T) \right\rangle = 0$. Now, by using the following identity,

$$\sum_{r=1}^{l-1} 2(l-r)(2-\lambda_{rn}) = 2\left(\frac{\lambda_{ln} - l\lambda_n}{\lambda_n}\right), \tag{2.68}$$

we can rewrite eq.(2.67) as

$$\begin{aligned} \left\langle \bar{Q}(l,T)^2 \right\rangle =& 2a(\bar{\rho})lT + a(\bar{\rho})T(1-\delta_{l,L}) - \\ & 2a(\bar{\rho})\frac{a'(\bar{\rho})}{L} \sum_q \frac{a'(\bar{\rho})\lambda_q T - 1 + \exp\left(-\lambda_q a'(\bar{\rho})T\right)}{\left(\lambda_q a'(\bar{\rho})\right)^2} \lambda_q \left(1 + \frac{\lambda_q}{4}\right) \frac{\lambda_{ql}}{\lambda_q}. \end{aligned} \tag{2.69}$$

In fig.2.4, we plot the subsystem current fluctuation $\left\langle \bar{Q}^2(l,T) \right\rangle$ obtained from simulations as a function of relative density $\Delta = \rho - \rho_c$ for various subsystem sizes l and final times T: $l = 2500$, $T = 100$ (upper solid sky-blue line) and $l = 100$, $T = 10^5$ (lower solid magenta line). In the same figure we also compare the simulation results with theory eq.(2.69): $l = 2500$, $T = 100$ and $l = 100$, $T = 10^5$ (both in black dashed line); we observe excellent agreement between simulations and theory. Here we note that the results for the larger subsystem size

l and smaller T (upper solid line) almost coincide with twice of local activity, $2a(\Delta)$, as a function of Δ (red dot-dashed line).

Importantly, the asymptotic expression of the variance of cumulative subsystem (space-time integrated) current as in eq.(2.69) depends on the order of limits of the two variables $T \gg 1$ and $l \gg 1$, i.e.,

$$\frac{\left\langle \bar{Q}^2(l,T)\right\rangle}{lT} \simeq \begin{cases} \frac{2a(\bar{\rho})}{\sqrt{\pi a'(\bar{\rho})}}\frac{l}{\sqrt{T}} & \text{for } T \gg 1, l \gg 1, \\ 2a(\bar{\rho}) - \frac{8a(\bar{\rho})\sqrt{a'(\bar{\rho})}}{3\sqrt{\pi}}\frac{\sqrt{T}}{l} & \text{for } l \gg 1, T \gg 1; \end{cases} \tag{2.70}$$

see appendix sec. A.2.3 for details. The first expression in the above equation have been obtained by taking the limit in the following order, first $T \gg 1$ and then the limit $l \gg 1$. In this particular order of limits, the scaled fluctuation $\left\langle \bar{Q}^2(l,T)\right\rangle / lT$ decreases as $1/\sqrt{T}$ and eventually vanishes in the limit of $T \to \infty$. On the other hand, if we take the limit in the opposite order, $l \gg 1$ first and then $T \gg 1$, we obtain the second asymptotic expression in eq.(2.70). That is, in the limit $l \to \infty$, the scaled subsystem-current fluctuation $\left\langle \bar{Q}^2(l,T)\right\rangle / lT$ tends to $2a(\bar{\rho})$ as one increases T,

$$\sigma_Q^2(\bar{\rho}) \equiv \lim_{l\to\infty}\lim_{T\to\infty} \frac{\left\langle \bar{Q}^2(l,T)\right\rangle}{lT} = 2a(\bar{\rho}); \tag{2.71}$$

here the infinite-subsystem-size limit is taken first, and then the infinite-time limit. Note that, in all the above cases, we have taken the large system size limit $L/l \gg 1$ at the very beginning. In fact, one can immediately identify the rhs of eq.(2.71) as the mobility (equivalently, the conductivity) for the Manna sandpile, as calculated in Ref.[38]. Indeed, eq. (2.71) can be thought of as a nonequilibrium version of the celebrated Green-Kubo relations well known for equilibrium systems [121].

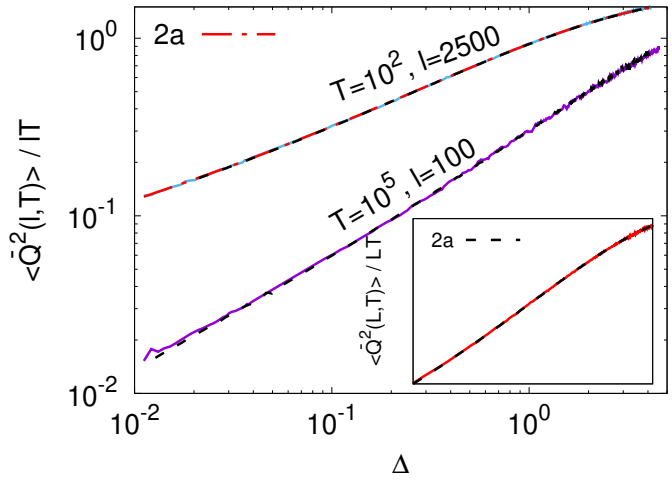

Figure 2.4: Scaled space-time-integrated current fluctuations as a function of relative density. The simulation data for subsystem size $l = 2500$ and $T = 100$ is plotted on top in *solid sky-blue line* and data for $l = 100$ and $T = 10^5$ is plotted at bottom in *solid magenta line*. We compared the analytical result eq.(2.69) (corresponding dashed black lines) with the simulation, which is in excellent agreement. Simulation data have been taken for $L = 5000$ in both cases. We note that the result for the larger subsystem size l and smaller T (upper solid line) almost coincide with twice of local activity, $2a(\Delta)$, as a function of Δ (red dot-dashed line). *In the inset* we compared the scaled total current fluctuation and twice of activity $2a(\bar{\rho})$ as a function of Δ.

Interestingly, if we take $l = L \gg 1$, which corresponds to the bond currents summed over the whole system, we have the following identity

$$\lim_{L\to\infty} \frac{\langle \bar{Q}^2(L,T)\rangle}{LT} = 2a(\rho) = \sum_r \Gamma_r. \tag{2.72}$$

Notably the above equality is valid for any finite time T. This is because the sum of the diffusive currents over the full system, $\sum_{i=1}^{L} \mathcal{J}_i^{(d)}$, is zero by definition (see eq.(2.16)). Consequently the rhs of eq.(2.72) is equal to the space-time inetgral of the fluctuating-current correlation function $\sum_{r=-\infty}^{\infty} \int_{-\infty}^{\infty} dt\, C_r^{\mathcal{J}^{(fl)}\mathcal{J}^{(fl)}}(t,0) = 2a(\bar{\rho})$, obtained using eqs.(2.47), (2.62) and (2.64). In the inset of fig.2.4, the scaled variance $\langle \bar{Q}^2(L,T)\rangle / LT$ (solid red line) and twice the local activity $2a(\Delta)$ (black dashed line) are plotted as a function of Δ, which is in excellent agreement with eq.(2.72). Clearly, below the critical point $\Delta < 0$, the system goes into an absorbing state and, as a result, the current fluctuation is identically zero. Usually activity is considered to be the order parameter in the sandpiles. Indeed, as the identity eq.(2.72) suggests, the space-time integrated current fluctuation can serve as an order parameter and thus characterizes the dynamical state of the system. Later we show that the self-diffusion coefficient of tagged particles can be expressed in terms of the activity and, as previously noted in [84], it can be considered an alternative description of the system's order parameter.

2.2.4.4 *Power spectrum*

The two-point time-dependent correlation function for instantaneous bond current can be characterized also through the power spectrum analysis, which we perform in this section. From the *Wiener-Khinchin* theorem [122], the power spectrum for the instantaneous bond current $\mathcal{J}_i(t)$ is expressed in terms of the Fourier transform of the time-correlation functions,

$$S_{\mathcal{J}}(f) = \int_{-\infty}^{\infty} \mathrm{d}t\, C_0^{\mathcal{J}\mathcal{J}}(t,0) e^{2\pi i f t}. \tag{2.73}$$

Setting $r = 0$ in eq.(2.54), we perform the integration in the rhs of the above equation, leading to the following expression,

$$S_{\mathcal{J}}(f) = \frac{2a(\bar{\rho})}{L} + \frac{2a(\bar{\rho})}{L} \sum_q \left(1 + \frac{\lambda_q}{4}\right) \frac{4\pi^2 f^2}{\lambda_q^2 a'(\bar{\rho})^2 + 4\pi^2 f^2}. \tag{2.74}$$

Now, by subtracting the $f = 0$ mode,

$$S_{\mathcal{J}}(0) = \lim_{T\to\infty} \frac{\langle \mathcal{Q}^2(T) \rangle}{T} = \frac{2a(\bar{\rho})}{L}, \tag{2.75}$$

from the lhs of eq.(2.74), we rewrite eq. (2.74) in terms of the modified power spectrum $\tilde{S}_{\mathcal{J}}(f) = S_{\mathcal{J}}(f) - S_{\mathcal{J}}(0)$,

$$\tilde{S}_{\mathcal{J}}(f) = \frac{2a(\bar{\rho})}{L} \sum_q \left(1 + \frac{\lambda_q}{4}\right) \frac{4\pi^2 f^2}{\lambda_q^2 a'(\bar{\rho})^2 + 4\pi^2 f^2}. \tag{2.76}$$

We can now straightforwardly obtain the asymptotic form of eq.(2.76) for small frequency $1/L^2 \ll f \ll 1$. To do this, we first replace the sum in eq.(2.76) as an integral over the variable $x = q/2\pi$,

$$\tilde{S}_{\mathcal{J}}(f) \simeq 4a(\bar{\rho}) \int_{1/L}^{1/2} \mathrm{d}x\, \frac{1 + \frac{\lambda(x)}{4}}{1 + \frac{\lambda^2(x) a'^2(\bar{\rho})}{4\pi^2 f^2}}, \tag{2.77}$$

where $\lambda(x) \simeq 4\pi^2 x^2$. Then, by performing the variable transformation

$$y = \frac{\lambda^2(x) a'^2(\bar{\rho})}{4\pi^2 f^2}, \tag{2.78}$$

and doing some algebraic manipulations, we immediately obtain the modified power spectrum of current,

$$\tilde{S}_{\mathcal{J}}(f) \simeq a(\bar{\rho})\sqrt{\frac{f}{2\pi a'(\bar{\rho})}}\int_0^\infty \mathrm{d}y\, \frac{y^{-\frac{3}{4}}}{(1+y)} = \frac{\sqrt{\pi}a(\bar{\rho})}{\sqrt{a'(\bar{\rho})}} f^{\frac{1}{2}}; \tag{2.79}$$

see appendix sec. A.1 for details. Again, by using the previous dimensional scaling argument where $a/\sqrt{a'} \sim f^{\mu}$ with μ given in eq.(2.51) (see sec.2.2.3), we obtain the desired scaling behavior of the subtracted power spectrum near criticality,

$$\tilde{S}_{\mathcal{J}}(f) \sim f^{\psi_{\mathcal{J}}}, \tag{2.80}$$

where $\psi_{\mathcal{J}} = 1/2 + \mu$. Since $\mu > 0$, with decreasing frequency, the near-critical power spectrum in the above equation (2.80) decays faster than that away from criticality (given by eq.(2.79)). In simulations, we calculate the power spectrum by discretizing time over a small interval δt and calculate the discrete Fourier transform

$$\tilde{\mathcal{J}}_{n;T} = \delta t \sum_{k=0}^{T-1} e^{i2\pi f_n k}\mathcal{J}_i(k), \tag{2.81}$$

where $f_n = n/T$ with T being large. Then we define the power spectrum of the bond current as

$$S_n = \lim_{T\to\infty} \frac{1}{T}\left\langle \left|\tilde{\mathcal{J}}_{n;T}\right|^2 \right\rangle. \tag{2.82}$$

In fig.(2.5), we plot the substracted power spectrum $\tilde{S}_{\mathcal{J}}(f)$, obtained from simulations in solid lines, for various densities $\rho = 2.0$ (red line), $\rho = 1.5$ (blue line), $\rho = 1.5$ (green line), $\rho = 1.0$ (purple line), $\rho = 0.97$ (orange line). The arrow through the solid lines denotes the incremental order of the density $\bar{\rho}$. For $\rho = 2.0$, we also plot $\tilde{S}_{\mathcal{J}}(f)$ obtained from theory eq.(2.76) (black dashed line), which shows an excellent agreement with simulation; top-most guiding line - $f^{1/2}$ [behavior away from criticality as in eq.(2.79)] and the bottom-most guiding line - $f^{1/2+\mu}$ [behavior near criticality as in eq.(2.80)].

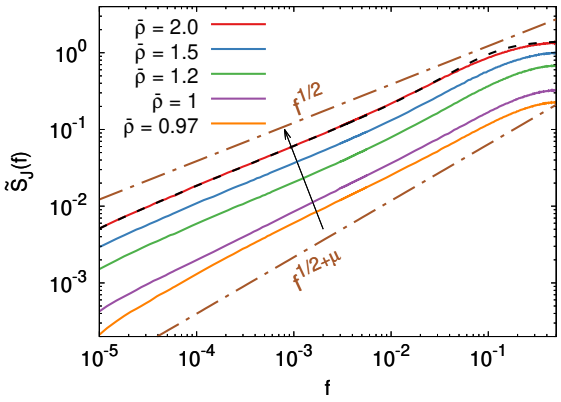

Figure 2.5: Power spectrum of instantaneous current, computed from simulations is plotted in solid lines as a function of frequency f for various densities $\rho = 2.0$ (red line), $\rho = 1.5$ (blue line), $\rho = 1.5$ (green line), $\rho = 1.0$ (purple line), $\rho = 0.97$ (orange line) and for system size $L = 1000$. The arrow accross the solid lines signifies the incremental order of the density $\bar{\rho}$. The top and bottom dashed guiding lines represent the asymptotic behaviors, the $f^{1/2}$ (far from criticality) and $f^{1/2+\mu}$ (near criticality) scaling, respectively, with $\mu \approx 0.24$, obtained by using $\beta \approx 0.42$, $\nu_\perp \approx 1.81$ and $z \approx 1.66$ in eq. (2.51). The dashed black line represents the theoretical result eq.(2.74) for $\rho = 2.0$ and is in excellent agreement with the correponding simulation (top red solid line).

2.2.5 *Tagged-particle displacement fluctuation*

In this section, we study the fluctuations in tagged particle displacements as a function of time. We can relate the sum of all individual time-integrated tagged particle displacement $\sum_{\alpha=1}^{N} X_\alpha(T)$, where the net displacement $X_\alpha(T)$ of α^{th} particle in a time interval $[0, T]$, to the space-time integrated current by the following relation,

$$\sum_{\alpha=1}^{N} X_\alpha(T) = \sum_{i=0}^{L-1} \mathcal{Q}_i(T) = \bar{\mathcal{Q}}(L, T). \tag{2.83}$$

In the limit of large $T \gg L^2$, the self-diffusion coefficient $\mathcal{D}_s(\bar{\rho})$ can be defined through the mean-square tagged particle displacement of the α^{th} particle as given below,

$$\left\langle X_\alpha^2(T) \right\rangle \simeq 2\mathcal{D}_s(\bar{\rho})T. \tag{2.84}$$

To compute the lhs of the above equation, we write the variance of the sum $\sum_{\alpha=1}^{N} X_\alpha(T)$ as

$$\begin{aligned} \left\langle \left[\sum_{\alpha=1}^{N} X_\alpha(T) \right]^2 \right\rangle &= \sum_{\alpha,n} \sum_{\alpha',n'} \langle \delta X_\alpha(t_n) \delta X_{\alpha'}(t_{n'}) \rangle \\ &= 2a(\bar{\rho})LT, \end{aligned} \tag{2.85}$$

where $\delta X_\alpha(t)$ is the microscopic displacement of the α^{th} particle in a small time interval $(t_n, t_n + \delta t)$

$$X_\alpha(T) = \sum_n \delta X_\alpha(t_n), \tag{2.86}$$

and we have used eq.(2.72) in the last line of eq.(2.85). Now using $\langle \delta X_\alpha(t) \delta X_{\alpha'}(t') \rangle \simeq 0$ for $t \neq t'$ and therefore $\langle X_\alpha^2(T) \rangle = \sum_n \langle \delta X_\alpha^2(t_n) \rangle$, we get

$$\left\langle \left[\sum_{\alpha=1}^{N} X_\alpha(T) \right]^2 \right\rangle \simeq \sum_{\alpha=1}^{N} \langle X_\alpha^2(T) \rangle = N \langle X_\alpha^2(T) \rangle . \tag{2.87}$$

Comparing eqs.(2.85), (3.94) and (2.87), we obtain the following relations,

$$\mathcal{D}_s(\bar{\rho}) = \frac{a(\bar{\rho})}{\bar{\rho}} = \frac{1}{\bar{\rho}} \left[\lim_{L,T\to\infty} \frac{\langle \bar{\mathcal{Q}}^2(L,T) \rangle}{2LT} \right], \tag{2.88}$$

which connects the self-diffusion coefficient, activity and the space-time integrated current fluctuation. Alternatively, one can show the above relation using a slightly different argument as follows. First we note that $\langle X_\alpha^2(T) \rangle = \left\langle N_\alpha^{(h)}(T) \right\rangle$, where $N_\alpha^{(h)}(T)$ is the total number of hops, performed by the α^{th} particle up to time T [84]. Summing over all partciles we obtain

$$\sum_\alpha \langle X_\alpha^2(T) \rangle = \sum_\alpha \left\langle N_\alpha^{(h)}(T) \right\rangle = 2 \left\langle N^{(tp)}(T) \right\rangle , \tag{2.89}$$

where $N^{(tp)}(T)$ is the total number of toppling in the whole system up to time T and we have used the fact that $\sum_\alpha N_\alpha^{(h)}(T) = 2N^{(tp)}(T)$. Also in the limit of large T, we have in the leading order of T,

$$\left\langle N^{(tp)}(T) \right\rangle \simeq a(\bar{\rho}) TL, \tag{2.90}$$

where $a(\bar{\rho})$ is the activity at density $\bar{\rho}$. By summing eq.(3.94) over all particles,

$$\sum_\alpha \langle X_\alpha^2(T) \rangle \simeq 2\mathcal{D}_s(\bar{\rho}) TN, \tag{2.91}$$

and, then by using eqs. (2.90) and (2.91) in eq.(2.89), we obtain the relation as given in eq.(2.88).

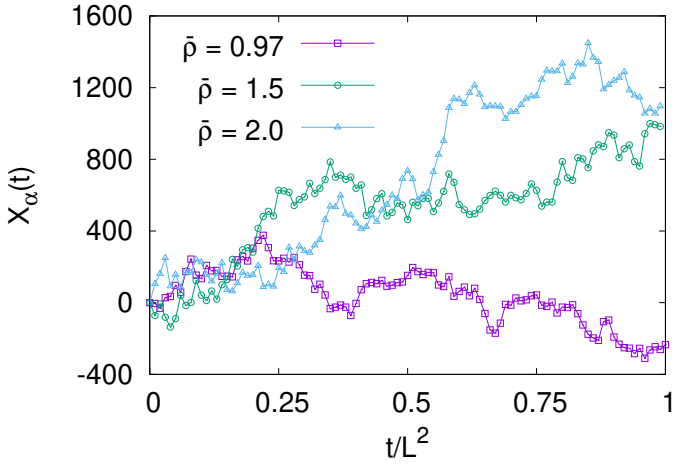

(a)

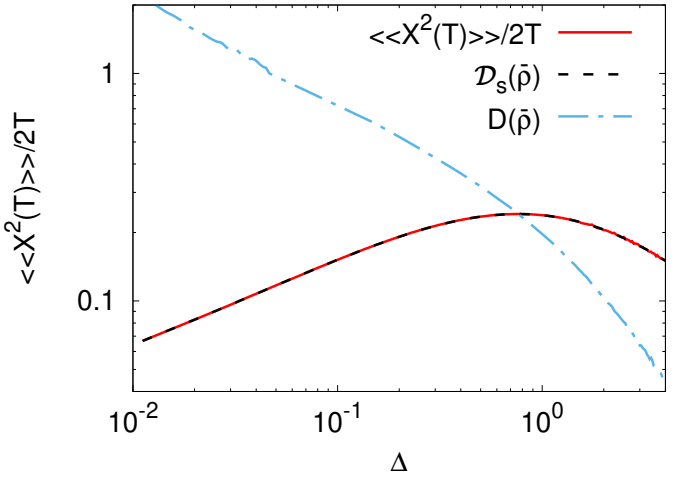

(b)

Figure 2.6: In the top panel, we display the typical space-time trajectories for three tagged particles corresponding to the densities $\rho = 0.97$ (violet square points), 1.5 (green circular points), 2.0 (blue triangular points) respectively with the scaled time axis. In the bottom panel, we plot the mean-square fluctuation of tagged particle displacement up to time T (solid red line) as a function of relative density Δ, where the double angular braces $\langle\langle X^2(T)\rangle\rangle = \sum_\alpha \langle X_\alpha^2(T)\rangle / N$ denote the average over trajectories as well as particles. Simulations (solid red line) show excellent agreement with the theoretically obtained self-diffusion coefficient $\mathcal{D}_s(\bar{\rho})$ (dashed black line) as in eq.(2.88). In the same panel, we also plot the bulk-diffusion coefficient $D(\bar{\rho}) = a'(\bar{\rho})$ as a function of $\Delta = \bar{\rho} - \rho_c$ (dot-dashed blue line), using eq.(2.10) from simulation, which has a contrasting behavior as compared to the self-diffusion coefficient $\mathcal{D}_s(\bar{\rho})$.

In fig. 2.6a, we plot typical trajectories of a particular tagged particle for different densities $\rho = 0.97$ (violet square points), 1.5 (green circular points), 2.0 (blue triangular points) as a function of scaled time. In fig. 2.6b, we plot the mean square fluctuation of tagged particle displacement (solid red line) up to time T, $\langle\langle X^2(T)\rangle\rangle / 2T$, as a function of $\Delta = \rho - \rho_c$, where

the double angular braces $\langle\langle X^2(T)\rangle\rangle = \sum_\alpha \langle X_\alpha^2(T)\rangle / N$ denote the average over trajectories as well as particles; in simulations, during the particle transfer at any site i, two particles are chosen randomly from a particular stack. Our theoretical expression of the density dependent self-diffusion coefficient $\mathcal{D}_s(\rho)$, as given in the equality eq.(2.88), is also plotted (dashed black line); one can see an excellent agreement between the simulation and the theoretical prediction. For comparison, we also plot the bulk-diffusion coefficient $D(\bar{\rho})$ (dot-dashed blue line), defined in eq.(2.10). Here one should note that the self-diffusion coefficient $\mathcal{D}_s(\bar{\rho})$ and the bulk-diffusion coefficient $D(\bar{\rho})$ are, in principle, two different quantities and strikingly they have quite contrasting behaviors, especially near criticality. Indeed, upon approaching criticality where activity decays as $a(\bar{\rho}) \sim (\bar{\rho} - \rho_c)^\beta$ with $\beta < 1$, the self-diffusion coefficient being the ratio of activity to density (see eq.(2.88)) vanishes as $\mathcal{D}_s(\bar{\rho}) \sim (\bar{\rho} - \rho_c)^\beta$ - exactly in the same manner as the activity behaves near criticality, but the bulk-diffusion coefficient being derivative of activity wrt the density [see eq.(2.10)] diverges as $D(\bar{\rho}) \sim 1/(\bar{\rho} - \rho_c)^{1-\beta}$ [38, 102]. Moreover, far from criticality and in the limit of large density $\bar{\rho} \gg 1$, though the self-diffusion coefficient and the bulk-diffusion coefficient both vanish, however they do so in different manners. In that case, as the activity is expected to behave as $a(\bar{\rho}) \simeq 1 - \text{const.}/\bar{\rho}$, the self-diffusivity decays as $\mathcal{D}_s(\bar{\rho}) \sim 1/\bar{\rho}$, but the bulk-diffusivity decays much faster, $D(\bar{\rho}) \sim 1/\bar{\rho}^2$. Lastly, in the active phase, where $\bar{\rho} > \rho_c$, while the bulk-diffusion coefficient $D(\bar{\rho})$ is a monotonically decreasing function of density $\bar{\rho}$ shown in fig. 2.6, the self-diffusion coefficient $\mathcal{D}_s(\bar{\rho})$ is however a non-monotonic function of $\bar{\rho}$.

Importantly, unlike in the symmetric simple exclusion process where both the time-integrated bond current and the tagged particle displacement fluctuations grow sub-diffusively as $T^{1/2}$ [116, 118], in the conserved Manna sandpile only the current fluctuation grows sub-diffusively, whereas the tagged particle displacement fluctuation always grows linearly with time. This is perhaps not surprising, given the fact that, in the Manna sandpile, there are no restrictions in the particle crossings, which are otherwise not allowed in the symmetric exclusion process.

2.2.6 *Mass fluctuation and power spectrum*

In the previous sections, we studied various properties of current fluctuations in detail. Similarly, in this section, starting from the microscopic update rules combined with the previously introduced truncation scheme, we shall derive various dynamic properties of mass fluctuations. The basic quantity is the two-point dynamic correlation function $C_r^{mm}(t, t') =$

$\langle m_0(t)m_r(t')\rangle - \langle m_0(t)\rangle \langle m_r(t')\rangle$. By using the microscopic update rules, we write the time evolution equation for $C_r^{mm}(t,0) \equiv C_r^{mm}(t)$ as

$$\frac{\mathrm{d}}{\mathrm{d}t}C_r^{mm}(t) = \sum_k \Delta_{0,k} \langle \hat{a}_k(t) m_r(0)\rangle \,. \tag{2.92}$$

Using the earlier truncation approximation eq.(2.26), we write the above equation as

$$\frac{\mathrm{d}}{\mathrm{d}t}C_r^{mm}(t) \simeq a'(\bar{\rho}) \sum_k \Delta_{r,k} C_k^{mm}(t). \tag{2.93}$$

The solution of eq.(2.93) can be written, by using the Fourier representation, as

$$\tilde{C}_q^{mm}(t) \simeq e^{-a'(\bar{\rho})\lambda_q t}\tilde{C}_q^{mm}(0), \tag{2.94}$$

where $\tilde{C}_q^{mm}$ is the Fourier transform of C_r^{mm}. The equal-time mass correlation can be solved by using the approximation eq.(2.26) in eq.(2.39) and we can write the time evolution of $C_r^{mm}(t,t)$ in the steady state as

$$\frac{\mathrm{d}}{\mathrm{d}t}C_r^{mm}(t,t) \simeq 2a'(\bar{\rho}) \sum_k \Delta_{0,k} \langle m_k m_r\rangle + B_r = 0. \tag{2.95}$$

Similar to what was done earlier to solve eq.(2.39), the above equation can be solved exactly using a generating function,

$$G(z) = \frac{1}{a'(\bar{\rho})}\left(\frac{3a(\bar{\rho})}{2} - \frac{a(\bar{\rho})}{4}z\right). \tag{2.96}$$

According to the above generating function, we have the steady-state correlations $C_0^{mm} = \langle m_0^2\rangle - \bar{\rho}^2 = 3a/2a'$, $C_1^{mm} = \langle m_0 m_1\rangle - \bar{\rho}^2 = -a/4a'$ and all other correlations being zero. Thus we immediately arrive at a relation between the scaled subsystem-mass fluctuation and the activity,

$$\sigma^2(\rho) \equiv \lim_{l\to\infty} \frac{\langle (\Delta M_l)^2\rangle}{l} = \sum_{r=-\infty}^{r=\infty} C_r^{mm} = \frac{a(\bar{\rho})}{a'(\bar{\rho})}, \tag{2.97}$$

where $\Delta M_l = M_l - \langle M_l\rangle$. Now, by using eqs. (2.10) and (2.71), the above identity can be recast into a nonequilibrium version of the Green-Kubo-like relation [38],

$$\sigma^2(\bar{\rho}) = \frac{\sigma_Q^2(\bar{\rho})}{2D(\bar{\rho})}, \tag{2.98}$$

connecting the (scaled) subsystem-mass fluctuation $\sigma^2(\bar{\rho})$, the (scaled) subsysten-current fluctuation $\sigma_Q^2(\bar{\rho})$ and the bulk-diffusion coefficient $D(\bar{\rho})$ (a slightly different form of the above

relation is usually referred as the Einstein relation in the literature [9, 38]). Remarkably, the fluctuation relation in eq. (2.97) implies that the scaled subsystem mass fluctuation $\sigma^2(\bar{\rho})$ varies linearly with the relative density Δ, i.e., $\sigma^2(\bar{\rho}) \sim \Delta^{1-\delta}$ with $\delta = 0$ [38]; interestingly, such behavior was indeed previously observed in simulations [123] in a variant of the conserved Manna sandpile, which is believed to be in the same universality class as that studied here.

Next we write the solution of eq.(2.94) using the generating function in eq.(2.96) as

$$\tilde{C}_q^{mm}(t) \simeq e^{-a'(\bar{\rho})\lambda_q t} \frac{a(\bar{\rho})}{a'(\bar{\rho})} \left(1 + \frac{\lambda_q}{4}\right). \tag{2.99}$$

Finally, using the inverse Fourier transformation, we get,

$$C_r^{mm}(t) \simeq \frac{1}{L} \sum_q e^{-iqr} e^{-a'(\bar{\rho})\lambda_q t} \frac{a(\bar{\rho})}{a'(\bar{\rho})} \left(1 + \frac{\lambda_q}{4}\right). \tag{2.100}$$

We now consider subsystem mass $M_l(t) = \sum_{r=0}^{l-1} m_r(t)$ for $l < L$ and calculate the equal-time correlation function for mass $C^{M_l M_l}(t,0) \equiv C^{M_l M_l}(t)$ by using the following expression,

$$C^{M_l M_l}(t) = l C_0^{mm}(t) + \sum_{r=1}^{l-1} (l-r)(C_r^{mm}(t) + C_{-r}^{mm}(t)). \tag{2.101}$$

Then by substituting eq.(2.100) in eq.(3.104), we get the equal-time correlation for subsystem mass,

$$C^{M_l M_l}(t) \simeq \frac{1}{L} \sum_q e^{-a'(\bar{\rho})\lambda_q t} \frac{a(\bar{\rho})}{a'(\bar{\rho})} \left(1 + \frac{\lambda_q}{4}\right) \frac{\lambda_{lq}}{\lambda_q}. \tag{2.102}$$

For $t = 0$, the correlation function $C^{M_l M_l}(0)$ is nothing but the equal-time subsystem mass fluctuation, which can be written in the large system size $L \to \infty$ limit as given below

$$C^{M_l M_l}(0) = \left\langle (M_l - \langle M_l \rangle)^2 \right\rangle = \frac{a(\bar{\rho})}{a'(\bar{\rho})} l \left[1 + \frac{1}{2l}\right]. \tag{2.103}$$

Then, by taking the large subsystem size $l \to \infty$ limit, where $1 \ll l \ll L$, we recover the Einstein relation, already derived in eq.(2.97). Moreover the asymptotic form of eq.(2.102) can be written as

$$C^{M_l M_l}(t) - C^{M_l M_l}(0) \simeq -\frac{2a(\bar{\rho})}{\sqrt{\pi a'(\bar{\rho})}} t^{\frac{1}{2}} \tag{2.104}$$

for large time $1 \ll t \ll L^2$; see appendix sec. A.2.4 for details.. Using the Fourier transform of eq.(2.102), we write the power spectrum of the subsystem mass fluctuation as

$$S_M(f) = \lim_{T\to\infty} \int_{-T}^{T} \mathrm{d}t\, C^{M_l M_l}(t) e^{2\pi i f t}, \tag{2.105}$$

which can be written, by using eq.(2.102), as

$$S_M(f) = \frac{1}{L} \sum_q \frac{a(\bar{\rho})}{a'(\bar{\rho})} \left(1 + \frac{\lambda_q}{4}\right) \frac{2\lambda_q a'(\bar{\rho})}{\lambda_q^2 a'(\bar{\rho})^2 + 4\pi^2 f^2} \frac{\lambda_{lq}}{\lambda_q}. \tag{2.106}$$

In fig. 2.7, we plot the power spectrum of the subsystem mass fluctuation, obtained from simulation for $L = 1000$ and $l = 500$ in solid lines, for various densities $\bar{\rho} = 2.0$ (red line), $\bar{\rho} = 1.5$ (blue line), $\bar{\rho} = 1.2$ (green line), $\bar{\rho} = 1.0$ (purple line), $\bar{\rho} = 0.97$ (orange line), where the arrow accross the solid lines denotes the ascending order of the density $\bar{\rho}$. We compare the analytical expression eq.(2.106) (dotted black line) with simulation result for $\bar{\rho} = 2.0$ (solid red line), which is in excellent agreement with theory. The asymptotic expression of the power spectrum in eq.(2.106) can be obtained by simplifying the integral as given below

$$\begin{aligned} S_M(f) =& 4a(\bar{\rho}) \int_{1/L}^{1/2} \mathrm{d}x\, \frac{\lambda(lx)(1+\lambda(x)/4)}{\lambda^2(x) a'^2(\bar{\rho}) + 4\pi^2 f^2} \\ \simeq& \frac{a(\bar{\rho})}{2\sqrt{\pi^3 a'(\bar{\rho})}} f^{-\frac{3}{2}}. \end{aligned} \tag{2.107}$$

Here, in the first step, we have replaced the sum in the rhs of eq.(2.106) as an integral $(1/L)\sum_q \to \int_0^{2\pi} \mathrm{d}q$ in the limit $L \to \infty$ and we used $q = 2\pi x$, $\lambda(x) = 4\pi^2 x^2$ and eq.(2.78); see appendix sec. A.2.5 for details. The above asymptotic form of the power spectrum can be used to calculate the behavior near criticality by using the dimensional scaling argument as performed before in eq.(2.50) where we write $a/\sqrt{a'} \sim f^{\mu}$. In other words, near criticality, the decay of the power spectrum $S_M(f)$ as a function of frequency f becomes slower and is given by

$$S_M(f) \sim f^{-\psi_M}, \tag{2.108}$$

where $\psi_M = 3/2 - \mu$. In fig. 2.7, we plot $S_M(f)$ as a function of frequency for densities $\bar{\rho} = 2.0$ (red), 1.5 (orange), 1.2 (blue), 1.0 (green), 0.97 (violet); we observe that, as one approaches criticality, the decay of the power spectrum indeed becomes slightly slower, in accordance with our theoretical prediction in eq.(2.108). The slower decay of the power spectrum up on approaching criticality can be physically understood from the current power spectrum as follows. Due to the slower temporal growth of the time-integrated bond current fluctuation

(see eq.(2.50)), the near-critical subsystem mass correlation also decays slower as a function of time, i. e.,

$$C^{M_l M_l}(t) - C^{M_l M_l}(0) \sim -t^{1/2-\mu}, \tag{2.109}$$

which is due to the fact that the time-integrated current grows slower with time and consequently the subsystem tends to retain a particular amount of mass for a much longer period. Indeed, this phenomenon can be thought of as the hyperuniformity of mass fluctuations in the temporal domain - a dynamic hyperuniformity of mass fluctuation, analogous to that of current fluctuations as described previously in eq.(2.50).

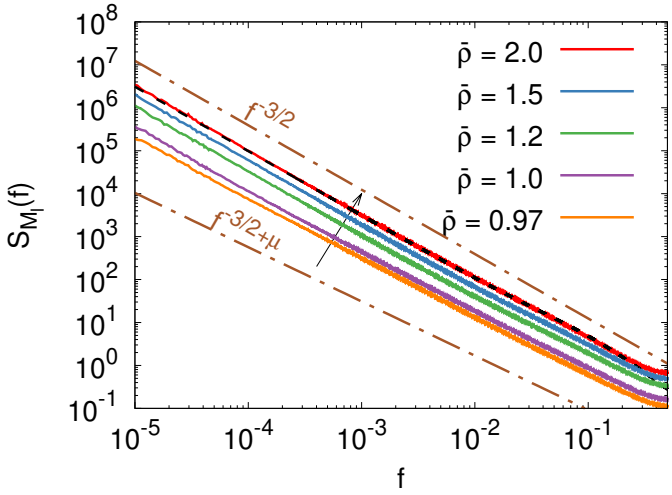

Figure 2.7: Power spectrum of subsystem mass fluctuations are plotted for $L = 1000$ and $l = 500$. The solid lines represent the simulation data for the densities $\bar{\rho} = 2.0$ (red), 1.5 (blue), 1.2 (green), 1.0 (purple), 0.97 (orange) respectively. The top-most guiding line represents the $f^{-3/2}$ (away from criticality) behavior [eq. (2.107)], whereas the bottom-most guiding line represents $f^{-\psi_M}$ (near criticality) behavior [eq.(2.108)] where $\psi_M = 3/2 - \mu \approx 1.26$. The dashed black line represents the theoretical result eq.(2.106) for $\rho = 2.0$. The arrow across the solid lines signifies the ascending order of densities $\bar{\rho}$.

We note that the two exponents $\psi_{\mathcal{J}}$ and ψ_M for the current and mass power spectra defined in eqs.(2.80) and (2.108), respectively, are in fact related, due to the mass conservation as expressed in the continuity equation (2.11). By using the Fourier transform of an observable $A_r(t) = \int_{-\infty}^{\infty} \mathrm{d}f \sum_q e^{-2\pi i f t} e^{-iqr} \tilde{\mathcal{A}}_q(f)$, we can write eq.(2.11) as $-2\pi i f \tilde{\mathcal{M}}_q(f) = \tilde{\mathcal{J}}_q(f)\left(e^{iq} - 1\right)$. On a large scale $q \to 0$, we have

$$S_M(f) \sim f^{-2} S_{\mathcal{J}}(f), \tag{2.110}$$

and therefore, from eqs.(2.80) and (2.108), we obtain the scaling relation

$$\psi_{\mathcal{J}} = 2 - \psi_M. \tag{2.111}$$

2.2.7 *Driven hydrodynamics of Manna model*

The driven diffusive version of the Manna sandpile model was introduced in Ref.[38] and it has been shown that the drift current is proportional to the applied force, where the proportionality constant is called conductivity. In the following we briefly describe the dynamics and show that the conductivity is the same as the half of intensive fluctuation of spacetime integrated current, taken in infinite volume.

We introduce a generalized version of a conserved Manna sandpile that exhibits a bias due to a constant force F applied to the local particle count. This force affects the rates at which particles hop in the system [9, 38]. During a toppling event in the biased Manna model, two particles are transferred independently but with unequal probabilities. Probabilities are determined based on the direction of particle transfer and the magnitude F of the biasing force field $\vec{F} = F\hat{x}$, which is present along the direction $\hat{x}$. The update rules of this dynamics can be written as follows:

$$m_i(t+dt) = \begin{cases} \textbf{events} & \textbf{probabilities} \\ m_i(t)+1 & \left(\hat{a}_{i+1}c^F_{i+1,0} + \hat{a}_{i-1}c^F_{i-1,0}\right)dt \\ m_i(t)+2 & \left(\hat{a}_{i+1}c^F_{i+1,-} + \hat{a}_{i-1}c^F_{i-1,+}\right)dt \\ m_i(t)-2 & \hat{a}_i\left(c^F_{i,-} + c^F_{i,+} + c^F_{i,0}\right)dt \\ m_i(t) & 1-\Sigma dt, \end{cases} \tag{2.112}$$

$1-\Sigma dt$ is the probability of happening no events that change the mass of site i and the biased hop rates are,

$$c^F_{i,\alpha} = c^{F=0}_{i,\alpha} \exp\left[\sum_j \Delta e_{ij}/2\right]. \tag{2.113}$$

Here, we consider three cases: $\alpha = 0$, $+$, and $-$, which correspond to the modified rates $c^F_{i,0}$, $c^F_{i,+}$, and $c^F_{i,-}$, respectively. These rates represent the transfer of one particle to the left and one to the right, the transfer of both particles to the right, and the transfer of both particles to the left. Furthermore, $\Delta e_{ij} = \Delta m_{i\to j} F(j-i)b$ represents the "energy cost" to move $\Delta m_{i\to j}$ particles from site i to j. The lattice spacing, denoted by b, is set to 1 for simplicity. It should be noted that when $F = 0$, the model corresponds to the unbiased Manna model, where the particle-hopping rates are actually given by $c^{F=0}_{i,0} = 1/2$ and $c^{F=0}_{i,+} = c^{F=0}_{i,-} = 1/4$ (as shown in Eq.(2.6)).

2.2.7.1 *Hydrodynamics*

The modified rates in linear order of biasing force F as given by

$$c^F_{i,0} = c^{F=0}_{i,0} \exp\left[(F-F)/2\right] = \frac{1}{2} \tag{2.114}$$

$$c^F_{i,+} = c^{F=0}_{i,+} \exp\left[(F+F)/2\right] = \frac{(1+F)}{4} \tag{2.115}$$

$$c^F_{i,-} = c^{F=0}_{i,-} \exp\left[(-F-F)/2\right] = \frac{(1-F)}{4}. \tag{2.116}$$

Using these rates, the evolution equation for the local density can be written as follows:

$$\frac{\partial \rho_i(t)}{\partial t} = \langle \hat{a}_{i-1} - 2\hat{a}_i + \hat{a}_{i+1} \rangle + F \frac{\hat{a}_{i-1} - \hat{a}_{i+1}}{2}, \tag{2.117}$$

After taking the diffusive limit, where $i \to x = i/L$ and $t \to \tau = t/L^2$, and assuming the local equilibrium condition, the equation can be further expressed as

$$\frac{\partial \rho(x,\tau)}{\partial \tau} = -\frac{\partial}{\partial x}\left(j^{(d)} + j^{(drift)}\right). \tag{2.118}$$

In Eq.(2.118), the diffusive current is represented by $j^{(d)} = -D(\rho)\partial\rho/\partial x$, where the bulk diffusivity $D(\rho)$ is defined as $D(\rho) = a'(\rho)$ according to Eq.(2.10). Moreover, the drift current $j^{(drift)}$ is given by

$$j^{(drift)} = \chi(\rho)\tilde{F}, \tag{2.119}$$

where we rescaled $F = \tilde{F}/L$ to obtain the mobility $\chi(\rho) = a(\rho)$, which can also be written using Eq.(2.71) in terms of fluctuation of space-time integrated current as

$$\chi(\rho) = \frac{\sigma^2_Q(\rho)}{2}. \tag{2.120}$$

The equation provided above represents the equilibrium-like Green-Kubo formula for the transport coefficient called mobility. This formula reveals that the mobility can also be obtained by directly analyzing the fluctuation of the space-time integrated current in a nonequilibrium steady state.

In Fig. 2.8, we present the relaxation of an initial density profile as a function of the scaled space for $\tilde{F} = 10$. The initial density profile is prepared by distributing L particles using a Gaussian random number generator with a variance of $L/10$ and a mean of $L/2$, while the background density is set to $\rho = 0.95$. The initial profile is represented by circular points at $\tau = 0$, triangular points at $\tau = 10^{-2}$, and pentagonal points at $\tau = 10^{-1}$. The solid

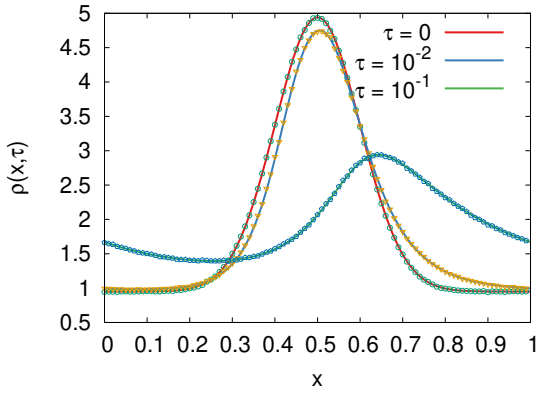

Figure 2.8: The driven-diffusive evolution of an initial density profile as a function of scaled space is plotted for $\tilde{F} = 10$. The profile is created by distributing particles using a Gaussian random number generator with a mean of $L/2$ and a variance of $L/10$, while the background density is set to $\rho = 0.95$. At $\tau = 0$, the initial profile is represented by circular data points, followed by triangular points at $\tau = 10^{-2}$ and pentagonal points at $\tau = 10^{-1}$. The solid lines depict the solution obtained from Eq. (2.118). All data are taken for $L = 1000$.

lines correspond to the solution of Eq. (2.118), which exhibits excellent agreement with the simulation data points.

2.3 SUMMARY AND CONCLUSIONS

In this paper, we study the steady-state dynamical properties of current and mass in the active phase of the one-dimensional conserved Manna sandpile, and we establish a direct quantitative relationship between the system's static and dynamic properties. First, starting with a microscopic dynamical description, we introduce a truncation scheme, that is approximate and is expected to be valid only for long (hydrodynamic) times, but allows us to theoretically investigate the time-dependent (two-point, unequal-time) correlation functions for current and mass, as well as the associated power spectra. In particular, we find that, in the thermodynamic limit, the two-point time-dependent correlation function for the (bond) current has a delta peak at time $t = 0$ and, for time $t > 0$, the correlation is *negative* and a long-ranged one, decaying as $t^{-(3/2+\mu)}$. Far from criticality, we show that the exponent $\mu = 0$, resulting in a subdiffusive, $T^{1/2}$, growth of the variance of the cumulative (*time-integrated*) current up to time T. This type of subdiffusive growth of temporal fluctuation, which has previously been obtained in symmetric simple exclusion processes [116], is somewhat expected for diffusive systems with normal fluctuation properties, such as sandpiles away from criticality [102]. However, the scenario changes near the critical point. Indeed, as one approaches criticality, the activity in the system vanishes, contributing to an anomalous suppression of the temporal current fluctuations and thus a positive value of the exponent $\mu > 0$, which has been expressed in terms of the standard static exponents [see eq.(2.51)];

likewise, near criticality, the power spectrum of current at low frequency f varies as $f^{1/2+\mu}$. A similar argument can be made for the temporal subsystem-mass fluctuation, which is induced by the boundary currents and is also suppressed near criticality because the current fluctuation is suppressed. The anomalously reduced mass fluctuation is manifested in the corresponding power spectrum, which, at low frequency and near criticality, varies as $f^{-3/2+\mu}$ with $\mu > 0$; on the other hand, far from criticality, the exponent $\mu = 0$, implying $f^{-3/2}$ power spectrum, expected in a normal diffusive system. We also derive, within our theory, a nonequilibrium version of the Green-Kubo-like fluctuation-response relation [see eq.(2.98)], or the Einstein relation [9, 38], which connects dynamic and static fluctuations in the system. Indeed our theoretical analysis suggests that, with appropriate (diffusive) rescaling of space and time, the fluctuation properties of the Manna sandpile should be governed by a continuum fluctuating hydrodynamic description as formulated in the recently developed macroscopic fluctuation theory for diffusive systems [9, 38].

We finally investigate the mean-square displacement of tagged-particles and show that the self-diffusion coefficient for an individual tagged particle is identically equal to the ratio of the activity to density [see first equality in eq.(2.88)]. The identity readily explains a previous simulation observation of Ref. [84] that the self-diffusion coefficient in the Manna sandpile vanishes in precisely the same fashion as the activity does upon approaching criticality. Notably, the near-critical behavior of the self-diffusion coefficient differs markedly from that of the bulk-diffusion coefficient, which was previously identified in Refs. [38, 102] as the derivative $a'(\bar{\rho})$ of the activity wrt density $\bar{\rho}$ and clearly diverges near criticality. Furthermore, while the bulk-diffusion coefficient is a monotonic function of density, the self-diffusion coefficient is a non-monotonic one. Interestingly, the self-diffusion coefficient can be related to the current fluctuation in the system as expressed in the second equality in eq.(2.88).

Our findings are reminiscent of somewhat similar observations of *dynamic hyperuniformity*, where the existence of anti-correlations in the temporal fluctuations in sandpiles were pointed out [92, 94]. However, until recently [38], the precise relationship between dynamic and static fluctuations, such as that between mass and current fluctuations, was unknown, and is encoded in the Green-Kubo-like fluctuation relation as derived here in eq.(2.98). The relationship demonstrates that there are indeed two mechanisms responsible for the vanishing of mass fluctuation near criticality: Physically, the anomalously suppressed current fluctuation, combined with the diverging bulk-diffusion coefficient, near criticality result in the vanishing, or hyperuniform, density fluctuation observed recently in the conserved Manna sandpiles [109].

Our results are in fact a consequence of the mass conservation, as reflected in the scaling relation (2.111), and are thus expected to be applicable in a broad class of conserved sandpiles. As our analysis suggests, the anomalous suppression of current fluctuations near criticality could be a generic feature of *hyperuniform* state of matter and should serve as the

dynamical signature of such states, which have been observed in similar other systems in the recent past [123, 124]. In particular, our findings could help in determining the precise dynamical nature of the off- and near-critical states in sandpiles by shedding light on the microscopic dynamical origin of long-ranged temporal correlations in these systems.

3

THE MANNA SANDPILE WITH SINGLE PARTICLE TRANSFER RULE

3.1 INTRODUCTION

This model, introduced by K. Jain [119], serves as a simple sandpile model displaying an active absorbing phase transition. It can be described as a variant of the Manna model [63], with the difference being that when an active site topples, it throws out a single particle with unit rate and the particle is distributed between two nearest neighbours with a probability of $1/2$. The critical height for threshold activation remains the same as the Manna model, which is 2. This simplification restores detailed balance to the model in the active state, and, as a consequence, the steady-state measure of the active microscopic configurations can be immediately known by mapping the system to a *zero-range process* [87, 119]. It can be shown that the exponent of the order parameter $\beta = 1$ describes the activity near the criticality, on a 1-dimensional periodic boundary, as $a(\Delta) \sim \Delta^{\beta}$, where $\Delta = \bar{\rho} - \rho_c$, since $\bar{\rho}$ is the global conserved density.

Immediately, from the scaling relation $z = 2 + (\beta - 1)/\nu_{\perp}$ proposed in Ref. [38], we find that $z = 2$, where z and $\nu_{\perp}$ are the dynamical and correlation length exponents near criticality, respectively. This implies that when approaching criticality from above or from the active state, no anomalous diffusion should be observed. Our study of the current fluctuation also supports this conclusion, as there is no emergence of dynamic hyperuniformity near criticality.

Notably, in the absorbing state of this model, detailed balance is broken, and as a result, the steady-state measures are not known, from simulations, it is known that the correlation length becomes large and negative [119]. However, the study of this phase lies outside the scope of the theoretical machinery developed in this thesis.

In this chapter, we investigate the dynamic properties of mass and current, similar to what has been done in the earlier chapter. From simulations, we found that even near criticality, our theoretical results excellently capture the simulation data.

In this section, we define a fixed-energy sandpile model, which obtains an exact product measure in steady state. As a result, the large-scale evolution equation of the conserved quantity, density, can be calculated exactly.

We define the model in a periodic lattice of size L, where an unbounded number of particles $m_i = 1, 2, \ldots, N$ can occupy a site i, and N is the total number of conserved particles in the system. Dynamics is governed by the toppling of active sites, where a site is called active if the corresponding particle number is more than one $m_i > 1$, and it topples a single particle with a unit rate. The toppled particle is randomly distributed between the nearest neighbours with probability $1/2$. The instantaneous update of the local mass $m_i(t)$ is as follows,

$$m_i(t+dt) = \begin{cases} \textit{events} & \textit{probabilities} \\ m_i(t)+1 & \frac{1}{2}\hat{a}_{i-1}(t)dt \\ m_i(t)+1 & \frac{1}{2}\hat{a}_{i+1}(t)dt \\ m_i(t)-1 & \hat{a}_i(t)dt \\ m_i(t) & (1-\Sigma dt)\,, \end{cases} \tag{3.1}$$

where $\Sigma = \frac{1}{2}\left(\hat{a}_{i-1}(t) + \hat{a}_{i+1}\right) + \hat{a}_i(t)$ and $\hat{a}_i$ is the activity operator indicating $\hat{a}_i = 1$ for $m_i > 1$ otherwise $\hat{a}_i = 0$. It is important to note that due to threshold-activated dynamics, below a critical density $\bar{\rho} = \rho_c$ ($\bar{\rho} = N/L$ is the global conserved density), all particles become immobile since there would be no site with $m_i > 1$. This state is called the absorbing state. But above the critical density $\rho > \rho_c$, there would always be an excess $(\rho - \rho_c)L$ of mobile particles, and such states are called active states. As, at most, only a single particle can hop out of a site, a site can never be vacated because, to topple a single particle to the nearest neighbours, a site must have at least two particles. Thus, the critical density $\rho_c = 1$ in this model and in the active state $\bar{\rho} > 1$, the probability of particle configuration can be written exactly in a product form, since the dynamics satisfies the detailed balance w.r.t. this probability distribution, which enables us to compute the critical exponents and the single site mass distribution exactly in the steady state.

As the system satisfies the detailed balance condition and consequently the product measure of configurations in the active states, we can recast the active regime of the system into a one-dimensional zero range process (ZRP) [125], with homogeneous hop rates $u(m')$, which

are functions of the relative particle number $m' = m - 1$ at a site with critical density $\rho_c = 1$. The hop rates, now can be defined as

$$u(m') = \begin{cases} \frac{1}{2} & \text{for } m' \geq 1, \\ 0 & \text{for } m' = 0, -1. \end{cases} \tag{3.2}$$

The canonical steady state probability distribution of finding the system in the configuration of relative masses $\{m'_l\} = \{m'_0, m'_1, \ldots, m'_L\}$ is given by the probability $P\left[m'_l\right]$, where

$$P\left[\{m'_l\}\right] = Z^{-1}_{L,N'} \prod_{l=i}^{L-1} f(m'_l), \tag{3.3}$$

where $Z_{L,N'}$ is the partition function for system size L and $N' = N - L$ with total conserved particle number N; the product factor at each site $f(m')$ is given by,

$$f(m') = \prod_{m'_i=1}^{m'} \frac{1}{u(m'_i)} = 2^{m'}. \tag{3.4}$$

The last equality in the above equation is obtained by using the definition of the rate functions $u(m')$, given in Eq.(3.2), where in the steady state we have $f(0) = 1$. The partition function $Z_{L,N'}$, given in Eq.(3.3), can be written explicitly using the product factor $f(n')$ as

$$Z_{L,N'} = \sum_{\{n'_l\}} \prod_{l=i}^{L-1} f(n'_l) \delta \left(\sum_l n'_l - N' \right) = \frac{(N' + L - 1)!}{N'!\,(L-1)!} 2^{N'}. \tag{3.5}$$

We are concerned with the marginal distribution of mass at a single site, which is easy to calculate in the granad-canonical formalism by considering the site as a system and the rest of the system with $L - 1$ sites as reservoirs. In the grand-canonical formalism, the probability of a site having relative particle number m' in the active-state is

$$p(m') = \frac{z^{m'} f(m')}{Z}, \tag{3.6}$$

where z is the fugacity and Z is the partition function for $L \to \infty$, $N \to \infty$ and $N/L \to \bar{\rho}$. This partition function can be obtained in terms of the fugacity z as

$$Z = \sum_{m'=0}^{\infty} z^{m'} f(m') = \sum_{m'=0}^{\infty} z^{m'} 2^{m'} = \frac{1}{1 - 2z}. \tag{3.7}$$

Then, we can fix the fugacity using the condition that the average density of a site should be $\bar{\rho}$, that is $\sum_{n'=0}^{\infty} m' p(m') = \bar{\rho}'$ ($\bar{\rho}' = \bar{\rho} - \rho_c$ is the relative global density in active-state), which gives us,

$$z = \frac{\bar{\rho}'}{2(\bar{\rho}' + 1)}. \tag{3.8}$$

Finally we write the occupancy probability of a single site in terms of the relative particle number $m' = m - 1$ and the actual density $\bar{\rho}$, using Eq.(3.6), as

$$p(m') = \frac{1}{\bar{\rho}} \left[\frac{(\bar{\rho} - 1)}{\bar{\rho}} \right]^{m'}, \tag{3.9}$$

Now, the probability that the site is active is given by, $a(\bar{\rho}) = \sum_{m' \geq 1}^{\infty} p(m')$, which using the above equation can be written explicitly as

$$a(\rho) = \frac{\rho - 1}{\rho}. \tag{3.10}$$

To find the hydrodynamic limit of this model, using the update rules in Eq.(3.1), we write the evolution equation of the local average mass at a site i, $\langle m_i(t) \rangle$, as

$$\frac{d}{dt} \langle m_i(t) \rangle = \frac{1}{2} \left(a_{i-1}(t) - 2a_i(t) + a_{i+1}(t) \right), \tag{3.11}$$

where $a_i(t) = \langle \hat{a}_i(t) \rangle$ is the local average of the activity operator. In the continuum limit $i \to x = i/L$, this average $a(x)$ should be a function of the local density field $\rho(x)$, and this functional dependence should be governed by the local equilibrium relation between activity, i.e., by Eq.(3.10). So, we must have $a(x) = a[\rho(x)] = (\rho(x) - 1)/\rho(x)$ and consequently the continuum limit of Eq.(3.11), would simply be obtained by using the Taylor expansion $a(x \pm 1/L) \simeq a(x) \pm a'(x)/L + a''(x)/2L^2$, which gives us the following diffusion equation in the limit $L \to \infty$,

$$\frac{\partial}{\partial \tau} \rho(x, \tau) = \frac{\partial}{\partial x} \left[D(\rho) \frac{\partial}{\partial x} \rho \right] = -\frac{\partial}{\partial x} j^d, \tag{3.12}$$

where $\tau = t/L^2$ is the diffusive time and $D(\rho)$ is the bulk-diffusivity, given by,

$$D(\rho) = \frac{a'(\rho)}{2} = \frac{1}{2\rho^2}. \tag{3.13}$$

We write Eq.(3.12) as a continuity equation at the second equal-to sign, where $j^{(d)}$ is the hydrodynamic current and can be written as the product of bulk diffusivity $D(\rho)$ and the local density gradient, i.e.,

$$j^{(d)} = -D(\rho)\frac{\partial \rho}{\partial x} \ . \tag{3.14}$$

Our goal is to study the properties of fluctuations around these hydrodynamic profiles, which are the solutions of Eq.(3.12). To achieve this, we derive the fluctuating properties of the actual time-integrated current across a bond using the theory described in detail in the following sections.

3.3 STUDY OF FLUCTUATIONS

3.3.1 *Theory*

To develop fluctuating hydrodynamics, we introduce the concept of the time-integrated bond current, denoted as $\mathcal{Q}_i(t)$. This quantity represents the net number of particles flowing through a bond connecting sites i and $i+1$ over a time interval $[0, t]$. The spatio-temporal correlations of $\mathcal{Q}_i(t)$ are crucial for our analysis, and we shall see that even in this equilibrium system, the dynamic correlations have a slowly varying long range and a delta-correlated part. In the following, we outline the method for obtaining these correlations.The evolution of $\mathcal{Q}_i(t)$ is simple and given by the following update rules,

$$\mathcal{Q}_i(t+dt) = \begin{cases} \textbf{\textit{events}} & \textbf{\textit{probabilities}} \\ \mathcal{Q}_i(t)+1 & \frac{1}{2}a_i(t)dt \\ \mathcal{Q}_i(t)-1 & \frac{1}{2}a_{i+1}(t)dt \\ \mathcal{Q}_i(t) & 1-\Sigma dt, \end{cases} \tag{3.15}$$

where $\Sigma = \left(a_i(t) + a_{i+1}(t)\right)/2$ and finally the evolution equation of the time-integrated bond current is given by,

$$\frac{d}{dt}\left\langle \mathcal{Q}_i(t)\right\rangle = \frac{1}{2}\left\langle \hat{a}_i(t) - \hat{a}_{i+1}(t)\right\rangle = \left\langle \mathcal{J}_i(t)\right\rangle, \tag{3.16}$$

where $\mathcal{J}_i(t)$ instantaneous current across the i^{th} bond, and it can be defined as the derivative of the integrated current $\mathcal{Q}_i(t)$,

$$\mathcal{J}_i(t) = \frac{d}{dt}\mathcal{Q}_i(t). \tag{3.17}$$

At the operator level, we can decompose the instantaneous current $\mathcal{J}_i(t)$ in to a diffusive part, $\mathcal{J}_i^{(d)}(t)$ and a fluctuating part $\mathcal{J}_i^{(fl)}(t)$ as

$$\mathcal{J}_i(t) = \mathcal{J}_i^{(d)}(t) + \mathcal{J}_i^{(fl)}(t); \tag{3.18}$$

we shall see all the long-range temporal correlation functions involve the diffusive instantaneous current $\mathcal{J}_i^{(d)}(t)$, whereas $\mathcal{J}_i^{(fl)}(t)$ is simply delta correlated. Also, due to consistency w.r.t Eq.(3.16), we must have,

$$\mathcal{J}_i^{(d)}(t) = \frac{1}{2}\left(\hat{a}_i(t) - \hat{a}_{i+1}(t)\right), \tag{3.19}$$

which enables us to write Eq.(3.16) as

$$\frac{d}{dt}\left\langle \mathcal{Q}_i(t)\right\rangle = \frac{1}{2}\left\langle \hat{a}_i(t) - \hat{a}_{i+1}(t)\right\rangle = \left\langle \mathcal{J}_i^{(d)}(t)\right\rangle. \tag{3.20}$$

Consequently, the mean of the fluctuating current is *zero*, $\left\langle \mathcal{J}_i^{(fl)}(t)\right\rangle = 0$.

The dynamical fluctuation of $\mathcal{Q}_i(t)$, i.e., $\left\langle \mathcal{Q}_i^2(t)\right\rangle - \left\langle \mathcal{Q}_i(t)\right\rangle^2$, can be calculated from the two-point current correlations of unequal time, unequal space, $C_r^{\mathcal{Q}\mathcal{Q}}(t,t')$, where the notation $C_r^{AB}(t,t')$ has the following definition,

$$C_r^{AB}(t,t') = \left\langle A_r(t)B_{i+r}(t')\right\rangle - \left\langle A_r(t)\right\rangle\left\langle B_{i+r}(t')\right\rangle \equiv \left\langle A_r(t)B_{i+r}(t')\right\rangle_c; \tag{3.21}$$

$\left\langle A_r(t)B_{i+r}(t')\right\rangle_c$ is called the cumulant of the random variables A and B. We also define the spatial Fourier transform of the correlation function $C_r^{AB}(t,t')$ as

$$\tilde{C}_q^{AB}(t,t') = \sum_{r=0}^{L-1} C_r^{AB}(t,t')e^{iqr}, \tag{3.22}$$

where $q = 2\pi k/L$ and $k = 0, 1, \ldots, L-1$ and the inverse Fourier transform as

$$C_r^{AB}(t,t') = \frac{1}{L}\sum_q \tilde{C}_q^{AB}(t,t')e^{-iqr}. \tag{3.23}$$

Moreover, note that, as we are interested in steady-state fluctuations, $\langle A_r(t)\mathcal{Q}_{i+r}(t')\rangle_c = \langle A_r(t)\mathcal{Q}_{i+r}(t')\rangle$, as $\langle \mathcal{Q}_i((t))\rangle = 0$ in steady states. To find the exact expression of $C_r^{\mathcal{Q}\mathcal{Q}}(t,t')$, we write the following update equation for $t > t'$,

$$\mathcal{Q}_i(t+dt)\mathcal{Q}_{i+r}(t') = \begin{cases} \textbf{\textit{events}} & \textbf{\textit{probabilities}} \\ (\mathcal{Q}_i(t)+1)\,\mathcal{Q}_{i+r}(t') & \frac{1}{2}a_i(t)dt \\ (\mathcal{Q}_i(t)-1)\,\mathcal{Q}_{i+r}(t') & \frac{1}{2}a_{i+1}(t)dt \\ \mathcal{Q}_i(t)\mathcal{Q}_{i+r}(t') & 1-\Sigma dt, \end{cases} \tag{3.24}$$

where $\Sigma = (a_i(t) + a_{i+1}(t))/2$. Using the above update rules, we obtain the following evolution equation of $C_r^{\mathcal{Q}\mathcal{Q}}(t,t')$,

$$\frac{\partial}{\partial t}C_r^{\mathcal{Q}\mathcal{Q}}(t,t') = \left\langle \mathcal{J}_i^{(d)}(t)\mathcal{Q}_{i+r}(t')\right\rangle_c = \frac{1}{2}\left(C_r^{\hat{a}\mathcal{Q}}(t,t') - C_{r-1}^{\hat{a}\mathcal{Q}}(t,t')\right). \tag{3.25}$$

The unequal-time and unequal-space correlation function of the activity operator and integrated current, $C_r^{\hat{a}\mathcal{Q}}(t,t')$, that appeared on the right-hand side of the above equation can be solved using the following dynamical equation,

$$\frac{\partial}{\partial t}C_r^{a\mathcal{Q}}(t,t') \equiv \frac{\partial}{\partial t}\left\langle \hat{a}_i(t)\mathcal{Q}_{i+r}(t')\right\rangle_c = \left\langle \left\{\frac{d}{dt}\hat{a}_i(t)\right\}\mathcal{Q}_{i+r}(t')\right\rangle_c. \tag{3.26}$$

The evolution equation of the local activity operator, which is present inside the curly bracket above, in-principle can be solved using the following update rules of the local activity operator $\hat{a}_i(t)$,

$$\hat{a}_i(t+dt) = \begin{cases} \textbf{\textit{events}} & \textbf{\textit{probabilities}} \\ \hat{a}_i(t)+1 & \frac{1}{2}\hat{a}_{i+1}(t)\hat{p}_i(t)dt \\ \hat{a}_i(t)+1 & \frac{1}{2}\hat{a}_{i-1}(t)\hat{p}_i(t)dt \\ \hat{a}_i(t)-1 & \hat{a}_i(t)\delta_{m_i,2}dt \\ \hat{a}_i(t) & 1-\Sigma dt, \end{cases} \tag{3.27}$$

and the observable $\hat{a}_i(t)$ evolves according to the equation,

$$\frac{d}{dt}\hat{a}_i(t) = \frac{1}{2}\hat{p}_i(t)\left(\hat{a}_i(t)+\hat{a}_{i-1}(t)\right) - \hat{a}_i\delta_{m_i(t),2}, \tag{3.28}$$

where $\hat{p}_i(t) = (1-\hat{a}_i(t))$ and $\Sigma = (\hat{p}_i(t)/2)\left(\hat{a}_{i+1}+\hat{a}_{i-1}\right) + \hat{a}_i\delta_{m_i,2}$. Putting the above equation in Eq.(3.26), we note that the resulting equation involves infinite hierarchy correlation

functions. Clearly, to determine $C_r^{a\mathcal{Q}}(t,t')$, it is necessary to calculate the correlation functions $\left\langle \delta_{m_i(t),2}\hat{a}_i(t)\mathcal{Q}_{i+r}(t')\right\rangle$, $\langle \hat{a}_i^2(t)\mathcal{Q}_{i+r}(t')\rangle$, and $\langle \hat{a}_i(t)\hat{a}_{i-1}(t)\mathcal{Q}_{i+r}(t')\rangle$. However, these calculations would involve additional sets of higher-order correlation functions. Consequently, this process leads to an infinite hierarchy of equations that poses a challenge to manage.

Similarly, like the Manna model [108], in this model also, we truncate the otherwise infinite hierarchy of equations by expressing the microscopic diffusive current, which is the difference of the local microscopic activity operator, as the local difference of mass times bulk diffusivity, i.e.,

$$\mathcal{J}_i^{(d)}(t) = \frac{1}{2}[\hat{a}_i(t) - \hat{a}_{i+1}(t)] \simeq D(\bar{\rho})[m_i(t) - m_{i+1}(t)]. \tag{3.29}$$

The bulk diffusion coefficient $D(\rho) = a'(\rho)/2$, as given in Eq.(3.13) and is constant in the steady state of periodic boundary construction. In the truncation scheme described above, we assume that deviations from the global density $\bar{\rho}$ are relatively small and that the local current, which represents the activity gradient, relaxes diffusively through the local mass gradient. As we approximate one operator $[\hat{a}_i(t) - \hat{a}_{i+1}(t)]/2$ with another $D(\bar{\rho})[m_i(t) - m_{i+1}(t)]$, it means that we now calculate the correlation between $\left\langle \mathcal{J}_i^{(d)}(t)\right\rangle$ and any other operator $A_j(t')$ in the following manner,

$$\left\langle \mathcal{J}_i^{(d)}(t)A_j(t')\right\rangle \equiv \left\langle \frac{1}{2}[\hat{a}_i(t) - \hat{a}_{i+1}(t)]A_j(t')\right\rangle \simeq \left\langle D(\bar{\rho})[m_i(t) - m_{i+1}(t)]A_j(t')\right\rangle. \tag{3.30}$$

As demonstrated later, this approximation excellently captures the dynamic correlations in this equilibrium system for all density regimes.

Due to this assumption, Eq.(3.25) can now be written as

$$\frac{d}{dt}C_r^{\mathcal{Q}\mathcal{Q}}(t,t') \simeq \frac{a'(\bar{\rho})}{2}\left(C_r^{m\mathcal{Q}}(t,t') - C_{r-1}^{m\mathcal{Q}}(t,t')\right), \tag{3.31}$$

where we replace $\mathcal{J}^{(d)}$ with the expression given in Eq.(3.29). Now, the dynamical equation of the correlation function of mass and current $C_r^{m\mathcal{Q}}(t,t')$ can be written from the following update rules for $t \geq t'$,

$$m_i(t+dt)\mathcal{Q}_{i+r}(t') = \begin{cases} \textbf{\textit{events}} & \textbf{\textit{probabilities}} \\ (m_i(t)+1)\,\mathcal{Q}_{i+r}(t') & \frac{1}{2}\hat{a}_{i+1}(t)dt \\ (m_i(t)+1)\,\mathcal{Q}_{i+r}(t') & \frac{1}{2}\hat{a}_{i-1}(t)dt \\ (m_i(t)-1)\,\mathcal{Q}_{i+r}(t') & \hat{a}_i(t)dt \\ m_i(t)\mathcal{Q}_{i+r}(t') & 1-\Sigma dt, \end{cases} \tag{3.32}$$

which gives us,

$$\frac{d}{dt}C_r^{m\mathcal{Q}}(t,t') = \left(C_{r+1}^{\mathcal{J}^{(d)}\mathcal{Q}}(t,t') - C_r^{\mathcal{J}^{(d)}\mathcal{Q}}(t,t')\right) \tag{3.33}$$

$$\simeq \frac{a'(\bar{\rho})}{2}\Delta_{r,k}C_r^{m\mathcal{Q}}(t,t'). \tag{3.34}$$

We use Eq. (3.29) to obtain Eq. (3.34), which, together with Eq. (3.31), constitutes a closed set of equations. To solve this set of linear equations, we take the discrete Fourier transform on both sides of Eq. (3.34) and Eq. (3.31), which provides us respectively with

$$\frac{\mathrm{d}}{\mathrm{d}t}\tilde{C}_q^{m\mathcal{Q}}(t,t') = -\frac{a'(\bar{\rho})}{2}\lambda_q\tilde{C}_q^{m\mathcal{Q}}(t,t'), \tag{3.35}$$

and

$$\frac{\mathrm{d}}{\mathrm{d}t}\tilde{C}_q^{\mathcal{Q}\mathcal{Q}}(t,t') = \frac{a'(\bar{\rho})}{2}\tilde{C}_q^{m\mathcal{Q}}(t,t')\left[1-e^{iq}\right], \tag{3.36}$$

where

$$\lambda_q = 2[1-\cos q]. \tag{3.37}$$

Integrating Eq.(3.36) and Eq.(3.35) we respectively get,

$$\tilde{C}_q^{m\mathcal{Q}}(t,t') = e^{-\frac{a'(\bar{\rho})}{2}\lambda_q(t-t')}\tilde{C}_q^{m\mathcal{Q}}(t',t'). \tag{3.38}$$

and

$$\tilde{C}_q^{\mathcal{Q}\mathcal{Q}}(t,t') = \int_{t'}^{t}\mathrm{d}t''\,\frac{a'(\bar{\rho})}{2}\tilde{C}_q^{m\mathcal{Q}}(t'',t')\left[1-e^{iq}\right] + \tilde{C}_q^{\mathcal{Q}\mathcal{Q}}(t',t'). \tag{3.39}$$

As observed in Eq. (3.39) and Eq. (3.38), it is apparent that to derive the complete solution of the current correlation function, we require the equal-time unequal-space correlations $C_r^{\mathcal{Q}\mathcal{Q}}(t,t)$ and $C_r^{m\mathcal{Q}}(t,t)$. The calculation of the correlation function for the equal-time and

unequal space, $C_r^{m\mathcal{Q}}(t,t)$, can be done by solving the dynamical equation generated by the following stochastic update equation:

$$m_i(t+dt)\mathcal{Q}_{i+r}(t+dt) = \begin{cases} \textit{events} & \textit{probabilities} \\ (m_i(t)-1)\,(\mathcal{Q}_{i+r}(t)+1) & \frac{1}{2}\hat{a}_i(t)\delta_{i,i+r}dt \\ (m_i(t)+1)\,(\mathcal{Q}_{i+r}(t)+1) & \frac{1}{2}\hat{a}_{i-1}(t)\delta_{i-1,i+r}dt \\ (m_i(t)-1)\,(\mathcal{Q}_{i+r}(t)-1) & \frac{1}{2}\hat{a}_i(t)\delta_{i-1,i+r}dt \\ (m_i(t)+1)\,(\mathcal{Q}_{i+r}(t)-1) & \frac{1}{2}\hat{a}_{i+1}(t)\delta_{i,i+r}dt \\ (m_i(t)-1)\,\mathcal{Q}_{i+r}(t) & \frac{1}{2}\hat{a}_i(t)\,(1-\delta_{i,i+r})\,dt \\ (m_i(t)+1)\,\mathcal{Q}_{i+r}(t) & \frac{1}{2}\hat{a}_{i-1}(t)\,(1-\delta_{i-1,i+r})\,dt \\ (m_i(t)-1)\,\mathcal{Q}_{i+r}(t) & \frac{1}{2}\hat{a}_i(t)\,(1-\delta_{i-1,i+r})\,dt \\ (m_i(t)+1)\,\mathcal{Q}_{i+r}(t) & \frac{1}{2}\hat{a}_{i+1}(t)\,(1-\delta_{i,i+r})\,dt \\ m_i(t)\,(\mathcal{Q}_{i+r}(t)+1) & \frac{1}{2}\hat{a}_{i+r}(t)\,(1-\delta_{i,i+r}-\delta_{i,i+r+1})\,dt \\ m_i(t)\,(\mathcal{Q}_{i+r}(t)-1) & \frac{1}{2}\hat{a}_{i+r+1}(t)\,(1-\delta_{i,i+r}-\delta_{i,i+r+1})\,dt \\ m_i(t)\mathcal{Q}_{i+r}(t) & (1-\Sigma dt)\,, \end{cases} \tag{3.40}$$

where $\Sigma =$ and from this we further get,

$$\frac{d}{dt}C_r^{m\mathcal{Q}}(t,t) \simeq \frac{a'(\bar{\rho})}{2}\Delta_{r,k}C_k^{m\mathcal{Q}}(t,t) + f_r, \tag{3.41}$$

where $f_r(t)$ is the source term of the above inhomogeneous equation and given as

$$f_r(t) = C_r^{m\mathcal{J}^{(d)}}(t,t) + \frac{1}{2}\left\langle \hat{a}_{L-1}\delta_{0,r+1} - \hat{a}_0\delta_{0,r}\right\rangle + \frac{1}{2}\left\langle \hat{a}_0\delta_{0,r+1} - \hat{a}_1\delta_{0,r}\right\rangle, \tag{3.42}$$

where we use translation invariance of the correlation functions and fix $i = 0$. Eq.(3.41) can be using Eq.(3.29) and applying the Fourier transform on both sides, which gives us,

$$\tilde{C}_q^{m\mathcal{Q}}(t,t) \simeq \int_0^t dt' e^{-\frac{a'(\bar{\rho})}{2}\lambda_q(t-t')}\tilde{f}_q(t'). \tag{3.43}$$

It is important to note that this source term $f_r(t)$ varies depending on the microscopic dynamics of the systems, although the large-scale dynamics is diffusive. As can be checked from the previous chapter, we obtain a different form of the source terms, as represented by the

equation (2.45) of Chapter 2. In the steady state, the source term becomes time independent and in the Fourier representation is given by,

$$\tilde{f}_q = \sum_{r=0}^{L-1} e^{iqr} f_r = \frac{\tilde{C}_q^{m\hat{a}}(t,t)}{2}\left(1 - e^{-iq}\right) - a\left(1 - e^{-iq}\right). \tag{3.44}$$

The final bit of information, i.e., the Fourier transform of the equal-time mass and activity operator correlation that appeared in $\tilde{f}_q$, can be obtained from the steady-state condition $dC_r^{mm}/dt = 0$, which gives us,

$$\frac{d}{dt}C_r^{mm}(t,t) = \sum_k \Delta_{rk} C_k^{m\hat{a}}(t,t) + B_r = 0, \tag{3.45}$$

where B_r is the source term having the form,

$$B_r(t) = \frac{\delta_{0,r}}{2}\left\langle 2\hat{a}_0 + \hat{a}_{L-1} + \hat{a}_1 \right\rangle - \frac{\delta_{0,r-1}}{2}\left\langle \hat{a}_0 + \hat{a}_1 \right\rangle - \frac{\delta_{0,r+1}}{2}\left\langle \hat{a}_{L-1} + \hat{a}_0 \right\rangle, \tag{3.46}$$

which can be derived from the following update rules,

$$m_i(t+dt)m_{i+r}(t+dt) = \begin{cases} \textit{events} & \textit{probabilities} \\ (m_i(t)-1)\,(m_{i+r}(t)-1) & \frac{1}{2}\hat{a}_i\delta_{i,i+r}dt \\ (m_i(t)-1)\,(m_{i+r}(t)+1) & \frac{1}{2}\hat{a}_i\delta_{i+1,i+r}dt \\ (m_i(t)+1)\,(m_{i+r}(t)+1) & \frac{1}{2}\hat{a}_{i-1}\delta_{i,i+r}dt \\ (m_i(t)+1)\,(m_{i+r}(t)-1) & \frac{1}{2}\hat{a}_{i-1}\delta_{i-1,i+r}dt \\ (m_i(t)+1)\,(m_{i+r}(t)+1) & \frac{1}{2}\hat{a}_{i+1}\delta_{i,i+r}dt \\ (m_i(t)+1)\,(m_{i+r}(t)-1) & \frac{1}{2}\hat{a}_{i+1}\delta_{i+1,i+r}dt \\ (m_i(t)-1)\,(m_{i+r}(t)-1) & \frac{1}{2}\hat{a}_i\delta_{i,i+r}dt \\ (m_i(t)-1)\,(m_{i+r}(t)+1) & \frac{1}{2}\hat{a}_i\delta_{i-1,i+r}dt \\ \textbf{continued on the next page} \end{cases} \tag{3.47}$$

$$m_i(t+dt)m_{i+r}(t+dt) = \begin{cases} \textbf{\textit{events}} & \textbf{\textit{probabilities}} \\ (m_i(t)-1)\,m_{i+r}(t) & \frac{1}{2}\hat{a}_i\,(1-\delta_{i+1,i+r}-\delta_{i,i+r})\,dt \\ (m_i(t)+1)\,m_{i+r}(t) & \frac{1}{2}\hat{a}_{i-1}\,(1-\delta_{i-1,i+r}-\delta_{i,i+r})\,dt \\ (m_i(t)-1)\,m_{i+r}(t) & \frac{1}{2}\hat{a}_i\,(1-\delta_{i-1,i+r}-\delta_{i,i+r})\,dt \\ (m_i(t)+1)\,m_{i+r}(t) & \frac{1}{2}\hat{a}_{i+1}\,(1-\delta_{i+1,i+r}-\delta_{i,i+r})\,dt \\ m_i(t)\,(m_{i+r}(t)-1) & \frac{1}{2}\hat{a}_{i+r}\,(1-\delta_{i,i+r+1}-\delta_{i,i+r})\,dt \\ m_i(t)\,(m_{i+r}(t)+1) & \frac{1}{2}\hat{a}_{i+r-1}\,(1-\delta_{i,i+r-1}-\delta_{i,i+r})\,dt \\ m_i(t)\,(m_{i+r}(t)-1) & \frac{1}{2}\hat{a}_{i+r}\,(1-\delta_{i,i+r-1}-\delta_{i,i+r})\,dt \\ m_i(t)\,(m_{i+r}(t)+1) & \frac{1}{2}\hat{a}_{i+r+1}\,(1-\delta_{i,i+r+1}-\delta_{i,i+r})\,dt \\ m_i(t)m_{i+r} & 1-\Sigma dt, \end{cases}$$

where $1-\Sigma dt$ represents the probability of nothing happening.

Eq.(3.45) can be solved using the generating function of form,

$$G(z) = \sum_{r=0}^{\infty} z^r C_r^{m\hat{a}}(t,t) \;\; for \;\; 0 \le z \le 1. \tag{3.48}$$

From the requirement of convergence of $G(z)$ at $z \to 1$, we obtain,

$$C_r^{m\hat{a}} = \begin{cases} a & for \;\; r = 0, \\ 0 & for \;\; r > 0; \end{cases} \tag{3.49}$$

finally we get

$$G(z) = a. \tag{3.50}$$

As the correlation function of mass and activity is simply delta-correlated, the corresponding Fourier transformation of this only contains a constant value, given as

$$\tilde{C}_q^{m\hat{a}}(t,t) = a. \tag{3.51}$$

By substituting Eq. (3.51) into Eq. (3.44), we obtain the final form of the source in Eq. (3.43) as

$$\tilde{f}_q = -\frac{a}{2}\left(1 - e^{-iq}\right). \tag{3.52}$$

Thus, in the steady state, we obtain the final solution of Eq. (3.38) by utilizing Eq. (3.43) and Eq. (3.52) as

$$\tilde{C}_q^{m\mathcal{Q}}(t,t') \simeq -\frac{a}{2}\int_0^{t'} dt'' e^{-\frac{a'(\bar{\rho})}{2}\lambda_q(t-t'')}\left(1 - e^{-iq}\right). \tag{3.53}$$

The remaining component required to solve Eq. (3.39) is the equal-time correlation function $C_r^{\mathcal{Q}\mathcal{Q}}(t',t')$. Similar to other correlation functions, we can derive its dynamical equation by using the following update equation:

$$\mathcal{Q}_i(t+dt)\mathcal{Q}_{i+r}(t+dt) = \begin{cases} \textbf{\textit{events}} & \textbf{\textit{probabilities}} \\ (\mathcal{Q}_i(t)+1)\,(\mathcal{Q}_{i+r}(t)+1) & \frac{1}{2}\hat{a}_i(t)\delta_{i,i+r}dt \\ (\mathcal{Q}_i(t)-1)\,(\mathcal{Q}_{i+r}(t)-1) & \frac{1}{2}\hat{a}_{i+1}(t)\delta_{i,i+r}dt \\ (\mathcal{Q}_i(t)+1)\,\mathcal{Q}_{i+r}(t) & \frac{1}{2}\hat{a}_i(t)\,(1-\delta_{i,i+r})\,dt \\ (\mathcal{Q}_i(t)-1)\,\mathcal{Q}_{i+r}(t) & \frac{1}{2}\hat{a}_{i+1}(t)\,(1-\delta_{i,i+r})\,dt \\ \mathcal{Q}_i(t)\,(\mathcal{Q}_{i+r}(t)+1) & \frac{1}{2}\hat{a}_{i+r}(t)\,(1-\delta_{i,i+r})\,dt \\ \mathcal{Q}_i(t)\,(\mathcal{Q}_{i+r}(t)-1) & \frac{1}{2}\hat{a}_{i+r+1}(t)\,(1-\delta_{i,i+r})\,dt \\ \mathcal{Q}_i(t)\mathcal{Q}_{i+r}(t) & 1-\Sigma dt, \end{cases} \tag{3.54}$$

where $\Sigma = \frac{1}{2}\left(\hat{a}_i(t)+\hat{a}_{i+1}(t)\right)\delta_{i,i+r} + \frac{1}{2}\left(1-\delta_{i,i+r}\right)\left(\hat{a}_i(t)+\hat{a}_{i+1}(t)+\hat{a}_{i+r}(t)+\hat{a}_{i+r+1}(t)\right)$. The corresponding evolution equation of $C_r^{\mathcal{Q}\mathcal{Q}}(t,t)$ is given by,

$$\frac{d}{dt}C_r^{\mathcal{Q}\mathcal{Q}}(t,t) = \Gamma_r(t) + C_r^{\mathcal{J}^{(d)}\mathcal{Q}}(t,t) + C_{L-r}^{\mathcal{J}^{(d)}\mathcal{Q}}(t,t), \tag{3.55}$$

$$\simeq \Gamma_r(t) + \frac{a'(\bar{\rho})}{2}\left\{C_r^{m\mathcal{Q}}(t,t) - C_{r-1}^{m\mathcal{Q}}(t,t)\right\} + \frac{a'(\bar{\rho})}{2}\left\{C_{L-r}^{m\mathcal{Q}}(t,t) - C_{L-r-1}^{m\mathcal{Q}}(t,t)\right\}, \tag{3.56}$$

where $\Gamma_r(t)$ is the strength of the fluctuating current and has the following form,

$$\Gamma_r(t) = \frac{1}{2}\left\langle \hat{a}_0(t) + \hat{a}_r(t)\right\rangle \delta_{0,r}. \tag{3.57}$$

The correlation function $C_r^{\mathcal{J}^{(d)}\mathcal{Q}}(t,t)$, as mentioned in Eq. (3.55), has been approximated using the scheme described in Eq. (3.29). This approximation leads to the simplified form given by Eq. (5.31).

3.3.2 *Time-integrated current fluctuation*

By further integrating Eq. (5.31) and expressing the correlation functions $C_r^{m\mathcal{Q}}(t,t)$ in terms of their Fourier transforms, we obtain the second term of Eq.(3.39),

$$C_r^{\mathcal{Q}\mathcal{Q}}(t,t) \simeq \int_0^t \mathrm{d}t'\,\Gamma_r(t') + \frac{1}{L}\int_0^t \mathrm{d}t'\,\frac{a'(\bar{\rho})}{2}\sum_{q=0}^{L-1}\tilde{C}_q^{m\mathcal{Q}}(t',t')\left[1-e^{iq}\right](2-\lambda_{qr}), \tag{3.58}$$

where $\lambda_{qr} = 2[1-\cos(qr)]$. In particular, the equal-time current correlation function mentioned in the equation above is identical to that of the Manna model [108]. However, it is important to note that in the Manna model, the time-reversal symmetry is broken, leading to significantly more nontrivial spatiotemporal correlations compared to its equilibrium counterpart that we are studying here. In the present model, which incorporates only a single-particle transfer rule, the equal-time mass activity correlations are delta-correlated in space. In contrast, in the Manna model, this correlation function exhibits nearest-neighbour correlations as well. Furthermore, although the function $\Gamma_r(t)$ has the same physical interpretation as the Manna model, i.e., the strength of the excess fluctuating microscopic current $\left\langle \mathcal{J}_i^{(fl)}(t)\mathcal{J}_{i+r}^{(fl)}(t')\right\rangle = \Gamma_r(t)\delta(t-t')$, it is also delta correlated in space, as given in Eq.(3.57). On the other hand, the Manna model exhibits nearest-neighbour correlations in $\Gamma_r(t)$. These simplifications, which are obviously the result of the time-reversible symmetry in the active phase, contribute to the simpler characteristics of our model.

Now, we substitute the Fourier transform of Eq. (3.58) and Eq. (3.53) into Eq. (3.36) and then perform the inverse Fourier transform of $\tilde{C}_q^{\mathcal{Q}\mathcal{Q}}(t,t')$ to obtain for $t \geq t'$,

$$\begin{aligned} C_r^{\mathcal{Q},\mathcal{Q}}(t,t') \simeq & t'\Gamma_r - \frac{1}{4L}\frac{(\bar{\rho}-1)}{\bar{\rho}^3}\sum_q \int_0^{t'} dt'' \int_0^{t''} dt''' e^{-\frac{1}{2\bar{\rho}^2}\lambda_q(t''-t''')}\lambda_q\,(2-\lambda_{qr}) \\ & - \frac{1}{4L}\frac{(\bar{\rho}-1)}{\bar{\rho}^3}\sum_q \int_{t'}^{t} dt'' \int_0^{t'} dt''' e^{-\frac{1}{2\bar{\rho}^2}\lambda_q(t''-t''')}\lambda_q e^{-iqr}. \end{aligned} \tag{3.59}$$

Using the steady state expression of Γ_r, defined in Eq.(3.57),

$$\Gamma_r = \frac{(\bar{\rho}-1)}{\bar{\rho}}\delta_{0,r}, \tag{3.60}$$

and substituting $r = 0$, $t = t' = T$ in Eq.(3.59), we obtain the fluctuation of cumulative current across a bond, $\mathcal{Q}(T)$ up to time T as

$$\left\langle \mathcal{Q}^2(T) \right\rangle = C_0^{\mathcal{Q}\mathcal{Q}}(T,T) = \frac{T}{L}\frac{(\bar{\rho}-1)}{\bar{\rho}} + 2\bar{\rho}(\bar{\rho}-1)\frac{1}{L}\sum_{q=1}^{L-1}\frac{1-e^{-\frac{1}{2\bar{\rho}^2}\lambda_q T}}{\lambda_q}. \tag{3.61}$$

From this above equation, we can get mobility $\chi(\bar{\rho})$ as defined in Eq.(1.43) in the limit $T \to \infty$ as

$$\lim_{T\to\infty}\frac{\left\langle \mathcal{Q}^2(T) \right\rangle}{T} = \frac{2\chi(\bar{\rho})}{L} \quad \Rightarrow \quad \chi(\bar{\rho}) = \frac{(\bar{\rho}-1)}{2\bar{\rho}}. \tag{3.62}$$

In the very short time of growth, i.e., when T is order of $1/D(\bar{\rho})$, the $\left\langle \mathcal{Q}^2(T) \right\rangle$, is given by the strength of fluctuating current Γ_0 across a bond, which can be written as

$$\left\langle \mathcal{Q}^2(T) \right\rangle \simeq \Gamma_0 T \ \ for \ \ 0 < T \leq \frac{1}{D(\bar{\rho})}. \tag{3.63}$$

When T becomes sufficiently large, we note that the growth of $\left\langle \mathcal{Q}^2(T) \right\rangle$ is determined by the three parameters of the system, that is, mobility χ, bulk diffusivity D, and system size L. Furthermore, by rescaling the cumulative current fluctuation on the right-hand side of the above equation as $\left\langle \mathcal{Q}^2(T) \right\rangle \to D(\bar{\rho})\left\langle \mathcal{Q}^2(T) \right\rangle / 2\chi(\bar{\rho})L$ and time as a scaling function of $D(\bar{\rho})T/L^2$; we rewrite Eq.(3.61) in the form of a universal scaling function $\mathcal{G}(y)$ as follows,

$$\frac{D(\bar{\rho})}{2\chi(\bar{\rho})L}\left\langle \mathcal{Q}^2(T) \right\rangle = \mathcal{G}\left(\frac{DT}{L^2}\right), \tag{3.64}$$

where the scaling function $\mathcal{G}(\tau)$ has the following form,

$$\mathcal{G}(\tau) = \tau + \lim_{L\to\infty}\frac{1}{L^2}\sum_q \frac{1-e^{-\lambda_q \tau L^2}}{\lambda_q}, \tag{3.65}$$

and $D(\bar{\rho})$ and $\chi(\bar{\rho})$ is defined in Eqs. (3.13) and (3.62), respectively. The above function can be approximately written in an integral as

$$\begin{aligned}\mathcal{G}(\tau) \simeq & \tau + \lim_{L\to\infty}\frac{1}{2\pi}\int_{4\pi^2}^{L^2\pi^2}\frac{1-e^{-z\tau}}{z^{3/2}}dz \\ = & \tau + \frac{1-e^{-4\pi^2\tau}+2\pi^{3/2}\sqrt{\tau}\,\mathrm{erfc}(2\pi\sqrt{\tau})}{2\pi^2} \simeq \tau + \frac{\sqrt{\tau}}{\sqrt{\pi}}.\end{aligned} \tag{3.66}$$

In the hydrodynamic timescale, fluctuations can be written using Eq. (3.66) as following.

(I) $0 < \tau \ll 1$

In this limit, the scaling function Eq.(3.65) can be written as

$$\mathcal{G}(\tau) \simeq \sqrt{\frac{\tau}{\pi}}, \tag{3.67}$$

using which the asymptotic of current fluctuation, $\langle \mathcal{Q}^2(T) \rangle \simeq T^{\alpha}$, in the corresponding limit in real time, $1 \ll T \ll L^2$ can be written as

$$\langle \mathcal{Q}^2(T) \rangle \simeq \frac{2\chi}{\sqrt{\pi D}} T^{\frac{1}{2}}, \tag{3.68}$$

implying $\alpha = 1/2$.

(II) $\tau \gg 1$

In this regime, the scaling function can be approximated as $\mathcal{G}(\tau) \simeq \tau$. This means that when $T \gg L^2$ for finite L, the current fluctuation becomes diffusive and written as

$$\langle \mathcal{Q}^2(T) \rangle \simeq \frac{2\chi T}{L}, \tag{3.69}$$

meaning $\alpha = 1$.

In comparison to the previous derivation of α near criticality in the context of the Manna model, as discussed in the previous chapter (Eq. (2.50)), where we obtained $\alpha = \frac{1}{2} - \mu$ and $\mu = (\beta + 1)/2\nu_{\perp} z$ in Eq. (2.51); in this model, since there is no anomalous behaviour present in the bulk diffusivity, which becomes constant $D \approx \frac{1}{2}$ near criticality, we immediately have $\mu = 0$. This means that no anomalous dynamic fluctuations are present in this model, which exhibits time-reversal symmetry in the active state.

In the *left panel* of Fig. (3.1), we plot the current fluctuation, scaled only by $2\chi L$, to observe collapse at a late time, as a function of the scaled time T/L^2 for a system size of $L = 1000$. Simulation data are plotted as solid lines for densities $\bar{\rho} = 1.001$ (violet), $\bar{\rho} = 1.005$ (green), 1.05 (blue), 1.5 (dark yellow), 2 (yellow), and 4 (dark blue). The analytical solution for $\bar{\rho} = 4$ obtained from Eq. (3.61) is plotted in a black dotted line and matches extremely well with the simulation data. Three guiding lines demonstrate linear growth in the initial time, the subdiffusive growth in the intermediate time, and again diffusive growth in the late time. Since bulk diffusivity is a quadratically decreasing function of density, $\langle \mathcal{Q}^2(T) \rangle$ for $\bar{\rho} = 4$ shows the longest initial linear growth at the initial time, since this regime was mentioned to extend up to $T = 1/D(\bar{\rho})$ time; consequently, the linear part at the late time arrives well beyond $T = L^2$ time.

On the *right panel* of the same figure, to observe the collapse as predicted by Eq. (3.65), we plot the rescaled current fluctuation, $D(\bar{\rho}) \langle \mathcal{Q}^2(T) \rangle / 2\chi(\bar{\rho}) L$, as a function of rescaled time $\tau = T/L^2$ for densities $\bar{\rho} = 1.001$, 1.005, 1.05, 1.5, 2, and 4 in solid lines for simulation data

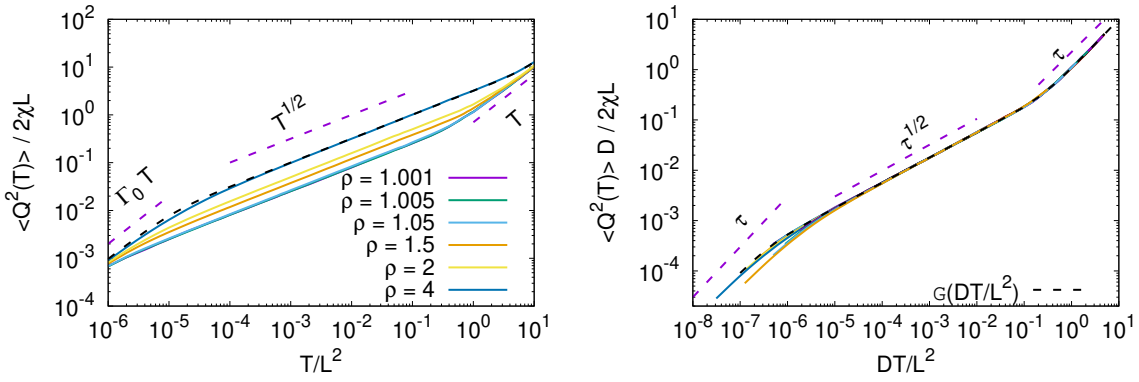

Figure 3.1: *Left panel:* Current fluctuation, scaled by $2\chi L$, is plotted as a function of scaled time T/L^2 for a system size of $L = 1000$ and for different densities. Simulation data are plotted in solid lines, and the analytical solution for $\bar{\rho} = 4$ obtained from Eq. (3.61) is plotted in a black dotted line. Three guiding lines demonstrate the linear growth in the initial time (Eq. (3.63)), the subdiffusive growth in the intermediate time (Eq. (3.68)), and again the diffusive growth at the late time (Eq. (3.69)). *Right panel:* Scaled current fluctuation $D(\bar{\rho})\left\langle \mathcal{Q}^2(T)\right\rangle /2\chi(\bar{\rho})L$ is plotted as a function of scaled time DT/L^2 for the same densities as in the left panel, for two different system sizes $L = 500$ and 1000. Simulation data are plotted in solid lines, which scale nicely on top of each other. The scaling function $\mathcal{G}$ obtained from Eq. (3.65) is plotted in a black dotted line and captures the collapse nicely.

for two system size $L = 500$ and 1000, all of which collapse nicely on top of each other. In addition, we include the scaling function $\mathcal{G}(\tau)$ in a dashed black line obtained from Eq. (3.65), which accurately captures the collapsed plot. From the scaling function $\mathcal{G}(\tau)$, one can observe three dynamical behaviours. Initially, the growth of the current fluctuation is linear. Then, when the scaled time is $1/L^2 \ll \tau \ll 1$, the growth becomes subdiffusive as $\tau^{1/2}$. As time increases, that is, $\tau \gg 1$, the growth of the fluctuation becomes diffusive or linear.

3.3.3 *Power spectrum of current fluctuations*

3.3.3.1 *Instantaneous current*

In this section, we demonstrate that the initial subdiffusive growth of cumulative current fluctuations can be explained by examining the dynamic correlation of instantaneous bond currents, as outlined below.

The instantaneous bond current correlation, $\langle \mathcal{J}_i(t)\mathcal{J}_{i+r}(0)\rangle - \langle \mathcal{J}_i(t)\rangle \langle \mathcal{J}_{i+r}(0)\rangle$, can be obtained by differentiating Eq.(3.59) for $t \geq t'$ in the following manner,

$$C_r^{\mathcal{J}\mathcal{J}}(t) \equiv \langle \mathcal{J}_i(t)\mathcal{J}_{i+r}(0)\rangle - \langle \mathcal{J}_i(t)\rangle \langle \mathcal{J}_{i+r}(0)\rangle = \left[\frac{d}{dt}\frac{d}{dt'}C_r^{\mathcal{Q}\mathcal{Q}}(t,t')\right]_{t'=0,t\geq 0}. \tag{3.70}$$

This differentiation further gives us the following analytical expression of the correlation function in steady state,

$$C_r^{\mathcal{J}\mathcal{J}}(t) = \Gamma_r \delta(t) - \frac{1}{L}\frac{(\bar{\rho}-1)}{4\bar{\rho}^3}\sum_q e^{-\frac{1}{2\bar{\rho}^2}\lambda_q t}\lambda_q e^{-iqr}. \tag{3.71}$$

It has been shown quite generically in [108, 116] that $\Gamma_r(t)$ represents the strength of the fluctuating current, which is valid at any time. The instantaneous current correlation function can be obtained by setting $r = 0$ in Eq.(3.71), and the only positive contribution to this correlation function comes from the delta-correlated part. The remaining term on the right-hand side of Eq.(3.71) actually cancels the contribution of the delta-correlated part. This cancellation can be observed by integrating Eq.(3.71) over a finite temporal interval $[-T, T]$, yielding the following expression:

$$\int_{-T}^{T} dt C_0^{\mathcal{J}\mathcal{J}}(t) = \frac{1}{L}\frac{(\bar{\rho}-1)}{\bar{\rho}} + \frac{1}{L}\frac{(\bar{\rho}-1)}{\bar{\rho}}\sum_q e^{-\frac{1}{2\bar{\rho}^2}\lambda_q T}. \tag{3.72}$$

In the limit of an infinite system size ($L \to \infty$) and a large temporal interval ($T \gg 1$), the sum on the right-hand side of the previous equation can be approximated by an integral. Thus, the equation can be rewritten as follows,

$$\lim_{L\to\infty}\int_{-T}^{T} dt C_0^{\mathcal{J}\mathcal{J}}(t) \simeq \frac{(\bar{\rho}-1)}{\sqrt{2\pi}}T^{-\frac{1}{2}}\int_0^\infty dy e^{-y}y^{-\frac{1}{2}} = \frac{(\bar{\rho}-1)}{\sqrt{2\pi}}T^{-\frac{1}{2}}, \tag{3.73}$$

where we have made the approximation $\lambda_q \simeq q^2$ and used the variable transformation $y = q^2T/4\bar{\rho}^2$. Furthermore, in the limit $T \to \infty$, it has been observed that the space-time integrated correlation function approaches zero as

$$\lim_{L\to\infty}\lim_{T\to\infty}\int_{-T}^{T} dt C_0^{\mathcal{J}\mathcal{J}}(t) = 0. \tag{3.74}$$

To further understand the underlying long-range negative correlation in the instantaneous current, which is the main factor contributing to the previous result, we can examine the right-hand side of Eq. (3.71) for $r = 0$ in the thermodynamic limit $L \to \infty$. Using the same variable transformation $y = \frac{q^2T}{4\bar{\rho}^2}$ as before, we can express it for, $t \gg 1$ as

$$\lim_{L\to\infty} C_0^{\mathcal{J}\mathcal{J}}(t) = -\frac{(\bar{\rho}-1)}{2\sqrt{2}\pi}t^{-\frac{3}{2}}\int_0^\infty dy e^{-y}\sqrt{y} = -\frac{(\bar{\rho}-1)}{4\sqrt{2\pi}}t^{-\frac{3}{2}}. \tag{3.75}$$

An important observation is the emergence of an integrable but long power-law temporal correlation in our equilibrium system. In particular, this correlation is independent of the system's proximity to the critical density $\bar{\rho} = 1$. Eq.(3.75) suggests that such dynamic long-range correlation functions are a characteristic feature of diffusive systems, exhibiting generic

behaviour. To verify Eq.(3.71) in simulation, we calculate the power spectrum of current fluctuations in the following section.

3.3.3.2 *Power spectrum*

The *Wiener-Khinchin* theorem [122] states that the spectral density of fluctuations can be obtained by taking the Fourier transform of the correlation function associated with those fluctuations. This implies that the power spectrum of the bond current fluctuation in the steady state, $S_{\mathcal{J}}(f)$ can be obtained by Fourier transforming the two-point correlation function described in Eq.(3.71) along with $r = 0$ as follows,

$$S_{\mathcal{J}}(f) = \int_{-\infty}^{\infty} dt C_0^{\mathcal{J}\mathcal{J}}(t) e^{2\pi i f t} = \frac{(\bar{\rho}-1)}{L\bar{\rho}} + \frac{(\bar{\rho}-1)}{L\bar{\rho}} \sum_q \frac{16 f^2 \pi^2 \bar{\rho}^4}{\lambda_q^2 + 16 f^2 \pi^2 \bar{\rho}^4}. \tag{3.76}$$

As mentioned in Eq.(3.64), in a diffusive system, the natural temporal scale is given by L^2/D. Therefore, it is expected that by rescaling the frequency f to fL^2/D, the power spectrum function can be expressed in terms of the following scaling function $\mathcal{S}$,

$$S_{\mathcal{J}}(f) = \frac{2\chi}{L} \mathcal{S}\left(\frac{fL^2}{D}\right), \tag{3.77}$$

where the mobility χ and diffusivity D are defined in Eqs.(3.62) and (3.13). By comparing the above equation with Eq.(3.76), we can obtain the scaling function $\mathcal{S}$ as follows,

$$\mathcal{S}(y) = 1 + \lim_{L\to\infty} \sum_q \frac{4y^2\pi^2}{\lambda_q^2 L^4 + 4y^2\pi^2}. \tag{3.78}$$

In the limit of large system size, $L \gg 1$, the asymptotic behaviour of the above sum when $1 \ll y \ll L^2/D$, can be obtained by approximating the sum by the following integral,

$$\mathcal{S}(y) \simeq 1 + 2L \int_{\frac{1}{L}}^{\frac{1}{2}} dx \frac{4y^2\pi^2}{\lambda(x)^2 L^4 + 4y^2\pi^2}, \tag{3.79}$$

where in the continuum limit, we perform the substitution $q \to 2\pi x$, which leads to $\lambda(x) \approx 4\pi^2 x^2$. Then by using the variable transformation, $x = \sqrt{y}/4\sqrt{2\pi} L z^{3/4}$, we convert the above integral into the following in the limit $L \to \infty$ and obtain,

$$\begin{aligned}\mathcal{S}(y) \simeq 1 + \frac{\sqrt{y}}{2\sqrt{2\pi}} \int_0^{\infty} \frac{dz}{z^{3/4}(1+z)} &= 1 + \sqrt{2}\left[\tan^{-1}\left(\frac{\sqrt{z}-1}{\sqrt{2}\sqrt[4]{z}}\right) + \tanh^{-1}\left(\frac{\sqrt{2}\sqrt[4]{z}}{\sqrt{z}+1}\right)\right]_0^{\infty} \\ &= 1 + \frac{\sqrt{y\pi}}{2}.\end{aligned} \tag{3.80}$$

From the asymptotic behaviour of the scaling function we find that the asymptotic behaviour of the power spectrum $S_{\mathcal{J}}(f) - S_{\mathcal{J}}(0) \sim f^{\psi_{\mathcal{J}}}$ as a function of unscaled frequency f,

$$S_{\mathcal{J}(f)} \simeq \frac{2\chi}{L} + \chi(\bar{\rho})\sqrt{\frac{\pi}{D(\bar{\rho})}} f^{1/2}, \tag{3.81}$$

implying $f^{\mathcal{J}} = 1/2$, where $S_{\mathcal{J}}(0) = 2\chi/L$, and in the thermodynamic limit, $L \to \infty$ we have $S_{\mathcal{J}(f)} \sim f^{1/2}$.

In simulations, we compute the power spectrum by discretizing the instantaneous current into small temporal intervals, typically denoted as δt, and then calculate the Fourier transform as follows,

$$\tilde{\mathcal{J}}_{n;T} = \delta t \sum_{k=0}^{T-1} \mathcal{J}_i(k) e^{2\pi i f_n k}, \tag{3.82}$$

where $f_n = n/T$ for $T \gg 1$. Finally, we define the power spectrum of a bond current as

$$S_{\mathcal{J}}(f_n) = \lim_{T\to\infty} \frac{1}{T} \langle |\tilde{\mathcal{J}}_{n;T}|^2 \rangle, \tag{3.83}$$

where $f_n = n/T$ for $T \gg 1$. The limit as T tends to infinity represents an average over an infinitely long time period. For a sufficiently smooth function, the Wiener-Khinchin theorem guarantees the convergence of the discrete sum in Eq.(3.83) to its continuum limit, as expressed in Eq.(3.76).

In the *left panel* of Fig. (3.2), we plot the relative power spectrum $S_{\mathcal{J}}(f) - S_{\mathcal{J}}(0)$ as a function of density for $L = 1000$. Simulation data are plotted as solid lines for density values 1.002 (violet), 1.004 (green), 1.05 (blue), 1.5 (orange), 2 (yellow), and 4 (dark blue). The corresponding theoretical line is plotted using Eq. (3.76) for $\bar{\rho} = 4$, which is in excellent agreement with the simulation data. In the *right panel*, we plot the scaled power spectrum $LS_{\mathcal{J}}(f)/2\chi - 1$ as a function of the scaled frequency fL^2/D for two systems sizes $L = 1000$ and 500. The simulation data are plotted for the same density values as in the left panel, which collapsed nicely, and our shifted scaling function $\mathcal{S} - 1$ given in Eq. (3.78) is plotted as a dashed red line, excellently capturing the collapse.

3.3.4 *Fluctuations of spacetime integrated current*

In this section, we compute the fluctuation of the space-time-integrated current $\bar{\mathcal{Q}}(l,T) = \sum_{i=0}^{l-1} \mathcal{Q}_i(T)$ using the most general current-current correlation function $C_r^{\mathcal{Q}\mathcal{Q}}(t,t')$ given in Eq. (3.59). Then, we show that the mobility of the particle current, derived by applying a small biasing force (as discussed in the section ...), is actually equal to the intensive fluctuation of $\bar{\mathcal{Q}}(l,T)$ in the appropriate limit. This relationship is simply known as the famous

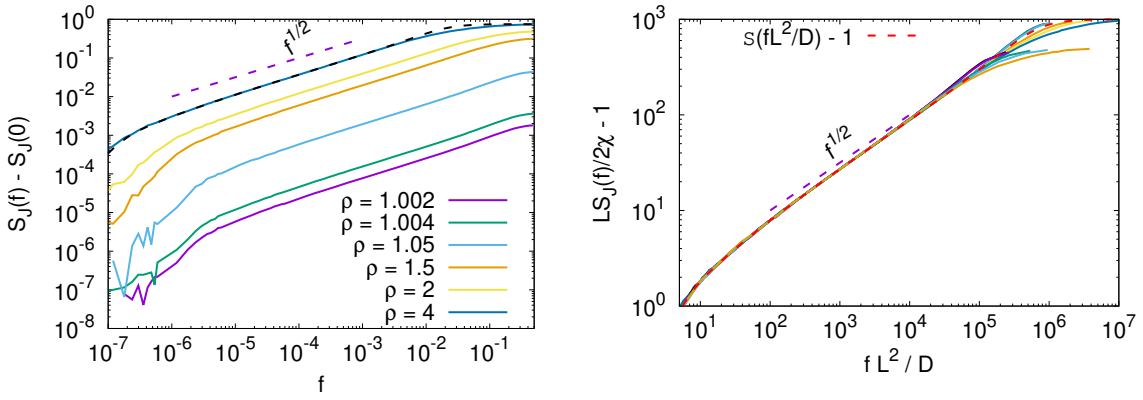

Figure 3.2: In the *left panel*, we present the plot of the relative power spectrum $S_{\mathcal{J}}(f) - S_{\mathcal{J}}(0)$ with respect to density for a system size of $L = 1000$. The simulation data are depicted as solid lines for densities 1.002 (violet), 1.004 (green), 1.05 (blue), 1.5 (orange), 2 (yellow), and 4 (dark blue). To complement this, we include the corresponding theoretical line obtained using Eq. (3.76) for $\bar{\rho} = 4$, which exhibits excellent agreement with the simulation data and the guiding line $f^{1/2}$ follows Eq. (3.81). In the *right panel*, we illustrate the scaled power spectrum $LS_{\mathcal{J}}(f)/2\chi - 1$ as a function of the scaled frequency fL^2/D for two system sizes, $L = 1000$ and 500. The simulation data are plotted for the same density values as in the left panel, and they exhibit a remarkable collapse. Additionally, we include our shifted scaling function $\mathcal{S} - 1$, given in Eq. (3.78), as a dashed red line, which captures the observed collapse.

Green-Kubo relation [5–8] for the transport coefficients. The steady state fluctuation of the integrated current across a subsystem of size l up to time T is given by,

$$\left\langle \bar{Q}^2(l,T)\right\rangle - \left\langle \bar{Q}(l,T)\right\rangle^2 = \left\langle \bar{Q}^2(l,T)\right\rangle = lC_0^{\mathcal{Q}\mathcal{Q}}(T,T) + \sum_{r=1}^{l-1} 2(l-r)C_r^{\mathcal{Q}\mathcal{Q}}(T,T), \tag{3.84}$$

along with the assumption that in the steady state the mean current is zero, $\langle \mathcal{Q}(l,T)\rangle = 0$. Substituting Eq.(3.59) in the previous equation and utilizing the identity,

$$\sum_{r=1}^{l-1} 2(l-r)(2-\lambda_{rn}) = 2\left(\frac{\lambda_{ln} - l\lambda_n}{\lambda_n}\right), \tag{3.85}$$

given in Ref.[108], we obtain the following expression for $\left\langle \bar{Q}^2(l,T)\right\rangle$,

$$\left\langle \bar{Q}(l,T)^2\right\rangle = 2\chi(\bar{\rho})lT - 2\chi(\bar{\rho})\frac{D(\bar{\rho})}{L}\sum_q \frac{D(\bar{\rho})\lambda_q T - 1 + \exp\left(-\lambda_q D(\bar{\rho})T\right)}{\left(\lambda_q D(\bar{\rho})\right)^2}\lambda_{ql}, \tag{3.86}$$

where $\chi(\bar{\rho}) = (\bar{\rho}-1)/2\bar{\rho}$ and $D(\bar{\rho}) = 1/2\bar{\rho}^2$. The relationship between the size of the subsystem l and the observation time T remains significant even in this equilibrium system. In the following discussion, we will examine the behavior of fluctuations, $\left\langle \bar{Q}(l,T)^2\right\rangle$, for $L \gg 1$, as we consider the infinite space-time volume by interchanging the limits of l and T.

Case I: Taking the limit $T \to \infty$ first, followed by $l \to \infty$. To obtain this limit, we first take $T \gg 1$, while keeping l small, which allows us to write the Eq.(3.86) as

$$\begin{aligned}\left\langle \bar{Q}(l,T)^2 \right\rangle \simeq & 2\chi(\bar{\rho})lT - 2\chi(\bar{\rho})\frac{D(\bar{\rho})}{L}\sum_q \frac{D(\bar{\rho})\lambda_q T - 1 + \exp\left(-\lambda_q D(\bar{\rho})T\right)}{\left(\lambda_q D(\bar{\rho})\right)^2}\lambda_{ql}, \\ \simeq & 4\chi(\bar{\rho})\frac{D(\bar{\rho})}{L}\int_{1/L}^{1/2} dx \frac{1-\exp\left(-\lambda(x)D(\bar{\rho})T\right)}{\left(\lambda(x)D(\bar{\rho})\right)^2}\lambda(lx),\end{aligned} \tag{3.87}$$

where the final integral is obtained in the thermodynamic limit $L \to \infty$, and $x = i/L$. This integral can be solved using the approximation $\lambda(lx) \simeq 4\pi^2 l^2 x^2$ for finite subsystem size l and a variable transformation $x = y^{1/2}/2\pi\sqrt{D(\bar{\rho})T}$, which gives us

$$\frac{1}{lT}\left\langle \bar{Q}^2(l,T)\right\rangle \simeq \frac{\chi(\bar{\rho})}{\pi\sqrt{D(\bar{\rho})}}\frac{l}{\sqrt{T}}\int_0^\infty dy(1-e^{-y})y^{-3/2} = \frac{2\chi(\bar{\rho})}{\sqrt{\pi D(\bar{\rho})}}\frac{l}{\sqrt{T}}. \tag{3.88}$$

Finally, if we take the limit, $T \to \infty$ the above intensive fluctuation goes to zero.

Case II: Taking the limit $l \to \infty$ first, followed by $T \to \infty$. On the other hand, to obtain this limit, we first use $\lambda_{lq} \simeq 2$ for $l \gg 1$, then write Eq.(3.86) in the thermodynamic limit as

$$\frac{1}{lT}\left\langle \bar{Q}^2(l,T)\right\rangle \simeq 2\chi(\bar{\rho}) - \frac{8\chi(\bar{\rho})D(\bar{\rho})}{lT}\int_{1/L}^{1/2} dx \frac{D(\bar{\rho})\lambda(x)T - 1 + \exp\left(-\lambda(x)D(\bar{\rho})T\right)}{\lambda^2(x)D^2(\bar{\rho})}, \tag{3.89}$$

which using the same variable transformation as in case-I, we write,

$$\begin{aligned}\frac{1}{lT}\left\langle \bar{Q}^2(l,T)\right\rangle \simeq & 2\chi(\bar{\rho}) - \frac{2\chi(\bar{\rho})D(\bar{\rho})}{lT}\int_0^\infty \mathrm{d}y\left(y-1+e^{-y}\right)y^{-5/2}\frac{T^{3/2}}{\pi\sqrt{D(\bar{\rho})}} \\ = & 2\chi(\bar{\rho}) - \frac{8\chi(\bar{\rho})}{3}\sqrt{\frac{D}{\pi}}\frac{\sqrt{T}}{l}.\end{aligned} \tag{3.90}$$

In the above equation by taking the limit $l \to \infty$, we obtain the convergence of the intensive fluctuation of the space-time integrated bond current as $2\chi(\bar{\rho})$. It has already been shown using a small bias that the mobility of this equilibrium model is the activity itself, or $(\bar{\rho} - 1)/2\bar{\rho}$ for a global density of $\bar{\rho}$ [87]. The Green-Kubo relation, in equilibrium [5–8] states that the mobility is the space-time-integrated correlation of the particle current when there is no bias and the same limiting condition is applied. In Eq.(3.90) we simply recover that result.

In Fig.(3.3), we plot $\left\langle \bar{Q}(l,T)^2\right\rangle$ as a function of relative density $\Delta = \bar{\rho} - 1$. The simulation data for $l = 2500$, $T = 100$ and $l = 100$, $T = 10^5$ are plotted respectively in solid blue and violet lines and the analytical solutions of Eq.(3.86) for the corresponding values of l and T are plotted in black dotted lines and match excellently with our simulation data. We also

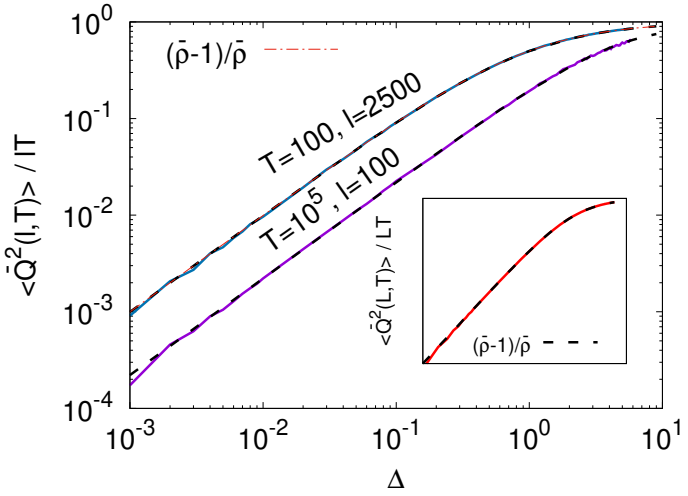

Figure 3.3: The scaled space-time-integrated current fluctuations are presented as a function of relative density. The simulation data for subsystem size $l = 2500$ and $T = 100$ is represented by the solid blue line, while the data for $l = 100$ and $T = 10^5$ is shown as the solid violet line. To assess the agreement between simulation and theory, we compare the analytical result given by equation (3.86) (depicted by the corresponding dashed black lines) with the simulation data, which exhibits excellent agreement. The simulations were conducted for a system size of $L = 5000$ in both cases. In the inset, we further obtained an excellent agreement between the scaled total current fluctuation and twice the activity, or $(\bar{\rho}-1)/\bar{\rho}$, as a function of Δ as predicted in Eq. (3.91).

plot twice the activity, $(\bar{\rho}-1)/\bar{\rho}$ in a blue dot-dashed line, which exactly superposed on the fluctuation curve of $l = 2500$ and $T = 100$. All simulation data are taken for $L = 5000$.

Interestingly, for a large system size $L \gg 1$, the fluctuation of total current $\bar{\mathcal{Q}}(L,T)$ is always extensive; by replacing the subsystem size l by the system size L in Eq.(3.86) we obtain,

$$\lim_{L\to\infty} \frac{1}{LT} \left\langle \bar{\mathcal{Q}}^2(L,T) \right\rangle = 2\chi = \sum_{r=0}^{L-1} \Gamma_r = \frac{\bar{\rho}-1}{\bar{\rho}}, \tag{3.91}$$

as $\lambda_{Lq} = 0$ for all values of q. Actually, this is the converging value of $\left\langle \bar{Q}^2(l,T) \right\rangle / lT$ if we take the limit $l \to \infty$ then $T \to \infty$ and we denote it as twice the mobility $\chi(\bar{\rho})$ of the system, i.e.,

$$\lim_{L\to\infty} \frac{1}{LT} \left\langle \bar{\mathcal{Q}}^2(L,T) \right\rangle = \frac{\bar{\rho}-1}{\bar{\rho}} = \sigma_{\mathcal{Q}}^2 \equiv \lim_{l\to\infty} \lim_{T\to\infty} \frac{1}{lT} \left\langle \bar{Q}^2(l,T) \right\rangle, \tag{3.92}$$

which equates $2\chi(\bar{\rho}) = a(\bar{\rho}) = \frac{\bar{\rho}-1}{\bar{\rho}}$.

3.3.5 *Tagged particle diffusion*

In this section, we study the fluctuations in the displacements of the tagged particles as a function of time. We establish a connection between the sum of the integrated displacements of each individual tagged particle, denoted as $\sum_{\alpha=1}^{N} X_\alpha(T)$, where $X_\alpha(T)$ represents the total displacement of the particle α within the time interval of $[0, T]$ with the total integrated current $\bar{\mathcal{Q}}(L, T)$. This relation is established by considering the integrated current across both space and time, which can be expressed using the following relationship,

$$\sum_{\alpha=1}^{N} X_\alpha(T) = \sum_{i=0}^{L-1} \mathcal{Q}_i(T) = \bar{\mathcal{Q}}(L, T). \tag{3.93}$$

In the limit of large $T \gg L^2$, the self-diffusion coefficient $\mathcal{D}_s(\bar{\rho})$ can be defined through the mean-square tagged particle displacement of the α^{th} particle as given below,

$$\left\langle X_\alpha^2(T) \right\rangle \simeq 2\mathcal{D}_s(\bar{\rho})T. \tag{3.94}$$

Earlier in Ref.[108] in the context of another sandpile model, the Manna model, it was shown that the bulk diffusivity coefficient $D(\bar{\rho})$ is very different from the self-diffusivity of a tagged particle. In fact, the tagged particle diffusion coefficient $\mathcal{D}_s(\bar{\rho})$ can be expressed as a ratio of the intensive fluctuation of total current $\langle \mathcal{Q}^2(L, T) \rangle$ and the global density $\bar{\rho}$,

$$\mathcal{D}_s(\bar{\rho}) = \frac{a(\bar{\rho})}{2\bar{\rho}} = \frac{1}{\bar{\rho}} \left[\lim_{L,T\to\infty} \frac{\left\langle \bar{\mathcal{Q}}^2(L, T) \right\rangle}{2LT} \right] = \frac{\bar{\rho} - 1}{2\bar{\rho}^2}; \tag{3.95}$$

for details see Ref.[108]. In Fig. (3.4), we present the plot of the mean square fluctuation of the displacement of tagged particles (indicated by the solid red line) up to time T, $\left\langle \left\langle X^2(T) \right\rangle \right\rangle / 2T$, as a function of $\Delta = \rho - 1$. Here, the double angular braces $\left\langle \left\langle X^2(T) \right\rangle \right\rangle = \sum_\alpha \left\langle X_\alpha^2(T) \right\rangle / N$ represent the average over trajectories and particles. During simulations, particle transfer at any site i involves the random selection of a single particle from a specific stack. Additionally, we include the theoretical expression of the density-dependent self-diffusion coefficient $\mathcal{D}_s(\rho) = (\bar{\rho} - 1)/2\bar{\rho}^2$, as given in equation (3.95), which is plotted as the dashed black line. Remarkably, there is excellent agreement between the simulation results and the theoretical prediction. For comparison, we also include the plot of the bulk diffusion coefficient $D(\bar{\rho})$ (represented by the dot-dot-dashed blue line), defined in equation (3.13). It is important to note that the self-diffusion coefficient $\mathcal{D}_s(\bar{\rho})$ and the bulk diffusion coefficient $D(\bar{\rho})$ are distinct quantities that exhibit contrasting behaviours, particularly near criticality. Specifically, as the system approaches criticality, where the activity decays as $a(\bar{\rho}) \sim (\bar{\rho} - 1)$, the self-diffusion coefficient, which being the ratio of activity to density (see equation (3.95)),

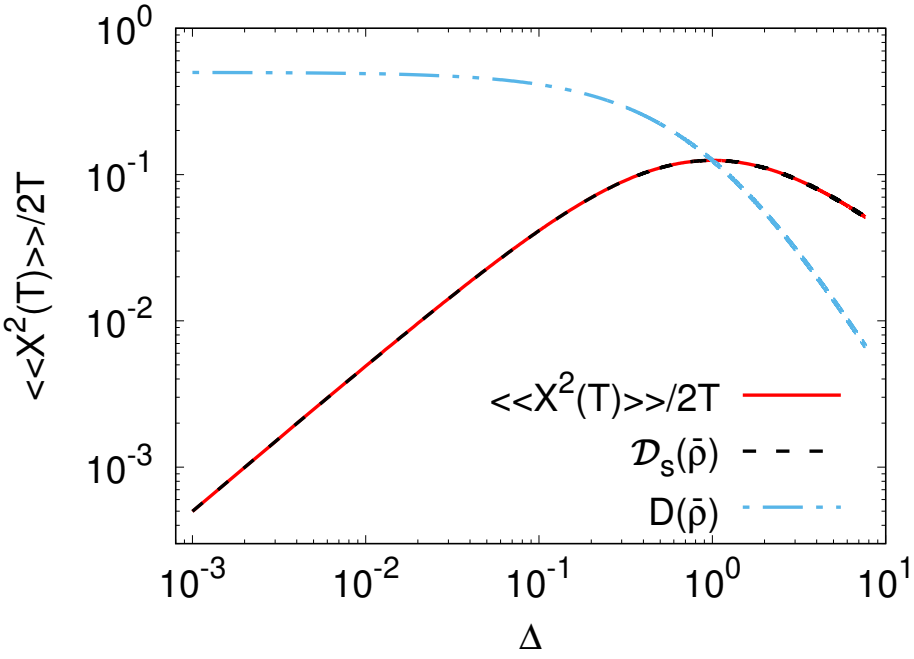

Figure 3.4: We plot the mean-square fluctuation of the displacement of tagged particles up to time T (represented by the solid red line) as a function of the relative density Δ. Here, the double angular braces $\langle\langle X^2(T)\rangle\rangle = \sum_\alpha \langle X_\alpha^2(T)\rangle / N$ indicate the average over trajectories and particles. The simulations (solid red line) demonstrate excellent agreement with the theoretically derived self-diffusion coefficient $\mathcal{D}_s(\bar{\rho})$ (depicted by the dashed black line) as shown in equation (3.95). Additionally, in the same graph, we plot the bulk diffusion coefficient $D(\bar{\rho}) = 1/2\bar{\rho}^2$ as a function of $\Delta = \bar{\rho} - 1$ (represented by the dot-dot-dashed blue line), which exhibits a contrasting behaviour compared to the self-diffusion coefficient $\mathcal{D}_s(\bar{\rho})$.

vanishes as $\mathcal{D}_s(\bar{\rho}) \sim (\bar{\rho} - 1)$, mirroring the behaviour of the activity near criticality. In contrast, the bulk diffusion coefficient, which is the derivative of activity with respect to density (see equation (3.13)), remains constant at a value of $1/2$. Moreover, when the system is far from criticality and in the limit of large density $\bar{\rho} \gg 1$, both the self-diffusion coefficient and the bulk diffusion coefficient approach zero, but with different decay patterns. In this case, since activity is expected to follow $a(\bar{\rho}) \simeq 1 - \text{const.}/\bar{\rho}$, the self-diffusivity decays as $\mathcal{D}_s(\bar{\rho}) \sim 1/\bar{\rho}$, while the bulk diffusivity decays much faster, with $D(\bar{\rho}) \sim 1/\bar{\rho}^2$.

Although Equation (3.95) has been proven to be valid for other models, such as simple symmetric exclusion processes [118], its applicability in our model comes from the absence of correlations among toppled particles in steady state. Consequently, the self-diffusivity can be determined by examining the fluctuations in the total integrated current. It is important to note the significant distinction between self-diffusivity and bulk diffusivity. Near the critical point, the bulk diffusivity remains constant at a value of $1/2$, while the self-diffusivity approaches zero as $(\bar{\rho} - 1)$. In the high-density limit, both of these transport coefficients

tend to zero, albeit in different manners. The self-diffusivity decays as $1/\bar{\rho}$, while the bulk diffusivity decays much faster as $1/\bar{\rho}^2$.

3.3.6 *Power spectrum of mass fluctuations*

In this section, we study the properties of fluctuations in the mass of a subsystem $M_l(t) = \sum_{i=0}^{l=1} m_i(t)$, for which we begin with the unequal-time and unequal-space correlation function of the mass of a single site in steady state for $t \geq 0$, $C_r^{\mathcal{Q}\mathcal{Q}}(t,0) = \langle m_i(t) m_{i+r}(0)\rangle - \langle m_i(t)\rangle \langle m_{i+r}(0)\rangle \equiv C_r^{mm}(t)$. Since the steady state is an equilibrium state and all particles in the steady state are essentially performing noninteracting random walks, it is expected that the spatial correlation among the sites should not exhibit any long-range correlation. In fact, in the following sections, we demonstrate that a single-site mass does not possess any correlation beyond $r = 0$.

The evolution equation of this quantity can be written as

$$\frac{d}{dt} C_r^{mm}(t) = \frac{1}{2} \sum_k \Delta_{0,k} \langle \hat{a}_k(t) m_r(0)\rangle \,, \tag{3.96}$$

which further can be solved using Eq.(3.29) that simplifies the above equation to,

$$\frac{d}{dt} C_r^{mm}(t) \simeq \frac{1}{2\bar{\rho}^2} \sum_k \Delta_{r,k} C_k^{mm}(t). \tag{3.97}$$

Solving the above equation using Fourier representation, we obtain,

$$\tilde{C}_q^{mm}(t) \simeq e^{-\frac{1}{2\bar{\rho}^2}\lambda_q t} \tilde{C}_q^{mm}(0,0), \tag{3.98}$$

where $\tilde{C}_q^{mm}$ is the Fourier transformation of C_r^{mm}. $\tilde{C}_q^{mm}(0,0)$ represents the Fourier transform of the equal-time correlation function. It can be obtained by using Eq.(3.29) in Eq.(3.45) and utilising the condition $dC_r^{mm}/dt = 0$ in steady state, which gives us

$$\frac{d}{dt} C_r^{mm}(t,t) \simeq \frac{1}{2\bar{\rho}^2} \sum_k \Delta_{0,k} \langle m_k m_r\rangle + B_r = 0, \tag{3.99}$$

where the source term B_r is given in Eq.(3.46). Using the generating function, $G'(z) = \sum_{z=0}^{\infty} C_r^{mm}(t,t) z^r$, similarly to Eq.(3.48), we can solve Eq.(3.99) by multiplying both sides of this equation by z^r and taking the sum over r from 0 to ∞, which finally gives us,

$$G'(z) = \bar{\rho}(\bar{\rho} - 1), \tag{3.100}$$

where we imposed the condition $G'(z) < \infty$ when $z \to 1$. This generating function tells us that $C_r^{mm}(t,t) = \rho(\rho-1)\delta_{0,r}$ and the Fourier transform of it is given by,

$$\tilde{C}_q^{mm}(t,t) = \bar{\rho}(\bar{\rho}-1). \tag{3.101}$$

We put the above equation to Eq.(3.98) to obtain,

$$\tilde{C}_q^{mm}(t) \simeq e^{-\frac{1}{2\bar{\rho}^2}\lambda_q t}\rho(\rho-1), \tag{3.102}$$

and finally, using the inverse Fourier transform we got the correlation function $C_r^{mm}(t)$ as

$$C_r^{mm}(t) \simeq \frac{1}{L}\sum_q e^{-iqr}e^{-\frac{1}{2\bar{\rho}^2}\lambda_q t}\rho(\rho-1). \tag{3.103}$$

Following the Ref.[108], we now consider subsystem mass $M_l(t) = \sum_{r=0}^{l-1} m_r(t)$ for $l < L$ and calculate the equal-time correlation function for mass $C^{M_lM_l}(t,0) \equiv C^{M_lM_l}(t)$ by using the following expression,

$$C^{M_lM_l}(t) = lC_0^{mm}(t) + \sum_{r=1}^{l-1}(l-r)(C_r^{mm}(t) + C_{-r}^{mm}(t)). \tag{3.104}$$

Substituting Eq.(3.105), in the above equation, we get the dynamic correlation of subsystem mass,

$$C^{M_lM_l}(t) \simeq \frac{1}{L}\sum_q e^{-\frac{1}{2\bar{\rho}^2}\lambda_q t}\bar{\rho}(\bar{\rho}-1)\frac{\lambda_{ql}}{\lambda_q}, \tag{3.105}$$

the equal-time part of which gives us the fluctuation of subsystem mass, $C^{M_lM_l}(0) = \langle M_l^2\rangle - \bar{\rho}^2 l^2 = \bar{\rho}(\bar{\rho}-1)l$, when $l \ll L$. Similarly to Eq. (2.97) in Chap. 2, by defining the scaled subsystem mass fluctuation $\sigma^2(\bar{\rho})$ as $\sigma^2(\bar{\rho}) = C^{M_lM_l}(0)/l = \bar{\rho}(\bar{\rho}-1)$, we can derive the Einstein relation that connects the scaled subsystem mass fluctuation and the scaled spacetime-integrated current fluctuation as

$$\sigma^2(\bar{\rho}) = \frac{\sigma_Q^2}{2D}, \tag{3.106}$$

where σ_Q^2 is given in Eq. (3.92).

As we mentioned previously, it is more convenient to observe the power spectrum of fluctuations than the correlation functions directly; we write the Fourier transform of $C^{M_l M_l}(t)$, which gives us the power spectrum of mass fluctuations, $S_{M_l}(f)$ as

$$S_{M_l}(f) = \lim_{T\to\infty} \int_{-T}^{T} \mathrm{d}t\, C^{M_l M_l}(t) e^{2\pi i f t} = \frac{1}{L}\sum_q \bar{\rho}(\bar{\rho}-1)\frac{2\lambda_q D(\bar{\rho})}{\lambda_q^2 D(\bar{\rho})^2 + 4\pi^2 f^2}\frac{\lambda_{lq}}{\lambda_q}. \tag{3.107}$$

By rescaling the frequency as a dimensionless quantity $f \to fL^2/D$, $S_{M_l}(f)$ can be written in terms of a scaling function $\mathcal{K}_M$ as

$$S_{M_l}(f) = \frac{2\chi(\bar{\rho})L^3}{D(\bar{\rho})^2}\mathcal{K}_M\left(\frac{fL^2}{D}\right), \tag{3.108}$$

where the scaling function $\mathcal{K}_M$ is given by,

$$\mathcal{K}_M(y) = \lim_{L\to\infty}\sum_q \frac{\lambda_{lq}}{\lambda_q^2 L^4 + 4\pi^2 y^2}. \tag{3.109}$$

To obtain the asymptotics of $\mathcal{K}_M$, we take the continuum limit $q \to 2\pi x$, where $x = n/L$ and $n = 1, 2, \ldots, L-1$ for $L \gg 1$. Then we define the variable transformation $x = z^{1/4}/2\pi L$, which lets us write Eq.(3.109) as

$$\begin{aligned}\mathcal{K}_M(y) &\simeq \int_{16\pi^4}^{L^4\pi^4} \frac{dz}{2\pi z^{3/4}\left(4\pi^2 y^2 + z\right)} = \left[\frac{\tanh^{-1}\left(\frac{2\sqrt{\pi}\sqrt{y}\sqrt[4]{z}}{2\pi y+\sqrt{z}}\right) - \tan^{-1}\left(\frac{2\pi y-\sqrt{z}}{2\sqrt{\pi}\sqrt{y}\sqrt[4]{z}}\right)}{4\pi^{5/2}y^{3/2}}\right]_{16\pi^4}^{L^4\pi^4}, \\ &\simeq \frac{y^{-3/2}}{4\pi^{3/2}} \;\; for \;\; L\to\infty.\end{aligned} \tag{3.110}$$

The above result tells us that in the low frequency regime $1/L^2 \ll f \ll 1$, we write the asymptotic behaviour of the power spectrum of subsystem mass, $S_{M_l}(f) \sim f^{-\psi_M}$ as a function of unscaled frequency f by,

$$S_{M_l}(f) \simeq \frac{1}{2\pi^{3/2}}\frac{\chi(\bar{\rho})}{\sqrt{D}} f^{-3/2}, \tag{3.111}$$

which gives us $\psi_M = 3/2$.

In the *left panel* of Fig. (3.5), we plot the power spectrum of the mass as a function of frequency for a system size of $L = 1000$ and a subsystem size of $l = L/2$. Simulation data are represented by solid lines for densities $\bar{\rho} = 1.002$ (violet), 1.004 (green), 1.05 (blue), 1.5 (orange), 2 (yellow), and 4 (dark blue). We also include the theoretical formula, Eq. (3.107), for $\bar{\rho} = 4$, represented by the dashed black line, which shows excellent agreement with the simulation data. In the *right panel*, we plot the scaled power spectrum of the mass, that is,

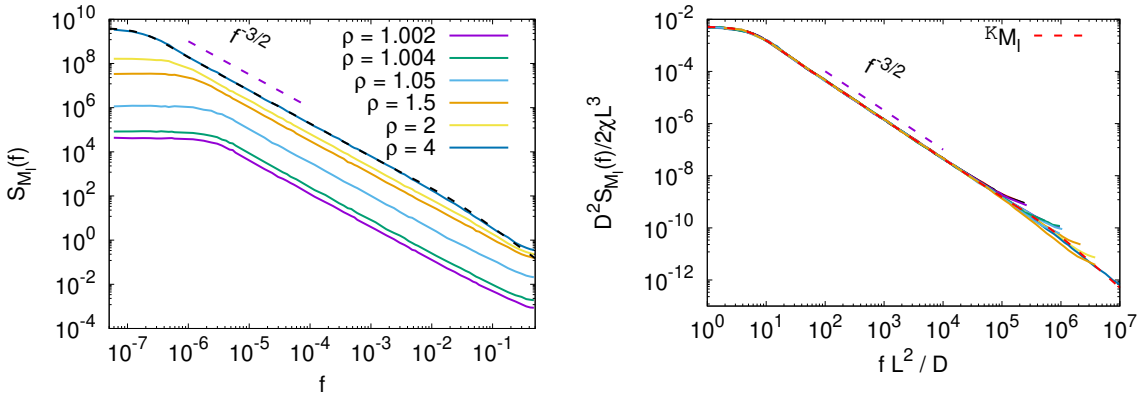

Figure 3.5: *The left panel* displays the power spectrum of the mass as a function of frequency for a system size of $L = 1000$ and a subsystem size of $l = L/2$. The simulation data are represented by solid lines for densities $\bar{\rho} = 1.002$ (violet), 1.004 (green), 1.05 (blue), 1.5 (orange), 2 (yellow), and 4 (dark blue). Additionally, the theoretical formula, Eq. (3.107), for $\bar{\rho} = 4$, is plotted as the dashed black line, showing excellent agreement with the simulation data and the guiding line $f^{-3/2}$ is obtained from Eq. (3.111). In the *right panel*, we plot the scaled power spectrum of the mass, $D(\bar{\rho})^2 S_{M_l}(f)/2\chi(\bar{\rho})L^3$, as a function of the scaled frequency fL^2/D, considering the same density values and two system sizes, $L = 500$ and 1000, with the subsystem size $l = L/2$. The simulation data are depicted as solid lines, and they collapse remarkably well on top of each other for both system sizes. The collapsed function, represented by the thick dashed red line, is precisely described by the scaling function $\mathcal{K}_M(y)$, given in Eq. (3.109). The scaling function is obtained using the system size $L = 1000$, which accounts for the excellent agreement observed in the collapsed data.

$D(\bar{\rho})^2 S_{M_l}(f)/2\chi(\bar{\rho})L^3$, as a function of the scaled frequency fL^2/D for the same density values and two sizes of the system, $L = 500$ and 1000, where the sizes of the subsystem are $l = L/2$. The simulation data are depicted as solid lines, and they collapse excellently on top of each other for both system sizes. The collapsed function, represented by the thick dashed red line, is accurately described by the scaling function $\mathcal{K}_M(y)$, given in Eq. (3.109). In obtaining the scaling function, we use the system size $L = 1000$, which accounts for the excellent agreement observed in the collapsed data.

3.4 DRIVEN HYDRODYNAMICS

The only equilibrium model studied in this thesis is the single particle transfer sandpile model (Chapter 3). In this model, we verify the Green-Kubo formula by calculating the mobility from the driven hydrodynamics and comparing it with the space-time integrated

current fluctuations. The dynamics of this model can be biased with the appropriate rate function $c^F_{i,\alpha}$, as defined in Eq.(4.77). The biased update rule of local mass is given as

$$m_i(t+dt) = \begin{cases} \textbf{events} & \textbf{probabilities} \\ m_i(t)+1 & \left(\hat{a}_{i+1}c^F_{i+1,-} + \hat{a}_{i-1}c^F_{i-1,+}\right) dt \\ m_i(t)-1 & \hat{a}_i \left(c^F_{i,-} + c^F_{i,+}\right) dt \\ m_i(t) & 1 - \Sigma dt, \end{cases} \tag{3.112}$$

where Σdt the probability of happening all events. The corresponding evolution equation of local density can be written as

$$\frac{\partial}{\partial t}\rho_i(t) = \frac{1}{2}\left\langle \hat{a}_{i+1} - 2\hat{a}_i + \hat{a}_{i+1} \right\rangle + \frac{1}{2}F\frac{(\hat{a}_{i-1} - \hat{a}_{i+1})}{2}. \tag{3.113}$$

In the diffusive limit, we rescale the biased force as $F = \tilde{F}/L$ to derive the corresponding hydrodynamic equation, which has a form similar to Eq.(2.118) in the driven Manna model and write it as

$$\frac{\partial \rho(x,\tau)}{\partial \tau} = \frac{\partial}{\partial x}\left[D(\bar{\rho})\partial x + \chi(\rho)\tilde{F}\right]. \tag{3.114}$$

The bulk diffusivity remains the same as that given in Eq.(3.13) of Chapter 3, while the mobility $\chi(\rho)$ has the same expression as in Eq.(3.92),

$$\chi(\rho) = \frac{\sigma^2_Q}{2} = \frac{(\rho-1)}{2\rho}. \tag{3.115}$$

In Fig. 3.6, we present the relaxation of an initial density profile as a function of the scaled space for $\tilde{F} = 10$. The initial density profile is prepared by distributing L particles using a Gaussian random number generator with a variance of $L/10$ and a mean of $L/2$, while the background density is set to $\rho = 1$. The initial profile is represented by circular points at $\tau = 0$, triangular points at $\tau = 10^{-2}$, and pentagonal points at $\tau = 10^{-1}$. The solid lines correspond to the solution of Eq. (3.114), which exhibits excellent agreement with the simulation data points.

3.5 SUMMARY AND CONCLUSIONS

In this study, we examined the dynamical correlations of current and the static correlations of mass in the active states of a sandpile model that adheres to a detailed balance condition.

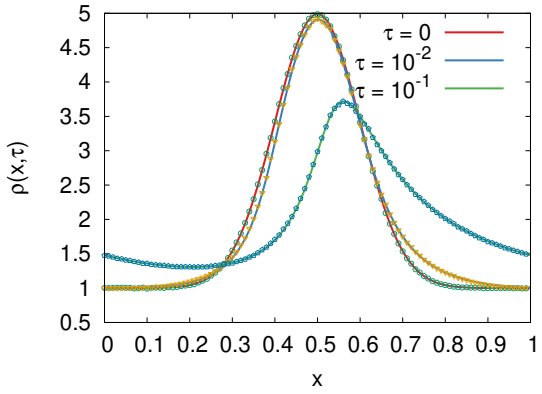

Figure 3.6: The driven-diffusive evolution of an initial density profile as a function of scaled space is plotted for $\tilde{F} = 10$. The profile is created by distributing particles using a Gaussian random number generator with a mean of $L/2$ and a variance of $L/10$, while the background density is set to $\rho = 1$. At $\tau = 0$, the initial profile is represented by circular data points, followed by triangular points at $\tau = 10^{-2}$ and pentagonal points at $\tau = 10^{-1}$. The solid lines depict the solution obtained from Eq. (3.114). All data is taken for $L = 1000$.

To begin, we utilized microscopic dynamical equations and introduced the truncation scheme proposed in Chap 2. Remarkably, this scheme is shown to be valid for both short and long (hydrodynamic) timescales. It enabled us to conduct theoretical investigations into the time-dependent correlation functions for current and mass, specifically focusing on the two-point correlation functions with unequal times and their corresponding power spectra. Our findings revealed following results:

(I) *Long range negative temporal correlation of instantaneous current*

The time-dependent two-point correlation function for the bond current exhibited a delta peak at time $t = 0$. Furthermore, for times $t > 0$, we observed a long-range negative correlation that decayed as $t^{-3/2}$ near and far from the criticality. Consequently, the resulting growth of the variance of the cumulative (*time-integrated*) current up to time T is subdiffusive, following $T^{1/2}$. Due to the presence of the detailed balance condition, the hyperuniformity exponent $\mu = 0$ in this model, while in the conserved Manna model, it was $\mu \approx 0.24$.

(II) *Power spectrum of current and mass*

The power spectrum of the current at low frequency f decays as f^{ψ_J}. As f approaches zero, ψ_J is found to be $1/2$. Additionally, we have demonstrated that the power spectrum of the temporal subsystem mass fluctuation, induced by boundary currents, decays as $f^{-\psi_M}$ at low frequency, where $\psi_M = 3/2$. Since the dynamics of our system is governed by the diffusion equation, the two exponents ψ_M and ψ_J are not independent; rather, they are connected by the relation $\psi_M = 2 - \psi_J$, as mentioned in Chap 2.

(III) *Spacetime integrated current fluctuation and derivation of the Einstein relation*

Using the microscopic current correlations, we calculated the spacetime-integrated current fluctuation and found that even in equilibrium systems, the fluctuation of this quantity is highly dependent on how we take the infinite-volume limit. If we first take the limit $T \to \infty$, followed by the limit $L \to \infty$, then the intensive current fluctuation goes to *zero*. On the other hand, if we take the limit $L \to \infty$ first, followed by the infinite time limit, then the intensive spacetime-integrated current fluctuation converges to twice the mobility. It has been shown that in this particular limit it is related to the scaled subsystem mass fluctuation divided by twice the bulk diffusivity, which corresponds to the Einstein relation or the fluctuation-dissipation theorem for this model.

(IV) *Tagged particle diffusion*

In this conserved model, we have also proved that the self-diffusion coefficient is the mobility divided by the global density. This result is consistent with what we found for the Manna sandpile model in Chap. 2.

4

MODEL OF ACTIVATED RANDOM WALKERS

4.1 INTRODUCTION

In this chapter, we investigate the hydrodynamics and current fluctuations in another interacting particle system known as the *activated random walk* (ARW) model. The ARW model is an Abelian variant [66] of the Manna sandpile model [62]. Similarly to the Manna model, the ARW model exhibits a continuous phase transition from an active phase to an absorbing phase near a critical global density ρ_c, which depends on the sleeping parameter (λ) inherent in the dynamics. The dynamics conserves the particle number unless it is added to some sink at the boundary. Classical analytic and probabilistic techniques fail in the cases of sandpile models due to long-range effects inherent in their conservative dynamics, making rigorous analysis of such systems a major mathematical challenge. However, significant progress has been made in recent decades in the context of the ARW model [66]. Some of these results for *one-dimensional* model are as follows:

- *Bounds and exact results of critical density.* It has been shown that in the infinite volume limit for the completely asymmetric case, the critical density is exactly equal to $\lambda/(1+\lambda)$[66, 126]. Meanwhile, in the symmetric ARW model, ρ_c is bounded [67] by

$$\frac{\lambda}{1+\lambda} \leq \rho_c \leq 1. \tag{4.1}$$

  It has also been predicted that $\rho_c < 1$ when $\lambda < \infty$ and $\rho_c \to 0$ if $\lambda \to 0$ [66].

- *Power laws near criticality*. At $\rho = \rho_c$, the active particle density or the activity ($u = \sum_i \langle n_i \rangle / L$, where n_i is the number of particles at the active site i) as a function of time t in this model decays as a power of t at the limit $t \to \infty$. On the other hand, for density $\rho > \rho_c$, the activity remains stationary for $t = \infty$, and it decays as Δ^β as ρ approaches ρ_c, where $\Delta = \rho - \rho_c$. The activity also scales as $u(\lambda, \rho, L) \sim L^{-\beta/\nu_\perp}$ with the system size L. For the completely asymmetric case, it is reported [126] that $\beta \approx 1$, $\nu_\perp \approx 2$, and the dynamic exponent $z \approx 1$, which do not depend on λ. On the other

hand, for the symmetric ARW model, from some initial studies, it is reported that $\beta/\nu_\perp \approx 0.23$, $z \approx 1.51$, although the exponents with satisfactory confidence are yet to be reported [126].

In this chapter, the determination of the hydrodynamic equation of density, governing the large-scale relaxation of perturbations, and the calculation of the dynamic correlation functions in the steady state of the symmetric ARW model are matters of interest.

4.2 MODEL

The activated random walk model is defined on a one-dimensional periodic lattice consisting of L sites [66]. Each site i can accommodate an unbounded number of particles denoted by $m_i = 0, 1, 2, \ldots$, while the total number of particles M is conserved, given by $M = \sum_{i=1}^{L} m_i$. Each particle can exist in one of two states: (I) active (A) or (II) sleepy (S).

In the continuous-time dynamics of the model, a randomly chosen active particle can undergo the following processes: (I) It transitions to a sleepy state with a rate λ ($0 < \lambda \leq \infty$), or (II) with a unit rate, it performs an unbiased random walk. In the random walk, an active particle residing at a site i has an equal probability of hopping to either of its nearest neighbours $j = i \pm 1$. Notably, an important aspect is that a sleepy particle will remain sleepy until an active particle jumps to that site from one of its nearest neighbours, following the transformation:

$$S + A \to 2A. \tag{4.2}$$

Additionally, it is worth mentioning that dynamically achieving a configuration where a site contains multiple sleepy particles is not possible. In other words, an active particle residing at a site already occupied by other particles will remain active indefinitely. If such an active particle transforms into a sleepy particle, it will regain its activity at an infinite rate. The stochastic time-evolution of $m_i(t)$ in an infinitesimal time-interval dt can be written as

$$m_i(t) = \begin{cases} \textbf{event} & \textbf{probability} \\ m_i(t) + 1 & \frac{1}{2}\frac{1}{1+\lambda} m_{i+1}\hat{a}_{i+1}\,\mathrm{d}t \\ m_i(t) + 1 & \frac{1}{2}\frac{1}{1+\lambda} m_{i-1}\hat{a}_{i-1}\,\mathrm{d}t \\ m_i(t) - 1 & \frac{1}{1+\lambda} m_i\hat{a}_i\,\mathrm{d}t \\ m_i(t) & 1 - \Sigma\,\mathrm{d}t \end{cases}. \tag{4.3}$$

Here, $\hat{a}_i = 1$ if there is at least one active particle on the i^{th} site and $\hat{a}_i = 0$ otherwise, and $\Sigma = \frac{1}{2}\frac{1}{1+\lambda} m_{i+1}\hat{a}_{i+1}\,\mathrm{d}t + \frac{1}{2}\frac{1}{1+\lambda} m_{i-1}\hat{a}_{i-1}\,\mathrm{d}t\,\frac{1}{1+\lambda} m_i\hat{a}_i\,\mathrm{d}t$. It is always true that $\hat{a}_i = 1$ whenever $m_i > 1$, but for an isolated particle where $m_i = 1$, $\hat{a}_i$ can either be 0 or 1. The following table is explaining the possible values of $\hat{a}_i$ can be written as

$$\hat{a}_i = \begin{cases} 1 \text{ for } m_i > 1, \\ 1 \text{ for } m_i = 1, \text{ but the particle is in state } A, \\ 0 \text{ for } m_i = 0, \\ 0 \text{ for } m_i = 1, \text{ but the particle is in state } S. \end{cases} \tag{4.4}$$

Due to the competition between the particle diffusion and the $A \to S$ transformation, the system undergoes an Active Absorbing phase transition at a finite critical particle density $\rho_c \equiv \rho_c(\lambda)$.

4.2.1 *Hydrodynamics*

Following the update rules given in Eq.(4.3), the infinitesimal-time evolution equation of local density $\rho_i(t) = \langle m_i(t)\rangle$ is given by

$$\frac{d}{dt}\rho_i(t) = \frac{1}{2(1+\lambda)}\left\langle m_{i-1}\hat{a}_{i-1} - 2m_i\hat{a}_i + m_{i+1}\hat{a}_{i+1}\right\rangle = \sum_k \frac{1}{2(1+\lambda)}\Delta_{i,k}\left\langle \hat{u}_k\right\rangle, \tag{4.5}$$

where $\hat{u}_i(t) = m_i(t)\hat{a}_i(t)$ is the active-particle number operator at a site i and $\Delta_{i,k}$ is the discrete Laplacian operator. The local diffusive current in Eq. (4.5) can be represented as the discrete gradient of a local observable, denoted as u_i. This property is referred to as "the gradient property" [9]. The presence of the gradient property allows for the direct identification of the bulk-diffusion coefficient and conductivity in the activated random walk (ARW) model. By recognizing the gradient property, one can relate the diffusive current to the gradient of the local observable, enabling a straightforward determination of the relevant transport coefficients in the ARW model.

Based on simple physical considerations in a large system on a macroscopic scale, where the density and activity fields vary slowly in space and time, it is reasonable to assume that the local activity is not independent but rather "*slave*" to the local density. This assumption arises from the notion that, at a coarse-grained level where a hydrodynamic theory is applicable, the relaxation timescales of the conserved density field (considered a "*slow*" variable) and the non-conserved activity field (considered a "*fast*" variable) are expected to be sepa-

rated. Therefore, the local activity should take on values corresponding to the instantaneous local density.

In other words, we assume the existence of a local steady state, where the average of any local observable $g(m_i)$ can be replaced by its steady-state average $\langle g(m_i)\rangle = \langle g(m_i)\rangle^{st}_{\rho_i}$, which corresponds to the local density ρ_i [9, 11, 38]. Specifically, by considering $g(m_i) \equiv m_i\hat{a}_i$, we can express the local activity as $m_i a_i = \langle \hat{m}_i a_i\rangle^{st}_{\rho_i} \equiv u[\rho_i(t)]$, where $u[\rho_i(t)]$ is now a function solely dependent on the local density $\rho_i(t)$. This assumption, known as the local-equilibrium assumption at a nonequilibrium steady state, allows us to establish a relationship between the local activity and the local density. From simulations, we observe the functional dependence of the active particle density $u(\rho) = \sum_r \hat{a}_i m_i/L$ as a function of density ρ in the steady state. Near the critical density ρ_c, we find that for all values of the sleeping parameter λ, the relationship follows the same form,

$$u(\rho) = A\Delta^{\beta}, \tag{4.6}$$

Here, A and β are independent of λ, and $\Delta = \rho - \rho_c$ represents the relative density with respect to the critical density ρ_c at which the continuous phase transition occurs. We obtained the value of ρ_c from simulations for three different values of $\lambda = 3/2$, 1 and $1/3$ as 0.9715, 0.929 and 0.6995, respectively.

Consequently, by taking the continuum limit where we rescale the spatial coordinates as $i \to x = i/L$ and time as $t \to \tau = t/L^2$, Eq. (4.5) leads to the following hydrodynamic equation:

$$\frac{1}{L^2}\frac{\partial\rho}{\partial\tau} = \lim_{L\to\infty}\frac{1}{2(1+\lambda)}\left[u\left(x-\frac{1}{L}\right) - 2u(x) + u\left(x+\frac{1}{L}\right)\right] = \frac{\partial}{\partial x}\left[D(\rho)\frac{\partial\rho}{\partial x}\right], \tag{4.7}$$

where $D(\rho)$ represents the bulk diffusivity, given by

$$D(\rho) = \frac{1}{2(1+\lambda)}\frac{du(\rho)}{d\rho}. \tag{4.8}$$

In this continuum limit, the time derivative is rescaled to $1/L^2$ to ensure proper scaling of the equation. The spatial derivative is represented by $\partial/\partial x$, and the diffusion coefficient $D(\rho)$ is derived from the function $u(\rho)$, which relates the local density ρ to the local activity.

To verify the hydrodynamic equation (4.7) numerically, we take two different sets of initial density profiles and let the system evolve in a Monte Carlo simulation. Below are the density evolution plots, which ensure the existence of the hydrodynamic structure we just derived from microscopic dynamical rules.

Gaussian initial condition. In Fig. 4.1, we present the scaled density relaxation profiles as a function of the rescaled space $x = i/L$ for different hydrodynamic times $t/L^2 = \tau = 0$,

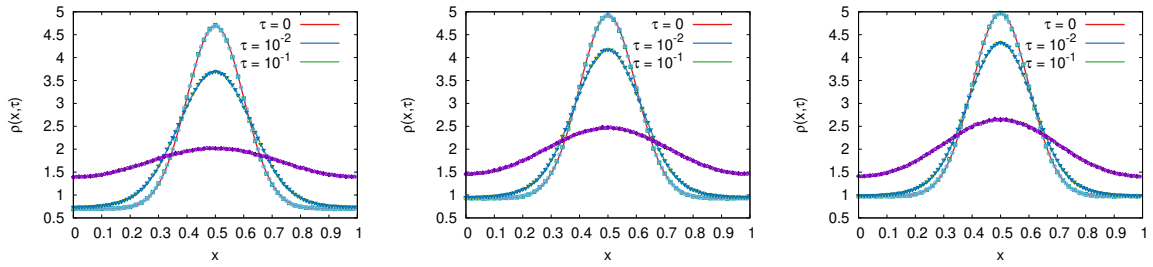

Figure 4.1: The density relaxation profiles are plotted for different sleeping rates λ and various hydrodynamic times τ, starting from an initial Gaussian distribution. The background densities are near critical, 0.7, 0.93, and 0.972 for different $\lambda = 1/3$ (left-most panel), 1 (middle panel), and 1.5 (right-most panel), respectively. On top of each background density, we distribute ρL particles, where $\rho = 1$, using a Gaussian distribution with a mean of $L/2$ and a variance of $L/10$, to prepare the initial conditions for system sizes $L = 500$ and 1000. In all three panels, the red solid line on top represents the hydrodynamic initial profile and the subsequent solid lines represent the numerical solutions of Eq. (4.7) for $\tau = 10^{-2}$ (blue line) and $\tau = 10^{-1}$ (green line), while the corresponding points denote simulation data for the corresponding hydrodynamic times.

10^{-2}, and 10^{-1}. Simulations are carried out for two different system sizes: $L = 1000$ and 500, starting from an initial Gaussian distribution with mean $L/2$ and variance $L/10$. The background densities near the criticality for different values of λ are 0.7, 0.93, and 0.972 corresponding to $\lambda = 1/3$ (left panel), 1 (middle panel) and 1.5 (right panel), respectively. To prepare the initial conditions for two different system sizes, $L = 500$ and 1000; ρL particles are distributed on top of each background density according to the Gaussian distribution mentioned above; we take $\rho = 1$. The solid red line represents the initial hydrodynamic profile, while subsequent solid lines illustrate the numerical solutions of Eq. (4.7) for $\tau = 10^{-2}$ (blue line) and $\tau = 10^{-1}$ (green line). The corresponding points for each solid line depict the simulation data for $L = 500$ and 1000, plotted as a function of the scaled space and the corresponding hydrodynamic time. We observe an excellent match between the simulation data and the numerical integration of Eq. (4.7).

Step initial condition. In Fig.4.2, we plot the relaxation of a density profile from a step initial condition as a function of continuous space. The step profiles are defined as

$$\rho(x) = \begin{cases} \rho_c + 2 & \textbf{for } 0 \leq x < \frac{1}{2} \\ \rho_c & \textbf{for } \frac{1}{2} \leq x < 1. \end{cases} \tag{4.9}$$

The critical densities coincide with those of the Gaussian initial condition, and snapshots of the density profiles are captured at the same hydrodynamic time for two system sizes: $L = 1000$ and 500. Remarkably, these snapshots collapse nicely when the diffusive limit is considered. The solid lines represent the solutions of Eq. (4.7) for different hydrodynamic

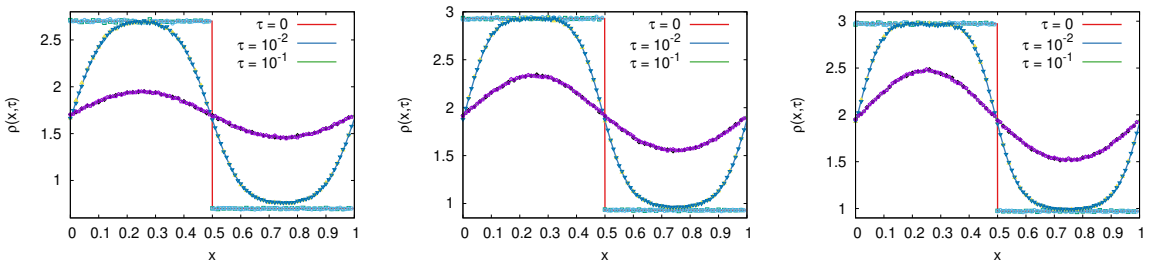

Figure 4.2: The scaled density relaxation profile is plotted for different sleeping rates λ and various hydrodynamic times τ, starting from an initial step density profile. The background densities are near critical for different λ, with corresponding values of 0.7, 0.93, and 0.972 for $\lambda = 1/3$ (left-most panel), 1 (middle panel), and 1.5 (right-most panel), respectively. On top of each background density, we distribute ρL particles, where $\rho = 1$, uniformly in the region $0 \leq i < L/2$. The red solid line on top represents the hydrodynamic initial profile, while the corresponding points denote simulation data. The subsequent solid lines represent the numerical solutions of Eq. (4.7) for $\tau = 10^{-2}$ (blue line) and $\tau = 10^{-1}$ (green line). Similarly, the points correspond to simulation data for the corresponding times for system sizes $L = 500$ and 1000.

times: $\tau = 0$ (red line), $\tau = 10^{-2}$ (blue line), and $\tau = 10^{-1}$ (green line). The corresponding points to each solid line signify the simulation data.

4.2.2 *Bond current fluctuation*

4.2.2.1 *Theory*

Although Eq.(4.5) is in a sense exact as a law of large numbers, the fluctuation around the average profile is indeed non-trivial, which we are going to calculate from the microscopic dynamics. We write Eq.(4.5) in the microscopic form,

$$\frac{d}{dt}\rho_i(t) = \langle \mathcal{J}_{i-1}(t) - \mathcal{J}_i(t) \rangle \,, \tag{4.10}$$

where $\mathcal{J}_i(t)$ is the local instantaneous microscopic current across a bond i connecting the sites $(i, i+1)$, can be decomposed in a diffusive part $\mathcal{J}_i^{(d)}(t)$ and in a fluctuating part $\mathcal{J}_i^{(fl)}(t)$ as

$$\mathcal{J}_i(t) = \mathcal{J}_i^{(d)}(t) + \mathcal{J}_i^{(fl)}(t). \tag{4.11}$$

From the consistency between Eqs.(4.5) and (4.10), we have

$$\left\langle \mathcal{J}_i^{(d)}(t) \right\rangle = \frac{1}{2(1+\lambda)} \left(u_i - u_{i+1}\right) \;\; and \;\; \left\langle \mathcal{J}_i^{(fl)}(t) \right\rangle = 0. \tag{4.12}$$

To obtain the properties of fluctuations of the instantaneous current, we study the time-integrated current $\mathcal{Q}_i(t)$, which represents the net particles that have flowed across a bond i,

connecting the sites i and $i+1$ within the interval $[0, t]$. The instantaneous current and $\mathcal{Q}_i(t)$ are related via the following relation:

$$\mathcal{J}_i(t) = \frac{d}{dt}\mathcal{Q}_i(t). \tag{4.13}$$

To infer the fluctuation properties of the system, we study the dynamic correlation functions $C_r^{\mathcal{Q}\mathcal{Q}}(t,t')$, $C_r^{\mathcal{J}\mathcal{J}}(t)$ and the corresponding power spectrums in the steady states, where the notation $C_r^{AB}(t,t')$ has the following definition,

$$C_r^{AB}(t,t') = \left\langle A_r(t)B_{i+r}(t')\right\rangle - \left\langle A_r(t)\right\rangle \left\langle B_{i+r}(t')\right\rangle, \tag{4.14}$$

whereas $C_r^{AB}(t) = C_r^{AB}(t,0)$. We also define the spatial Fourier transform of the correlation function $C_r^{AB}(t,t')$ as

$$\tilde{C}_q^{AB}(t,t') = \sum_{r=0}^{L-1} C_r^{AB}(t,t')e^{iqr}, \tag{4.15}$$

where $q = 2\pi k/L$ and $k = 0, 1, \ldots, L-1$ and the inverse Fourier transform as

$$C_r^{AB}(t,t') = \frac{1}{L}\sum_q \tilde{C}_q^{AB}(t,t')e^{-iqr}. \tag{4.16}$$

Using the truncation scheme proposed in Ref.[108], we compute the statistics of different combinations of various local currents $\mathcal{J}_i$, $\mathcal{J}_i^{(d)}$, $\mathcal{J}_i^{(fl)}$, as well as mass m_i, essentially in terms of the following two correlation functions $\langle \mathcal{Q}_i(t)\mathcal{Q}_{i+r}(t')\rangle$ and $\left\langle \mathcal{J}_i^{(d)}(t)m_{i+r}(t')\right\rangle$.

As we explicitly want to calculate the correlation function $C_r^{\mathcal{Q}\mathcal{Q}}(t,t')$, we write the evolution equation of this quantity for $t > t'$ as

$$\frac{d}{dt}C_r^{\mathcal{Q}\mathcal{Q}}(t,t') = \left\langle \frac{d}{dt}\mathcal{Q}_i(t)\mathcal{Q}_{i+r}(t')\right\rangle. \tag{4.17}$$

Since we are mostly interested in the steady-state fluctuation of current in this "fixed energy" model, we can safely set $\mathcal{Q}_i(t) = 0$ in the definition of $C_r^{\mathcal{Q}\mathcal{Q}}(t,t')$. The quantity $d\mathcal{Q}_i(t)/dt$, appeared in Eq.(4.17), can be obtained from the following evolution equations,

$$\mathcal{Q}_i(t+dt) = \begin{cases} \textit{events} & \textit{probabilities} \\ (\mathcal{Q}_i(t)+1) & \frac{1}{2(1+\lambda)}m_i\hat{a}_i(t)dt \\ (\mathcal{Q}_i(t)-1) & \frac{1}{2(1+\lambda)}m_{i+1}\hat{a}_{i+1}(t)dt \\ \mathcal{Q}_i(t) & 1-\Sigma dt, \end{cases} \tag{4.18}$$

where $\Sigma = (\hat{u}_i(t) + \hat{u}_{i+1}(t))/2(1+\lambda)$. The above update rules give us the following exact expression of $d\mathcal{Q}_i(t)/dt$,

$$\frac{d}{dt}\mathcal{Q}_i(t) = \frac{1}{2(1+\lambda)}\left(\hat{u}_i(t) - \hat{u}_{i+1}(t)\right) \equiv \mathcal{J}_i^{(d)}(t); \tag{4.19}$$

the equivalence between $d\mathcal{Q}_i(t)/dt$ and $\mathcal{J}_i^{(d)}(t)$ is obtained from Eq.(4.12), where we define the microscopic expression of the instantaneous diffusive current $\mathcal{J}^{(d)}$ as

$$\mathcal{J}_i^{(d)}(t) = \frac{1}{2(1+\lambda)}\left(\hat{u}_i(t) - \hat{u}_{i+1}(t)\right). \tag{4.20}$$

In other words, Eq.(4.17) can be reduced to the correlation between $\mathcal{J}^{(d)}$ and $\mathcal{Q}$, i.e.,

$$\frac{d}{dt}C_r^{\mathcal{Q}\mathcal{Q}}(t,t') = \left\langle \mathcal{J}_i^{(d)}(t)\mathcal{Q}_{i+r}(t')\right\rangle, \tag{4.21}$$

solving this equation, gives us,

$$C_r^{\mathcal{Q}\mathcal{Q}}(t,t') = \int_{t'}^{t} dt'' \left\langle \mathcal{J}_i^{(d)}(t'')\mathcal{Q}_{i+r}(t')\right\rangle + C_r^{\mathcal{Q}\mathcal{Q}}(t',t'). \tag{4.22}$$

To further solve the correlation on the right-hand side of the above equation, we need to write the evolution equation of $\mathcal{J}_i^{(d)}(t)\mathcal{Q}_{i+r}(t')$, which would contain,

$$\begin{aligned}\frac{d}{dt}\left\langle \mathcal{J}_i^{(d)}(t)\mathcal{Q}_{i+r}(t')\right\rangle &= \left\langle \frac{d}{dt}\mathcal{J}_i^{(d)}(t)\mathcal{Q}_{i+r}(t')\right\rangle \\ &= \frac{1}{2(1+\lambda)}\left\langle \frac{d}{dt}\left\{\hat{u}_i(t) - \hat{u}_{i+1}(t)\right\}\mathcal{Q}_{i+r}(t')\right\rangle.\end{aligned} \tag{4.23}$$

The main difficulty on the right-hand side of the second equality in the above equation is that the hierarchy of the evolution equations for the first moment of the operator $\hat{u}$ is not closed, which can be seen from the following update rules of the corresponding operator,

$$
\begin{aligned}
& m_i(t+dt)\hat{a}_i(t+dt) = \\
& \begin{cases}
\textbf{\textit{events}} & \textbf{\textit{probabilities}} \\
(m_i(t)+1)\,(\hat{a}_i(t)+1) & \frac{1}{2(1+\lambda)}\hat{p}_i(t)\left\{\hat{a}_{i+1}(t)m_{i+1}(t)+\hat{a}_{i-1}(t)m_{i-1}(t)\right\}dt \\
(m_i(t)-1)\,(\hat{a}_i(t)-1) & \frac{1}{(1+\lambda)}\delta_{m_i,1}m_i(t)\hat{a}_i(t)dt \\
m_i(t)\,(\hat{a}_i(t)-1) & \frac{\lambda}{(1+\lambda)}\delta_{m_i,1}m_i(t)\hat{a}_i(t)dt \\
(m_i(t)-1)\,\hat{a}_i(t) & \frac{1}{(1+\lambda)}m_i(t)\hat{a}_i(t)\,(1-\delta_{m_i,1})\,dt \\
(m_i(t)+1)\,\hat{a}_i(t) & \frac{1}{2(1+\lambda)}\hat{a}_i(t)\left\{\hat{a}_{i+1}(t)m_{i+1}(t)+\hat{a}_{i-1}(t)m_{i-1}(t)\right\}dt \\
m_i(t)\hat{a}_i(t) & 1-\Sigma dt,
\end{cases}
\end{aligned}
\tag{4.24}
$$

where $\Sigma = (\hat{u}_{i+1}+\hat{u}_{i-1})/2(1+\lambda)+\delta_{m_i,1}\hat{u}_i+\hat{u}_i(1-\delta_{m_1,1})/(1+\lambda)$, $\hat{p}_i = (1-\hat{a}_i)$ and the corresponding evolution equation of $\hat{u}_i = m_i\hat{a}_i$ can be obtained as

$$
\frac{d}{dt}\hat{u}_i(t) = \frac{\hat{u}_{i+1}+\hat{u}_{i-1}}{2(1+\lambda)}\,(1-\hat{u}_i-m_i)+\frac{\hat{u}_i}{1+\lambda}\,(\delta_{m_i,1}-1-\lambda-\hat{a}_i)\,. \tag{4.25}
$$

It is straightforward to see that substituting Eq.(4.25) into Eq. (4.23) would generate higher-order correlation functions, such as $\langle\hat{u}_{i+1}(t)\hat{u}_i(t)\mathcal{Q}_{i+r}(t')\rangle$, $\langle\hat{u}_{i+1}(t)m_i(t)\mathcal{Q}_{i+r}(t')\rangle$, etc. Solving these higher-order correlation functions in terms of microscopic dynamics would further complicate the situation by generating even more higher-order correlation functions to solve a lower-order correlation functions. The occurrence of an infinite hierarchy of correlation functions arises commonly when attempting to solve the space-time correlation function among the diffusive current $\mathcal{J}^{(d)}$ and the integrated current $\mathcal{Q}$, the mass of a site m_i or any other observable, in nonequilibrium systems governed by a non-linear diffusion equation. One example of such a system is the Manna model [108].

To address this challenge, a truncation scheme has been proposed in Ref.[108]. This scheme offers a solution for the correlation functions $\left\langle\mathcal{J}_i^{(d)}(t)\mathcal{Q}_{i+r}(t')\right\rangle_c$ and $\left\langle\mathcal{J}_i^{(d)}(t)m_{i+r}(t')\right\rangle_c$, which would otherwise be difficult to solve. This truncation scheme assumes that in the steady state, the fluctuation around the hydrodynamic density profiles are small and any local difference of the operator $\hat{u}$ would relax following the local difference of mass, in other words,

$$
\mathcal{J}_i^{(d)}(t) = \frac{1}{2(1+\lambda)}\,(\hat{u}_i-\hat{u}_{i+1}) \simeq D(\bar{\rho})\,(m_i-m_{i+1}) = \frac{u'(\bar{\rho})}{2(1+\lambda)}\,(m_i-m_{i+1})\,, \tag{4.26}
$$

where $\bar{\rho}$ is global average density and $D(\bar{\rho}) \propto u'(\bar{\rho})$ is the bulk-diffusivity. This immediately simplifies the Eq.(4.21), and gives us,

$$\left\langle \mathcal{J}_i^{(d)}(t)\mathcal{Q}_{i+r}(t')\right\rangle = \frac{u'(\bar{\rho})}{2(1+\lambda)}\left\langle (m_i - m_{i+1})\,\mathcal{Q}_{i+r}(t')\right\rangle. \tag{4.27}$$

Now, instead of finding the correlation of $\langle \hat{u}_i(t)\mathcal{Q}_{i+r}(t')\rangle_c$, we have to solve $\langle m_i(t)\mathcal{Q}_{i+r}(t')\rangle_c$, the evolution equation of which now can easily be written as

$$\frac{d}{dt}\left\langle m_i(t)\mathcal{Q}_{i+r}(t')\right\rangle = \left\langle \frac{d}{dt}m_i(t)\mathcal{Q}_{i+r}(t')\right\rangle = \left\langle \left\{\mathcal{J}_{i-1}^{(d)}(t) - \mathcal{J}_i^{(d)}(t)\right\}\mathcal{Q}_{i+r}(t')\right\rangle \tag{4.28}$$

$$\simeq \sum_k \frac{u'(\bar{\rho})}{2(1+\lambda)}\Delta_{i,k}\left\langle m_k(t)\mathcal{Q}_{i+r}(t')\right\rangle, \tag{4.29}$$

where to obtain the final simplification we used Eq.(4.26) and $\Delta_{i,k}$ is the same discrete Laplacian operator that appeared in Eq.(4.5). This equation can be solved by taking the Fourier transformation, defined in Eq.(4.15), of both sides, which obtains,

$$\tilde{C}_q^{m\mathcal{Q}}(t,t') = \exp\left[-\frac{u'(\bar{\rho})}{2(1+\lambda)}\lambda_q(t-t')\right]\tilde{C}_q^{m\mathcal{Q}}(t',t'). \tag{4.30}$$

But on the right-hand side, we have once again the Fourier transform of another correlation function to solve, namely, the equal-time mass and integrated current correlation $C_r^{m\mathcal{Q}}(t,t)$. The evolution equation of this quantity in the steady state can be written using the approximation in Eq.(4.26) as follows:

$$\frac{d}{dt}C_r^{m\mathcal{Q}}(t,t) \simeq \frac{u'(\bar{\rho})}{2(1+\lambda)}\sum_k \Delta_{i,k}C_k^{m\mathcal{Q}}(t,t) + f_r, \tag{4.31}$$

where f_r is the source term, given in Eq.(B.4); for details, see appendix (B.1). By taking the Fourier transform of both sides of Eq.(4.31), we can solve the corresponding equation and obtain,

$$\tilde{C}_q^{m\mathcal{Q}}(t,t) = \int_0^t dt' \exp\left[-\frac{u'(\bar{\rho})}{2(1+\lambda)}\lambda_q(t-t')\right]\tilde{f}_q(t'), \tag{4.32}$$

where $\tilde{f}_q$ is the Fourier transformed of the source term, and it can be written as

$$\tilde{f}_q = \frac{\tilde{C}_q^{m\hat{u}}}{2(1+\lambda)}\left(1-e^{-iq}\right) - \frac{u(\bar{\rho})}{(1+\lambda)}\left(1-e^{-iq}\right). \tag{4.33}$$

The next correlation function, $C_r^{m\hat{u}}(t,t)$, the unequal space and equal-time correlation of mass and operator $\hat{u}$ that appeared in $\tilde{f}_q$ can also be obtained from the steady state condition of

dynamical evolution equation of the equal-time mass-mass correlation function, which can be written as

$$\frac{d}{dt}C_r^{mm}(t,t) = \sum_k \Delta_{rk} C_k^{m\hat{u}}(t,t) + B_r = 0, \tag{4.34}$$

where B_r is the source term having the form in the steady state,

$$B_r(t) = \delta_{0,r} 2u(\bar{\rho}) - \delta_{0,r-1} u(\bar{\rho}) - \delta_{0,r+1} u(\bar{\rho}). \tag{4.35}$$

Interestingly, we note that the dynamical similarity between the ARW model and the Manna model with single-particle toppling, which we studied in Chap.3, i.e., each model is governed by the hopping of a single particle only from an active site, although with different rates. Due to this similarity, we find that the evolution equation of $C_r^{mm}(t,t)$ is the same if we simply replace the quantity $\hat{a}_i$ in the update Eq. (3.47) of Chap.3 with $\hat{u}_i/(1+\lambda)$. Thus, we obtain Eqs. (4.34) and Eq. (4.35). One should keep in mind that the similarity between the two models is only algebraic; the physical properties are entirely different.

Eq. (4.34) can be solved using the generating function $G(z) = \sum_{r=0}^{\infty} z^r C_r^{m\hat{u}}(t,t)$, which has the following form: $G(z) = u(\bar{\rho})$. This implies that

$$C_r^{m\hat{u}} = \begin{cases} u(\bar{\rho}) & \text{for } r = 0, \\ 0 & \text{for } r > 0. \end{cases} \tag{4.36}$$

Alternatively, the Fourier transform of this correlation function is simply $\tilde{C}_q^{m\hat{u}} = u(\bar{\rho})$. Putting this in Eq.(4.33) we obtain,

$$\tilde{f}_q = \frac{u(\bar{\rho})}{2(1+\lambda)}\left(1 - e^{-iq}\right) - \frac{u(\bar{\rho})}{(1+\lambda)}\left(1 - e^{-iq}\right) = -\frac{u(\bar{\rho})}{2(1+\lambda)}\left(1 - e^{-iq}\right). \tag{4.37}$$

Thus, in steady state, we obtain the final solution of Eq.(4.30) by utilizing Eq. (4.32) and Eq. (4.37) as

$$\tilde{C}_q^{m\mathcal{Q}}(t,t') \simeq -\frac{u}{2(1+\lambda)} \int_0^{t'} dt'' e^{-\frac{u'(\bar{\rho})}{2(1+\lambda)}\lambda_q (t-t'')} \left(1 - e^{-iq}\right). \tag{4.38}$$

Now, to obtain the explicit expression of the correlation function $C_r^{\mathcal{Q}\mathcal{Q}}(t,t')$, we take the Fourier transform of Eq.(4.22), which gives us,

$$\tilde{C}_q^{\mathcal{Q}\mathcal{Q}}(t,t') = \int_{t'}^{t} dt'' \, \frac{u'(\bar{\rho})}{2(1+\lambda)} \tilde{C}_q^{m\mathcal{Q}}(t'',t') \left[1 - e^{iq}\right] + \tilde{C}_q^{\mathcal{Q}\mathcal{Q}}(t',t'), \tag{4.39}$$

and further finding the equal-time integrated current correlation function, present on the right-hand side allows us to solve this unequal time correlation function.

4.2.2.2 *Result*

Again, it is important to note that the dynamics of the *activated random walk* (ARW) model is quite similar to the Manna model with *single particle transfer* that we studied in Chap. 3, with the exception that in the ARW model, an active site topples with a rate of $m_i(t)/(1+\lambda)$, while in the single particle transfer model, an active site topples with a unit rate. Additionally, in the single-particle transfer model, a site with single-particle occupancy is strictly inactive, resulting in an equilibrium model. However, in the ARW model, such sites can be in an active state, thus generating much richer physical properties. We exploit the algebraic similarity between these two models to calculate our results in this and the following sections.

The equal-time correlation of integrated current can similarly be written following Eq.(3.58) of Chapter 3 as

$$C_r^{\mathcal{Q}\mathcal{Q}}(t,t) \simeq \int_0^t \mathrm{d}t'\,\Gamma_r(t') + \frac{1}{L}\int_0^t \mathrm{d}t'\,\frac{u'(\bar{\rho})}{2(1+\lambda)}\sum_q \tilde{C}_q^{m\mathcal{Q}}(t',t')\left[1-e^{iq}\right]\left(2-\lambda_{qr}\right), \tag{4.40}$$

where $\lambda_{qr} = 2[1-\cos(qr)]$. In this model also, Γ_r is the strength of the fluctuating current $\mathcal{J}^{(fl)}$, i.e., $\left\langle \mathcal{J}_i^{(fl)}(t)\mathcal{J}_{i+r}^{(fl)}(t')\right\rangle = \Gamma_r(t)\delta(t-t')$ and we obtain the expression of Γ_r in the steady state as

$$\Gamma_r(t) = \frac{u(\bar{\rho})}{(1+\lambda)}\delta_{0,r}. \tag{4.41}$$

Putting the Fourier transform of Eq.(4.40) and Eq.(4.38) in Eq.(4.39) and then again taking the inverse Fourier of the resulting equation to write,

$$\begin{aligned} C_r^{\mathcal{Q},\mathcal{Q}}(t,t') \simeq & t'\Gamma_r - \frac{1}{L}\frac{u(\bar{\rho})u'(\bar{\rho})}{4(1+\lambda)^2}\sum_q \int_0^{t'} dt'' \int_0^{t''} dt''' e^{-\frac{u'(\bar{\rho})}{2(1+\lambda)}\lambda_q(t''-t''')}\lambda_q\left(2-\lambda_{qr}\right) \\ & - \frac{1}{L}\frac{u(\bar{\rho})u'(\bar{\rho})}{4(1+\lambda)^2}\sum_q \int_{t'}^{t} dt'' \int_0^{t'} dt''' e^{-\frac{u'(\bar{\rho})}{2(1+\lambda)}\lambda_q(t''-t''')}\lambda_q e^{-iqr}. \end{aligned} \tag{4.42}$$

The fluctuation of the time-integrated bond current can be obtained from the above correlation function by putting $r=0$ and $t=t'=T$ in $C_r^{\mathcal{Q},\mathcal{Q}}(t,t')$, which gives us,

$$\left\langle \mathcal{Q}^2(T)\right\rangle = C_0^{\mathcal{Q}\mathcal{Q}}(T,T) = \frac{T}{L}\frac{u}{(1+\lambda)} + 2\frac{u}{u'}\frac{1}{L}\sum_q \frac{1-e^{-\frac{u'(\bar{\rho})}{2(1+\lambda)}\lambda_q T}}{\lambda_q}. \tag{4.43}$$

From this above equation, we can get mobility $\chi(\bar{\rho})$ as defined in Eq.(1.43) in the limit $T \to \infty$ as

$$\lim_{T\to\infty} \frac{\langle \mathcal{Q}^2(T)\rangle}{T} = \frac{2\chi(\bar{\rho})}{L} \quad \Rightarrow \quad \chi(\bar{\rho}) = \frac{u(\bar{\rho})}{2(1+\lambda)}. \tag{4.44}$$

In the initial time when $T \leq 1/D(\bar{\rho})$, $\langle \mathcal{Q}^2(T)\rangle$, following Eq. (3.63), is given as

$$\langle \mathcal{Q}^2(T)\rangle \simeq \Gamma_0 T, \tag{4.45}$$

where $\Gamma_0 = u(\bar{\rho})/(1+\lambda)$; given in Eq. (4.41).

Similarly, like Eq.(3.64), we can rescale the cumulative current fluctuation on the right-hand side of the above equation as $\langle \mathcal{Q}^2(T)\rangle \to D(\bar{\rho})/2\chi(\bar{\rho})L \langle \mathcal{Q}^2(T)\rangle$ and time as $T \to \tau = D(\bar{\rho})T/L^2$, we rewrite Eq.(4.43) in the form of a universal scaling function $\mathcal{G}(y)$ as follows,

$$\frac{D(\bar{\rho})}{2\chi(\bar{\rho})L} \langle \mathcal{Q}^2(T)\rangle = \mathcal{G}\left(\frac{DT}{L^2}\right), \tag{4.46}$$

where $\mathcal{G}(\tau)$ is the same as in Eq. (3.65) and has the following asymptotic behaviour as given in Eq. (3.66),

$$\mathcal{G}(\tau) \simeq \begin{cases} \sqrt{\frac{\tau}{\pi}} & \textbf{for } \ 0 \ll \tau \ll 1, \\ \tau & \textbf{for } \ \tau \gg 1. \end{cases} \tag{4.47}$$

Using the asymptotic behaviour of the scaling function $\mathcal{G}(\tau)$, we write the asymptotics of $\langle \mathcal{Q}^2(T)\rangle \sim T^{\alpha}$ for $1 \ll T \ll L^2$ as

$$\langle \mathcal{Q}^2(T)\rangle \simeq \frac{\sqrt{2}}{\sqrt{\pi(1+\lambda)}} \frac{u(\bar{\rho})}{\sqrt{u'(\bar{\rho})}} T^{1/2}. \tag{4.48}$$

Near criticality, where $u(\bar{\rho}) \sim (\bar{\rho} - \rho_c)^{\beta}$, using the dimensional analysis of the prefactor on the right-hand side of Eq. (4.48), we obtain

$$\langle \mathcal{Q}^2(T)\rangle \simeq T^{\alpha} = T^{\frac{1}{2}-\mu}, \tag{4.49}$$

where μ is given by the same equation, $\mu = (\beta+1)/2\nu_{\perp}z$, that was derived in Eq. (2.51) in Chapter 2, where $\nu_{\perp}$ is the correlation length exponent and z is the dynamical exponent. Since these exponents have not been reported for the ARW model, from simulation near criticality for $1 \ll T \ll L^2$, we obtain,

$$\langle \mathcal{Q}^2(T)\rangle \sim T^{\alpha} \ \ \textit{with} \ \ \alpha \approx 0.4. \tag{4.50}$$

which gives $\alpha = 1/2 - \mu \approx 0.4$ or $\mu \approx 0.1$. This decay in the growth of the time-integrated current is known as dynamical hyperuniformity and is discussed in Chapter 2 at great length.

In the large time limit, $T \gg L^2$, the corresponding current fluctuation becomes,

$$\left\langle \mathcal{Q}^2(T) \right\rangle = \frac{2\chi T}{L}, \tag{4.51}$$

implying $\alpha = 1$ which is valid both for near and away from critical densities.

We plot the corresponding simulation data of time-integrated bond current fluctuation as a function of rescaled time in Fig. 4.3, where the arrangement of the plots as follows:

1. *Left panel:* In this panel, we plot the current fluctuation, scaled only by $2\chi L$, to observe the collapse at the late time, as a function of scaled time T/L^2 for a system size of $L = 1000$.

    a) *Top figure:* This figure corresponds to the sleeping parameter $\lambda = 1.5$, and for this parameter, the critical density is approximately given by $\rho_c \approx 0.9715$. We plot the simulation data in solid lines for densities $\bar{\rho} = 0.985$ (violet), 0.99 (green), 1 (blue), 2 (orange), 3 (yellow), and 4 (dark blue). The corresponding theoretical line is plotted for $\bar{\rho} = 4$ in a black dotted line using Eq. (4.43), which matches extremely well with the simulation data. As we can see, near criticality, the current fluctuation grows as T^{α}, where $\alpha \approx 0.4$, and remains the same for all sleeping parameters near criticality. The decay in the growth of fluctuation corresponds to the dynamical hyperuniformity near criticality. Away from criticality, the current fluctuation grows subdiffusively which can be seen from the $\tau^{1/2}$ guiding line as given in Eq. (4.48) in the intermediate time, and diffusively at the late times. From now on, we shall denote $\bar{\rho} = 1$, 2, 3, and 4 for the data away from the criticality, for all parameter values of λ, and we will use the same colour coding as in this figure.

    b) *Middle figure:* Corresponding to the sleeping parameter $\lambda = 1$, and for this parameter, the critical density is approximately given by $\rho_c \approx 0.929$. Simulation data of $\left\langle \mathcal{Q}^2(T) \right\rangle$ for near-critical density values $\bar{\rho} = 0.945$ (violet) and 0.95 (green) are plotted in solid lines, which grow as $T^{0.4}$ in intermediate time. Similarly, as in the top figure, the analytical line is plotted using Eq. (4.43) for $\bar{\rho} = 4$, which is in excellent agreement with the simulation data.

    c) *Bottom figure:* Corresponding to the sleeping parameter $\lambda = 1/3$, and for this parameter, the critical density is approximately given by $\rho_c \approx 0.6995$. Simulation data of $\left\langle \mathcal{Q}^2(T) \right\rangle$ for near-critical density values $\bar{\rho} = 0.72$ (violet) and 0.75 (green) are plotted in solid lines.

2. *Right panel:* To observe the collapse as predicted by Eq. (4.46), we plot the rescaled current fluctuation, $D(\bar{\rho})\left\langle \mathcal{Q}^2(T)\right\rangle /2\chi(\bar{\rho})L$, as a function of rescaled time $\tau = T/L^2$ for the same densities as in the left panel and the sleeping parameter λ. In the top, bottom, and middle figures, the scaling function $\mathcal{G}(\tau)$ (plotted with a red dashed line) captures the growth of current fluctuations, excellently, away from the critical density for all the parameter values of λ. However, near-criticality, where the bulk diffusion constant becomes singular, the growth of current fluctuation becomes much slower, as shown in Eq. (4.50), resulting in the phenomenon known as temporal hyperuniformity.

4.2.3 *Instantaneous current correlations and power spectrum*

The corresponding instantaneous current correlation function can be obtained by differentiating Eq.(4.42) w.r.t. to time and can be written as

$$C_r^{\mathcal{J}\mathcal{J}}(t) = \Gamma_r\delta(t) - \frac{1}{L}\frac{u(\bar{\rho})u'(\bar{\rho})}{4(1+\lambda)^2}\sum_q e^{-\frac{u'(\bar{\rho})}{2(1+\lambda)}\lambda_q t}\lambda_q e^{-iqr}. \tag{4.52}$$

Similarly to Eq. (3.73), it can also be shown using the above equation that $\lim_{L\to\infty}\int_{-T}^{T} dt C_0^{\mathcal{J}\mathcal{J}}(t)$ decays as $T^{-1/2}$ away from the criticality for all sleeping parameter λ, and near the criticality, the decay becomes faster as $T^{-(1/2+\mu)}$. The corresponding long-time negative tail of $C_0^{\mathcal{J}\mathcal{J}}(t)$ decays as $t^{-3/2}$ away from the criticality, as described in Eq. (3.75). However, due to the presence of temporal hyperuniformity, the decay of the temporal bond current correlation becomes faster as $t^{-(1/2+\mu)}$ at near-critical densities for all sleeping parameters λ; $\mu \approx 0.1$ for the ARW model. This behaviour can be observed more vividly in the power spectrum of the bond current.

The power spectrum of instantaneous current can be defined as the Fourier transform of this correlation function and can be written as

$$S_{\mathcal{J}}(f) = \frac{u(\bar{\rho})}{L(1+\lambda)} + \frac{u(\bar{\rho})}{L(1+\lambda)}\sum_q \frac{16f^2\pi^2(1+\lambda)^2}{\lambda_q^2(u')^2 + 16f^2\pi^2(1+\lambda)^2}, \tag{4.53}$$

and similarly like Eq.(3.77) of Chap. 3, $S_{\mathcal{J}}(f)$ can be scaled as

$$S_{\mathcal{J}}(f) = \frac{2\chi}{L}\mathcal{S}\left(\frac{fL^2}{D}\right), \tag{4.54}$$

with $D(\bar{\rho})$ and $\chi(\bar{\rho})$ defined in Eqs.(4.8) and (4.44); the scaling function $\mathcal{S}$ is defined in Eq.(3.78).

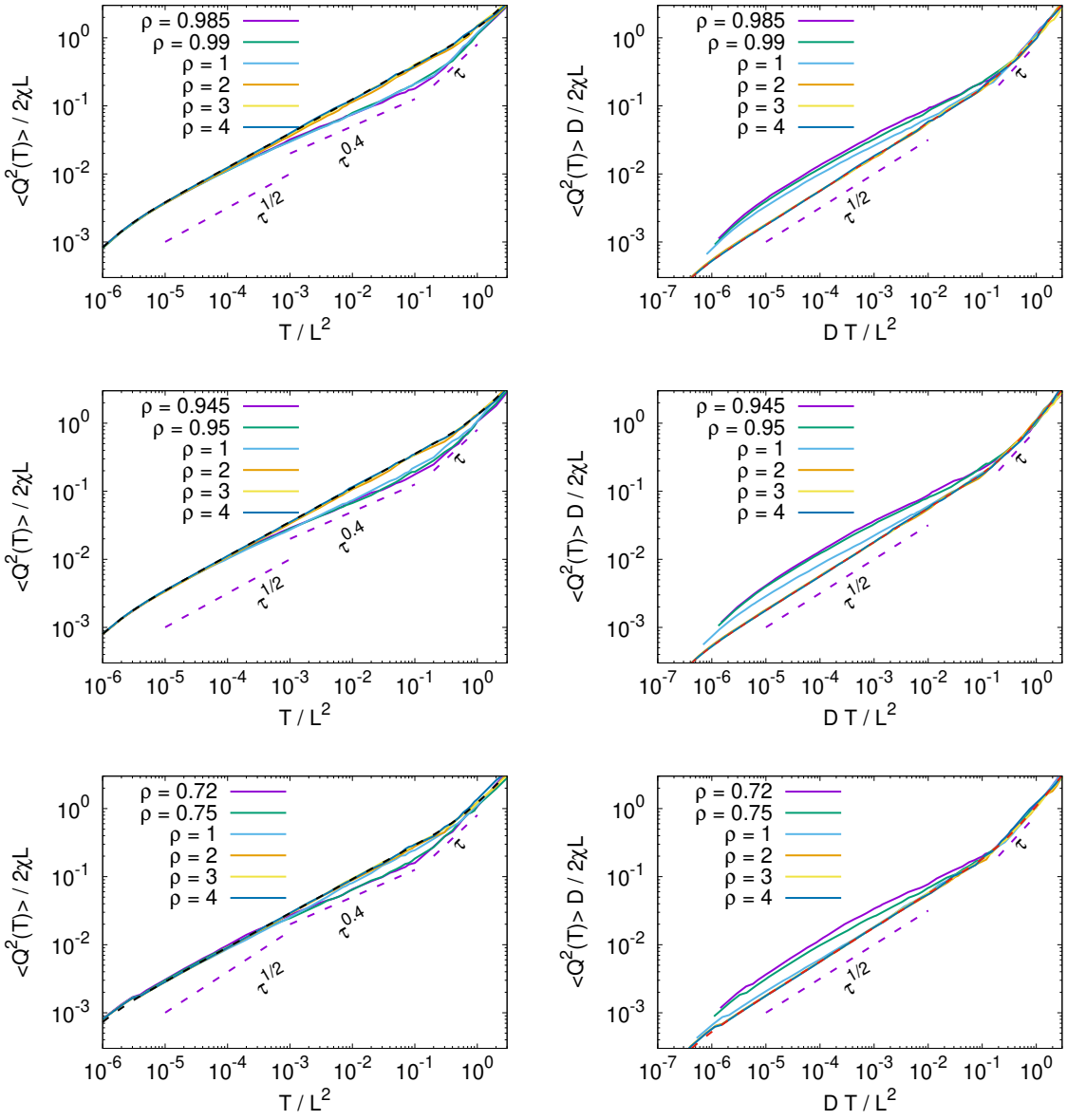

Figure 4.3: *Left panel:* Current fluctuation scaled by $2\chi L$ is plotted as a function of scaled time T/L^2 for $\lambda = 1.5$ (top figure), 1 (middle figure), and $1/3$ (bottom figure) with $L = 1000$. Simulation data are plotted in solid lines for both near-critical and away-from-critical densities, where the critical density values $\rho_c \approx 0.9715$ (for $\lambda = 1.5$), 0.929 (for $\lambda = 1$), and 0.6995 (for $\lambda = 1/3$) correspond to the top, middle, and bottom figures, respectively. Theoretical lines are plotted using Eq. (4.43) for $\bar{\rho} = 4$ in all three figures, which are in excellent agreement with the simulations. Near criticality at initial time, the current fluctuation grows as T^{α} with $\alpha \approx 0.4$, signifying the dynamical hyperuniformity, whereas away from criticality the growth is given by $\alpha = 1/2$ as obtained in Eq. (4.48). Both for near and away from critical densities, the diffusive or linear growth is given by Eq. (4.51) when time is much larger than the unit hydrodynamic time scale (L^2). *Right panel:* The scaled current fluctuation $\langle \mathcal{Q}^2(\tau) \rangle D/2\chi L$ is plotted as a function of DT/L^2, which, away from criticality, collapses nicely on top of each other, and is well captured by the scaling function $\mathcal{G}(y)$ (plotted with a red dashed line and given in Eq. (3.65)). Deviation from this scaling function corresponds to the emergence of dynamical hyperuniformity near criticality.

Away from criticality, using the asymptotics of $\mathcal{S}$, given in Eq. (3.80), we obtain the asymptotics of $S_{\mathcal{J}}(f) - S_{\mathcal{J}}(0) \sim f^{\psi_{\mathcal{J}}}$ similarly as in Eq. (3.81),

$$S_{\mathcal{J}(f)} \simeq \frac{u(\bar{\rho})}{L(1+\lambda)} + \frac{1}{\sqrt{2\pi(1+\lambda)}} \frac{u(\bar{\rho})}{\sqrt{u'(\bar{\rho})}} f^{1/2}, \tag{4.55}$$

where $S_{\mathcal{J}}(0) = u(\bar{\rho})/L(1+\lambda)$ and we obtain $\psi_{\mathcal{J}} = 1/2$. However, note that the same density-dependent prefactor $u/\sqrt{u'}$ has appeared on the right-hand side as it was for the current fluctuation in Eq. (4.48), which near criticality ($\bar{\rho} \approx \rho_c$) scales as f^{μ} thus near criticality we obtain

$$\psi_{\mathcal{J}} = \frac{1}{2} + \mu \simeq 0.6, \tag{4.56}$$

which gives us

$$S_{\mathcal{J}}(f) - S_{\mathcal{J}}(0) \sim f^{0.6}; \tag{4.57}$$

we used $\mu \approx 0.1$ which we obtained from the current fluctuation simulation data.

We plot the corresponding simulation data in Fig. 4.4, where the arrangement of the plots as follows:

1. *Left panel:* In this panel, we plot the relative power spectrum of current, $S_{\mathcal{J}}(f) - S_{\mathcal{J}}(0)$ as a function of frequency f for a system size of $L = 1000$.
   a) *Top figure:* This figure corresponds to the sleeping parameter $\lambda = 1.5$, and for this parameter, the critical density is approximately given by $\rho_c \approx 0.9715$. We plot the simulation data in solid lines for densities $\bar{\rho} = 0.985$ (red), 1 (blue), 2 (green), and 4 (violet). The corresponding theoretical line is plotted for $\bar{\rho} = 4$ in a black dashed line using Eq. (4.53), which matches extremely well with the simulation data. As we can see, near criticality, the current power spectrum decays as $f^{0.6}$ for $f \to 0$, as given in Eq. (4.57). $\psi_{\mathcal{J}} \approx 0.6$ remains the same for all sleeping parameters near criticality. The increase in the steepness of the decay of the power spectrum for $f \to 0$ corresponds to the dynamical hyperuniformity near criticality. Away from criticality, the current power spectrum decays as with $\psi_{\mathcal{J}} = 1/2$, as can be seen from the guiding lines,obtained from Eq. (4.55). In the remaining plots, we denote $\bar{\rho} = 1$, 2, and 4 for data away from the criticality, for all the parameter values of λ, and we will use the same colour coding as in this figure.
   b) *Middle figure:* Corresponding to the sleeping parameter $\lambda = 1$, and for this parameter, the critical density is approximately given by $\rho_c \approx 0.929$. Simulation data of $S_{\mathcal{J}}(f)$ for near-critical density values $\bar{\rho} = 0.945$ (red) plotted in a solid line, which

grows with $\psi_{\mathcal{J}} \approx 0.6$. Similarly, as in the top figure, the analytical line is plotted using Eq. (4.53) for $\bar{\rho} = 4$.

c) *Bottom figure:* Corresponding to the sleeping parameter $\lambda = 1/3$, and for this parameter, the critical density is approximately given by $\rho_c \approx 0.6995$. Simulation data of $S_{\mathcal{J}}(f)$ for the near-critical density value $\bar{\rho} = 0.725$ is plotted in the solid red line and the numerical value of Eq. (4.53) plotted in black dashed $\bar{\rho} = 4$.

2. *Right panel:* To observe the collapse as predicted by Eq. (4.54), we plot the rescaled power spectrum of current, $S_{\mathcal{J}}(f)L/2\chi(\bar{\rho}) - 1$, as a function of the rescaled frequency fL^2/D for the same densities as in the left panel and the sleeping parameter λ. In the top, bottom, and middle figures, the scaling function $\mathcal{S}(y) - 1$ (plotted with a black dashed line) captures the decay of the current power spectrum, as $f \to 0$, away from the critical density for all parameter values of λ. However, in near-criticality, where the bulk diffusion constant becomes singular, the growth of the current power spectrum becomes faster and deviates from the scaling function, resulting in the phenomenon known as temporal hyperuniformity, as discussed in Chapter 2.

4.2.4 *Fluctuation of spacetime integrated current*

The fluctuation of the space-time-integrated current $\bar{\mathcal{Q}}(l,T) = \sum_{i=0}^{l-1} \mathcal{Q}_i(T)$ can be computed using the most general current-current correlation function $C_r^{\mathcal{Q}\mathcal{Q}}(t,t')$ given in Eq. (4.42). The fluctuation of the integrated current across a subsystem of size l up to time T is given by,

$$\left\langle \bar{Q}^2(l,T) \right\rangle - \left\langle \bar{Q}(l,T) \right\rangle^2 = \left\langle \bar{Q}^2(l,T) \right\rangle = l C_0^{\mathcal{Q}\mathcal{Q}}(T,T) + \sum_{r=1}^{l-1} 2(l-r) C_r^{\mathcal{Q}\mathcal{Q}}(T,T). \tag{4.58}$$

In the steady state, using Eq. (4.42) the above expression can further be written, similarly like Eq.(3.86) as

$$\left\langle \bar{Q}(l,T)^2 \right\rangle = 2\chi(\bar{\rho}) lT - 2\chi(\bar{\rho}) \frac{D(\bar{\rho})}{L} \sum_q \frac{D(\bar{\rho})\lambda_q T - 1 + \exp\left(-\lambda_q D(\bar{\rho}) T\right)}{\left(\lambda_q D(\bar{\rho})\right)^2} \lambda_{ql}, \tag{4.59}$$

where $D(\bar{\rho})$ and $\chi(\bar{\rho})$ are given in Eqs.(4.8) and (4.44). From the above equation, it should be immediately noted that for $l = L$, the spacetime integrated current will be, in the limit of $L \to \infty$ for any arbitrary value of time T,

$$\lim_{L\to\infty} \frac{\left\langle \bar{Q}(L,T)^2 \right\rangle}{LT} = 2\chi(\bar{\rho}), \tag{4.60}$$

since $\lambda_{qL} = 0$.

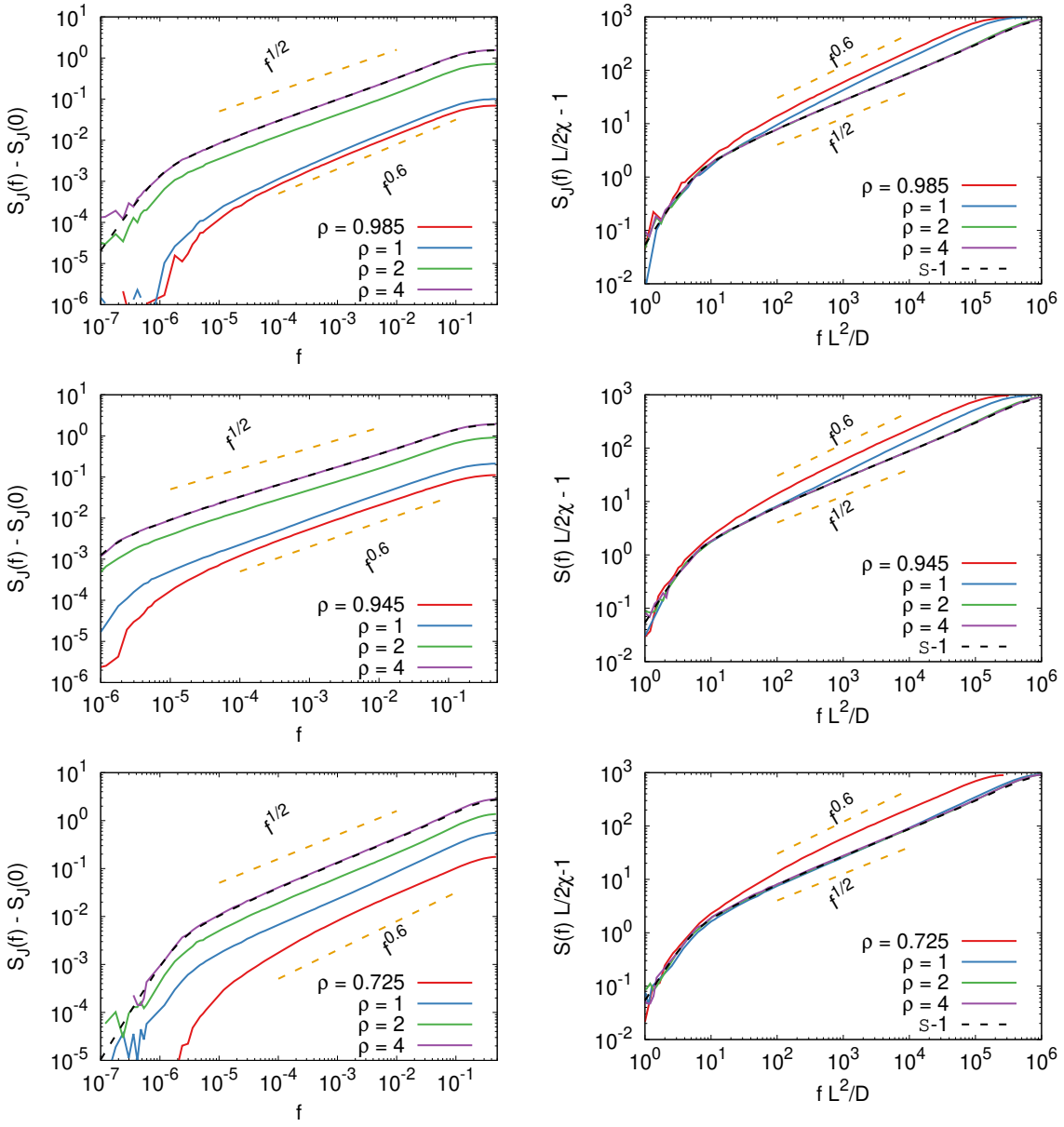

Figure 4.4: *Left panel:* Power spectrum of current is plotted as a function of frequency f for $\lambda = 1.5$ (top figure), 1 (middle figure), and $1/3$ (bottom figure) with $L = 1000$. Simulation data are plotted in solid lines for both near-critical and away-from-critical densities, where the critical density values $\rho_c \approx 0.9715$ (for $\lambda = 1.5$), 0.929 (for $\lambda = 1$), and 0.6995 (for $\lambda = 1/3$) correspond to the top, middle, and bottom figures, respectively. Theoretical lines are plotted using Eq. (4.53) for $\bar{\rho} = 4$ in all three figures, which are in excellent agreement with the simulations. Near criticality, the current power spectrum decays as $f^{\psi_\mathcal{J}}$ with $\psi_\mathcal{J} \approx 0.6$ as $f \to 0$, signifying the dynamical hyperuniformity. Away from criticality, the decay of the power spectrum is given by Eq. (4.55), using which we draw guiding lines for $S_\mathcal{J}(f) \sim f^{1/2}$. *Right panel:* The scaled current power spectrum $S_\mathcal{J}(f)L/2\chi(\bar{\rho}) - 1$ is plotted as a function of rescaled frequency fL^2/D, which, away from criticality, collapses nicely on top of each other, and is well captured by the scaling function $\mathcal{S} - 1$ (plotted with a black dashed line). Deviation from this scaling function corresponds to the emergence of dynamical hyperuniformity near criticality.

In the infinite system size limit $L \to \infty$, the convergence of $\langle \bar{Q}(l,T)^2 \rangle / lT$ can only be obtained if we take $l \gg 1$ limit followed by $T \gg 1$ limit, which is gives as

$$\frac{1}{lT} \langle \bar{Q}^2(l,T) \rangle \simeq 2\chi(\bar{\rho}) - \frac{8\chi(\bar{\rho})}{3} \sqrt{\frac{D}{\pi}} \frac{\sqrt{T}}{l}. \tag{4.61}$$

By taking the infinite subsystem volume limit we finally obtain

$$\sigma_Q^2 = \lim_{l\to\infty} \lim_{T\to\infty} \frac{1}{lT} \langle \bar{Q}^2(l,T) \rangle = 2\chi(\bar{\rho}) = \lim_{L\to\infty} \frac{\langle \bar{Q}(L,T)^2 \rangle}{LT} = \frac{u(\bar{\rho})}{1+\lambda}, \tag{4.62}$$

where $\chi(\bar{\rho})$ is same as given in Eq.(4.44). The above equation establishes a relationship between the subsystem time-integrated current fluctuation in the infinite space-time volume limit and the fluctuation of the total current $\langle \bar{Q}(L,T)^2 \rangle$ for a very large system size. This relation can be used to find mobility in interacting particle systems [127] using the periodic boundary condition as a function of density.

In Fig. 4.5, we plot $\lim_{l\to\infty} \lim_{T\to\infty} \langle \bar{Q}^2(l,T) \rangle / lT$ as a function of relative density $\Delta = \bar{\rho} - \rho_c$, where in the left, middle and right panels, we have $\rho_c \approx 0.9715$ (for $\lambda = 1.5$), 0.929 (for $\lambda = 1$), and 0.6995 (for $\lambda = 1/3$), respectively, and we use the system size $L = 5000$ to prepare the plots. In all panels, the fluctuations are plotted for two limits of the subsystem size l and time T. The top curve in all figures corresponds to the simulation data $l = 2500$ and $T = 100$ (solid blue line), while the lower curve corresponds to the simulation data for $l = 100$ and $T = 10^4$ (solid violet). The theoretical lines are plotted for the two sets of parameter values using Eq. (4.59) in black dashed lines for the three panels. We also plot twice the mobility $2\chi(\bar{\rho})$ using Eq. (4.62) (dot-dashed red line), which nicely collapses with the data for $l = 2500$ and $T = 100$, demonstrating the validity of the limit defined in Eq. (4.62).

4.2.5 *Diffusivity of tagged particle or self diffusivity*

Now, we present the fluctuations in the displacements of tagged particles as a function of time. We establish a relationship between the sum of the integrated displacements of the individual tagged particles, denoted as $\sum_{\alpha=1}^{N} X_\alpha(T)$, where $X_\alpha(T)$ represents the total displacement of the particle α within the time interval $[0,T]$, with the total integrated current $\bar{\mathcal{Q}}(L,T)$. This can be expressed as

$$\sum_{\alpha=1}^{N} X_\alpha(T) = \sum_{i=0}^{L-1} \mathcal{Q}_i(T) = \bar{\mathcal{Q}}(L,T). \tag{4.63}$$

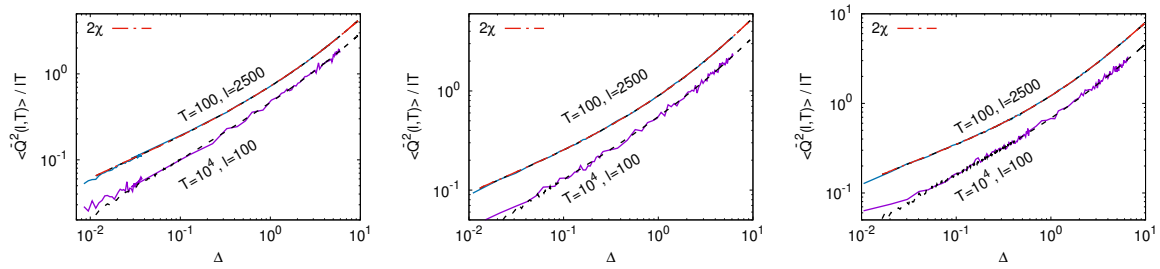

Figure 4.5: We plot the quantity $\lim_{l\to\infty}\lim_{T\to\infty}\left\langle \bar{Q}^2(l,T)\right\rangle/lT$ against the relative density $\Delta=\bar{\rho}-\rho_c$ in three separate panels. The respective values of ρ_c are 0.9715 (for $\lambda=1.5$) in the left panel, 0.929 (for $\lambda=1$) in the middle panel, and 0.6995 (for $\lambda=1/3$) in the right panel for the system size $L=5000$. For each panel, we plot fluctuations for two subsystem size and time limits. The upper curve in each panel represents the simulation data for $l=2500$ and $T=100$ (solid blue line), while the lower curve corresponds to the simulation data for $l=100$ and $T=10^4$ (solid violet). To compare with theory, we also include two sets of theoretical lines obtained using Eq. (4.59) represented as black dashed lines. Additionally, we plot twice the mobility $2\chi(\bar{\rho})$ using Eq. (4.62) as a dot-dashed red line which remarkably coincides with the data for $l=2500$ and $T=100$, demonstrating the accuracy of the limit defined in Eq. (4.62).

In the limit of large $T\gg L^2$, the self-diffusion coefficient $\mathcal{D}_s(\bar{\rho})$ can be defined through the mean-square tagged particle displacement of the α^{th} particle, as given below:

$$\left\langle X_\alpha^2(T)\right\rangle\simeq 2\mathcal{D}_s(\bar{\rho})T. \tag{4.64}$$

As the hopping of particles is unrestricted, we can use a simple argument of random walk to write the self-diffusivity as follows:

$$\mathcal{D}_s(\bar{\rho})=\frac{a(\bar{\rho})}{\bar{\rho}}=\frac{1}{\bar{\rho}}\left[\lim_{L,T\to\infty}\frac{\left\langle\bar{\mathcal{Q}}^2(L,T)\right\rangle}{2LT}\right]=\frac{u(\bar{\rho})}{2\bar{\rho}(1+\lambda)}; \tag{4.65}$$

for details see Sec. 2.2.5 of Chap. 2.

Similarly to previous models, we find that the behaviour of self-diffusivity $\mathcal{D}_s(\bar{\rho})$ is very different from bulk diffusivity $D(\bar{\rho})$. Bulk diffusivity is proportional to the derivative of the active particle density $u'(\bar{\rho})$, while $\mathcal{D}_s(\bar{\rho})\propto u(\bar{\rho})$. Thus, near criticality, $D(\bar{\rho})\to\infty$ as $\bar{\rho}\to\rho_c$, and for the same limit, $\mathcal{D}_s(\bar{\rho})\to 0$. At the opposite limit of high density, where the activity becomes $u(\bar{\rho})\simeq\bar{\rho}$, both diffusivities become equal.

In Fig. 4.6, we plot and compare self-diffusivity and bulk diffusivity as functions of relative density Δ. In the simulation, we calculate the scaled fluctuation of $\left\langle X_\alpha^2(T)\right\rangle/2T$ and plot it as the solid red line. The corresponding theoretical value of $\mathcal{D}_s(\bar{\rho})$ obtained from Eq. (4.65) and plotted in dashed black line agrees remarkably well with the simulation data. To compare it with the bulk diffusivity, we use Eq. (4.8) to plot $D(\rho)$ as a dot-dashed blue line, which diverges near criticality but becomes equal to self-diffusivity $\mathcal{D}_s(\bar{\rho})$ in the high-density limit.

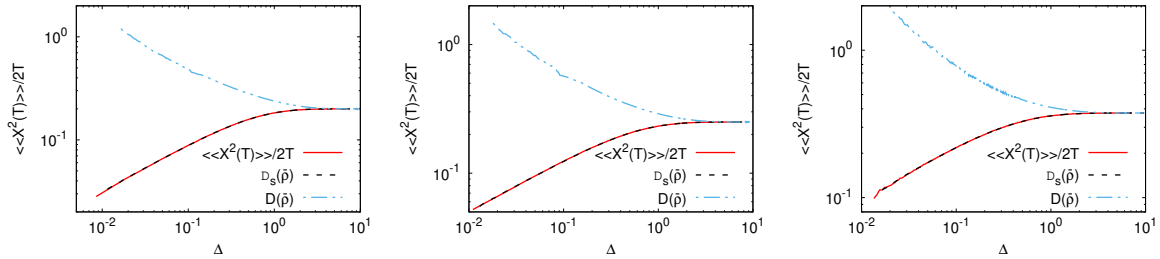

Figure 4.6: In Fig. 4.6, we plot and compare the self-diffusivity $\mathcal{D}_s(\bar{\rho})$ and bulk diffusivity $D(\bar{\rho})$ with respect to the relative density Δ. Using simulations, we calculate the scaled fluctuation of $\left\langle\left\langle X^2(T)\right\rangle\right\rangle/2T$, where the double angular bracket denotes the average over trajectories and particles, and represent it as the solid red line. Remarkably, the corresponding theoretical value of $\mathcal{D}_s(\bar{\rho})$, obtained from Eq. (4.65) and plotted as a dashed black line, shows excellent agreement with the simulation data. To further examine its relationship with the bulk diffusivity, we use Eq. (4.8) to plot $D(\rho)$ and plot it as a dot-dashed blue line. Near criticality, $D(\rho)$ diverges, but in the high-density limit, it converges to the self-diffusivity $\mathcal{D}_s(\bar{\rho})$. The three panels, from left to right, correspond to different values of the parameter λ, specifically $\lambda = 1.5$, 1, and $1/3$, respectively.

In the three panels from left to right, the values of the parameters λ are $\lambda = 1.5$, 1, and $1/3$, respectively.

4.2.6 *Power spectrum of subsystem mass fluctuation*

In this section, we explore the characteristics of fluctuations in the mass of a subsystem $M_l(t) = \sum_{i=0}^{l=1} m_i(t)$. We begin by investigating the unequal time and unequal space correlation function of the mass of a single site in steady state, specifically for $t \geq 0$. This correlation function is denoted as $C_r^{\mathcal{Q}\mathcal{Q}}(t,0) = \langle m_i(t) m_{i+r}(0)\rangle - \langle m_i(t)\rangle \langle m_{i+r}(0)\rangle$, which can also be expressed as $C_r^{mm}(t)$.

Similarly, like Eq.(3.97), the unequal time mass-mass correlation follows the following evolution equation,

$$\frac{d}{dt} C_r^{mm}(t) \simeq \frac{u'(\bar{\rho})}{2(1+\lambda)} \sum_k \Delta_{r,k} C_k^{mm}(t), \tag{4.66}$$

which has the following solution in the Fourier space,

$$\tilde{C}_q^{mm}(t) \simeq e^{-\frac{u'(\bar{\rho})}{2(1+\lambda)}\lambda_q t} \tilde{C}_q^{mm}(0,0). \tag{4.67}$$

By utilizing the approximation given in Eq. (4.26) in the equation (4.34), we can derive the evolution equation for $C^{mm}r(0,0)$. To solve this equation, we introduce the generating

function $G'(z) = \sum_{r=0}^{\infty} C_r^{mm}(t,t)z^r$. Drawing an algebraic analogy with Eq. (3.99), we can readily express $G'(z)$ as

$$G'(z) = \frac{u(\bar{\rho})}{u'(\bar{\rho})}, \tag{4.68}$$

and correspondingly,

$$\tilde{C}_q^{mm}(t,t) = \frac{u(\bar{\rho})}{u'(\bar{\rho})}. \tag{4.69}$$

This result tells us that $C_r^{mm}(0,0)$ is delta correlated, that is,$C_r^{mm}(0,0) \simeq \delta_{0,r}u/u'$. Finally, comparing with Eq.(3.105), we write the $C_r^{mm}(t)$ as

$$C_r^{mm}(t) \simeq \frac{1}{L}\sum_q e^{-iqr}e^{-\frac{u'(\bar{\rho})}{2(1+\lambda)}\lambda_q t}\frac{u(\bar{\rho})}{u'(\bar{\rho})}. \tag{4.70}$$

The temporal correlation of the subsystem mass $M_l(t) = \sum_{r=0}^{l-1} m_r(t)$ for $l < L$, is given by Eq.(3.104), which using Eq.(4.71) can be written as

$$C^{M_lM_l}(t) \simeq \frac{1}{L}\sum_q e^{-\frac{u'(\bar{\rho})}{2(1+\lambda)}\lambda_q t}\frac{u(\bar{\rho})}{u'(\bar{\rho})}\frac{\lambda_{ql}}{\lambda_q}. \tag{4.71}$$

In particular, the fluctuation in the mass of the subsystem, denoted by $\langle M_l^2\rangle - \langle M_l\rangle^2$, is given by $C^{M_lM_l}(0) = lu/u'$. Similar to Eq. (3.106), we can relate the scaled subsystem mass fluctuation, $\sigma^2(\bar{\rho}) = \left[\langle M_l^2\rangle - \langle M_l\rangle^2\right]/l$, to the intensive space-time integrated current fluctuation, σ_Q^2, as follows:

$$\sigma^2(\bar{\rho}) = \frac{\sigma_Q^2}{2D}, \tag{4.72}$$

where σ_Q^2 is given in Eq. (4.62). This is the derivation of an equilibrium-like Einstein relation [11] for the ARW model.

To compare this result with simulation, we take the Fourier transform of Eq.(4.71) to obtain the power spectrum of the subsystem mass, $S_{M_l}(f)$, similarly like Eq.(3.107) as

$$S_{M_l}(f) = \lim_{T\to\infty}\int_{-T}^{T} \mathrm{d}t\, C^{M_lM_l}(t)e^{2\pi ift} = \frac{1}{L}\sum_q \frac{u(\bar{\rho})}{u'(\bar{\rho})}\frac{2\lambda_q D(\bar{\rho})}{\lambda_q^2 D(\bar{\rho})^2 + 4\pi^2 f^2}\frac{\lambda_{lq}}{\lambda_q}. \tag{4.73}$$

By rescaling the frequency as a dimensionless quantity $f \to fL^2/D$, $S_{M_l}(f)$ can be written in terms of a scaling function $\mathcal{K}_M$ as

$$S_{M_l}(f) = \frac{2\chi(\bar{\rho})L^3}{D(\bar{\rho})^2}\mathcal{K}_M\left(\frac{fL^2}{D}\right), \tag{4.74}$$

where the scaling function $\mathcal{K}_M$ is given by Eq.(3.109). The asymptotic behaviour of $S_{M_l}(f) \sim f^{-\psi_M}$ is one of the quantities of interest to us. Away from criticality, we obtain ψ_M simply by putting the expressions of D (Eq. (4.8)) and χ (Eq. (4.44)) in Eq. (3.111) as

$$S_{M_l}(f) \simeq \frac{1}{\sqrt{8\pi^2(1+\lambda)}}\frac{u}{\sqrt{u'}}f^{-3/2}, \tag{4.75}$$

which gives us $\psi_M = 3/2$ away from criticality and near criticality $u/\sqrt{u'} \sim f^{\mu}$ further gives us,

$$S_{M_l}(f) \simeq f^{-\frac{3}{2}+\mu}, \tag{4.76}$$

and using $\mu \approx 0.1$, we obtain $\psi_M \approx 1.4$ near criticality.

We plot the corresponding simulation data of subsystem mass power spectrum in Fig. 4.7, where the arrangement of the plots as follows:

1. *Left panel:* In this panel, we plot the relative power spectrum of current, $S_{M_l}(f)$ as a function of frequency f for a system size of $L = 1000$ and subsystem size $l = 500$.
    a) *Top figure:* This figure corresponds to the sleeping parameter $\lambda = 1.5$, and for this parameter, the critical density is approximately given by $\rho_c \approx 0.9715$. We plot the simulation data in solid lines for densities $\bar{\rho} = 0.985$ (violet), 1 (green), 2 (blue), and 4 (orange). The corresponding theoretical line is plotted for $\bar{\rho} = 4$ in a black dashed line using Eq. (4.73), which matches extremely well with the simulation data.Away from criticality, we have $\psi_M = 3/2$, given by Eq. (4.75), which can be seen from the $f^{-3/2}$ guiding lines. As we can see, near criticality, the power spectrum decays more slowly as $f^{-\psi_M}$, where $\psi_M \approx 1.4$ as given in Eq. (4.76), and remains the same for all sleeping parameters near criticality. The slowly decaying power spectrum of the mass of the subsystem corresponds to the dynamical hyperuniformity near criticality. In the remaining plots, we denote $\bar{\rho} = 1$, 2, and 4 for data away from the criticality, for all parameter values of λ, and we will use the same colour coding as in this figure.
    b) *Middle figure:* Corresponding to the sleeping parameter $\lambda = 1$, and for this parameter, the critical density is approximately given by $\rho_c \approx 0.929$. Simulation data of $S_{M_l}(f)$ for near-critical density values $\bar{\rho} \approx 0.945$ (violet) plotted in a solid line,

which decays with $\psi_M \approx 1.4$. Similarly, as in the top figure, the analytical line is plotted using Eq. (4.73) for $\bar{\rho} = 4$.

c) *Bottom figure:* Corresponding to the sleeping parameter $\lambda = 1/3$, and for this parameter, the critical density is approximately given by $\rho_c \approx 0.6995$. Simulation data of $S_{\mathcal{J}}(f)$ for the near-critical density value $\bar{\rho} \approx 0.725$ is plotted in the solid violet line and the numerical value of Eq. (4.73) plotted in black dashed $\bar{\rho} = 4$.

2. *Right panel:* To observe the collapse as predicted by Eq. (4.74), we plot the rescaled power spectrum of current, $D^2 S_{M_l}(f)/2\chi L^3$, as a function of the rescaled frequency fL^2/D for the same densities as in the left panel and the sleeping parameter λ. In the top, bottom, and middle figures, the scaling function $\mathcal{K}_M(y)$ (plotted with a red dashed line) captures the decay of the power spectrum of the mass of a subsystem away from the critical density for all the parameter values of λ. However, near-criticality, where the bulk diffusion constant becomes singular, the decay of the power spectrum becomes slower and deviates from the scaling function, resulting in the phenomenon known as temporal hyperuniformity, as discussed in Chapter 2.

4.3 DRIVEN HYDRODYNAMICS OF ARW MODEL

In this section, we show that mobility, which is microscopically defined by Eqs.(4.44) and (4.62), can also be computed macroscopically as the proportionality constant between the drift current and the small external bias as described by the framework of MFT [9].

The dynamics of this model can also be modified using the biased particle hopping rates $c^F_{i,\alpha}$ to find the transport coefficient, mobility. In this particular dynamics, only a single particle can hop to any of its nearest neighbours. To incorporate the bias, we modify the hopping rates as follows:

$$c^F_{i,\alpha} = c^{F=0}_{i,\alpha} \exp\left(\frac{\Delta e_{ij}}{2}\right), \tag{4.77}$$

here, the definition of Δe_{ij} remains the same as before. The biased evolution equation of local mass is following,

$$m_i(t+dt) = \begin{cases} \textbf{events} & \textbf{probabilities} \\ m_i(t)+1 & \frac{1}{1+\lambda}\left(m_{i+1}\hat{a}_{i+1}c^F_{i+1,-} + m_{i-1}\hat{a}_{i-1}c^F_{i-1,+}\right)dt \\ m_i(t)-1 & \frac{m_i\hat{a}_i}{1+\lambda}\left(c^F_{i,-} + c^F_{i,+}\right)dt \\ m_i(t) & 1-\Sigma dt, \end{cases} \tag{4.78}$$

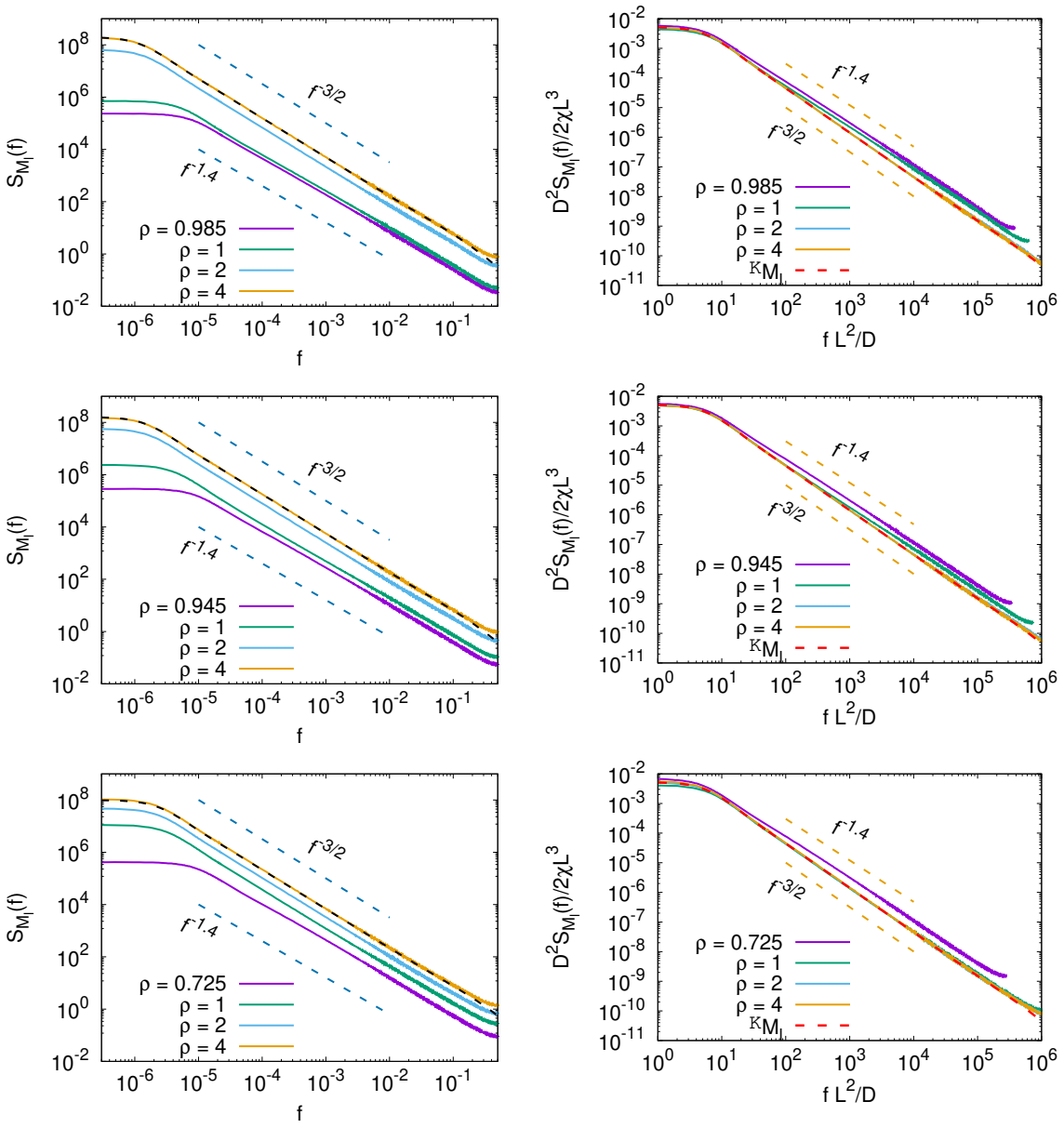

Figure 4.7: *Left panel:* Power spectrum of mass of subsystem size l is plotted as a function of frequency f for $\lambda = 1.5$ (top figure), 1 (middle figure), and $1/3$ (bottom figure) with $L = 1000$ and $l = 500$. Simulation data are plotted in solid lines for both near-critical and away-from-critical densities, where the critical density values $\rho_c \approx 0.9715$ (for $\lambda = 1.5$), 0.929 (for $\lambda = 1$), and 0.6995 (for $\lambda = 1/3$) correspond to the top, middle, and bottom figures, respectively. Theoretical lines are plotted using Eq. (4.73) for $\bar{\rho} = 4$ in all three figures, which are in nice agreement with the simulations. Near criticality, the power spectrum decays as $f^{-\psi_M}$ with $\psi_M \approx 1.4$ (Eq. (4.76)), slower than the $f^{-3/2}$ decay (given in Eq. (4.75)), signifying the dynamical hyperuniformity. *Right panel:* The scaled current power spectrum $D^2 S_{M_l}(f)/2\chi L^3$ is plotted as a function of rescaled frequency fL^2/D, which, away from criticality, collapses nicely on top of each other, and is well captured by the scaling function $\mathcal{K}_M$ (plotted with a red dashed line). Deviation from this scaling function corresponds to the emergence of dynamical hyperuniformity near criticality.

where Σdt the probability of happening all events. In the dynamics of the activated random walk (ARW), the parameter α takes values other than zero. Specifically, when $\alpha = +$, it corresponds to the hopping of a particle to the right along the bias, while $\alpha = -$ represents the hopping of a particle to the left in the opposite direction of the bias. The unbiased rates in the ARW dynamics are simply $c_{i,-}^{F=0} = c_{i,+}^{F=0} = 1/2$.

The evolution equation of the local density can be written using the update rules given in Eq.(4.78) as

$$\frac{\partial}{\partial t}\rho_i(t) = \frac{1}{2(1+\lambda)}\left\langle \hat{u}_{i+1} - 2\hat{u}_i + \hat{u}_{i+1} \right\rangle + \frac{1}{2(1+\lambda)} F \frac{(\hat{u}_{i-1} - \hat{u}_{i+1})}{2}. \tag{4.79}$$

By taking the diffusive limit and assuming the local equilibrium, the hydrodynamic limit of the above equation can be written as

$$\frac{\partial \rho(x,\tau)}{\partial \tau} = -\frac{\partial}{\partial x}\left(j^{(d)} + j^{(drift)} \right). \tag{4.80}$$

The diffusive current $j^{(d)}$ is given by

$$j^{(d)} = -D(\rho)\frac{\partial \rho}{\partial x}, \tag{4.81}$$

bulk-diffusivity $D(\rho)$ is given in Eq.(4.8) and the drift current $j^{(drift)}$ can be written as

$$j^{(drift)} = \chi(\rho)\tilde{F}, \tag{4.82}$$

where the mobility $\chi(\rho) = \frac{u(\rho)}{2(1+\lambda)}$ is exactly same with that we obtained in Eq.(4.44) and $F = \tilde{F}/L$. Indeed, Eq. (4.62) can now be regarded as a nonequilibrium version of the celebrated Green-Kubo relation [5–8]. Through this relation, we show that the microscopic definition of mobility, i.e., the intensive fluctuation of space-time integrated current or, alternatively, the intensive fluctuation of time-integrated bond current at the limit $T \to \infty$, is actually equal to the proportionality constant of the drift current and a small biasing force.

In Fig.(4.8), we plot the simulation data for density relaxation from a Gaussian initial profile (var $= 1/10$ and mean $= 1/2$) for $\lambda = 1.5$ (left panel), $\lambda = 1$ (middle panel) and $\lambda = 1/3$ (right panel) as a function of scaled space x for hydrodynamic time $\tau = 0$ (circular points), $\tau = 10^{-2}$ (triangular points) and $\tau = 10^{-1}$ (pentagonal points) with a bias $\tilde{F} = 10$ in the $\hat{x}$ direction. The corresponding solid lines are obtained by solving Eq.(4.80) for different parameter values, and we found that our hydrodynamic equation excellently captures the simulation data for all temporal points.

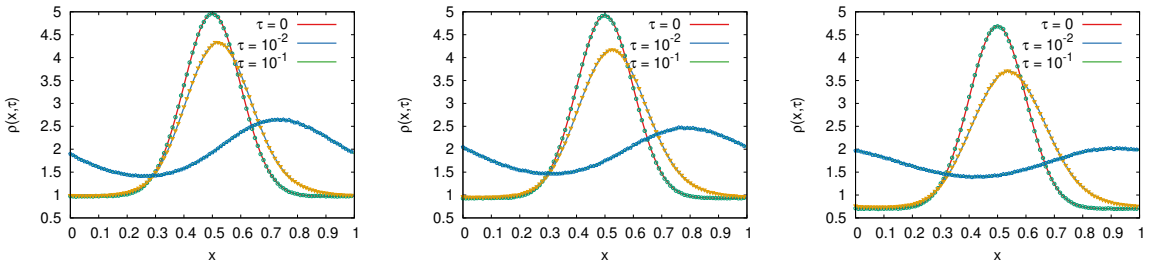

Figure 4.8: Simulation data is shown for density relaxation from a Gaussian initial profile with variance $1/10$ and mean $1/2$. The data are presented for different values of λ (1.5, 1, and $1/3$ respectively from left to right) and plotted against the scaled space x. Hydrodynamic times $\tau = 0$, 10^{-2}, and 10^{-1} are indicated by circular, triangular, and pentagonal points, respectively. A bias $\tilde{F} = 10$ is applied in the $\hat{x}$ direction. Solid lines represent solutions obtained from Eq.(4.80). All data are taken for $L = 1000$.

4.4 SUMMARY AND CONCLUSIONS

In this study, we investigated the dynamical correlations of current and the static correlations of mass in the activated random walk model. We demonstrated that, away from criticality, this model exhibits similarities with the Manna model with single particle transfer rules, which we studied in Chapter 3. However, unlike the previous model, the activated random walk model breaks detailed balance and undergoes an active absorbing phase transition at a critical density ρ_c, which is a function of the sleeping parameter λ.

By employing a similar truncation scheme (Eq. (4.26)) as used in Chapter 2, we computed various dynamical correlation functions and their power spectra in the activated random walk model. Our main findings are summarized as follows:

(I) *Subdiffusive growth of time-integrated bond current fluctuation and dynamical hyperuniformity*

The variance of the cumulative (time-integrated) current exhibits subdiffusive growth, following $T^{1/2}$ when $1 \ll T \ll L^2$ in the regime away from criticality. However, near criticality, this fluctuation becomes slower and increases with time as T^{α}, with a measured value of $\alpha \approx 0.4$ from simulations. This behaviour is indicative of the system's dynamical hyperuniformity near the critical point. Additionally, at large times $T \gg L^2$, the fluctuation of the cumulative current increases linearly in time both near and far from the critical density values, and the coefficient is directly related to the system's mobility. The time-dependent two-point correlation function for the bond current reveals a delta peak in time at $t = 0$. Beyond this initial time, we observe a long-range negative correlation that decays as $t^{-3/2}$ away from the criticality. However, near criticality, this decay becomes faster due to the presence of dynamic hyperuniformity.

(II) *Power spectrum of current and mass*

The power spectrum of the current displays a decay with frequency f characterized by an exponent $\psi_{\mathcal{J}}$. Away from criticality, this exponent is found to be $1/2$. However, near criticality, $\psi_{\mathcal{J}}$ becomes faster and is governed by $\psi_{\mathcal{J}} \approx 1.6$, reflecting the faster decay of the instantaneous current correlation due to dynamical hyperuniformity.

Similarly, the power spectrum of subsystem mass fluctuation, induced by boundary currents, exhibits a decay with frequency characterized by an exponent ψ_M. Away from criticality, $\psi_M = 3/2$, while near criticality, $\psi_M \approx 1.4$. These exponents are not independent and are related by equation $\psi_M = 2 - \psi_{\mathcal{J}}$, as discussed in Chapter 2, since the diffusion equation governs the dynamics of the system.

(III) *Spacetime integrated current fluctuation and nonequilibrium Green-Kubo relation*

The calculation of spacetime-integrated current fluctuation revealed that the fluctuation of this quantity is highly dependent on the order in which we take the infinite-volume limit. If we first take the limit $T \to \infty$, followed by the limit $L \to \infty$, then the intensive current fluctuation converges to zero. However, if we take the limit $L \to \infty$ first, followed by the infinite time limit, then the intensive spacetime-integrated current fluctuation converges to twice the mobility.

Furthermore, it was found that this intensive spacetime-integrated current fluctuation is related to the scaled subsystem mass fluctuation divided by twice the bulk diffusivity, which corresponds to the Einstein relation or the fluctuation-dissipation theorem for this model. Additionally, using the macroscopic fluctuation theory (MFT) prescription and introducing a biasing force, we calculated the mobility macroscopically, which was found to be exactly equal to the microscopic definition of mobility. This provides a verification of the nonequilibrium Green-Kubo relation for the model.

(IV) *Tagged particle diffusion*

In this conserved model, we have also proved that the self-diffusion coefficient is the mobility divided by the global density. This result is consistent with what we found for the Manna sandpile model in Chap. 2.

5

THE OSLO RICEPILE MODEL

5.1 INTRODUCTION

Whether sandpiles can generate a power law distribution has been a long-standing debate. In addition to numerical simulations, some actual studies have been conducted to explore this phenomenon. For example, investigations have been carried out on the outflux in sand [60] and the famous Oslo ricepile experiment [61], which studied the residence time of a rice grain tagged in the system, along with the distribution of the size of the avalanche. Although no signature of a power law in the distribution of sand grains from the system was found in the first experiment, the second experiment actually demonstrated a power law in the avalanche statistics for nearly $1\frac{1}{2}$ decades [61]. In addition to this, the residence time of the particles was also studied in this experiment (see Sec. 1.5.6 for a discussion). These experiments have provided valuable insights into the role of anisotropy [128] and the importance of conserved quantities in the context of sandpile dynamics.

Inspired by the results of the ricepile experiment, the Oslo model was proposed [64]. This model introduced stochasticity to the one-dimensional BTW model (although it can be generalized to higher dimensions), where now the critical height for a site to become active can be either 2 or 3 with equal probability; each active site topples exactly two particles to the nearest neighbours deterministically in opposite directions. The critical properties of this model have been studied extensively by Grassberger, Dhar, and Mohanty in Ref.[65]. The main exponents characterizing the critical states of this model are the order parameter exponent $\beta = 5/21$, correlation length exponent $\nu_\perp = 4/3$, and dynamic exponent $z = 10/7$[65]. Reportedly, these exponents are the same for both the fixed-energy and self-organized criticality (SOC) versions of the Oslo model [65]. Near criticality, the mass fluctuation in this model becomes hyperuniform, meaning that the subsystem mass fluctuation, $\sigma^2(M)$, scales as l^λ, where l is the subsystem size, and $\lambda = 1/2$, contrasting with the disordered system where $\lambda = 1$.

In this chapter, using our analytical scheme, we calculated the dynamical correlations away from criticality, while the near-critical dynamical fluctuations have been obtained from simulation.

5.1.1 *Model*

The dynamics of the Oslo model are described on a periodic boundary condition as follows: Each lattice site, denoted by $i = 0, 1, 2, \ldots, L-1$, is characterized by two coupled dynamical variables. The first variable is the number of particles or height, denoted by $m_i = 0, 1, 2, \ldots, N$, where $\bar{\rho} = N/L$ represents the global conserved density. Here, L is the system size, and N is the total number of particles. The second variable is the threshold or critical height, denoted by $n_c = 2$ and 3. Initially, the threshold variable n_c at each site is chosen randomly and independently as 2 or 3. A site is considered active if the number of particles m_i at that site exceeds or equals the critical height n_c. In such a case, an active site topples by deterministically transferring two particles, one to its right-nearest neighbour and another to its left-nearest neighbour. After each toppling event, the threshold height of each site is updated randomly. Consequently, the stochastic nature of this model arises from random updates of threshold heights.

The Oslo ricepile model exhibits power-law scaling behaviour near the critical point. The reported critical density for the Oslo model is approximately $\rho_c \approx 1.732594$ as documented in [65].

The update rules of local particles at a site in this model are given as

$$m_i(t) = \begin{cases} \textbf{events} & \textbf{probabilities} \\ m_i(t)+1 & (\hat{a}_{i+1} + \hat{a}_{i-1})\, dt \\ m_i(t)-2 & \hat{a}_i dt \\ m_i(t) & 1 - \Sigma dt, \end{cases} \tag{5.1}$$

where $\Sigma = (\hat{a}_{i+1} + \hat{a}_{i-1} + \hat{a}_i)\, dt$ and $\hat{a}_i$ is defined as

$$\hat{a}_i = \begin{cases} 1, & \text{when } m_i \geq n_c, \\ 0, & \text{otherwise.} \end{cases} \tag{5.2}$$

The corresponding density evolution equation can be written as

$$\frac{\partial}{\partial t}\rho_i(t) = \langle \hat{a}_{i+1} - 2\hat{a}_i + \hat{a}_{i-1} \rangle = \Delta_{i,k} \langle \hat{a}_k \rangle\,, \tag{5.3}$$

where $\rho_i(t) = \langle m_i(t) \rangle$ and $\Delta_{i,k}$ is the discrete Laplacian operator. By taking the diffusive limit, $i \to x = i/L$ and $t \to \tau = t/L^2$, and assuming the local equilibrium, where the statistical properties of the fast variable $\hat{a}_i$ are determined by the local density ρ_i, we write the above equation as the following diffusive equation,

$$\frac{\partial \rho(x,\rho)}{\partial \tau} = \frac{\partial}{\partial x}\left[D(\rho)\frac{\partial \rho}{\partial x}\right], \tag{5.4}$$

where the bulk-diffusivity is given by,

$$D(\rho) = \frac{da(\rho)}{\partial \rho}; \tag{5.5}$$

$a(\rho) = \langle \hat{a}_i \rangle_{\rho_i}^{steady\ state}$, meaning the average value of activity operator $\hat{a}_i$ when the local density is ρ_i. At the operational level, $a(\rho)$ can be computed as the steady-state average of $a(\rho) = \sum_i \hat{a}_i/L$ when the global density is ρ.

In the upcoming sections, we will compute the current and mass fluctuations generated by this dynamic process, as well as analyse the relevant power spectrum.

5.2 FLUCTUATION PROPERTIES OF OSLO MODEL

The evolution equation of local mass can be written as a microscopic continuity equation as

$$\frac{d}{dt}m_i(t) = \mathcal{J}_{i-1}(t) - \mathcal{J}_i(t), \tag{5.6}$$

where $\mathcal{J}_i(t)$ is the microscopic instantaneous current across a bond i, connecting the sites i and $i+1$, in an interval $[t, t+dt]$. Formally, the instantaneous bond current is defined as the derivative of the time-integrated bond current $\mathcal{Q}_i(t)$, which represents the number of net particles that cross the bond i in the time interval $[0, t]$. The value of $\mathcal{J}_i(t)$ can be obtained directly from the definition,

$$\mathcal{J}_i(t) = \frac{d}{dt}\mathcal{Q}_i(t). \tag{5.7}$$

Following the Manna sandpile [108] and using the gradient property of the density evolution Eq.(5.6) of the Oslo model, we can decompose $\mathcal{J}_i(t)$ into a microscopic diffusive part $\mathcal{J}_i^{(d)}(t)$ and a fluctuating part $\mathcal{J}_i^{(fl)}(t)$ as

$$\mathcal{J}_i(t) = \mathcal{J}_i^{(d)}(t) + \mathcal{J}_i^{(fl)}(t). \tag{5.8}$$

Moreover to satisfy the convergence of Eq.(5.6) in to the Eq.(5.3) on average, we must have the following constraints,

$$\left\langle \mathcal{J}_i^{(d)}(t) \right\rangle = (\hat{a}_i - \hat{a}_{i+1}) \;\; and \;\; \left\langle \mathcal{J}_i^{(fl)}(t) \right\rangle = 0, \tag{5.9}$$

upon $\mathcal{J}_i^{(d)}(t)$ and $\mathcal{J}_i^{(fl)}(t)$. To infer the fluctuation properties of the system, we study the dynamic correlation functions $C_r^{\mathcal{Q}\mathcal{Q}}(t,t')$, $C_r^{\mathcal{J}\mathcal{J}}(t)$ and the corresponding power spectrums in the steady states, where the notation $C_r^{AB}(t,t')$ has the following definition,

$$C_r^{AB}(t,t') = \left\langle A_r(t) B_{i+r}(t') \right\rangle - \left\langle A_r(t) \right\rangle \left\langle B_{i+r}(t') \right\rangle, \tag{5.10}$$

whereas $C_r^{AB}(t) = C_r^{AB}(t,0)$. We also define the spatial Fourier transform of the correlation function $C_r^{AB}(t,t')$ as

$$\tilde{C}_q^{AB}(t,t') = \sum_{r=0}^{L-1} C_r^{AB}(t,t') e^{iqr}, \tag{5.11}$$

where $q = 2\pi k/L$ and $k = 0, 1, \ldots, L-1$ and the inverse Fourier transform as

$$C_r^{AB}(t,t') = \frac{1}{L} \sum_q \tilde{C}_q^{AB}(t,t') e^{-iqr}. \tag{5.12}$$

5.2.0.1 *Integrated current correlation and the truncation scheme*

As we want to calculate the correlation function $C_r^{\mathcal{Q}\mathcal{Q}}(t,t')$, we start by writing the evolution equation for $t > t'$ as

$$\frac{d}{dt} C_r^{\mathcal{Q}\mathcal{Q}}(t,t') = \left\langle \frac{d}{dt} \mathcal{Q}_i(t) \mathcal{Q}_{i+r}(t') \right\rangle, \tag{5.13}$$

where $d\mathcal{Q}_i(t)/dt$ can be obtained from the following evolution equations,

$$\mathcal{Q}_i(t+dt) = \begin{cases} \textbf{\textit{events}} & \textbf{\textit{probabilities}} \\ (\mathcal{Q}_i(t)+1) & \hat{a}_i(t)dt \\ (\mathcal{Q}_i(t)-1) & \hat{a}_{i+1}(t)dt \\ \mathcal{Q}_i(t) & 1-\Sigma dt, \end{cases} \tag{5.14}$$

where $\Sigma = (\hat{a}_i(t) + \hat{a}_{i+1}(t))$. The above update rules give us the following exact expression of $d\mathcal{Q}_i(t)/dt$,

$$\frac{d}{dt}\mathcal{Q}_i(t) = (\hat{a}_i(t) - \hat{a}_{i+1}(t)) \equiv \mathcal{J}_i^{(d)}(t); \tag{5.15}$$

the equivalence between $d\mathcal{Q}_i(t)/dt$ and $\mathcal{J}_i^{(d)}(t)$ is obtained from Eq.(5.7), where we define the microscopic expression of the instantaneous diffusive current $\mathcal{J}^{(d)}$ as

$$\mathcal{J}_i^{(d)}(t) = (\hat{a}_i(t) - \hat{a}_{i+1}(t))\,. \tag{5.16}$$

Substituting Eq. (5.15) into Eq. (5.13), we obtain,

$$\frac{d}{dt}C_r^{\mathcal{Q}\mathcal{Q}}(t,t') = \left\langle \mathcal{J}_i^{(d)}(t)\mathcal{Q}_{i+r}(t')\right\rangle. \tag{5.17}$$

By solving this equation, we obtain the exact expression for the unequal-time unequal-space correlation function of the integrated current, $C_r^{\mathcal{Q}\mathcal{Q}}(t,t')$, as

$$C_r^{\mathcal{Q}\mathcal{Q}}(t,t') = \int_{t'}^{t} dt'' \left\langle \mathcal{J}_i^{(d)}(t'')\mathcal{Q}_{i+r}(t')\right\rangle_c + C_r^{\mathcal{Q}\mathcal{Q}}(t',t'), \tag{5.18}$$

which contains two other correlation functions: the unequal-time unequal-space diffusive current and integrated current, as well as the equal-time unequal-space integrated currents. To solve these additional correlation functions, we begin with $\left\langle \mathcal{J}_i^{(d)}(t)\mathcal{Q}_{i+r}(t')\right\rangle$ (as we are interested in steady states, we set $\langle \mathcal{Q}_{i+r}(t)\rangle = 0$), for which we need to solve the evolution equation of $\langle \hat{a}_i(t)\mathcal{Q}_{i+r}(t')\rangle$, which is given as

$$\frac{d}{dt}\left\langle \hat{a}_i(t)\mathcal{Q}_{i+r}(t')\right\rangle = \left\langle \frac{d}{dt}\hat{a}_i(t)\mathcal{Q}_{i+r}(t')\right\rangle. \tag{5.19}$$

But, similar to other models of self-organized criticality, in the Oslo model, $\hat{a}_i$ is also not a conserved quantity. As a result, it is not possible to express the evolution equation of $\hat{a}_i(t)$ in a closed form. Furthermore, due to the stochastic nature of the threshold mass for a site to become active, it is extremely challenging to formulate an update equation for the activity operator in the Oslo model. To bypass this difficulty altogether, similarly to Eq. (2.26) of the Manna model in Chap. 2, we propose an approximation to write the microscopic diffusive current in terms of the difference of local mass, which is a conserved quantity, instead of the difference of local activity,

$$\mathcal{J}_i^{(d)}(t) \simeq D(\bar{\rho})\,(m_i(t) - m_{i+1}(t))\,, \tag{5.20}$$

where $D(\bar{\rho}) = a'(\bar{\rho})$ as defined in Eq. (5.5). The main assumptions to obtain Eq.(5.20) from Eq.(5.16) are that any difference of local activity should follow the difference of local mass and the fluctuations around the global conserved density $\bar{\rho}$ are small. Now, by substituting Eq.(5.20) in Eq.(5.18) we obtain,

$$C_r^{\mathcal{Q}\mathcal{Q}}(t,t') \simeq \int_{t'}^{t} dt'' D \left\langle \{m_i(t'') - m_{i+1}(t'')\} \, \mathcal{Q}_{i+r}(t') \right\rangle_c + C_r^{\mathcal{Q}\mathcal{Q}}(t',t'); \tag{5.21}$$

as a result, we need to compute the unequal-time mass and integrated current correlation function, which follows the following evolution equation,

$$\begin{aligned} \frac{d}{dt} C_r^{m\mathcal{Q}}(t,t') = \left\langle \frac{d}{dt} m_i(t) \mathcal{Q}_{i+r}(t') \right\rangle &= \left\langle \left\{ \mathcal{J}_{i-1}^{(d)}(t) - \mathcal{J}_i^{(d)}(t) \right\} \mathcal{Q}_{i+r}(t') \right\rangle \\ &\simeq D\Delta_{i,k} \left\langle m_k(t) \mathcal{Q}_{i+r}(t') \right\rangle . \end{aligned} \tag{5.22}$$

In the above equation, the final closure of the equation is achieved by employing the approximation given in Eq. (5.20). We can write the solution of this equation using the Fourier transform, which is defined in Eq. (5.11), as

$$\tilde{C}_q^{m\mathcal{Q}}(t,t') = \exp\left[-D\lambda_q(t-t')\right] \tilde{C}_q^{m\mathcal{Q}}(t',t'), \tag{5.23}$$

where $\tilde{C}_q^{m\mathcal{Q}}(t,t')$ is the Fourier transformed $C_r^{m\mathcal{Q}}(t,t')$. To continue, we need to determine the equal-time unequal-space correlation function of mass and current. This correlation function is governed by the following evolution equation,

$$\frac{d}{dt} C_r^{m\mathcal{Q}}(t,t') \simeq D\Delta_{i,k} \left\langle m_k(t) \mathcal{Q}_{i+r}(t) \right\rangle + f_r(t), \tag{5.24}$$

where $f_r(t)$ is the source of the corresponding correlation function; for details, see appendix (C.1). Using the Fourier transformation, we can solve this equation and obtain,

$$\tilde{C}_q^{m\mathcal{Q}}(t,t) = \int_0^t dt' \exp\left[-D\lambda_q(t-t')\right] \tilde{f}_q(t'), \tag{5.25}$$

In Appendix (C.2), we further calculated the correlation function $C_r^{m\hat{a}}(t,t)$ using the steady state condition of equal-time mass-mass correlation, that gives us,

$$C_r^{m\hat{a}}(t,t) = a\delta_{0,r} - \frac{a}{2}\left(\delta_{0,r-1} - \delta_{0,r+1}\right), \tag{5.26}$$

which has the following Fourier transformation,

$$\tilde{C}_q^{m\hat{a}}(t,t) = \frac{\lambda_q}{2}. \tag{5.27}$$

Using the above result, we can write the Fourier-transformed source $\tilde{f}_q$, by using the explicit expression of f_r, given in Eq.(C.4), as

$$\tilde{f}_q = -a\frac{\lambda_q}{2}\left(1 - e^{-iq}\right). \tag{5.28}$$

By substituting, Eq.(5.28) in Eq.(5.25) and then putting Eq.(5.25) in Eq.(5.23), we finally obtain,

$$\tilde{C}_q^{m\mathcal{Q}}(t,t') = -a\int_0^{t'} dt'' \exp\left[-D\lambda_q(t-t'')\right]\frac{\lambda_q}{2}\left(1 - e^{-iq}\right), \tag{5.29}$$

and thus, taking the inverse Fourier of Eq. (5.29), we obtain the first part of the r.h.s. of Eq. (5.21).

5.2.1 *Current correlations*

The second part on the right-hand side of Eq.(5.21) is the equal-time integrated current correlation, which satisfies the following evolution equation,

$$\frac{d}{dt}C_r^{\mathcal{Q}\mathcal{Q}}(t,t) = \Gamma_r(t) + C_r^{\mathcal{J}^{(d)}\mathcal{Q}}(t,t) + C_{L-r}^{\mathcal{J}^{(d)}\mathcal{Q}}(t,t), \tag{5.30}$$

$$\simeq \Gamma_r(t) + D\left\{C_r^{m\mathcal{Q}}(t,t) - C_{r-1}^{m\mathcal{Q}}(t,t)\right\} + D\left\{C_{L-r}^{m\mathcal{Q}}(t,t) - C_{L-r-1}^{m\mathcal{Q}}(t,t)\right\}, \tag{5.31}$$

where to obtain Eq.(5.31) from Eq.(5.30) we used the approximation diffusive current in Eq.(5.20). Γ_r is the strength of the fluctuating current $\mathcal{J}^{(fl)}$ as given in Eq. (2.62) of Chapter 2, which can be easy to prove quite generically [108] and has the following expression in the steady state,

$$\Gamma_r = 2a\delta_{0,r} - a\delta_{0,r+1} - a\delta_{0,r-1}, \tag{5.32}$$

which is derived in Eq. (C.15); for details see Appendix (C.3). The solution of the Eq. (5.30) is the following,

$$C_r^{\mathcal{Q}\mathcal{Q}}(t,t) \simeq \int_0^t \mathrm{d}t'\,\Gamma_r(t') + \frac{1}{L}\int_0^t \mathrm{d}t'\,D\sum_{q=0}^{L-1}\tilde{C}_q^{m\mathcal{Q}}(t',t')\left[1 - e^{iq}\right](2-\lambda_{qr}), \tag{5.33}$$

$$= \int_0^t dt'\Gamma_r(t') - Da\sum_{q=0}^{L-1}\frac{1}{L}\int_0^t dt'\int_0^{t'} dt''\exp\left[-D\lambda_q(t'-t'')\right]\frac{\lambda_q^2}{2}(2-\lambda_{qr}), \tag{5.34}$$

where to obtain Eq.(5.34) from Eq.(5.33), we replaced $\tilde{C}_q^{m\mathcal{Q}}(t',t')$ using the Eq.(5.25). Now, we finally write the unequal-time unequal-space current correlation, by putting Eq.(5.34) and the

inverse Fourier transform of Eq.(5.29) in Eq.(5.21) and obtain the most general unequal-time unequal-space correlation function of integrated current as following,

$$C_r^{\mathcal{Q}\mathcal{Q}}(t,t') = \int_0^{t'} dt''\Gamma_r(t') - Da\sum_q \frac{1}{L}\int_0^{t'} dt'' \int_0^{t''} dt''' \exp\left[-D\lambda_q(t''-t''')\right]\frac{\lambda_q^2}{2}(2-\lambda_{qr}) \\ - Da\sum_q \frac{1}{L}\int_t^{t'} dt'' \int_0^{t'} dt''' \exp\left[-D\lambda_q(t''-t''')\right]\frac{\lambda_q^2}{2}e^{-iqr}. \tag{5.35}$$

The fluctuation of the time-integrated current, $\mathcal{Q}_i(t)$, across a bond can be obtained from Eq. (5.35) by setting $r = 0$ and $t = t' = T$, resulting in,

$$C_0^{\mathcal{Q}\mathcal{Q}}(T,T) = \left\langle \mathcal{Q}^2(T)\right\rangle = \frac{a}{D}\frac{1}{L}\sum_q \left(1 - e^{-D\lambda_q T}\right). \tag{5.36}$$

Interestingly, the large time ($T \gg L^2$) behaviour of $\left\langle \mathcal{Q}^2(T)\right\rangle$ in the thermodynamic limit $L \to \infty$ is given by

$$\lim_{T\to\infty}\lim_{L\to\infty}\left\langle \mathcal{Q}^2(T)\right\rangle \simeq \frac{a}{D}. \tag{5.37}$$

The interesting aspect is that the fluctuation saturates at a particular value of a/D instead of following a linear growth function over time, as observed in earlier chapters 2, 3 and 4, where the growth gradient was given by $2\chi(\bar{\rho})/L$. This saturation to a specific value implies mobility $\chi(\rho) = 0$ for any arbitrary global density $\bar{\rho}$. Therefore, the asymptotics of $\langle \mathcal{Q}^2(T)\rangle$ can be expressed as follows

$$\left\langle \mathcal{Q}^2(T)\right\rangle \sim T^{\alpha}, \;\; \textit{with} \;\; \alpha = 0 \;\; \textit{for} \;\; T \gg L^2, \tag{5.38}$$

Now to address the question of how the fluctuation saturates from its initial value, or its initial time growth, we study the asymptotics of the relative value of $\left\langle \mathcal{Q}^2(T)\right\rangle$ w.r.t to its saturated value at large time, i.e., $a/D - \left\langle \mathcal{Q}^2(T)\right\rangle$, which can be simply written as

$$\frac{a}{D} - \left\langle \mathcal{Q}^2(T)\right\rangle = \frac{a}{D}\frac{1}{L}\sum_q e^{-D\lambda_q T}, \tag{5.39}$$

which in the thermodynamic limit can be written by taking the variable transform $i \to i/L = x$ in the following way,

$$\frac{a}{D} - \left\langle \mathcal{Q}^2(T)\right\rangle \simeq 2\frac{a}{D}\int_{1/L}^{1/2} e^{-D\lambda(x)T} \simeq \frac{a}{2\pi D^{\frac{3}{2}}}T^{-1/2}\int_0^{\infty} dz\frac{e^{-z}}{z} = \frac{a}{2\sqrt{\pi}D^{\frac{3}{2}}}T^{-1/2}, \tag{5.40}$$

where $\lambda(x) \simeq 4\pi^2 x^2$ and we further take the variable transformation $z = 4\pi^2 x^2 DT$ with the assumption $T \gg 1$ to obtain the final result. Using this asymptotics, Eq.(5.36) can be written as

$$\left\langle \mathcal{Q}^2(T) \right\rangle \simeq \frac{a}{D} - \frac{a}{2\sqrt{\pi} D^{\frac{3}{2}}} T^{-1/2}. \tag{5.41}$$

In the left panel of Fig. 5.1, we plot the simulation data of $a/D - \left\langle \mathcal{Q}^2(T) \right\rangle$ as a function of T for density values $\bar{\rho} = 2$ (red), 3 (blue) and 4 (green) using solid lines. The numerical values from Eq. (5.36) are also shown for $\bar{\rho} = 2$, 3, and 4 using dot-dot-dashed, dot-dashed, and dotted lines, respectively for $L = 1000$. The $T^{-1/2}$ decay of this quantity indeed verifies Eq. (5.41), and we observe that the agreement between theory and simulation gradually improves as $\bar{\rho}$ increases.

Near criticality, we know that $a \sim \Delta^{\beta}$; therefore, in the dimensional analysis of Eq. (5.37), we see that $a/a' \sim \Delta$ ($D = a'$ as defined in Eq. (5.5)), where $\Delta = \rho - \rho_c$ is the relative density with respect to the critical density value ρ_c. This implies that near criticality, the current fluctuation should vanish at criticality as $\Delta = 0$. However, contrary to this expectation, our simulations show a different behaviour.

In the right panel of Fig. 5.1, we observe that $\left\langle \mathcal{Q}^2(T) \right\rangle$ for $\bar{\rho} = 1.7344$ (solid red line) is much greater than $\left\langle \mathcal{Q}^2(T) \right\rangle$ for $\bar{\rho} = 1.736$ (solid blue line), and similarly, $\left\langle \mathcal{Q}^2(T) \right\rangle$ for $\bar{\rho} = 1.736$ is greater than $\mathcal{Q}^2(T)$ for $\bar{\rho} = 1.738$ (solid green line), all of which for $L = 5000$. From which we conclude that the time-integrated bond current fluctuation is non-monotonic. Although the growth of current fluctuation away from criticality is mainly due to the increase in the number of particles that contribute more to the bond current fluctuation, the near-critical divergence of current fluctuation at large times is attributed to the singular behaviour of the bulk diffusivity $D(\bar{\rho}) \to \infty$ as $\bar{\rho} \to \rho_c$ and the presence of the centre of mass conservation law along with density. In other words, as the system approaches criticality ($\bar{\rho} \to \rho_c$), the bulk diffusivity diverges, leading to significant fluctuations in the current even at large times. Moreover, the growth exponent is found to be $\alpha \approx 1/3$ near the criticality.

5.2.2 *Instantaneous current fluctuation: Argument of maximal hyperuniformity*

In this section, we demonstrate that the exponent governing the decay of instantaneous current correlation is quite different from other diffusive systems, such as the Manna model, despite being a diffusive system. Furthermore, the $T^{-1/2}$ decay of the relative fluctuation of the integrated current over a bond can also be understood from this correlation function.

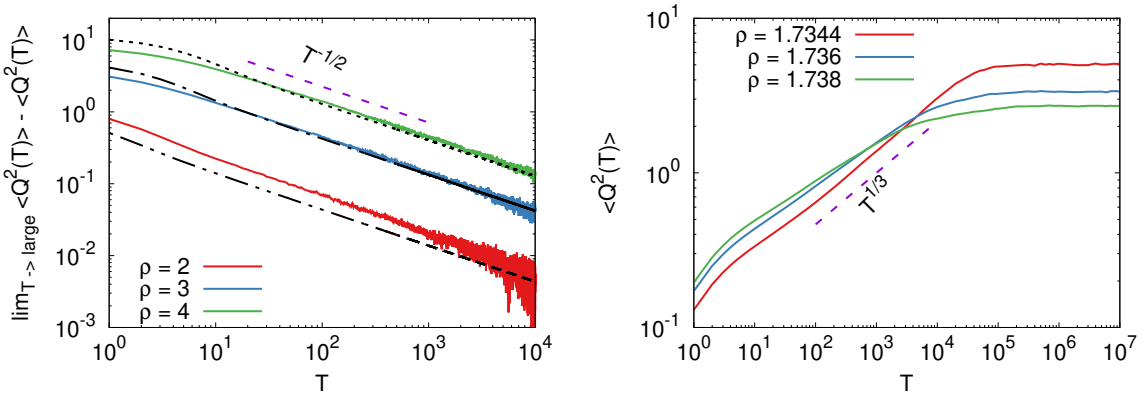

Figure 5.1: *Left panel:* Relative integrated bond current fluctuation is plotted for different densities as a function of time for system size $L = 1000$. Simulation data are plotted in a solid line for densities $\bar{\rho} = 2$ (red line), $\bar{\rho} = 3$ (blue line), $\bar{\rho} = 4$ (green line). The y-axis denotes the relative value of $\langle Q^2(T)\rangle$ subtracted from its steady state value at large times, i.e., $\lim_{T\gg 1}\langle Q^2(T)\rangle - \langle Q^2(T)\rangle$, which decays as $T^{-1/2}$, as predicted by Eq.(5.41). The theoretical values of the same quantity are plotted using Eq.(5.39) in the dot-dot-dashed line for $\bar{\rho} = 2.0$ and in the dot-dashed line for $\bar{\rho} = 3.0$, and in the dotted line for $\bar{\rho} = 4.0$. *Right panel:* Integrated bond current fluctuation is plotted as a function of time near criticality ($\rho_c \approx 1.732$) for system size $L = 5000$. The simulation data are plotted in solid lines for densities $\bar{\rho} = 1.7344$ (red line), 1.736 (blue line), and 1.738 (green line). The guiding dotted line demonstrates the growth of bond current fluctuation as $T^{1/3}$ near critical densities. Notably, in both away and near criticality the current fluctuation saturates at large time limit, signifying *zero* mobility in the system.

The instantaneous bond current correlation, $\langle \mathcal{J}_i(t)\mathcal{J}_{i+r}(0)\rangle - \langle \mathcal{J}_i(t)\rangle\langle \mathcal{J}_{i+r}(0)\rangle$, can be obtained by differentiating Eq.(5.35) for $t \geq t'$ in the following manner,

$$C_r^{\mathcal{J}\mathcal{J}}(t) \equiv \langle \mathcal{J}_i(t)\mathcal{J}_{i+r}(0)\rangle - \langle \mathcal{J}_i(t)\rangle\langle \mathcal{J}_{i+r}(0)\rangle = \left[\frac{d}{dt}\frac{d}{dt'}C_r^{\mathcal{Q}\mathcal{Q}}(t,t')\right]_{t'=0,t\geq 0}, \tag{5.42}$$

which gives us,

$$C_r^{\mathcal{J}\mathcal{J}}(t) = \Gamma_r\delta(t) - aD\frac{1}{L}\sum_q e^{-\lambda_q Dt}\frac{\lambda_q^2}{2}e^{-iqr}. \tag{5.43}$$

The decay of the current correlation is governed by the second part of the right-hand side of the above equation. Its asymptotics for $t \gg 1$ can be understood by converting the sum into an integral in the thermodynamic limit using $i \to x = i/L$, where λ_q can be approximated as $\lambda_q \to \lambda(x) \simeq 4\pi^2x^2$. Then, using the variable transformation $z = 4\pi^2x^2Dt$, we can write Eq.(5.43) for $t \gg 1$ as follows:

$$C_0^{\mathcal{J}\mathcal{J}}(t) \simeq -\frac{a}{4\pi D^{3/2}}t^{-5/2}\int_0^\infty e^{-z}z^{3/2}dz = -\frac{3a}{16\sqrt{\pi}D^{3/2}}t^{-5/2}. \tag{5.44}$$

In Fig. (5.2) the negative instantaneous bond current correlation $-C_0^{\mathcal{J}\mathcal{J}}(t)$ is plotted as a function of time for different away from criticality densities. Simulation data are plotted as solid lines for $\bar{\rho} = 2$ (red line), $\bar{\rho} = 3$ (blue line), and $\bar{\rho} = 4$ (green line) for $L = 1000$. The corresponding theoretical curves are plotted using Eq.(5.43) for $r = 0$ for $\bar{\rho} = 2$ (black dotted line), $\bar{\rho} = 3$ (black dot-dashed line), $\bar{\rho} = 4$ (black dot-dot-dashed line). The guiding line denotes the $t^{-5/2}$ decay of the correlation function, as predicted by our theory in Eq. (5.44).

The asymptotic expression of $C_0^{\mathcal{J}\mathcal{J}}(t)$ derived in Eq.(5.44), can also be written as $C_0^{\mathcal{J}\mathcal{J}}(t) \sim -t^{\alpha-2}$, where the exponent α captures the dynamic growth of $\langle \mathcal{Q}^2(T) \rangle$ in the thermodynamic limit $L \to \infty$. We can summarize this result for away and near criticality as

$$C_0^{\mathcal{J}\mathcal{J}}(t) \sim \begin{cases} -t^{-5/2}, & \alpha = -1/2 \ \textit{for} \ \ \bar{\rho} \gg \rho_c, \\ -t^{-5/3}, & \alpha \approx 1/3 \ \textit{for} \ \ \bar{\rho} \simeq \rho_c. \end{cases} \tag{5.45}$$

In the Manna model, the current correlation becomes steeper near criticality compared to away from criticality, as given in Eq. (2.58). This steeper decay of the correlation function indicates a faster reduction of dynamical fluctuation, and we identify this phenomenon as dynamical hyperuniformity.

On the other hand, from Eq. (5.45), we observe that the current fluctuation is steeper away from criticality than near criticality. However, when comparing with our benchmark for a normal diffusive system, i.e., $C_0^{\mathcal{J}\mathcal{J}}(t) \sim -t^{-3/2}$, as obtained in Eq. (2.57) of Chapter 2, we find that in the Oslo model near criticality, the decay of the correlation function is still steeper, specifically $t^{-5/3}$. Thus, the near critical fluctuations of current still exhibit *dynamical hyperuniformity*, while the fluctuations away from criticality achieve the maximum possible hyperuniformity, becoming *maximally hyperuniform*.

This result indicates the high importance of conserved quantities in determining the large-scale fluctuations in interacting particle systems.

We also calculated how the time-integrated bond current fluctuations decays at later times due to such steep decay of the correlation function. We integrate the $C_r^{\mathcal{J}\mathcal{J}}(t)$ in the window of $[-T, T]$ and obtain,

$$\int_{-T}^{T} C_0^{\mathcal{J}\mathcal{J}}(t)dt = \frac{1}{L} a \sum_q \lambda_q e^{-DT\lambda_q} \simeq \frac{a}{2\pi D^{3/2}} T^{-3/2} \int_0^\infty e^{-z} \sqrt{z} dz = \frac{a}{4\sqrt{\pi} D^{3/2}} T^{-3/2}, \tag{5.46}$$

which is quite faster compared to the dynamic behaviour of the same quantity computed for the Manna model in Eq. (2.55), which decays as $T^{-1/2}$ in the Manna model.

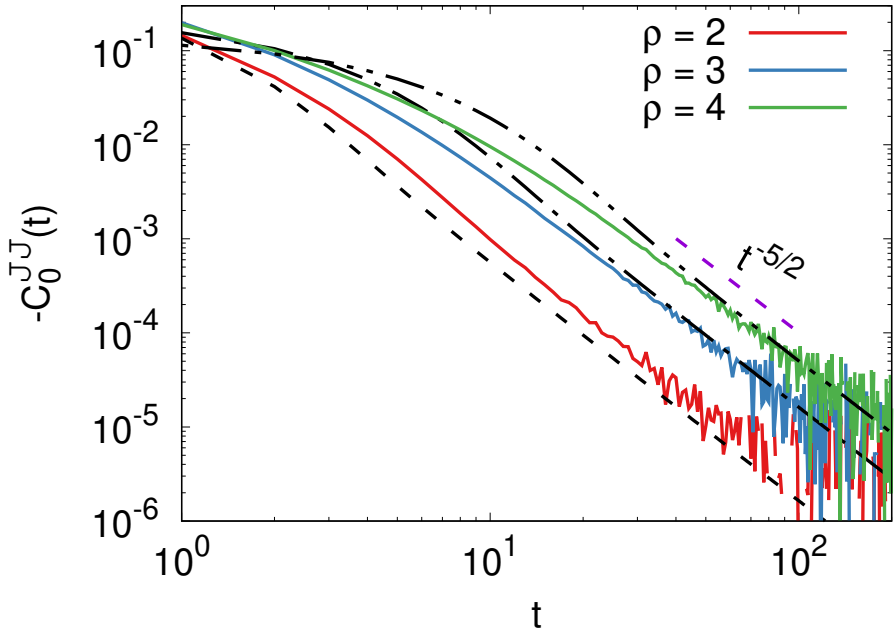

Figure 5.2: The negative instantaneous bond current correlation $-C_0^{\mathcal{J}\mathcal{J}}(t)$ is plotted as a function of time for different away from criticality densities. The simulation data are plotted in solid lines for $\bar{\rho} = 2$ (red line), $\bar{\rho} = 3$ (blue line), $\bar{\rho} = 4$ (green line). The corresponding theoretical curves are plotted using the Eq.(5.43) for $r = 0$ for $\bar{\rho} = 2$ (black dotted line), $\bar{\rho} = 3$ (black dot-dashed line), $\bar{\rho} = 4$ (black dot-dot-dashed line). All data is taken for system size $L = 1000$. The guiding line denotes the $t^{-5/2}$ decay of the correlation function as predicted by our theory in Eq. (5.44).

5.2.2.1 *Fluctuating current and its relation to total current in the system*

Now we discuss the dynamic properties of the fluctuating part $\mathcal{J}_i^{(fl)}(t)$ in the instantaneous bond current, which has already been defined in eq.(5.8) and whose strength Γ_r appears in the actual current correlation functions (e.g., see Eqs.(5.35) and (5.43)). In Eq. (2.62), we have proven the generic expression:

$$C_r^{\mathcal{J}^{(fl)}\mathcal{J}^{(fl)}}(t, t' = 0) \equiv C^{\mathcal{J}^{(fl)}\mathcal{J}^{(fl)}} r(t) = \delta(t)\Gamma_r(\bar{\rho}), \tag{5.47}$$

where Γ_r is the same as given in Eq. (5.32). This implies that although the fluctuation of current across a single bond is *nonzero* (as shown by setting $r = 0$ in Eq. (5.32)):

$$\Gamma_0 = 2a(\bar{\rho}), \tag{5.48}$$

the total integrated fluctuating current is exactly *zero*, as indicated by:

$$\sum_{r=0}^{L-1} \Gamma_r = 0. \tag{5.49}$$

Furthermore, we can also study the steady-state variance $\langle \bar{Q}^2(L,T) \rangle - \langle \bar{Q}(L,T) \rangle^2$ of the cumulative (space-time integrated) actual particle current $\bar{Q}(L,T) = \sum_{i=0}^{L-1} \mathcal{Q}_i(T)$ across a system of size L and up to time T. Using the instantaneous current, this quantity can be written as

$$\bar{Q}(L,T) = \sum_{i=0}^{L-1} \mathcal{Q}_i(T) = \int_0^T dt \sum_{i=0}^{L-1} \mathcal{J}_i(T) = \int_0^T dt \sum_{i=0}^{L-1} \mathcal{J}_i^{(fl)}(T). \tag{5.50}$$

The equality in the above equation can be obtained by noting that $\mathcal{J}^{(d)}$ is the local difference of the activity operator and, when taking the sum over the total system size, it cancels exactly. Thus, the fluctuation of $\bar{Q}(L,T)$ can be written exactly the same as that of Eq. (2.72):

$$\lim_{L\to\infty} \frac{\langle \bar{Q}^2(L,T) \rangle}{LT} = \sum_r \Gamma_r = 0. \tag{5.51}$$

From the above relation, one can conclude that in the Oslo model, the mobility, which is given by the fluctuation of the total integrated current in the system, is *zero*. This result also justifies our earlier finding of current fluctuation as $\langle \mathcal{Q}^2(T) \rangle \sim T^\alpha$ with $\alpha = 0$ when $T \gg L^2$. The gradient of bond current, particularly in the region where $T \gg L^2$, provides us with a measure of mobility, as given in Eq. (1.43).

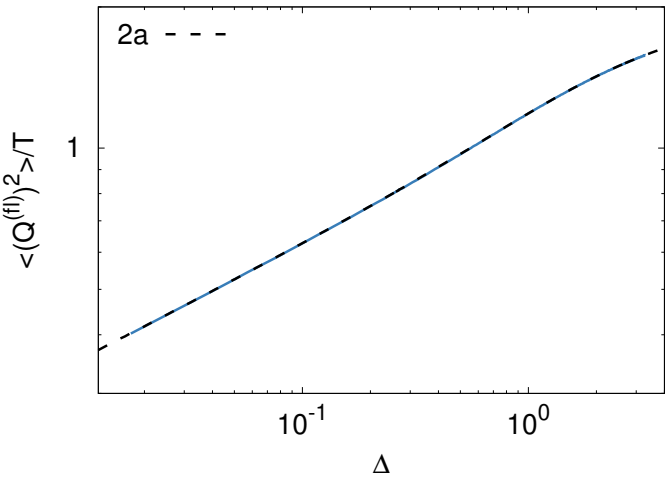

Figure 5.3: Intensive fluctuation of the excess bond current is shown as a function of relative density $\Delta = \bar{\rho} - \rho_c$ ($\rho_c \approx 1.732$) for a system size of $L = 1000$ and $T = 100$, represented by the solid blue line. Additionally, we plot twice the activity $2a$ as a function of Δ in the same plot, represented by the dotted black line, which exhibits an excellent match with the intensive excess current fluctuation as described by Eq. (5.53).

To verify eq.(5.48) in simulation, let us first define a time-integrated fluctuating current up to time T,

$$\mathcal{Q}^{(fl)}(T) = \int_0^T dt \mathcal{J}_i^{(fl)}(t). \tag{5.52}$$

Then, using Eq. (5.32) we obtain, a fluctuation relation, which immediately connects the scaled current fluctuation and the density-dependent activity,

$$\frac{1}{T}\left\langle \left(\mathcal{Q}^{(fl)}(T)\right)^2 \right\rangle = 2a(\bar{\rho}). \tag{5.53}$$

In Fig. 5.3, we plotted the simulation data of $\left\langle \left(\mathcal{Q}^{(fl)}(T)\right)^2 \right\rangle / T$ across a bond and up to time $T = 100$ as a function of the relative density $\Delta = \rho - \rho_c$, shown as a solid blue line. We observe an excellent agreement with twice the activity, represented by the black dotted line, as given in Eq. (5.53).

5.2.2.2 *Power spectrum*

Similarly, as in the earlier chapters, using the *Wiener-Khinchin* theorem [122] the spectral density of instantaneous current fluctuations can be obtained by taking the Fourier transform of the correlation function associated with those fluctuations. The power spectrum of the

bond current fluctuation in the steady state, $S_{\mathcal{J}}(f)$ can be obtained by Fourier transforming the two-point correlation function given in Eq.(5.43) along with $r = 0$ as follows,

$$S_{\mathcal{J}}(f) = \int_{-\infty}^{\infty} dt C_0^{\mathcal{J}\mathcal{J}}(t) e^{2\pi i f t} = \frac{a(\bar{\rho})}{L} \sum_q \lambda_q \frac{4f^2\pi^2}{D^2\lambda_q^2 + 4f^2\pi^2}. \tag{5.54}$$

In the limit of large system size, $L \gg 1$, the asymptotic behaviour of the above sum when $1/L^2 \ll f \ll 1$, can be obtained by approximating the above sum by the following integral,

$$S_{\mathcal{J}}(f) \simeq 2a \int_{\frac{1}{L}}^{\frac{1}{2}} dx \lambda(x) \frac{4\pi^2 f^2}{\lambda(x)^2 D^2 + 4\pi^2 f^2}, \tag{5.55}$$

where in the continuum limit, we perform the substitution $q \to 2\pi x$, which leads to $\lambda(x) \approx 4\pi^2 x^2$. Then by using the variable transformation, $x = \sqrt{f} y^{1/4}/\sqrt{2\pi}\sqrt{D}$, we convert the above integral into the following in the limit $L \to \infty$ and obtain,

$$S_{\mathcal{J}}(f) = f^{3/2} \frac{a\sqrt{\pi}}{\sqrt{2}D^{3/2}} \int_0^{\infty} \frac{dy}{y^{1/4}(1+y)} = a \frac{\pi^{3/2}}{D^{3/2}} f^{3/2}. \tag{5.56}$$

However, as discussed in Sec. 5.2.2 in detail, in the power spectrum, we also identify the appearance of both dynamic hyperuniformity and dynamic maximal hyperuniformity. The functional dependence of $S_{\mathcal{J}}(f)$ can be written as:

$$S_{\mathcal{J}}(f) \sim f^{\psi_{\mathcal{J}}}, \tag{5.57}$$

where

$$\psi_{\mathcal{J}} \begin{cases} = \frac{3}{2} & for \;\; \bar{\rho} \gg \rho_c, \\ \approx \frac{2}{3} & for \;\; \bar{\rho} \simeq \rho_c; \end{cases} \tag{5.58}$$

we derived $\psi_{\mathcal{J}} = 3/2$ away from criticality, and from simulation, we obtained $\psi_{\mathcal{J}} \approx 2/3$ near criticality.

Compared to normal diffusive systems, where we have derived $\psi_{\mathcal{J}} = 1/2$, the near-criticality value of $\psi_{\mathcal{J}}$ satisfying $\psi_{\mathcal{J}} \approx 2/3 > 1/2$ signifies the presence of dynamic hyperuniformity in the Oslo model. Moreover, $\psi_{\mathcal{J}} = 3/2 \gg 1/2$ away from criticality indicates the presence of maximal dynamic hyperuniformity in current fluctuation, as the power spectrum decays with decreasing frequencies, it characterizes how fast or slow current fluctuation is vanishing. The steeper the decay, the faster the vanishing.

In simulations, we compute the power spectrum by discretizing the instantaneous current into small temporal intervals, typically denoted as δt, and then calculate the Fourier transform as follows,

$$\tilde{\mathcal{J}}_{n;T} = \delta t \sum_{k=0}^{T-1} \mathcal{J}_i(k) e^{2\pi i f_n k}, \tag{5.59}$$

where $f_n = n/T$ for $T \gg 1$. Finally, we define the power spectrum of a bond current as

$$S_{\mathcal{J}}(f_n) = \lim_{T\to\infty} \frac{1}{T} \langle |\tilde{\mathcal{J}}_{n;T}|^2 \rangle, \tag{5.60}$$

where $f_n = n/T$ for $T \gg 1$. The limit as T tends to infinity represents an average over an infinitely long time period. In the large system size limit, $L \to \infty$ the convergence of the discrete sum in Eq.(5.60) to its continuum limit is expected, as expressed in Eq.(5.54).

In the left panel of Fig. (5.4), we plot the power spectrum $S_{\mathcal{J}}(f)$ as a function of the frequency f for away from criticality densities $\bar{\rho}$ of 2 (red), 3 (blue), and 4 (green) in solid lines. The corresponding theoretical curves, obtained using Eq. (5.54), for the corresponding densities are plotted in dashed, dot-dashed, and dot-dot-dashed lines, respectively. As the density increases, the theoretical curves rapidly converge to the simulation data. The guiding line denotes the $f^{\psi_{\mathcal{J}}}$, with $\psi_{\mathcal{J}} = 3/2$ decay of the power spectrum as $f \to 0$, as predicted by Eq. (5.56). *In the right panel* of the same plot, we present the simulation data of the power spectrum for near-critical densities $\bar{\rho} = 1.7344$ (green line), 1.736 (blue line), and 1.738 (red line) for $L = 5000$. The longest power-law regime is governed by $\psi_{\mathcal{J}} \approx 2/3$, indicating less fluctuating behaviour of the current compared to away from criticality densities.

5.2.3 *Tagged particle diffusion*

In this section, we examine the variance of the displacements $X_\alpha(T)$ of a tagged particle α over a temporal interval $[0, T]$.

Since a particle can only hop a distance of $+1$ or -1 from the toppled site, the variance of the total hop length $\langle X_\alpha^2(T) \rangle$ depends solely on the number of topplings experienced by the tagged particle within this time interval, denoted as $N_\alpha^{(h)}(T)$, as shown in the following equation,

$$\langle X_\alpha^2(T) \rangle = N_\alpha^{(h)}(T). \tag{5.61}$$

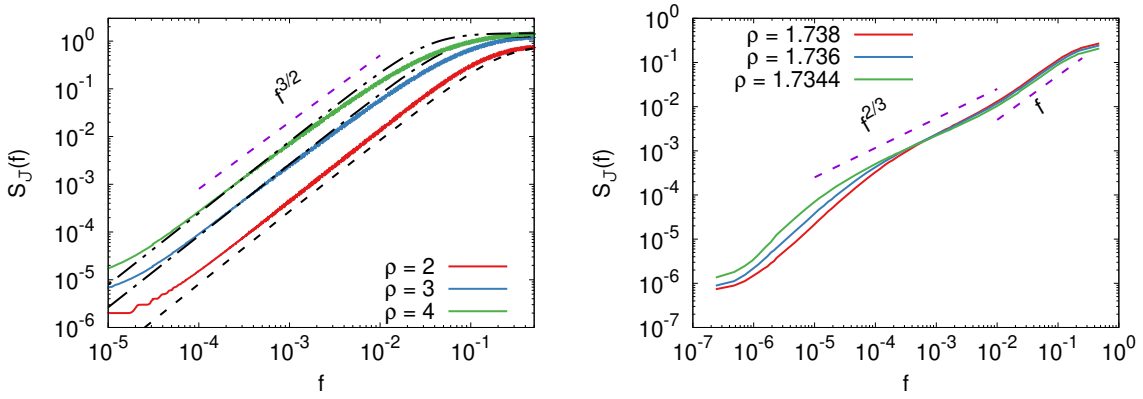

Figure 5.4: The power spectrum of the bond current is plotted as a function of frequency. *Left panel:* This corresponds to the density regime away from criticality ($\rho_c \approx 1.732$). Simulation data, taken with $L = 1000$, are plotted as solid lines for $\bar{\rho} = 2$ (red), $\bar{\rho} = 3$ (blue), and $\bar{\rho} = 4$ (green). Theoretical lines, obtained from Eq.(5.54), are represented by dotted, dot-dashed, and dot-dot-dashed lines for the same densities, respectively. The guiding line denotes the $f^{\psi_{\mathcal{J}}}$, with $\psi_{\mathcal{J}} = 3/2$ decay of the power spectrum as $f \to 0$, as predicted by Eq. (5.56). *Right panel:* This corresponds to the power spectrum of current to the density regime near criticality. Simulation data, taken with $L = 5000$, are plotted as solid lines for densities $\bar{\rho} = 1.738$ (red), 1.736 (blue), and 1.7344 (green). The guiding lines demonstrate the power spectrum initially decays linearly, followed by $f^{2/3}$ decay as the frequency approaches the minimum value.

By summing over all the tagged particles of the system, the total variance can be written in terms of twice of the total topplings $N^{(tp)}(T)$ during that interval as

$$\sum_{\alpha} \langle X_{\alpha}^2(T) \rangle = \sum_{\alpha} N_{\alpha}^{(h)}(T) = 2N^{(tp)}(T), \tag{5.62}$$

as at each toppling two particle jumps out the site. The number of total toppling in the system, $N^{(tp)}(T)$, on average, is equal to the number of active site density $a(\bar{\rho})$ times corresponding spacetime volume,

$$N^{(tp)}(T) = a(\bar{\rho})LT. \tag{5.63}$$

Due to the homogeneity of the system, we can express the left-hand side of Equation (5.62) as the total number of particles multiplied by the variance of a particle tagged $\langle X^2(T) \rangle$. Using Equation (5.63), we can rewrite Equation (5.62) as follows,

$$N\langle X^2(T) \rangle = 2a(\bar{\rho})LT \;\; or \;\; \langle X^2(T) \rangle = 2\frac{a(\bar{\rho})}{\bar{\rho}}T. \tag{5.64}$$

The self-diffusion coefficient $\mathcal{D}_s(\bar{\rho})$ can be defined in terms of $\langle X^2(T)\rangle$ in the steady state as

$$\langle X^2(T)\rangle = 2\mathcal{D}_s(\bar{\rho})T, \tag{5.65}$$

comparing which with Eq.(5.64), we obtain the exact expression of self-diffusivity in terms of the activity and the corresponding global density $\bar{\rho}$ as

$$\mathcal{D}_s(\bar{\rho}) = \frac{a(\bar{\rho})}{\bar{\rho}}. \tag{5.66}$$

In Fig. 5.5, we plot the mean-square fluctuation of tagged particle displacement up to time T (represented by the solid red line) as a function of the relative density Δ. The notation $\langle\langle X^2(T)\rangle\rangle = \sum_\alpha \langle X_\alpha^2(T)\rangle / N$ signifies averaging over trajectories and particles. The simulations (solid red line) show excellent agreement with the theoretically obtained self-diffusion coefficient $\mathcal{D}_s(\bar{\rho})$ (shown as the dashed black line) as defined in Eq.(5.66). Additionally, we display the bulk-diffusion coefficient $D(\bar{\rho}) = a'(\bar{\rho})$ as a function of $\Delta = \bar{\rho} - \rho_c$ (depicted by the dot-dashed blue line) obtained from simulation, using Eq.(5.5). Notably, the behaviour of the bulk-diffusion coefficient contrasts with that of the self-diffusion coefficient $\mathcal{D}_s(\bar{\rho})$ near criticality. Since, near criticality activity of the system tends to zero rapidly, so does the self diffusion coefficient, whereas due to the anomalous transport in this density regime, it goes to infinity. Away from criticality, both diffusivities go to zero but in different manners.

One should note that the self-diffusion coefficient of the Manna sandpile, which we derived in Eq. (2.88), is the same as the one we derived in Eq. (5.66). In the Manna model, activity $a(\rho)$ also has the meaning of mobility, so we can also relate $\mathcal{D}_s(\bar{\rho})$ to the total current fluctuation of the system. However, in the Oslo model, the mobility $\chi = 0$, and thus, the total integrated current, so $a(\bar{\rho})$ does not have the meaning of a transport coefficient.

5.2.4 *Power spectrum of mass fluctuations*

In this section, we study the properties of fluctuations in the mass of a subsystem $M_l(t) = \sum_{i=0}^{l=1} m_i(t)$, for which we begin with the unequal time and unequal space correlation function of the mass of a single site in steady state for $t \geq 0$, $C_r^{mm}(t,0) = \langle m_i(t)m_{i+r}(0)\rangle - \langle m_i(t)\rangle \langle m_{i+r}(0)\rangle \equiv C_r^{mm}(t)$. It is evident that due to the microscopic dynamics, which allows for the change in mass of three sites simultaneously, more than single site spatial correlation is expected in the steady state.

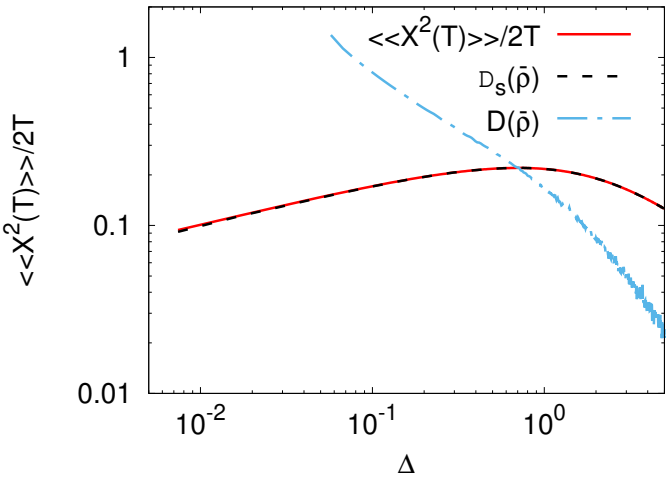

Figure 5.5: We plot the mean-square fluctuation of tagged particle displacement up to time T (solid red line) as a function of relative density Δ, where the double angular braces $\langle\langle X^2(T)\rangle\rangle = \sum_\alpha \langle X_\alpha^2(T)\rangle / N$ denote the average over trajectories as well as particles. Simulations (solid red line) show excellent agreement with the theoretically obtained self-diffusion coefficient $\mathcal{D}_s(\bar{\rho})$ (dashed black line) as in Eq.(5.66). We also plot the bulk-diffusion coefficient $D(\bar{\rho}) = a'(\bar{\rho})$ as a function of $\Delta = \bar{\rho} - \rho_c$ (dot-dashed blue line), using Eq.(5.5) from simulation, which has a contrasting behaviour as compared to the self-diffusion coefficient $\mathcal{D}_s(\bar{\rho})$.

The evolution equation of $C_r^{mm}(t)$ can be written as

$$\frac{d}{dt}C_r^{mm}(t) = \sum_k \Delta_{i,k} \langle \hat{a}_k(t) m_{i+r}(0)\rangle \,, \tag{5.67}$$

which further can be simplified using Eq.(5.20) that gives us,

$$\frac{d}{dt}C_r^{mm}(t) \simeq D(\bar{\rho}) \sum_k \Delta_{r,k} C_k^{mm}(t). \tag{5.68}$$

Solving the above equation using Fourier representation, we obtain,

$$\tilde{C}_q^{mm}(t) \simeq e^{-D\lambda_q t}\tilde{C}_q^{mm}(0), \tag{5.69}$$

where $\tilde{C}_q^{mm}$ is the Fourier transformation of C_r^{mm}. $\tilde{C}_q^{mm}(0)$ represents the Fourier transform of the equal-time correlation function. This correlation function can be found by solving the equation, that is obtained from the condition $dC_r^{mm}/dt = 0$ using Eq.(5.20), in steady state, which gives us

$$\frac{d}{dt}C_r^{mm}(t,t) \simeq D\sum_k \Delta_{0,k} \langle m_k m_r\rangle + B_r = 0, \tag{5.70}$$

where the source term B_r is given in Eq.(C.9). The corresponding generating function $G'(z) = \sum_{z=0}^{\infty} C_r^{mm}(t,t)z^r$, can be derived in a similar way to Eq. (C.10), by multiplying the above equation by z^r and taking the sum over r from 0 to ∞, which finally gives us,

$$G'(z) = \frac{a}{D} - \frac{a}{2D}z; \tag{5.71}$$

see Appendix C.2 for details. This generating function tells us that equal-time mass-mass correlation in the steady state has a nearest neighbour contribution, and can be expressed as

$$C_r^{mm}(0) = \frac{a}{D}\delta_{0,r} - \frac{a}{2D}\left(\delta_{0,r-1} + \delta_{0,r+1}\right). \tag{5.72}$$

The Fourier transform of the above correlation function is given by,

$$\tilde{C}_q^{mm}(t,t) = \frac{a}{2D}\lambda_q. \tag{5.73}$$

We put the above equation into Eq.(5.69) to obtain,

$$\tilde{C}_q^{mm}(t) \simeq e^{-D\lambda_q t}\frac{a}{2D}\lambda_q, \tag{5.74}$$

and finally, using the inverse Fourier transform we got the correlation function $C_r^{mm}(t)$ as

$$C_r^{mm}(t) \simeq \frac{1}{L}\frac{a}{2D}\sum_q e^{-iqr}e^{-D\lambda_q t}\lambda_q. \tag{5.75}$$

We now compute the temporal correlation and power spectrum of the subsystem mass $M_l(t) = \sum_{r=0}^{l-1} m_r(t)$ for $l < L$ following Ref.[108]. The equal-time correlation function for mass $C^{M_l M_l}(t,0) \equiv C^{M_l M_l}(t)$ can be written using the following expression,

$$C^{M_l M_l}(t) = lC_0^{mm}(t) + \sum_{r=1}^{l-1}(l-r)(C_r^{mm}(t) + C_{-r}^{mm}(t)). \tag{5.76}$$

Substituting Eq.(5.75), in the above equation, we get the dynamic correlation of subsystem mass as

$$C^{M_l M_l}(t) \simeq \frac{1}{L}\frac{a}{2D}\sum_q e^{-D\lambda_q t}\lambda_{ql}, \tag{5.77}$$

the equal-time part of which gives us the fluctuation of subsystem mass can be written as a function of global density $\bar{\rho}$ using the transport coefficient bulk diffusivity D and active site density $a(\bar{\rho})$ as,

$$C^{M_l M_l}(0) = \sigma_{M_l}^2(\bar{\rho}) = \langle M_l^2 \rangle - \bar{\rho}^2 l^2 = \frac{a}{D}, \tag{5.78}$$

for $l \ll L$ in the limit $L \to \infty$. The insensitivity of the fluctuation of the mass of the subsystem to the size of the subsystem l, or the fixed amount of fluctuation that arises solely from the boundary sites, is a distinct property of maximal hyperuniform systems [111, 112]. This behaviour is due to the correlation structure of the mass at equal time, derived in Eq. (5.72), where the nearest-neighbor correlation exactly cancels the correlation of a mass of the same site. As a result, when we take the sum over this correlation function to calculate, $\sigma^2_{M_l}(\bar{\rho})$ the fluctuations only come from the boundary sites of a subsystem and do not depend on the size of the subsystem.

Moreover, comparing Eq.(5.37) and Eq.(5.78) we propose a new fluctuation relation for the Oslo model, given as

$$\lim_{T\to\infty}\lim_{L\to\infty}\left\langle \mathcal{Q}^2(T)\right\rangle = \lim_{l\to\infty}\lim_{L\to\infty}\sigma^2_{M_l}(\bar{\rho}), \tag{5.79}$$

which in the thermodynamic limit $L \to \infty$ equates the large time integrated bond current fluctuation in the limit $T \to \infty$ with the subsystem mass fluctuation for $l \to \infty$ and $l/L \ll 1$.

To check the fluctuation relation Eq. (5.79) numerically, in the *left panel* of Fig.5.6 we plot $\left\langle \mathcal{Q}^2(T)\right\rangle$, obtained from simulation, for $L = 1000$ and $T \gg 1$ in solid violet line. The corresponding simulation data for $\sigma^2_{M_l}(\bar{\rho})$ are shown in a dashed green line for $L = 1000$ and $l = 500$, both as a function of relative density $\Delta = \bar{\rho} - \rho_c$. The equality between the two data sets, for the away and near-criticality density regime, indicates the validity of the fluctuation relation (5.79).

In the *right panel*, we plot the scaled fluctuation of the subsystem mass $\sigma^2(M_l)/l$, as a function of the subsystem size l. Simulation data for $\bar{\rho} = 4$ (violet line), 2 (green line) and 1.74 (blue line) are shown for $L = 5000$, while $\bar{\rho} = 1.735$ (orange line) and 1.734 (red line) are plotted for $L = 10000$. Away from the criticality, it indicates l^{-1} decay of the scaled fluctuation or the maximal possible hyperuniformity in a *one-dimensional* system, verifying our theoretical result obtained in Eq. (5.78). In contrast, near criticality the decay becomes much slower, approximately $l^{-0.6}$, as obtained from simulations, indicating hyperuniform fluctuations. Comparing the exponent $\lambda = 1/2$ reported in [65] to characterize $\sigma^2_{M_l}(\bar{\rho})/l \sim l^{-\lambda}$, we observe a slight difference between the reported value and the one we obtained here. This discrepancy can be attributed to the finite size of the system we considered and the finite difference between $\bar{\rho}$ and ρ_c, which remains finite even for the minimum possible value for which we were able to collect data. The transition from maximal hyperuniformity ($\lambda = 1$) to hyperuniformity ($\lambda \approx 0.6$) of the density fluctuation indicates an increase in the fluctuations of the system near criticality, both in mass and current, as they are related by Eq. (5.79). This observation is consistent with our earlier results on instantaneous current fluctuation and power spectrum obtained in Sec. 5.2.2 and 5.2.2.2.

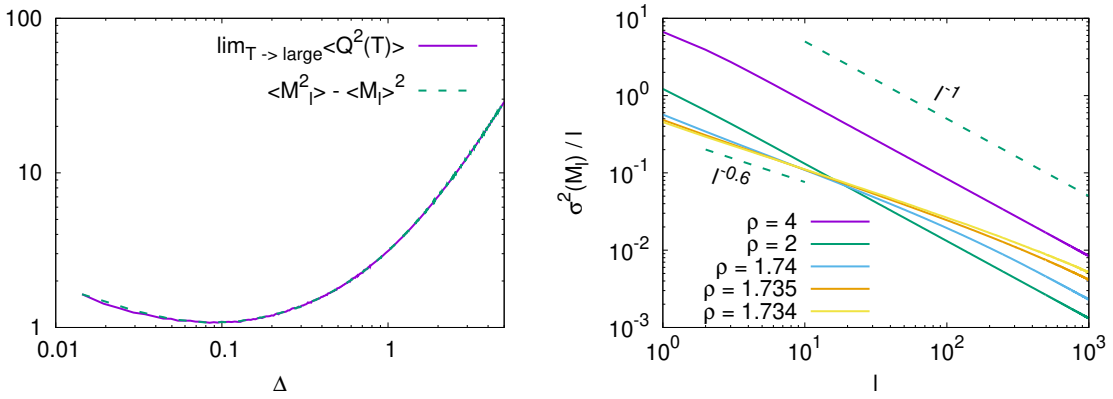

Figure 5.6: *Left panel:* Comparison of bond current fluctuation $\langle \mathcal{Q}^2(T) \rangle$ for $T \gg 1$ and $\sigma^2_{M_l}(\bar{\rho})$ is plotted as a function of relative density $\Delta = \bar{\rho} - \rho_c$. Simulation data for current fluctuation is shown in a solid violet line for $L = 1000$. Corresponding simulation data for $\sigma^2(M_l)$ is shown in a dashed green line for $L = 1000$ and $l = 500$, which shows excellent agreement with the bond current fluctuation, confirming our theoretical prediction of Eq. (5.79). *Right panel:* Scaled mass fluctuation, $\sigma^2_{M_l}(\bar{\rho})/l$, as a function of subsystem size, l, is plotted. Simulation data for $\bar{\rho} = 4$ (violet line), 2 (green line), and 1.74 (blue line) are shown for $L = 5000$, whereas $\bar{\rho} = 1.735$ (orange line) and 1.734 (red line) are plotted for $L = 10000$. Away from criticality, it indicates l^{-1} decay of the scaled fluctuation of maximal hyperuniformity as given in Eq. (5.78). Near criticality, the decay becomes much slower, approximately $l^{-0.6}$, as obtained from simulations, indicating hyperuniform fluctuations.

To check our results with simulation, we computed the power spectrum of temporal correlation of subsystem mass by taking the Fourier transform of $C^{M_l M_l}(t)$, which can be written as

$$S_{M_l}(f) = \lim_{T\to\infty} \int_{-T}^{T} \mathrm{d}t\, C^{M_l M_l}(t) e^{2\pi i f t} = \frac{1}{L}\frac{a}{2D} \sum_q \frac{2\lambda_q D(\bar{\rho})}{\lambda_q^2 D(\bar{\rho})^2 + 4\pi^2 f^2} \lambda_{lq}. \tag{5.80}$$

Similarly, like the current power spectrum, this expression can also be written as an integral for the large system size limit $L \gg 1$ by taking the continuum limit $i \to x = i/L$. In the limit of the size of the large subsystem $l \gg 1$ and $l/L \ll 1$, we can also approximate $\lambda_{lq} \simeq 2$. Furthermore, using the variable transformation, $x = \sqrt{f} y^{1/4} / \sqrt{2\pi}\sqrt{D}$, the mass power spectrum is given by,

$$S_{M_l}(f) \simeq \frac{2a}{D} \frac{1}{4\sqrt{2}\pi^{3/2}\sqrt{D}\sqrt{f}} \int_0^\infty \frac{dy}{y^{1/4}(1+y)} = \frac{a}{2\sqrt{\pi}D^{3/2}} f^{-1/2}. \tag{5.81}$$

But due to the transition from maximal hyperuniformity to hyperuniformity as we approach $\bar{\rho} \to \rho_c$, the frequency dependence of $S_{M_l}(f) \sim f^{-\psi_M}$ changes as follows,

$$\psi_M \begin{cases} = \frac{1}{2} & for \;\; \bar{\rho} \gg \rho_c, \\ \approx \frac{4}{3} & for \;\; \bar{\rho} \simeq \rho_c. \end{cases} \tag{5.82}$$

We obtain $\psi_M \simeq 4/3$ from simulation near criticality, which is still slower than the $\psi_M = 3/2$ observed in normal diffusive systems. Away from criticality, $\psi_M = 1/2 \ll 3/2$, demonstrating a very slow relaxation of the power spectrum and indicating a prolonged temporal correlation in the mass of the subsystem. The slower the decay, the more pronounced the growth of hyperuniformity. Furthermore, the exponents $\psi_{\mathcal{J}}$ and ψ_M that govern the behaviour of the power spectrum of current and mass satisfy the relation $\psi_M = 2 - \psi_{\mathcal{J}}$, as reported in Eq. (2.111) in Chapter 2. This relationship holds both away from and near criticality, resulting from the large-scale diffusive dynamics of the model.

In the *left panel* of Fig. (5.7), we plot the mass power spectrum obtained for the subsystem size $l = 500$ and the system size $L = 1000$ as a function of the frequency f, represented by solid lines, for density values away from the criticality: $\bar{\rho} = 2$ (red), 3 (blue), and 4 (green). The corresponding theoretical curves, obtained using Eq. (5.80), are plotted for densities $\bar{\rho} = 2$ (dot-dot-dashed line), $\bar{\rho} = 3$ (dot-dashed line), and $\bar{\rho} = 4$ (dotted line). In the higher density limit, our analytical result nicely captures the simulation data and the decay of the mass power spectrum follows $f^{-1/2}$ in accordance with our analytical prediction given in Eq. (5.81).

In the *right panel*, we present similar data, but for the size of the subsystem $l = 2500$ and the size of the system $L = 5000$, plotted for the near-critical density values of $\bar{\rho} = 1.7344$ (green line), 1.736 (blue line), and 1.738 (red line). We observe that, near criticality, the exponent ψ_M changes from $1/2$ to $4/3$ in the low-frequency regime, indicating the transition from the hyperuniform to maximal hyperuniform state away from criticality.

5.3 SUMMARY AND CONCLUSIONS

In this chapter, we study the dynamical properties of the Oslo model, which has two conserved quantities: center-of-mass conservation and density conservation. This additional conservation law drastically changes the dynamic properties of the system both in the near- and away-criticality regimes compared to the other three models studied in Chapters 2, 3 and 4, which have only one conserved quantity. The main results of this chapter are as follows.

(I) *Saturation of fluctuations in the time-integrated bond current*

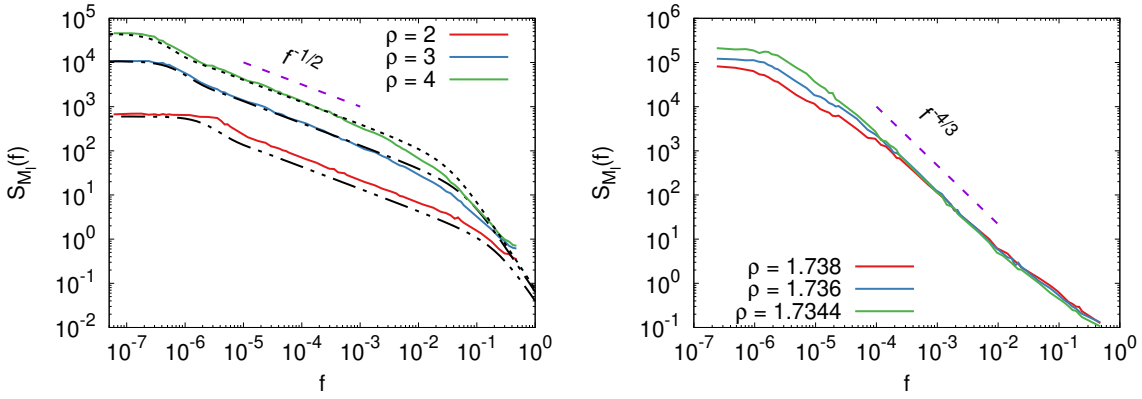

Figure 5.7: The power spectrum of the subsystem mass is plotted against frequency. *Left panel:* Simulation data of the power spectrum for subsystem size $l = 500$ and system size $L = 1000$ are plotted for density values away from criticality, namely $\bar{\rho} = 2$ (red), 3 (blue), and 4 (green) as solid lines. The corresponding theoretical lines, obtained using Eq. (5.80), are plotted for densities $\bar{\rho} = 2$ (dot-dot-dashed line), $\bar{\rho} = 3$ (dot-dashed line), and $\bar{\rho} = 4$ (dotted line), confirming that away from criticality, the mass power spectrum decays as $f^{-1/2}$ at low frequency in accordance with our analytical prediction given in Eq. (5.81). *Right panel:* The same data, obtained from simulation for system size $L = 5000$ and subsystem size $l = 2500$, are plotted for near-critical density values $\bar{\rho} = 1.7344$ (green line), 1.736 (blue line) and 1.738 (red line). As the density approaches the critical value, the decay of the power spectrum tends to a power law of $f^{-4/3}$ in the low frequency regime, as shown by the guiding line indicating the hyperuniformity of the system.

We calculated the fluctuations of the time-integrated bond current, $\langle \mathcal{Q}^2(T) \rangle$, which away from the criticality saturates to the value a/D ($D = a'$ is the bulk diffusivity) as $T \to \infty$ followed by $L \to \infty$. Interestingly, the speed of saturation to this value is so fast that we find a power law behaviour when we plot the relative fluctuation of $\langle \mathcal{Q}^2(T) \rangle$ with respect to its saturation value, that is, $\lim_{T\to\infty} \lim_{L\to\infty} \langle \mathcal{Q}^2(T) \rangle - \langle \mathcal{Q}^2(T) \rangle$, which decays as $T^{-1/2}$, in agreement with our theory.

Near criticality, the fluctuation property undergoes significant changes. The fluctuation $\lim_{T\to\infty} \lim_{L\to\infty} \langle \mathcal{Q}^2(T) \rangle$ saturates at a certain value and this value gradually increases as we approach critical densities, indicating a non-monotonic behaviour of $\langle \mathcal{Q}^2(T) \rangle$ in the limit $T \to \infty$, $L \to \infty$. Near criticality, in the early time regime $T \ll L^z$, the current fluctuation increases as $\langle \mathcal{Q}^2(T) \rangle \sim T^{\alpha}$ with $\alpha \approx 1/3$.

(II) *Power spectrum of current and maximal dynamic hyperuniformity*

We calculated the corresponding power spectrum of the instantaneous current, unlike the previous models, where the power spectrum decays as $f^{\psi_{\mathcal{J}}}$ with $\psi_{\mathcal{J}} = 1/2$ as the frequency approaches *zero* away from the criticality, in this case the Oslo model demonstrates $\psi_{\mathcal{J}} = 3/2$ away from the criticality. This indicates that the correlation of the current is negative for $t > 0$ and decays as $-t^{-5/2}$, which is much faster compared to previous models, where the correlation decays relatively slowly as $-t^{-3/2}$

for away from criticality densities. As a result, there is extensive suppression of current fluctuation in the Oslo model, leading to what we identify as maximal dynamic hyperuniformity away from criticality.

Near criticality, the power spectrum is governed by $\psi_{\mathcal{J}} \approx 2/3$, indicating that the suppression of fluctuation is less pronounced compared to the similar phenomenon in the regime of far from critical density. However, the suppression of current fluctuations is still faster than in a purely diffusive system. Therefore, we categorize this behaviour as dynamic hyperuniformity.

(III) *Subsystem mass fluctuation and a new fluctuation relation*

We find that the static fluctuation of the mass of the subsystem $\langle M_l^2 \rangle - \langle M_l \rangle^2$ is intensive, similar to the saturation value of the integrated current, $\lim_{T\to\infty} \lim_{L\to\infty} \langle \mathcal{Q}^2(T) \rangle$. In fact, both quantities are the same in the limit $L \to \infty$ and $l \to \infty$, where $l/L \ll 1$, i.e., $\langle M_l^2 \rangle - \langle M_l \rangle^2 = \lim_{T\to\infty} \lim_{L\to\infty} \langle \mathcal{Q}^2(T) \rangle$. This is a new fluctuation relation, that connects the static fluctuation of mass and dynamic fluctuation of current.

To study the corresponding dynamic correlation of mass, we calculated the power spectrum near and away from the critical regimes. Our theory captures the decay $f^{-\psi_M}$ of the power spectrum away from criticality with $\psi_M = 1/2$, which is in good agreement with the simulations. Near criticality, we obtain $\psi_M \approx 4/3$ from the simulation, indicating a faster decay of the correlation of the mass of the subsystem in time and the transition from maximal dynamic hyperuniformity, when $\bar{\rho} \gg \rho_c$, to hyperuniformity, when $\bar{\rho} \simeq \rho_c$. The exponents $\psi_{\mathcal{J}}$ and ψ_M satisfy the relation $\psi_M = 2 - \psi_{\mathcal{J}}$ both in the near- and away-critical density regimes.

(IV) *Self diffusion coefficient of a tagged particle*

We calculated the self-diffusion coefficient $\mathcal{D}_s$, which has the same expression as in the Manna sandpile model studied in Chap. 2, given by $a(\bar{\rho})/\bar{\rho}$. We verified this result with simulations, and it shows excellent agreement with the simulated data.

6

SUMMARY OF THE THESIS

In this thesis, we conducted a comprehensive investigation of dynamical fluctuations in four variants of one-dimensional "fixed-energy / conserved" stochastic sandpile models with periodic boundary conditions. These models include the Manna sandpile, Manna sandpile with single particle toppling, activated random walk, and Oslo ricepile model. Earlier, it was assumed that all these stochastic sandpile models belonged to the same universality class based on their conserved quantities and dynamics. However, our study revealed distinct fluctuation properties in these models, which are determined by their microscopic rules. Despite this, all the models exhibit a diffusive hydrodynamic behaviour, at least away from criticality.

Now, let's summarize our findings for both types of models with single and double conserved quantities as follows:

- *Dynamic correlations and their power spectrums: emergence of dynamic hyperuniformity*

  In our study of all models, we calculated the dynamic correlations of time-integrated bond current and mass, as well as the corresponding power spectra, which are simply the Fourier transform of the temporal correlation functions. In the thermodynamic limit, $L \to \infty$, the asymptotic behaviour of the time-integrated bond current fluctuation $\langle \mathcal{Q}^2(T) \rangle$ is T^{α}, correspondingly the power spectrum of current $S_{\mathcal{J}}(f)$ and subsystem mass $S_M(f)$ are written as $f^{\psi_{\mathcal{J}}}$ and $f^{-\psi_M}$, respectively. All three exponents, α, $\psi_{\mathcal{J}}$, and ψ_M, are related by $\alpha = 1 - \psi_{\mathcal{J}}$ and $\psi_{\mathcal{J}} = 2 - \psi_M$, characterizing the fluctuation relation both near and away from criticality. The "normal" behaviour of this asymptotics can be straightforwardly found in the Manna model with one particle transfer rule.

  - *The Manna model with one particle transfer.*

    Due to the particular dynamics, this model does not violate the detailed balance condition and hence satisfies time-reversal symmetry, leading to the absence of any anomalous fluctuations both near and far from criticality. The steady state measure is known for this model, allowing for the exact calculation of the critical density, which is $\rho_c = 1$.

In the thermodynamic limit, our calculations yield the dynamic exponents $\alpha = 1/2$, $\psi_{\mathcal{J}} = 1/2$, and $\psi_M = 3/2$, capturing the growth of time-integrated current fluctuation, frequency dependence of the power spectrum of current and mass, respectively. This set of critical exponent values serves as a benchmark for normal diffusive fluctuation, against which we compare the fluctuation in other models.

Notably, the power spectrum of current goes to *zero* as the frequency $f \to 0$, meaning that the instantaneous current correlation has only positive correlation at $t = 0$. For $t > 0$, the correlation becomes negative and decays as $t^{-3/2}$, resulting in subdiffusive growth of the time-integrated current.

– *The Manna model with two particle transfer.*

In the famous Manna model, two particles are transferred to the nearest neighbours, leading to the violation of the detailed balance condition. As a result, the steady state measure is not known for this model. The breaking of time-reversal symmetry gives rise to anomalous fluctuations, making the system more interesting.

The dynamical exponents governing the fluctuation properties are calculated as $\alpha = 1/2 - \mu$, $\psi_{\mathcal{J}} = 1/2 + \mu$, and $\psi_M = 3/2 - \mu$, where μ represents the anomalous fluctuation near criticality. We derive $\mu = (\beta + 1)/2\nu_\perp z$, where β, $\nu_\perp$, and z are the order parameter, correlation length, and dynamical exponents, respectively. Near criticality, we find $\mu \approx 0.24$, while away from criticality, fluctuations behave similarly to normal diffusive systems, with $\mu = 0$.

Since $\mu > 0$ near criticality, we observe that cumulative bond current fluctuations grow much more slowly as T^α over time T, where $\alpha = 1/2 - \mu$. This decay of fluctuation is identified as dynamic hyperuniformity, a phenomenon similar to the spatial hyperuniformity extensively studied by Torquato *et al.* Furthermore, the emergence of dynamic hyperuniformity implies that the current power spectrum decays more steeply as $f \to 0$, while the decay of the mass power spectrum becomes slower.

– *Model of activated random walkers.*

Firstly, it's worth noting that although the large-scale behavior of the model is diffusive, the dynamics are not solely governed by the active site density anymore. Instead, the density of active particles, which enters the diffusion equation, plays a crucial role. Thus, making the hydrodynamic structure of the model becomes different from what was observed in the previous cases. Moreover, the model violates detailed balance, leading to the generation of anomalous fluctuations near criticality.

The dynamical exponents that govern the fluctuation properties are still calculated as $\alpha = 1/2 - \mu$, $\psi_{\mathcal{J}} = 1/2 + \mu$, and $\psi_M = 3/2 - \mu$, the expression of μ remains the same, $\mu = (\beta + 1)/2\nu_\perp z$ remains the same. Since the hydrodynamics is now governed by the density of active particles, the critical exponents should also be characterized by the critical behaviour of the same quantity. Unfortunately, the values of these critical exponents could not be found in the literature, so we had to obtain $\mu \approx 0.1$ from simulations. This value is quite different from what has been obtained for the Manna model with two-particle transfer.

Overall, these observations highlight the distinct nature of the fluctuation properties in this model compared to previous ones, emphasizing the importance of microscopic rules and hydrodynamic structures in determining the behaviour of fluctuations near criticality.

– *The Oslo model.*

Let's now discuss the *Oslo model*, which exhibits quite different fluctuations compared to the Manna and ARW models due to the presence of an extra conserved quantity, despite following the same hydrodynamic equation as the Manna model with two-particle transfer. When we calculated the behaviour of dynamical fluctuations in the Oslo model *away from criticality*, we find that $\psi_{\mathcal{J}} = 3/2$, indicating a decay of instantaneous current correlations (which are negative) as $t^{-5/2}$ when $t > 0$. Consequently, the power spectrum exponent mass is obtained as $\psi_M = 1/2$, and this result agrees well with our simulation data. Furthermore, because of momentum conservation, unlike the models with single conserved quantity, the current fluctuation does not grow for an infinite time, instead, after initial growth of the fluctuation, $\langle \mathcal{Q}^2(T) \rangle$ becomes a plateau at a value of a/D. Actually, we calculated the relative decay of current fluctuation w.r.t. a/D, which is given by $a/D - \langle \mathcal{Q}^2(T) \rangle \sim T^{-1/2}$.

However, our theoretical approach fails to capture the anomalous behaviour of current and mass fluctuations near criticality. From simulations, we found that $\psi_{\mathcal{J}} \approx 2/3$, implying that the decay of instantaneous current correlation becomes slower as $t^{-5/3}$ compared to the decay away from criticality. As a result, the time-integrated bond current fluctuation is suppressed, and we obtain $\langle \mathcal{Q}^2(T) \rangle \sim T^{\alpha}$ with $\alpha \approx 1/3$, which is still less than the $\alpha = 1/2$ observed in the diffusive case.

To characterize the hyperuniformity in this model, we particularly use the exponent $\psi_{\mathcal{J}}$. Near criticality, $\psi_{\mathcal{J}} \approx 2/3 > 1/2$, and thus identify the fluctuations are dynamically hyperuniform. On the other hand, away from criticality, $\psi_{\mathcal{J}} = 3/2 \gg 1/2$, indicating a strong suppression of dynamic fluctuations. In this regime, we identify the state as a maximal dynamic hyperuniform state. Thus, in

the Oslo model, dynamic fluctuations behave completely opposite to what we observed in the previous model, where fluctuations away from criticality were more pronounced than those near criticality. Here, it is the opposite, with fluctuations being more prominent near criticality.

- *Derivation of the fluctuation relations in nonequilibrium steady states.*

  In the nonequilibrium Manna model (Eq. (2.98)) and in ARW (Eq. (4.72)) with a single conserved quantity, we have derived that the scaled subsystem mass fluctuation equals the intensive spacetime-integrated current fluctuation in the infinite volume limit, divided by twice the bulk diffusivity. This relation can similarly be written in terms of $\langle \mathcal{Q}^2(T) \rangle$ as

$$\lim_{T\to\infty} \lim_{L\to\infty} \frac{L}{2T} \langle \mathcal{Q}^2(T) \rangle = D(\rho) \lim_{L\to\infty} \lim_{l\to\infty} \frac{\sigma^2_{M_l}(\rho)}{l}, \tag{6.1}$$

  where $\sigma^2_{M_l}(\rho)$ is the steady state fluctuation of mass of a subsystem size l for global density $\bar{\rho}$. On the other hand, due to the maximal hyperuniformity in the Oslo model, we obtained in Eq. (5.79) that

$$\lim_{T\to\infty} \lim_{L\to\infty} \langle \mathcal{Q}^2(T) \rangle = \lim_{l\to\infty} \lim_{L\to\infty} \sigma^2_{M_l}(\bar{\rho}), \tag{6.2}$$

- *Transport of a tagged particle, self-diffusion coefficient.*

  The diffusive transport of a tagged particle is the most unifying feature in all of these sandpile models, which is equal to the activity divided by the global density, upto some model dependent parameters, and goes to *zero* as the system approaches criticality. Furthermore, in the Manna-type models, we also proved that self-diffusivity can be obtained from current fluctuation also.

- *Mobility and driven hydrodynamics.*

  In the introduction of this thesis, we mentioned the derivation of mobility, defined as the gradient of $\langle \mathcal{Q}^2(T) \rangle$ for $T \gg L^2$, where L is large but finite. Using the theoretical methods developed in this thesis, we were able to calculate $\langle \mathcal{Q}^2(T) \rangle$ in the limit of large T. As a result, we performed a formal theoretical derivation of mobility and also equated it with the intensive fluctuation of spacetime integrated current. This allowed us to derive a Green-Kubo type formula for nonequilibrium systems.

  In the case of the Oslo model, we found that $\langle \mathcal{Q}^2(T) \rangle$ becomes flat when $T \gg L^2$, leading to a mobility of *zero*. This result was expected in the Oslo model due to the conservation of the centre of mass.

Furthermore, for stochastic models with a single conserved quantity, we used the prescription of macroscopic fluctuation theory to show that the expression of mobility, which appeared as the transport coefficient in the drift current, is the same as the one we computed from the current fluctuation in the periodic boundary setting. This provided verification of the nonequilibrium Green-Kubo type relation that was proved in this thesis.

- *Existence of three scaling functions, capturing the dynamic fluctuations and power spectrums away from criticality.*

  The away from criticality behaviour of the sandpiles exhibits diffusive dynamics, and we have shown that the fluctuations properties can be described using two transport coefficients, bulk diffusivity D and mobility χ, along with the size of the system L. By rescaling the time-integrated current fluctuation as $D\left\langle \mathcal{Q}^2(T)\right\rangle /2\chi L$, we found that it can be written in terms of a system-independent scaling function $\mathcal{G}(DT/L^2)$, as given in Eq. (3.65). In the thermodynamic limit $L \to \infty$, this scaling function exhibits an asymptotic behaviour of $\mathcal{G}(y) \sim y^{1/2}$.

  Similarly, rescaling the current power spectrum as $LS_{\mathcal{J}}(f)/2\chi$ allows us to write it as a universal scaling function $\mathcal{S}(fL^2/D)$, as given in Eq. (3.78). Likewise, rescaling the power spectrum of the subsystem mass as $D^2S(M_l)(f)/2\chi L^3$ allows us to write it as a scaling function of $\mathcal{K}_M(fL^2/D)$, as given in Eq. (3.109), where fL^2/D is the scaling variable in the last two cases.

  In Chapter 3, where no anomalous fluctuations occur, these three scaling functions capture the scaled collapses of $\left\langle \mathcal{Q}^2(T)\right\rangle$, $S_{\mathcal{J}}(f)$, and $S_{M_l}(f)$, as defined here. In the case of ARW in Chapter 4, we utilized these scaling functions to plot the scaled $\left\langle \mathcal{Q}^2(T)\right\rangle$ in Fig. 4.3, scaled $S_{\mathcal{J}}(f)$ in Fig. 4.4, and scaled $S_{M_l}(f)$ in Fig. 4.7 as functions of their respective scaling variables. We observed that these scaling functions indeed capture the corresponding fluctuations and power spectra away from the criticality. However, near criticality, the deviation from the scaled collapse indicates the emergence of dynamic hyperuniformity, rendering the scaling functions invalid in this regime.

We also compactly present the results in the following table format.

6.1 FINAL CONCLUSION

Characterization of universality classes for nonequilibrium active-absorbing phase transitions in sandpile models has been a subject of debate for a long time [129–131]. It is generally believed that due to the presence of an additional conservation law (density) in the

Observables	*The Manna model* - 1	*The Manna model* - 2	*ARW*	*Oslo*
Bulk diffusivity: D	$a'(\bar{\rho})$	$\frac{a'(\bar{\rho})}{2}$	$\frac{u'(\bar{\rho})}{2(1+\lambda)}$	$a'(\bar{\rho})$
Mobility: χ	$a(\bar{\rho})$	$\frac{a(\bar{\rho})}{2}$	$\frac{u(\bar{\rho})}{2(1+\lambda)}$	0
Self diffusivity: $\mathcal{D}_s$	$\frac{a(\bar{\rho})}{\bar{\rho}}$	$\frac{a(\bar{\rho})}{2\bar{\rho}}$	$\frac{u(\rho)}{2(1+\lambda)\bar{\rho}}$	$\frac{a(\bar{\rho})}{\bar{\rho}}$
$\langle \mathcal{Q}^2(T) \rangle \sim T^{\alpha}$ $\alpha = \frac{1}{2} - \mu$	$\mu = 0, \bar{\rho} \gg \rho_c$ $\mu \approx 0.24, \bar{\rho} \simeq \rho_c$	$\mu = 0$	$\mu = 0, \bar{\rho} \gg \rho_c$ $\mu \approx 0.1, \bar{\rho} \simeq \rho_c$	$a/D - \langle \mathcal{Q}^2(T) \rangle$ $\sim T^{-1/2}, \bar{\rho} \gg \rho_c$ $\alpha \approx \frac{1}{3}, \bar{\rho} \simeq \rho_c$
$S_{\mathcal{J}}(f) \sim f^{\psi_{\mathcal{J}}}$ $\psi_{\mathcal{J}} = \frac{1}{2} + \mu$	$\psi_{\mathcal{J}} = \frac{1}{2}, \bar{\rho} \gg \rho_c$ $\psi_{\mathcal{J}} \approx 0.74, \bar{\rho} \simeq \rho_c$	$\psi_{\mathcal{J}} = \frac{1}{2}$	$\psi_{\mathcal{J}} = \frac{1}{2}, \bar{\rho} \gg \rho_c$ $\psi_{\mathcal{J}} \approx 0.6, \bar{\rho} \simeq \rho_c$	$\psi_{\mathcal{J}} = \frac{3}{2}, \bar{\rho} \gg \rho_c$ $\psi_{\mathcal{J}} \approx \frac{2}{3}, \bar{\rho} \simeq \rho_c$
$S_M(f) \sim f^{-\psi_M}$ $\psi_M = \frac{3}{2} - \mu$	$\psi_M = \frac{3}{2}, \bar{\rho} \gg \rho_c$ $\psi_M \approx 1.26, \bar{\rho} \simeq \rho_c$	$\psi_M = \frac{3}{2}$	$\psi_M = \frac{3}{2}, \bar{\rho} \gg \rho_c$ $\psi_M \approx 1.4, \bar{\rho} \simeq \rho_c$	$\psi_M = \frac{1}{2}, \bar{\rho} \gg \rho_c$ $\psi_M \approx \frac{4}{3}, \bar{\rho} \simeq \rho_c$

Table 6.1: List of critical exponents related to dynamical fluctuations for different models that we studied in this thesis. In particular, Manna model - 1 refers to the Manna model with two particle transfer, whereas Manna model - 2 refers to the Manna model with one particle transfer.

sandpile models, the critical behaviour is different from directed percolation (DP); although there are counterclaims that the Manna sandpile belongs to the DP [130]. Indeed, initially stochastic sandpile models with isotropic particle transfer were hypothesized to belong to the conserved directed percolation (C-DP) or the "Manna universality class", irrespective of the details of their microscopic dynamics. Since most studies rely heavily on simulations, differences in critical behaviour are mainly attributed to system size limitations; on the other hand, the field-theoretic descriptions were not rigorously derived and phenomenological; therefore, they cannot really be expected to capture the subtlety involved with the minute variations of dynamical details [129, 131]. In these scenarios, our studies of dynamic fluctuations near criticality in stochastic sandpile models suggest that there may not be a single universality class for stochastic isotropic sandpiles, and microscopic details are important. We found that even though the Manna sandpile (with two-particle transfer) and the Oslo sandpile model satisfy the same hydrodynamic equation, their dynamic fluctuations are actually diverse. For example, near criticality, the current fluctuations in the Oslo model, which in fact possesses two conserved quantities, increase compared to that away from criticality, while in the Manna model, the fluctuation decays compared to that away from criticality. As can be seen in Table 6.1, the dynamic exponents are also quite different for the Manna and Oslo sandpiles. The difference in exponents cannot be simply accounted for by the number of conserved quantities present in the model if one considers the following. The ARW model, which is an Abelian variant of the Manna model, has a different hydrodynamic structure from the Manna sandpile, and the dynamical exponent μ through which all dynamic fluctuations can be characterized has a value of $\mu \approx 0.24$ for the Manna model and $\mu \approx 0.1$ for the ARW model. Thus, the change in microscopic dynamics can indeed induce a change in

the properties of critical dynamic fluctuation. Indeed, our studies have strong evidence that there might not be a single universality class even for the stochastic (isotropic) sandpiles. The exact fluctuation properties depend not only on how many conserved quantities are present in the model but also on the microscopic details of the dynamics.

Moreover, although the Manna, ARW, and Oslo models violate detailed balance (even in the periodic boundary case), they are shown, albeit within our truncation scheme, to possess equilibrium-like fluctuation response relations. With the derivation of the two most important transport coefficients, bulk diffusivity (D) and mobility (χ), one could enquire about the possibility of dynamic phase transitions in the open boundary limit, by using a rigorous fluctuating hydrodynamic formalism such as the macroscopic fluctuation theory (MFT). Alternatively, one can explore the calculation of current fluctuations in the driven dissipative case, which could potentially be solved using the techniques developed in this thesis.

7

APPENDIX

A

THE MANNA SANDPILE

A.1 SOME ALGEBRAIC IDENTITIES AND SPECIAL INTEGRALS

We can deduce several algebric properties of λ_n, which are the following,

$$\sum_{n=1}^{L-1} \frac{\lambda_{nl}}{\lambda_n^2} = \frac{1}{12} l(l-L)\left(l^2 - lL - 2\right); \tag{A.1}$$

$$\sum_{n=1}^{L-1} \frac{1}{\lambda_n} = \frac{L^2-1}{12}; \tag{A.2}$$

$$\sum_{n=1}^{L-1} \frac{\lambda_{nr}}{\lambda_n} = r(L-r); \tag{A.3}$$

$$\sum_{r=1}^{l-1} 2(l-r)(2-\lambda_{rn}) = 2\left(\frac{\lambda_{ln} - l\lambda_n}{\lambda_n}\right). \tag{A.4}$$

$$\sum_{n=1}^{L-1} \lambda_{nl} = 2L, \text{ for } l = 1, 2, \ldots. \tag{A.5}$$

Eq.(A.2) is a special case of eq.(A.1) for $l = 1$.

The integrals appeared in the context of asymptotic analysis, i.e., in eq.(2.79) and later in eq.(A.31) have very generic solutions in terms of hypergeometric functions. Generically, we can write those integrals in the following form,

$$I(y) = \int_0^y \mathrm{d}z \, \frac{z^{-k}}{1+z} = \frac{y^{1-k}\, {}_2F_1(1, 1-k; 2-k; -y)}{1-k}, \tag{A.6}$$

where ${}_2F_1$ is the hypergeometric function [132], defined as

$$ {}_2F_1(a,b;c;z) = \frac{\Gamma(c)}{\Gamma(b)\Gamma(c-b)} \int_0^1 \mathrm{d}t\, t^{b-1}(1-t)^{c-b-1}(1-tz)^{-a}. \tag{A.7} $$

In the limit of $y \to \infty$, we have,

$$ \lim_{y\to\infty} I(y) = \sqrt{2}\pi \;\text{ for }\; k = \frac{1}{4}, \frac{3}{4}. \tag{A.8} $$

We have used the above result in eqs. (2.79), (A.31) to obtain the asymptotic for of the power spectrum of current and subsystem mass respectively.

A.2 ASYMPTOTIC ANALYSIS

In this section, we provide the calculation details of the results eq.(2.49), (2.55), (2.57), (2.70), (2.104), presented in the main text.

A.2.1 *Time-integrated bond current fluctuation*

We now derive the asymptotic approximation of the time-integrated bond current correlation using eq.(2.49). We can write the unequal-time time-integrated bond current correlation as

$$ \begin{aligned} C_0^{\mathcal{Q}\mathcal{Q}}(t,t') =& \frac{2a(\bar{\rho})}{L}t' + 2a(\bar{\rho})a'(\bar{\rho})\frac{1}{L}\sum_q \frac{1-e^{-\lambda_q a'(\bar{\rho})t'}}{\lambda_q^2 a'^2}\lambda_q\left(1+\frac{\lambda_q}{4}\right) - \\ & a(\bar{\rho})a'(\bar{\rho})\frac{1}{L}\sum_q \frac{1-e^{-\lambda_q a'(\bar{\rho})t'}+e^{-\lambda_q a'(\bar{\rho})t}-e^{-\lambda_q a'(\bar{\rho})(t-t')}}{\lambda_q^2 a'^2}\lambda_q\left(1+\frac{\lambda_q}{4}\right) \end{aligned} \tag{A.9} $$

In the infinite system size limit $L \to \infty$, we write the above sum in the following integral form,

$$ \begin{aligned} C_0^{\mathcal{Q}\mathcal{Q}}(t,t') \simeq& 4a'(\bar{\rho})a(\bar{\rho}) \int_0^{1/2} \mathrm{d}x\, \frac{1-e^{-\lambda(x)a'(\bar{\rho})t'}}{\lambda(x)^2 a'(\bar{\rho})^2}\lambda(x)\left(1+\frac{\lambda(x)}{4}\right) \\ & - 2a'(\bar{\rho})a(\bar{\rho}) \int_0^{1/2} \mathrm{d}x\, \frac{1-e^{-\lambda(x)a'(\bar{\rho})t'}+e^{-\lambda(x)a'(\bar{\rho})t}-e^{-\lambda(x)a'(\bar{\rho})(t-t')}}{\lambda^2(x)a'^2(\bar{\rho})} \\ & \times \lambda(x)\left(1+\frac{\lambda(x)}{4}\right). \end{aligned} \tag{A.10} $$

Note that the integral in the above equation can be expressed in terms of an integral of the form as given below,

$$a(\bar{\rho})a'(\bar{\rho})\int_0^{1/2} dx\,\frac{1-e^{-\lambda(x)a'(\bar{\rho})t'}}{\lambda^2(x)a'^2(\bar{\rho})}\lambda(x)\left(1+\frac{\lambda(x)}{4}\right)\simeq\frac{a(\bar{\rho})\sqrt{t'}}{2\sqrt{\pi a'(\bar{\rho})}},\tag{A.11}$$

where, for $t\gg 1$, we have defined $x=\left(y/4\pi^2a'(\bar{\rho})t'\right)^{1/2}$ and used $\lambda(x)\simeq 4\pi^2x^2$ and $\int_0^\infty dy\,y^{-3/2}(1-e^{-y})=2\sqrt{\pi}$, to explicitly calculate the integral. Using eq.(A.11) in each of the relevant terms of the rhs in eq.(A.10) and then after some straightforward algebraic manipulations, we obtain the following asymptotic form of the time-dependent integrated bond-current correlation,

$$C_0^{\mathcal{Q}\mathcal{Q}}(t,t')\simeq\frac{a(\bar{\rho})}{\sqrt{\pi a'(\bar{\rho})}}\left(\sqrt{t}+\sqrt{t'}-\sqrt{|t-t'|}\right).\tag{A.12}$$

Now, by putting $t'=t\equiv T$, the above asymptotic leads to the first part (i.e., corresponding to the limit $1\ll T\ll L^2$) of eq.(2.49) in the main text.

A.2.2 *Time-dependent instantaneous current correlation*

The steady state unequal-time correlation of instantaneous bond current $C_0^{\mathcal{J}\mathcal{J}}(t,0)$ $=\langle\mathcal{J}_0(0)\mathcal{J}_r(t)\rangle-\langle\mathcal{J}_0(0)\rangle\langle\mathcal{J}_r(0)\rangle$, for $t\geq 0$, is given by the following expression as derived in main text (see eq.(2.54))

$$C_0^{\mathcal{J}\mathcal{J}}(t,0)=\delta(t)3a(\bar{\rho})-a'(\bar{\rho})a(\bar{\rho})\frac{1}{L}\sum_q e^{-a'(\bar{\rho})\lambda_q t}\lambda_q\left(1+\frac{\lambda_q}{4}\right).\tag{A.13}$$

First, we perform the time integral in a finite time domain $[-T,T]$ as given below,

$$\int_{-T}^{T} C_0^{\mathcal{J}\mathcal{J}}(t,0)\,dt=\Gamma_0(\bar{\rho})-\frac{2a(\bar{\rho})}{L}\sum_q\left(1+\frac{\lambda_q}{4}\right)+2a(\bar{\rho})\left[\frac{1}{L}\sum_q e^{-\lambda_q a'(\bar{\rho})T}\left(1+\frac{\lambda_q}{4}\right)\right],\tag{A.14}$$

which, using the relations eq.(A.5) and $\Gamma_0(\bar{\rho})=3a(\bar{\rho})$ as in the main text in eq.(2.63), we simplify the above sum as

$$\int_{-T}^{T} C_0^{\mathcal{J}\mathcal{J}}(t,0)\,dt=\frac{2a(\bar{\rho})}{L}+2a(\bar{\rho})\left[\frac{1}{L}\sum_q e^{-\lambda_q a'(\bar{\rho})T}\left(1+\frac{\lambda_q}{4}\right)\right].\tag{A.15}$$

Now, first taking the infinite-system size limit, i.e., the limit $L \to \infty$, we can further write the sum as an integral,

$$\lim_{L\to\infty} \int_{-T}^{T} C_0^{\mathcal{J}\mathcal{J}}(t,0)\,\mathrm{d}t = 4a(\bar{\rho}) \int_0^{1/2} \mathrm{d}x\, e^{-\lambda(x)a'(\bar{\rho})T}\left(1+\frac{\lambda(x)}{4}\right), \tag{A.16}$$

where $q = 2\pi x$. Now using $\lambda(x) \simeq 4\pi^2x^2$, $\int_0^\infty \mathrm{d}y\, e^{-y}y^{-1/2} = \sqrt{\pi}$ and a variable transformation $x = y^{1/2}/2\pi\sqrt{a'(\bar{\rho})T}$, we can explicitly calculate the integral as in eq.(A.16) as

$$\lim_{L\to\infty} \int_{-T}^{T} C_0^{\mathcal{J}\mathcal{J}}(t,0)\,\mathrm{d}t \simeq \frac{a(\bar{\rho})}{\pi\sqrt{a'(\bar{\rho})T}} \int_0^\infty \mathrm{d}y\, e^{-y}y^{-1/2} = \frac{a(\bar{\rho})}{\sqrt{\pi a'(\bar{\rho})}} T^{-1/2}, \tag{A.17}$$

which is the result in the main text in eq.(2.55). Finally, by taking the limit $T \to \infty$, we get

$$\int_{-\infty}^{\infty} C_0^{\mathcal{J}\mathcal{J}}(t,0)\,\mathrm{d}t = 0, \tag{A.18}$$

which is the result presented in main text in eq.(2.56).

Similarly, we can find the asymptotic form of $c_0^{\mathcal{J}\mathcal{J}}(t,0)$ presented in main text in eq.(2.57). In the limit $L \to \infty$, the temporal current correlation $c_0^{\mathcal{J}\mathcal{J}}(t,0)$ for $t > 0$ can be written as an integral, as given below

$$c_0^{\mathcal{J}\mathcal{J}}(t,0) \simeq -2a'(\bar{\rho})a(\bar{\rho}) \int_0^{1/2} \mathrm{d}x\, e^{-a'(\bar{\rho})\lambda(x)t}\lambda(x)\left(1+\frac{\lambda(x)}{4}\right). \tag{A.19}$$

Now, again using $\lambda(x) \simeq 4\pi^2x^2$ and a variable transformation $x = y^{1/2}/2\pi\sqrt{a'(\bar{\rho})T}$, we calculate the above integral as

$$c_0^{\mathcal{J}\mathcal{J}}(t,0) \simeq -\frac{a(\bar{\rho})}{\sqrt{4\pi^2a'(\bar{\rho})}} t^{-3/2} \int_0^\infty \mathrm{d}y\, \sqrt{y}e^{-y}, \tag{A.20}$$

where we have ignored the subleading term $\mathcal{O}\left(t^{-5/2}\right)$. Finally, using $\int_0^\infty \mathrm{d}y\, \sqrt{y}e^{-y} = \sqrt{\pi}/2$, we get the result presented in main text in eq.(2.57),

$$c_0^{\mathcal{J}\mathcal{J}}(t,0) \simeq -\frac{a(\bar{\rho})}{4\sqrt{\pi a'(\bar{\rho})}} t^{-3/2}. \tag{A.21}$$

A.2.3 *Spacetime-integrted current fluctuation*

Here we derive the asymptotic dependence of eq.(2.69) on subsystem size l and time T (see eq.(2.70)); first by taking the limit $T \gg 1$ and $l \gg 1$ and then followd by the reverse order of limit $l \gg 1$ and $T \gg 1$. In both cases, we take infinite system size limit $L \to \infty$, therefore $l/L \to 0$ is always satisfy.

A.2.3.1 *Case I: $T \gg 1$, $l \gg 1$*

In this case, we write eq.(2.69) in the following simplified form,

$$\left\langle \bar{Q}^2(l,T) \right\rangle = \frac{2a(\bar{\rho})Tl^2}{L} + 2a(\bar{\rho})a'(\bar{\rho})\frac{1}{L}\sum_q \frac{1-e^{-a'(\bar{\rho})\lambda_q T}}{\lambda_q^2 a'^2}\left(1+\frac{\lambda_q}{4}\right)\lambda_{ql}. \tag{A.22}$$

In the limit $L \to \infty$, the sum in the above equation can be converted in to the following integral,

$$\left\langle \bar{Q}^2(l,T) \right\rangle \simeq 4a(\bar{\rho})a'(\bar{\rho}) \int_0^{1/2} \mathrm{d}x \, \frac{1-e^{-a'(\bar{\rho})\lambda(x)T}}{\lambda^2(x)a'^2}\left(1+\frac{\lambda(x)}{4}\right)\lambda(lx). \tag{A.23}$$

Using the approximation $\lambda(lx) \simeq 4\pi^2 l^2 x^2$ for finite subsystem size l and a variable transformation $x = y^{1/2}/2\pi\sqrt{a'(\bar{\rho})T}$, we get

$$\frac{1}{lT}\left\langle \bar{Q}^2(l,T) \right\rangle \simeq \frac{a(\bar{\rho})}{\pi\sqrt{a'(\bar{\rho})}}\frac{l}{\sqrt{T}} \int_0^{\infty} \mathrm{d}y \, (1-e^{-y})y^{-3/2} = \frac{2a(\bar{\rho})}{\sqrt{\pi a'(\bar{\rho})}}\frac{l}{\sqrt{T}}, \tag{A.24}$$

where we use $\int_0^{\infty} \mathrm{d}y \, (1-e^{-y})y^{-3/2} = 2\sqrt{\pi}$. This result appeared in eq.(2.70) of the main-text.

A.2.3.2 *Case II: $l \gg 1$, $T \gg 1$*

To compute the asymptotic form in this limit, we use the approximation $\lambda(lx) \simeq 2$ to write eq.(2.69) in the following form,

$$\frac{1}{lT}\left\langle \bar{Q}^2(l,T) \right\rangle_c \simeq 2a(\bar{\rho}) + \frac{a(\bar{\rho})}{l} - \frac{8a(\bar{\rho})a'(\bar{\rho})}{lT} \int_0^{1/2} \frac{a'(\bar{\rho})\lambda(x)T - 1 + \exp\left(-\lambda(x)a'(\bar{\rho})T\right)}{\lambda^2(x)a'^2(\bar{\rho})}\left(1+\frac{\lambda(x)}{4}\right). \tag{A.25}$$

Again using the variable transform $x = y^{1/2}/2\pi\sqrt{a'(\bar{\rho})T}$ and $\int_0^\infty \mathrm{d}y\,(y-1+e^{-y})y^{-5/2} = 4\sqrt{\pi}/3$, we get

$$\begin{aligned}\frac{1}{lT}\left\langle \bar{Q}^2(l,T)\right\rangle_c \simeq& 2a(\bar{\rho}) + \frac{a(\bar{\rho})}{l} - \frac{2a(\bar{\rho})a'(\bar{\rho})}{lT}\int_0^\infty \mathrm{d}y\,(y-1+e^{-y})y^{-5/2}\frac{T^{3/2}}{\pi\sqrt{a'(\bar{\rho})}} \\ =& 2a(\bar{\rho}) + \frac{a(\bar{\rho})}{l} - \frac{8a(\bar{\rho})}{3}\sqrt{\frac{a'(\bar{\rho})}{\pi}}\frac{\sqrt{T}}{l},\end{aligned} \tag{A.26}$$

which also appeared in eq.(2.70).

A.2.4 *Temporal-correlation of subsystem mass*

The asymptotic form of subsystem mass temporal correlation $C^{M_lM_l}(t,0)$, appeared in eq.(2.104) is derived here. At $t = 0$, $C^{M_lM_l}(t,0)$ is maximum and after that, it decays as a function of time t. So, in order to extract the temporal dependence of $C^{M_lM_l}(t,0)$, we write eq.(2.102) as

$$C^{M_lM_l}(0,0) - C^{M_lM_l}(t,0) = \frac{1}{L}\sum_q \left(1 - e^{-\lambda_q a'(\bar{\rho})t}\right)\left(1 + \frac{\lambda_q}{4}\right)\frac{\lambda_{lq}}{\lambda_q}, \tag{A.27}$$

which, in the limit $L \to \infty$, $l \gg 1$, can be written as

$$C^{M_lM_l}(0,0) - C^{M_lM_l}(t,0) \simeq 4\int_0^{1/2} \mathrm{d}x\,\frac{a(\bar{\rho})}{a'(\bar{\rho})}\left(1 - e^{-\lambda(x)a't}\right)\left(1 + \frac{\lambda(x)}{4}\right)\frac{1}{\lambda(x)}. \tag{A.28}$$

The above equation can be further simplified using the approximation and exact results of the previous sec. A.2.3.1 and we get

$$C^{M_lM_l}(0,0) - C^{M_lM_l}(t,0) = \frac{a(\bar{\rho})}{\sqrt{a'(\bar{\rho})\pi^2}}t^{\frac{1}{2}}\int_0^\infty \mathrm{d}y\,y^{-\frac{3}{2}}(1 - e^{-y}) = \frac{2a(\bar{\rho})}{\sqrt{\pi a'(\bar{\rho})}}t^{\frac{1}{2}}. \tag{A.29}$$

Thus we derived eq.(2.104) of the main-text.

A.2.5 *Power spectrum of subsystem mass fluctuation*

In order to find the asymptotic form of the power spectrum of subsystem mass fluctuation $S_{M_l}(f)$, in the limit $L \to \infty$ and $l \gg 1$, we write eq.(2.106) as

$$S_{M_l}(f) \simeq \frac{8a(\bar{\rho})}{a'(\bar{\rho})}\int_0^{1/2} \frac{\lambda(x)a'(\bar{\rho})}{\lambda^2(x)a'^2(\bar{\rho}) + 4\pi^2 f^2}\left(1 + \frac{\lambda(x)}{4}\right)\frac{1}{\lambda(x)}. \tag{A.30}$$

Using the variable transform defined in eq.(2.78) and $\lambda(x) = 4\pi^2x^2$, the above equation can be written in the following simplified form,

$$\tilde{S}_{M_l}(f) \simeq \frac{a}{2\pi^2\sqrt{2\pi a'(\bar{\rho})}} f^{-3/2} \times \int_0^\infty \frac{y^{-3/4}}{1+y}\,\mathrm{d}y = \frac{a}{2\sqrt{\pi^3 a'(\bar{\rho})}} f^{-3/2}, \tag{A.31}$$

where, we used eq.(A.8) and ignored the term of $\mathcal{O}\big(f^{1/2}\big)$. Thus we derive eq.(2.106), appeared in the main-text.

A.3 EVOLUTION EQUATIONS OF CORRELATION FUNCTIONS

A.3.1 *Different time current-current correlation*

The stochastic update rules for the different-time and different-space product function of currents $\mathcal{Q}_i(t)\mathcal{Q}_j(t')$, can be written for $t > t'$ as

$$\mathcal{Q}_i(t+\mathrm{d}t)\mathcal{Q}_j(t') = \begin{cases} \textbf{events} & \textbf{probabilities} \\ (\mathcal{Q}_i(t)+1)\mathcal{Q}_j(t') & \frac{1}{2}\hat{a}_i(t)\,\mathrm{d}t \\ (\mathcal{Q}_i(t)+2)\mathcal{Q}_j(t') & \frac{1}{4}\hat{a}_i(t)\,\mathrm{d}t \\ (\mathcal{Q}_i(t)-1)\mathcal{Q}_j(t') & \frac{1}{2}\hat{a}_{i+1}(t)\,\mathrm{d}t \\ (\mathcal{Q}_i(t)-2)\mathcal{Q}_j(t') & \frac{1}{4}\hat{a}_{i+1}(t)\,\mathrm{d}t \\ \mathcal{Q}_i(t)\mathcal{Q}_j(t') & 1-\Sigma\,\mathrm{d}t\,, \end{cases} \tag{A.32}$$

where $\Sigma = 3(\hat{a}_i(t)+\hat{a}_{i+1}(t))/4$. Using these rules, we write the evolution equation of the two point current-current correlation function as

$$\frac{\partial}{\partial t}C_r^{\mathcal{Q}\mathcal{Q}}(t,t') = \big\langle[\hat{a}_0(t)-\hat{a}_1(t)]\mathcal{Q}_r(t')\big\rangle = \Big[C_r^{\hat{a}\mathcal{Q}}(t,t') - C_{r-1}^{\hat{a}\mathcal{Q}}(t,t')\Big], \tag{A.33}$$

which has appeared in eq.(2.22) in the main-text.

A.3.2 *Different time mass-current correlation*

The stochastic update rules for the different-time and different-space product function of mass and current $m_i(t)\mathcal{Q}_j(t')$, can be written for $t > t'$ as

$$m_i(t+\mathrm{d}t)\mathcal{Q}_j(t') = \begin{cases} (m_i(t)+1)\mathcal{Q}_j(t') & \frac{1}{2}\hat{a}_{i+1}(t)dt \\ (m_i(t)+1)\mathcal{Q}_j(t') & \frac{1}{2}\hat{a}_{i-1}(t)dt \\ (m_i(t)+1)\mathcal{Q}_j(t') & \frac{1}{4}\hat{a}_{i+1}(t)dt \\ (m_i(t)+2)\mathcal{Q}_j(t') & \frac{1}{4}\hat{a}_{i-1}(t)dt \\ (m_i(t)-2)\mathcal{Q}_j(t') & \hat{a}_i(t)dt \\ m_i(t)\mathcal{Q}_j(t') & [1-\Sigma dt], \end{cases} \tag{A.34}$$

where $\Sigma = 3(\hat{a}_i(t)+\hat{a}_{i+1}(t))/4 + \hat{a}_i(t)$. Using these rules, we write the evolution equation of the two point mass-current correlation function as

$$\frac{\partial}{\partial t}C_r^{m\mathcal{Q}}(t,t') = \left\langle [\hat{a}_{L-1}(t) - 2\hat{a}_0(t) + \hat{a}_1(t)]\mathcal{Q}_r(t')\right\rangle \simeq a'(\bar{\rho})\sum_k \Delta_{r,k}C_k^{m\mathcal{Q}}(t,t'), \tag{A.35}$$

which has appeared in the eq.(2.29).

A.3.3 *Equal time current-current correlation*

In the Manna sandpile, during each toppling two particles can hop to each neighbouring site independently, and it may simultaneously create current at two neighbouring bonds. In

the following, we write the update equation of the two point product function of integrated current,

$$\mathcal{Q}_i(t+\mathrm{d}t)\mathcal{Q}_j(t+\mathrm{d}t) = \begin{cases} \textbf{\textit{events}} & \textbf{\textit{probabilities}} \\ (\mathcal{Q}_i(t)-1)(\mathcal{Q}_j(t)+1) & \frac{1}{2}\hat{a}_{i+1}\delta_{i+1,j}\,\mathrm{d}t \\ (\mathcal{Q}_i(t)-1)(\mathcal{Q}_j(t)-1) & \frac{1}{2}\hat{a}_{i+1}\delta_{i,j}\,\mathrm{d}t \\ (\mathcal{Q}_i(t)+1)(\mathcal{Q}_j(t)+1) & \frac{1}{2}\hat{a}_{i}\delta_{i,j}\,\mathrm{d}t \\ (\mathcal{Q}_i(t)+1)(\mathcal{Q}_j(t)-1) & \frac{1}{2}\hat{a}_{i}\delta_{i-1,j}\,\mathrm{d}t \\ (\mathcal{Q}_i(t)-1)\mathcal{Q}_j(t) & \frac{1}{2}\hat{a}_{i+1}(1-\delta_{i+1,j}-\delta_{i,j})\,\mathrm{d}t \\ (\mathcal{Q}_i(t)+1)\mathcal{Q}_j(t) & \frac{1}{2}\hat{a}_{i}(1-\delta_{i-1,j}-\delta_{i,j})\,\mathrm{d}t \\ \mathcal{Q}_i(t)(\mathcal{Q}_j(t)-1) & \frac{1}{2}\hat{a}_{j+1}(1-\delta_{i-1,j}-\delta_{i,j})\,\mathrm{d}t \\ \mathcal{Q}_i(t)(\mathcal{Q}_j(t)+1) & \frac{1}{2}\hat{a}_{j}(1-\delta_{i+1,j}-\delta_{i,j})\,\mathrm{d}t \\ (\mathcal{Q}_i(t)+2)(\mathcal{Q}_j(t)+2) & \frac{1}{4}\hat{a}_{i}\delta_{i,j}\,\mathrm{d}t \\ (\mathcal{Q}_i(t)-2)(\mathcal{Q}_j(t)-2) & \frac{1}{4}\hat{a}_{i+1}\delta_{i,j}\,\mathrm{d}t \\ (\mathcal{Q}_i(t)+2)\mathcal{Q}_j(t) & \frac{1}{4}\hat{a}_{i}(1-\delta_{i,j})\,\mathrm{d}t \\ \mathcal{Q}_i(t)(\mathcal{Q}_j(t)+2) & \frac{1}{4}\hat{a}_{j}(1-\delta_{i,j})\,\mathrm{d}t \\ (\mathcal{Q}_i(t)-2)\mathcal{Q}_j(t) & \frac{1}{4}\hat{a}_{i+1}(1-\delta_{i,j})\,\mathrm{d}t \\ \mathcal{Q}_i(t)(\mathcal{Q}_j(t)-2) & \frac{1}{4}\hat{a}_{j+1}(1-\delta_{i,j})\,\mathrm{d}t \\ \mathcal{Q}_i(t)\mathcal{Q}_j(t) & (1-\Sigma\,\mathrm{d}t), \end{cases} \tag{A.36}$$

where $\Sigma\,\mathrm{d}t$ is the probability of happening all the events, mentioned in the update rules in the time-interval t and $t+\mathrm{d}t$. Using this update rules and eq.(2.26), we can write the evolution equation of the equal-time correlation function of current as

$$\begin{aligned} \frac{\mathrm{d}}{\mathrm{d}t}C_r^{\mathcal{Q}\mathcal{Q}}(t,t) =& \Gamma_r(t) + \langle[\hat{a}_0(t)-\hat{a}_1(t)]\mathcal{Q}_r(t)\rangle_c + \langle\mathcal{Q}_0[\hat{a}_r-\hat{a}_{r+1}]\rangle_c \\ \simeq& \Gamma_r(t) + a'\left[c_r^{m\mathcal{Q}}(t,t)-c_{r-1}^{m\mathcal{Q}}(t,t)\right] + a'\left[c_{L-r}^{m\mathcal{Q}}(t,t)-c_{L-r-1}^{m\mathcal{Q}}(t,t)\right]. \end{aligned} \tag{A.37}$$

where,

$$\Gamma_r \equiv \Gamma_{i,j} = \frac{3}{2}\delta_{i,j}\langle\hat{a}_{i+1}+\hat{a}_i\rangle - \frac{1}{2}\delta_{i+1,j}\langle\hat{a}_{i+1}\rangle - \frac{1}{2}\delta_{i-1,j}\langle\hat{a}_i\rangle\,. \tag{A.38}$$

The solution of eq.(A.37) appeared in eq.(2.46) in the main-text.

A.3.4 *Mass and integrated current correlation*

The update rules of the temporal evolution equation of the product function of mass and integrated current, are given as

$$
m_i(t+\mathrm{d}t)\mathcal{Q}_j(t+\mathrm{d}t) = \begin{cases}
\textbf{\textit{events}} & \textbf{\textit{probabilities}} \\
(m_i(t)+1)\big(\mathcal{Q}_j(t)-1\big) & \frac{1}{2}\hat{a}_{i+1}\delta_{i,j}\,\mathrm{d}t \\
(m_i(t)+1)\big(\mathcal{Q}_j(t)+1\big) & \frac{1}{2}\hat{a}_{i+1}\delta_{i+1,j}\,\mathrm{d}t \\
(m_i(t)-2)\big(\mathcal{Q}_j(t)-1\big) & \frac{1}{2}\hat{a}_{i}\delta_{i-1,j}\,\mathrm{d}t \\
(m_i(t)-2)\big(\mathcal{Q}_j(t)+1\big) & \frac{1}{2}\hat{a}_{i}\delta_{i,j}\,\mathrm{d}t \\
(m_i(t)+1)\big(\mathcal{Q}_j(t)-1\big) & \frac{1}{2}\hat{a}_{i-1}\delta_{i-2,j}\,\mathrm{d}t \\
(m_i(t)+1)\big(\mathcal{Q}_j(t)+1\big) & \frac{1}{2}\hat{a}_{i-1}\delta_{i-1,j}\,\mathrm{d}t \\
(m_i(t)-2)\big(\mathcal{Q}_j(t)+2\big) & \frac{1}{4}\hat{a}_{i}\delta_{i,j}\,\mathrm{d}t \\
(m_i(t)+2)\big(\mathcal{Q}_j(t)+2\big) & \frac{1}{4}\hat{a}_{i-1}\delta_{i-1,j}\,\mathrm{d}t \\
(m_i(t)+2)\big(\mathcal{Q}_j(t)-2\big) & \frac{1}{4}\hat{a}_{i+1}\delta_{i,j}\,\mathrm{d}t \\
(m_i(t)-2)\big(\mathcal{Q}_j(t)-2\big) & \frac{1}{4}\hat{a}_{i}\delta_{i-1,j}\,\mathrm{d}t \\
(m_i(t)+1)\mathcal{Q}_j(t) & \frac{1}{2}\hat{a}_{i+1}\big(1-\delta_{i,j}-\delta_{i+1,j}\big)\,\mathrm{d}t \\
(m_i(t)+1)\mathcal{Q}_j(t) & \frac{1}{2}\hat{a}_{i-1}\big(1-\delta_{i-1,j}-\delta_{i-2,j}\big)\,\mathrm{d}t \\
(m_i(t)-2)\mathcal{Q}_j(t) & \frac{1}{2}\hat{a}_{i}\big(1-\delta_{i,j}-\delta_{i-1,j}\big)\,\mathrm{d}t \\
(m_i(t)+2)\mathcal{Q}_j(t) & \frac{1}{4}\hat{a}_{i+1}\big(1-\delta_{i,j}\big)\,\mathrm{d}t \\
(m_i(t)-2)\mathcal{Q}_j(t) & \frac{1}{4}\hat{a}_{i}\big(1-\delta_{i-1,j}\big)\,\mathrm{d}t \\
(m_i(t)-2)\mathcal{Q}_j(t) & \frac{1}{4}\hat{a}_{i}\big(1-\delta_{i,j}\big)\,\mathrm{d}t \\
(m_i(t)+2)\mathcal{Q}_j(t) & \frac{1}{4}\hat{a}_{i-1}\big(1-\delta_{i-1,j}\big)\,\mathrm{d}t \\
m_i(t)\big(\mathcal{Q}_j(t)+1\big) & \frac{1}{2}\hat{a}_{j}\big(1-\delta_{i,j}-\delta_{i,j-1}-\delta_{i,j+1}\big)\,\mathrm{d}t \\
m_i(t)\big(\mathcal{Q}_j(t)-1\big) & \frac{1}{2}\hat{a}_{j+1}\big(1-\delta_{i,j}-\delta_{i,j+1}-\delta_{i,j+2}\big)\,\mathrm{d}t \\
m_i(t)\big(\mathcal{Q}_j(t)+2\big) & \frac{1}{4}\hat{a}_{j}\big(1-\delta_{i,j}-\delta_{i,j+1}\big)\,\mathrm{d}t \\
m_i(t)\big(\mathcal{Q}_j(t)-2\big) & \frac{1}{4}\hat{a}_{j+1}\big(1-\delta_{i,j}-\delta_{i,j+1}\big)\,\mathrm{d}t \\
m_i(t)\mathcal{Q}_j(t) & (1-\Sigma dt),
\end{cases}
\tag{A.39}
$$

where clearly $(1 - \Sigma dt)$ is the probability of happening nothing. Using these rules, we write the evolution equation of the two point mass and integrated current correlation as

$$\frac{\mathrm{d}}{\mathrm{d}t} C_r^{m\mathcal{Q}}(t,t) = f_r(t) + \sum_k \Delta_{r,k} C_k^{\hat{a}\mathcal{Q}}(t,t), \tag{A.40}$$

where $f_r(t)$, the source term of the equal time mass-integrated current correlation, which, in the steady state can be written as

$$f_r(t) = \left[C_r^{m\hat{a}}(t,t) - C_{r+1}^{m\hat{a}}(t,t)\right] + \frac{7a(\bar{\rho})}{2}\delta_{0,r+1} - \frac{7a(\bar{\rho})}{2}\delta_{0,r} + \frac{a(\bar{\rho})}{2}(\delta_{0,r-1} - \delta_{0,r+2}). \tag{A.41}$$

The Fourier transform of eq. (A.40) is used to get eq.(2.35) in the main-text.

A.3.5 *Mass-mass correlation function*

The equal time mass-mass correlation function is important to calculate the mass-activity correlation function and the power spectrum of subsystem mass. The update rules are the following,

$$
m_i(t+\mathrm{d}t)m_j(t+\mathrm{d}t) = \begin{cases}
\textbf{\textit{events}} & \textbf{\textit{probabilities}} \\
\big(m_i(t)+1\big)\big(m_j(t)+1\big) & \frac{1}{2}\hat{a}_{i+1}\delta_{i,j}\,\mathrm{d}t \\
\big(m_i(t)+1\big)\big(m_j(t)-2\big) & \frac{1}{2}\hat{a}_{i+1}\delta_{i+1,j}\,\mathrm{d}t \\
\big(m_i(t)+1\big)\big(m_j(t)+1\big) & \frac{1}{2}\hat{a}_{i+1}\delta_{i+2,j}\,\mathrm{d}t \\
\big(m_i(t)-2\big)\big(m_j(t)+1\big) & \frac{1}{2}\hat{a}_{i}\delta_{i-1,j}\,\mathrm{d}t \\
\big(m_i(t)-2\big)\big(m_j(t)-2\big) & \frac{1}{2}\hat{a}_{i}\delta_{i,j}\,\mathrm{d}t \\
\big(m_i(t)-2\big)\big(m_j(t)+1\big) & \frac{1}{2}\hat{a}_{i}\delta_{i+1,j}\,\mathrm{d}t \\
\big(m_i(t)+1\big)\big(m_j(t)+1\big) & \frac{1}{2}\hat{a}_{i-1}\delta_{i-2,j}\,\mathrm{d}t \\
\big(m_i(t)+1\big)\big(m_j(t)-2\big) & \frac{1}{2}\hat{a}_{i-1}\delta_{i-1,j}\,\mathrm{d}t \\
\big(m_i(t)+1\big)\big(m_j(t)+1\big) & \frac{1}{2}\hat{a}_{i-1}\delta_{i,j}\,\mathrm{d}t \\
\big(m_i(t)+1\big)m_j(t) & \frac{1}{2}\hat{a}_{i+1}\big(1-\delta_{i,j}-\delta_{i+1,j}-\delta_{i+2,j}\big)\,\mathrm{d}t \\
\big(m_i(t)-2\big)m_j(t) & \frac{1}{2}\hat{a}_{i}\big(1-\delta_{i-1,j}-\delta_{i,j}-\delta_{i+1,j}\big)\,\mathrm{d}t \\
\big(m_i(t)+1\big)m_j(t) & \frac{1}{2}\hat{a}_{i-1}\big(1-\delta_{i-2,j}-\delta_{i-1,j}-\delta_{i,j}\big)\,\mathrm{d}t \\
m_i(t)\big(m_j(t)+1\big) & \frac{1}{2}\hat{a}_{j+1}\big(1-\delta_{i,j}-\delta_{i,j+1}-\delta_{i,j+2}\big)\,\mathrm{d}t \\
m_i(t)\big(m_j(t)-2\big) & \frac{1}{2}\hat{a}_{j}\big(1-\delta_{i,j-1}-\delta_{i,j}-\delta_{i,j+1}\big)\,\mathrm{d}t \\
m_i(t)\big(m_j(t)+1\big) & \frac{1}{2}\hat{a}_{j-1}\big(1-\delta_{i,j-2}-\delta_{i,j-1}-\delta_{i,j}\big)\,\mathrm{d}t \\
\big(m_i(t)+2\big)\big(m_j(t)+2\big) & \frac{1}{4}\hat{a}_{i+1}\delta_{i,j}\,\mathrm{d}t \\
\big(m_i(t)+2\big)\big(m_j(t)-2\big) & \frac{1}{4}\hat{a}_{i+1}\delta_{i+1,j}\,\mathrm{d}t \\
\big(m_i(t)-2\big)\big(m_j(t)+2\big) & \frac{1}{4}\hat{a}_{i}\delta_{i-1,j}\,\mathrm{d}t \\
\big(m_i(t)-2\big)\big(m_j(t)-2\big) & \frac{1}{4}\hat{a}_{i}\delta_{i,j}\,\mathrm{d}t \\
\big(m_i(t)+2\big)m_j(t) & \frac{1}{4}\hat{a}_{i+1}\big(1-\delta_{i,j}-\delta_{i+1,j}\big)\,\mathrm{d}t \\
\big(m_i(t)-2\big)m_j(t) & \frac{1}{4}\hat{a}_{i}\big(1-\delta_{i-1,j}-\delta_{i,j}\big)\,\mathrm{d}t \\
m_i(t)\big(m_j(t)+2\big) & \frac{1}{4}\hat{a}_{j+1}\big(1-\delta_{i,j}-\delta_{i,j+1}\big)\,\mathrm{d}t \\
m_i(t)\big(m_j(t)-2\big) & \frac{1}{4}\hat{a}_{j}\big(1-\delta_{i,j-1}-\delta_{i,j}\big)\,\mathrm{d}t\,,
\end{cases}
$$

continued,

$$m_i(t+\mathrm{d}t)m_j(t+\mathrm{d}t) = \begin{cases} \textbf{\textit{events}} & \textbf{\textit{probabilities}} \\ (m_i(t)-2)\big(m_j(t)-2\big) & \frac{1}{4}\hat{a}_i\delta_{i,j}\,\mathrm{d}t \\ (m_i(t)-2)\big(m_j(t)+2\big) & \frac{1}{4}\hat{a}_i\delta_{i+1,j}\,\mathrm{d}t \\ (m_i(t)+2)\big(m_j(t)-2\big) & \frac{1}{4}\hat{a}_{i-1}\delta_{i-1,j}\,\mathrm{d}t \\ (m_i(t)+2)\big(m_j(t)+2\big) & \frac{1}{4}\hat{a}_{i-1}\delta_{i,j}\,\mathrm{d}t \\ (m_i(t)-2)m_j(t) & \frac{1}{4}\hat{a}_i\big(1-\delta_{i,j}-\delta_{i+1,j}\big)\,\mathrm{d}t \\ (m_i(t)+2)m_j(t) & \frac{1}{4}\hat{a}_{i-1}\big(1-\delta_{i-1,j}-\delta_{i,j}\big)\,\mathrm{d}t \\ m_i(t)\big(m_j(t)+2\big) & \frac{1}{4}\hat{a}_{j-1}\big(1-\delta_{i,j}-\delta_{i,j-1}\big)\,\mathrm{d}t \\ m_i(t)\big(m_j(t)-2\big) & \frac{1}{4}\hat{a}_j\big(1-\delta_{i,j+1}-\delta_{i,j}\big)\,\mathrm{d}t \\ m_i(t)m_j(t) & (1-\Sigma dt), \end{cases} \tag{A.42}$$

where $(1-\Sigma dt)$ is the probability of happening nothing. From these update rules, we can write the evolution equation of $C_r^{mm}(t,t)$ as

$$\frac{\mathrm{d}}{\mathrm{d}t}\left\langle m_i(t)m_j(t)\right\rangle = \sum_k \left\langle m_i\Delta_{j,k}\hat{a}_k + \Delta_{i,k}\hat{a}_k m_j\right\rangle_c + B_{i,j}. \tag{A.43}$$

where

$$\begin{aligned} B_{i,j} =& \frac{1}{2}\left\langle 3\hat{a}_{i-1}+8\hat{a}_i+3\hat{a}_{i+1}\right\rangle\delta_{i,j} \\ &- \frac{1}{2}\left\langle 4\hat{a}_{i+1}+4\hat{a}_i\right\rangle\delta_{i+1,j} - \frac{1}{2}\left\langle 4\hat{a}_{i-1}+4\hat{a}_i\right\rangle\delta_{i+1,j} \\ &+ \frac{1}{2}\left\langle \hat{a}_{i+1}\right\rangle\delta_{i+2,j} + \frac{1}{2}\left\langle \hat{a}_{i-1}\right\rangle\delta_{i-2,j}, \end{aligned} \tag{A.44}$$

is the source of the equal-time mass correlation. In the steady state, where $\langle\hat{a}_i(t)\rangle = a(\bar{\rho})$, we can write $B_{i,j}$ as a translationally invariant form, $B_{i,j} \equiv B_r$ as

$$B_r = 7a(\bar{\rho})\delta_{0,r} - 4a(\bar{\rho})(\delta_{0,r+1}+\delta_{0,r-1}) + \frac{a(\bar{\rho})}{2}(\delta_{0,r+2}+\delta_{0,r-2}). \tag{A.45}$$

Equation (A.43) has appeared in eq.(2.39) in the main-text. Using the steady state condition, we must have $d\left\langle m_i m_j\right\rangle_c/dt = 0$, which implies,

$$2\big[C_{r-1}^{m\hat{a}} - 2C_r^{m\hat{a}} + C_{r+1}^{m\hat{a}}\big] + B_r = 0. \tag{A.46}$$

Eq.(A.46) can be solved by considering the following generating function,

$$G(z) = \sum_{r=0}^{\infty} C_r^{m\hat{a}} z^r. \tag{A.47}$$

We multiply both side of eq.(A.46) with z^r and sum over r to get,

$$G(z) = \frac{4C_0^{m\hat{a}} - 4zC_1^{m\hat{a}} - za[(z-8)z+14]}{4(1-z)^2}, \tag{A.48}$$

where we use the identities,

$$\begin{aligned}
\sum_{r=0}^{\infty} C_{r-1}^{m\hat{a}} z^r &= C_1^{m\hat{a}} + zG(z), \\
\sum_{r=0}^{\infty} C_{r+1}^{m\hat{a}} z^r &= \frac{G(z) - C_0^{m\hat{a}}}{z}.
\end{aligned} \tag{A.49}$$

As we are dealing with truncated correlation functions, in the limit $z \to 1$, we must have $\lim_{z\to 1} G(z) < \infty$. Using a new variable $w \to 1 - z$, we write eq.(A.48) as

$$G(w) = \frac{1}{4w^2}\left[a(\bar{\rho})w^3 + 5a(\bar{\rho})w^2 + (a(\bar{\rho}) + 4C_1^{m\hat{a}})w + -7a(\bar{\rho}) + 4C_0^{m\hat{a}} - 4C_1^{m\hat{a}}\right] \tag{A.50}$$

For the convergence of $G(w)$ in the limit $w \to 0$, we set

$$a(\bar{\rho}) + 4C_1^{m\hat{a}} = 0; -7a(\bar{\rho}) + 4C_0^{m\hat{a}} - 4C_1^{m\hat{a}} = 0, \tag{A.51}$$

leading to the following exact relations,

$$C_0^{m\hat{a}} = \frac{3a(\bar{\rho})}{2}, \tag{A.52}$$

$$C_1^{m\hat{a}} = -\frac{a(\bar{\rho})}{4}. \tag{A.53}$$

Finally, putting eq.(A.52) in eq.(A.48) we get the generating function

$$G(z) = \frac{3a(\bar{\rho})}{2} - \frac{a(\bar{\rho})}{4}z. \tag{A.54}$$

B

ACTIVATED RANDOM WALK MODEL

B.1 EQUAL-TIME MASS AND INTEGRATED CURRENT CORRELATION FUNCTION

The update rules of the function $m_i(t)\mathcal{Q}_{i+r}(t)$ can be written as following,

$$
m_i(t+dt)\mathcal{Q}_{i+r}(t+dt) = \begin{cases}
\textit{events} & \textit{probabilities} \\
(m_i(t)+1)\,(\mathcal{Q}_{i+r}(t)+1) & \frac{1}{2(1+\lambda)}\hat{a}_{i-1}m_{i-1}\delta_{i-1,i+r}dt \\
(m_i(t)+1)\,(\mathcal{Q}_{i+r}(t)-1) & \frac{1}{2(1+\lambda)}\hat{a}_{i+1}m_{i+1}\delta_{i,i+r}dt \\
(m_i(t)-1)\,(\mathcal{Q}_{i+r}(t)-1) & \frac{1}{2(1+\lambda)}\hat{a}_{i}m_{i}\delta_{i-1,i+r}dt \\
(m_i(t)-1)\,(\mathcal{Q}_{i+r}(t)+1) & \frac{1}{2(1+\lambda)}\hat{a}_{i}m_{i}\delta_{i,i+r}dt \\
(m_i(t)+1)\,\mathcal{Q}_{i+r}(t) & \frac{1}{2(1+\lambda)}\hat{a}_{i-1}m_{i-1}\,(1-\delta_{i-1,i+r})\,dt \\
(m_i(t)+1)\,\mathcal{Q}_{i+r}(t) & \frac{1}{2(1+\lambda)}\hat{a}_{i+1}m_{i+1}\,(1-\delta_{i,i+r})\,dt \\
(m_i(t)-1)\,\mathcal{Q}_{i+r}(t) & \frac{1}{2(1+\lambda)}\hat{a}_{i}m_{i}\,(1-\delta_{i-1,i+r})\,dt \\
(m_i(t)-1)\,\mathcal{Q}_{i+r}(t) & \frac{1}{2(1+\lambda)}\hat{a}_{i}m_{i}\,(1-\delta_{i,i+r})\,dt \\
m_i(t)\,(\mathcal{Q}_{i+r}(t)+1) & \frac{1}{2(1+\lambda)}\hat{a}_{i+r}m_{i+r} \\
 & (1-\delta_{i,i+r}-\delta_{i,i+r+1})\,dt \\
m_i(t)\,(\mathcal{Q}_{i+r}(t)-1) & \frac{1}{2(1+\lambda)}\hat{a}_{i+r+1}m_{i+r+1} \\
 & (1-\delta_{i,i+r}-\delta_{i,i+r+1})\,dt \\
m_i(t)\mathcal{Q}_{i+r}(t) & (1-\Sigma dt).
\end{cases}
\tag{B.1}
$$

From the update rules, we obtain the temporal evolution equation of $\langle m_i(t)\mathcal{Q}_{i+r}(t)\rangle$ as

$$\frac{d}{dt}\langle m_i(t)\mathcal{Q}_{i+r}(t)\rangle = \left\langle \left\{ \mathcal{J}_{i-1}^{(d)}(t) - \mathcal{J}_i^{(d)}(t) \right\} \mathcal{Q}_{i+r}(t) \right\rangle + f_{i,i+r}(t), \tag{B.2}$$

where the microscopic diffusive current $\mathcal{J}^{(d)}$ is defined in Eq.(4.20) and the source of the above correlation function, $f_{i,i+r}(t)$ is given as

$$\begin{aligned} f_{i,i+r}(t) =& \frac{1}{2(1+\lambda)} \langle \hat{a}_{i-1}m_{i-1} + \hat{a}_i m_i \rangle \delta_{i-1,i+r} - \frac{1}{2(1+\lambda)} \langle \hat{a}_{i+1}m_{i+1} + \hat{a}_i m_i \rangle \delta_{i,i+r} \\ &+ \frac{1}{2(1+\lambda)} \langle m_i \left(\hat{u}_{i+r} - \hat{u}_{i+r+1} \right) \rangle . \end{aligned} \tag{B.3}$$

In the steady state $f_{i,i+r}(t)$ does not depend on the index i, and we have,

$$f_r(t) = \frac{1}{(1+\lambda)} u(\bar{\rho}) \left(\delta_{0,r+1} - \delta_{0,r} \right) + \frac{1}{2(1+\lambda)} \left(C_r^{m\hat{u}}(t,t) - C_{r+1}^{m\hat{u}}(t,t) \right) . \tag{B.4}$$

Thus, taking the steady state representation of Eq.(B.3) we can derive Eq.(4.31) of the main text.

C

THE OSLO RICEPILE

C.1 EQUAL-TIME MASS AND INTEGRATED CURRENT CORRELATION FUNCTION

To obtain the Eq. (5.24) of Chapter 5, using the update rules of the function $m_i(t)\mathcal{Q}_{i+r}(t)$ given as

$$
m_i(t+dt)\mathcal{Q}_{i+r}(t+dt) = \begin{cases}
\textit{events} & \textit{probabilities} \\
(m_i(t)+1)\,(\mathcal{Q}_{i+r}(t)+1) & \hat{a}_{i+1}\delta_{i+r,i+1}dt \\
(m_i(t)+1)\,(\mathcal{Q}_{i+r}(t)-1) & \hat{a}_{i+1}\delta_{i+r,i}dt \\
(m_i(t)+1)\,(\mathcal{Q}_{i+r}(t)+1) & \hat{a}_{i-1}\delta_{i+r,i-1}dt \\
(m_i(t)+1)\,(\mathcal{Q}_{i+r}(t)-1) & \hat{a}_{i-1}\delta_{i+r,i-2}dt \\
(m_i(t)-2)\,(\mathcal{Q}_{i+r}(t)+1) & \hat{a}_{i}\delta_{i+r,i}dt \\
(m_i(t)-2)\,(\mathcal{Q}_{i+r}(t)-1) & \hat{a}_{i}\delta_{i+r,i-1}dt \\
(m_i(t)+1)\,\mathcal{Q}_{i+r}(t) & \hat{a}_{i+1}\left(1-\delta_{i+r,i+1}-\delta_{i+r,i}\right)dt \\
(m_i(t)+1)\,\mathcal{Q}_{i+r}(t) & \hat{a}_{i-1}\left(1-\delta_{i+r,i-1}-\delta_{i+r,i-2}\right)dt \\
(m_i(t)-2)\,\mathcal{Q}_{i+r}(t) & \hat{a}_{i}\left(1-\delta_{i+r,i}-\delta_{i+r,i-1}\right)dt \\
m_i(t)\,(\mathcal{Q}_{i+r}(t)+1) & \hat{a}_{i+r} \\
 & \left(1-\delta_{i+r,i}-\delta_{i+r+1,i}-\delta_{i+r-1,i}\right)dt \\
m_i(t)\,(\mathcal{Q}_{i+r}(t)-1) & \hat{a}_{i+r+1} \\
 & \left(1-\delta_{i+r,i}-\delta_{i+r+1,i}-\delta_{i+r+2,i}\right)dt \\
m_i(t)\mathcal{Q}_{i+r}(t) & 1-\Sigma dt,
\end{cases}
\tag{C.1}
$$

where Σdt is the sum of probabilities of all previous events. This update rules gives us the following evolution equation of the correlation of equal-time mass and current,

$$\frac{d}{dt}\left\langle m_i(t)\mathcal{Q}_{i+r}(t)\right\rangle = \Delta_{i,k}\left\langle \hat{a}_k(t)\mathcal{Q}_{i+r}(t)\right\rangle + f_{i,r}(t); \tag{C.2}$$

the source term $f_{i,r}(t)$ has the following representation,

$$\begin{aligned} f_{i,r}(t) = &\left\langle m_i(t)\hat{a}_{i+r}(t)\right\rangle - \left\langle m_i(t)\hat{a}_{i+r+1}(t)\right\rangle + \\ &\left\langle \hat{a}_{i+1}\right\rangle\left(\delta_{i+r,i+1}-\delta_{i+r,i}\right) + \left\langle \hat{a}_{i-1}\right\rangle\left(\delta_{i+r,i-1}-\delta_{i+r,i-2}\right) - 2\left\langle \hat{a}_i\right\rangle\left(\delta_{i+r,i}-\delta_{i+r,i-1}\right), \end{aligned} \tag{C.3}$$

and in the steady state, it will simply be,

$$f_r(t) = C_r^{m\hat{a}}(t,t) - C_{r+1}^{m\hat{a}}(t,t) + a\left\{3\left(\delta_{0,r+1}-\delta_{0,r}\right) + \left(\delta_{0,r-1}-\delta_{0,r+2}\right)\right\}. \tag{C.4}$$

This completes the derivation of Eq.(5.24).

The corresponding correlation function $C_r^{m\hat{a}}(t,t)$ is derived in the following section.

To obtain Eq. (5.26) in the main text of Chapter 5, we write the evolution equation of the equal-time and unequal space mass-mass correlation function using the following update rules,

$$
\begin{aligned}
&m_i(t+dt)m_{i+r}(t+dt) = \\
&\begin{cases}
\textbf{\textit{events}} & \textbf{\textit{probabilities}} \\
(m_i(t)-2)\,(m_{i+r}(t)-2) & \hat{a}_i\delta_{i,i+r}dt \\
(m_i(t)-2)\,(m_{i+r}(t)+1) & \hat{a}_i\delta_{i+1,i+r}dt \\
(m_i(t)-2)\,(m_{i+r}(t)+1) & \hat{a}_i\delta_{i-1,i+r}dt \\
(m_i(t)+1)\,(m_{i+r}(t)+1) & \hat{a}_{i-1}\delta_{i,i+r}dt \\
(m_i(t)+1)\,(m_{i+r}(t)-2) & \hat{a}_{i-1}\delta_{i-1,i+r}dt \\
(m_i(t)+1)\,(m_{i+r}(t)+1) & \hat{a}_{i-1}\delta_{i-2,i+r}dt \\
(m_i(t)+1)\,(m_{i+r}(t)+1) & \hat{a}_{i+1}\delta_{i,i+r}dt \\
(m_i(t)+1)\,(m_{i+r}(t)-2) & \hat{a}_{i+1}\delta_{i+1,i+r}dt \\
(m_i(t)+1)\,(m_{i+r}(t)+1) & \hat{a}_{i+1}\delta_{i+2,i+r}dt \\
(m_i(t)-2)\,m_{i+r}(t) & \hat{a}_i\left(1-\delta_{i+1,i+r}-\delta_{i,i+r}-\delta_{i-1,i+r}\right)dt \\
(m_i(t)+1)\,m_{i+r}(t) & \hat{a}_{i-1}\left(1-\delta_{i-1,i+r}-\delta_{i,i+r}-\delta_{i-2,i+r}\right)dt \\
(m_i(t)+1)\,m_{i+r}(t) & \hat{a}_{i+1}\left(1-\delta_{i+1,i+r}-\delta_{i,i+r}-\delta_{i+2,i+r}\right)dt \\
m_i(t)\,(m_{i+r}(t)-2) & \hat{a}_{i+r}\left(1-\delta_{i,i+r+1}-\delta_{i,i+r}-\delta_{i,i+r-1}\right)dt \\
m_i(t)\,(m_{i+r}(t)+1) & \hat{a}_{i+r+1}\left(1-\delta_{i,i+r+1}-\delta_{i,i+r+2}-\delta_{i,i+r}\right)dt \\
m_i(t)\,(m_{i+r}(t)+1) & \hat{a}_{i+r-1}\left(1-\delta_{i,i+r-1}-\delta_{i,i+r}-\delta_{i,i+r-2}\right)dt \\
m_i(t)m_{i+r}(t) & 1-\Sigma dt,
\end{cases}
\end{aligned}
\tag{C.5}
$$

where Σdt is the sum of probabilities of all previous events. The corresponding evolution equation of $C_r^{mm}(t,t)$ can be written using the above update rules as

$$
\frac{d}{dt}C_r^{mm}(t,t) = \sum_k \Delta_{i,k}\left\langle \hat{a}_k m_{i+r}\right\rangle + \sum_k \Delta_{i+r,k}\left\langle m_i\hat{a}_k\right\rangle + B_{i,i+r}, \tag{C.6}
$$

where $B_{i,i+r}$ is the source part of this correlation, given as

$$\begin{aligned} B_{i,i+r} =& \delta_{i,i+r}\left(4\hat{a}_i + \hat{a}_{i-1} + \hat{a}_{i+1}\right) - 2\delta_{i-1,i+r}\left(\hat{a}_i + \hat{a}_{i-1}\right) - 2\delta_{i+1,i+r}\left(\hat{a}_i + \hat{a}_{i+1}\right) + \\ & \delta_{i-2,i+r}\hat{a}_{i-1} + \delta_{i+2,i+r}\hat{a}_{i+1}. \end{aligned} \tag{C.7}$$

In the steady state we must have $\frac{d}{dt}C_r^{mm}(t,t) = 0$ and using the translation symmetry, Eq.(C.6) can be written as

$$2\left(C_{r-1}^{\hat{a}m} - C_r^{\hat{a}m} + C_{r+1}^{\hat{a}m}\right) + B_r = 0, \tag{C.8}$$

where

$$B_r = 6a(\bar{\rho})\delta_{0,r} - 4a(\bar{\rho})\left(\delta_{0,r+1} + \delta_{0,r-1}\right) + a(\bar{\rho})\left(\delta_{0,r+2} + \delta_{0,r-2}\right). \tag{C.9}$$

We can solve Eq.(C.8) by multiplying both sides by z^r and defining the generating function $G(z) = \sum_{r=0}^{\infty} z^r C_r^{\hat{a}m}$. Imposing the convergence of $G(z) < \infty$ when $z < \infty$, we can write the generating function as

$$G(z) = a(\bar{\rho}) - \frac{a(\bar{\rho})}{2}z. \tag{C.10}$$

From the generating function of above, we write the correlation function $C_r^{\hat{a}m}$ as

$$C_r^{\hat{a}m} = a(\bar{\rho})\delta_{0,r} - \frac{a}{2}\left(\delta_{r+1} + \delta_{r-1}\right), \tag{C.11}$$

and thus we prove Eq. (5.26).

To derive Eq. (5.30), we write the evolution equation of the equal-time unequal-space correlation of integrated current using the following update equation,

$$\mathcal{Q}_i(t+dt)\mathcal{Q}_{i+r}(t+dt) = \begin{cases} \textbf{\textit{events}} & \textbf{\textit{probabilities}} \\ (\mathcal{Q}_i(t)+1)\,(\mathcal{Q}_{i+r}(t)+1) & \hat{a}_i(t)\delta_{i,i+r}dt \\ (\mathcal{Q}_i(t)+1)\,(\mathcal{Q}_{i+r}(t)-1) & \hat{a}_i(t)\delta_{i-1,i+r}dt \\ (\mathcal{Q}_i(t)-1)\,(\mathcal{Q}_{i+r}(t)-1) & \hat{a}_{i+1}(t)\delta_{i,i+r}dt \\ (\mathcal{Q}_i(t)-1)\,(\mathcal{Q}_{i+r}(t)+1) & \hat{a}_{i+1}(t)\delta_{i+1,i+r}dt \\ (\mathcal{Q}_i(t)+1)\,\mathcal{Q}_{i+r}(t) & \hat{a}_i(t)\,(1-\delta_{i,i+r}-\delta_{i-1,i+r})\,dt \\ (\mathcal{Q}_i(t)-1)\,\mathcal{Q}_{i+r}(t) & \hat{a}_{i+1}(t)\,(1-\delta_{i,i+r}-\delta_{i+1,i+r})\,dt \\ \mathcal{Q}_i(t)\,(\mathcal{Q}_{i+r}(t)+1) & \hat{a}_{i+r}(t)\,(1-\delta_{i,i+r}-\delta_{i,i+r-1})\,dt \\ \mathcal{Q}_i(t)\,(\mathcal{Q}_{i+r}(t)-1) & \hat{a}_{i+r+1}(t)\,(1-\delta_{i,i+r}-\delta_{i,i+r+1})\,dt \\ \mathcal{Q}_i(t)\mathcal{Q}_{i+r}(t) & 1-\Sigma dt, \end{cases} \tag{C.12}$$

where Σdt is the probability of happening nothing in the time interval dt. The corresponding dynamical equation can be written as

$$\frac{\partial}{\partial t}C_r^{\mathcal{Q}\mathcal{Q}}(t,t) = \Gamma_{i,i+r}(t) + \left\langle \mathcal{J}_i^{(d)}(t)\mathcal{Q}_{i+r}(t)\right\rangle + \left\langle \mathcal{Q}_i(t)\mathcal{J}_{i+r}^{(d)})(t)\right\rangle, \tag{C.13}$$

where $\Gamma_{i,i+r}$ is the source of the equation or correlation functions can be written as

$$\Gamma_{i,i+r}(t) = \hat{a}_i(t)\,(\delta_{i,i+r}-\delta_{i-1,i+r}) + \hat{a}_{i+1}(t)\,(\delta_{i,i+r}-\delta_{i+1,i+r})\,. \tag{C.14}$$

In the steady state, this source function can be written as

$$\Gamma_r(t) = a(\bar{\rho})\,(2\delta_{0,r}-\delta_{0,r+1}-\delta_{0,r-1})\,, \tag{C.15}$$

which is the derivation of Eq. (5.32) in the main text.

BIBLIOGRAPHY

[1] L. Onsager, "Reciprocal Relations in Irreversible Processes. II.," Phys. Rev. **38**, 2265–2279 (1931) (cit. on pp. 2, 6).

[2] L. Onsager, "Reciprocal Relations in Irreversible Processes. I.," Phys. Rev. **37**, 405–426 (1931) (cit. on pp. 2, 6).

[3] L. Onsager and R. M. Fuoss, "Irreversible Processes in Electrolytes. Diffusion, Conductance and Viscous Flow in Arbitrary Mixtures of Strong Electrolytes," J. Phys. Chem. **36**, 2689–2778 (1932) (cit. on p. 2).

[4] L. Onsager and S. Machlup, "Fluctuations and Irreversible Processes," Phys. Rev. **91**, 1505–1512 (1953) (cit. on pp. 2, 6, 8).

[5] M. S. Green, "Markoff random processes and the statistical mechanics of time-dependent phenomena," The Journal of Chemical Physics **20**, 1281–1295 (1952) (cit. on pp. 2, 90, 91, 128).

[6] M. S. Green, "Markoff random processes and the statistical mechanics of time-dependent v phenomena. ii. irreversible processes in fluids," The Journal of Chemical Physics **22**, 398–413 (1954) (cit. on pp. 2, 90, 91, 128).

[7] R. Kubo, "Statistical-mechanical theory of irreversible processes. i. general theory and simple applications to magnetic and conduction problems," Journal of the Physical Society of Japan **12**, 570–586 (1957) (cit. on pp. 2, 90, 91, 128).

[8] R. Kubo, M. Yokota, and S. Nakajima, "Statistical-mechanical theory of irreversible processes. ii. response to thermal disturbance," Journal of the Physical Society of Japan **12**, 1203–1211 (1957) (cit. on pp. 2, 90, 91, 128).

[9] L. Bertini, A. De Sole, D. Gabrielli, G. Jona-Lasinio, and C. Landim, "Macroscopic fluctuation theory," Reviews of Modern Physics **87**, 593–636 (2015) (cit. on pp. 3, 14–17, 38, 51, 62, 65, 68, 104, 105, 126).

[10] C. Arita, P. L. Krapivsky, and K. Mallick, "Generalized exclusion processes: Transport coefficients," Phys. Rev. E **90**, 052108 (2014) (cit. on p. 3).

[11] L. Bertini, A. De Sole, D. Gabrielli, G. Jona-Lasinio, and C. Landim, Journal of Statistical Physics **107**, 635–675 (2002) (cit. on pp. 3, 14–17, 105, 124).

[12] N. G. Van Kampen, *Stochastic Processes in Physics and Chemistry* (Elsevier Science, Oxford, England, UK) (cit. on p. 3).

[13]C. Gardiner, *Stochastic Methods* (Springer, Berlin, Germany) (cit. on p. 3).

[14]B. Derrida, "Non-equilibrium steady states: fluctuations and large deviations of the density and of the," J. Stat. Mech.: Theory Exp. **2007**, P07023 (2007) (cit. on pp. 5, 10–12, 14).

[15]H. Touchette, "Introduction to dynamical large deviations of Markov processes," Physica A **504**, 5–19 (2018) (cit. on p. 5).

[16]A. W. C. Lau and T. C. Lubensky, "State-dependent diffusion: Thermodynamic consistency and its path integral formulation," Phys. Rev. E **76**, 011123 (2007) (cit. on pp. 6–8).

[17]P. C. Hohenberg and B. I. Halperin, "Theory of dynamic critical phenomena," Rev. Mod. Phys. **49**, 435–479 (1977) (cit. on p. 9).

[18]U. C. Täuber, *Critical Dynamics: A Field Theory Approach to Equilibrium and Non-Equilibrium Scaling Behavior* (Cambridge University Press, Cambridge, England, UK, Mar. 2014) (cit. on p. 9).

[19]B. Derrida, J. L. Lebowitz, and E. R. Speer, "Large Deviation of the Density Profile in the Steady State of the Open Symmetric Simple Exclusion Process," J. Stat. Phys. **107**, 599–634 (2002) (cit. on p. 11).

[20]B. Derrida, J. L. Lebowitz, and E. R. Speer, "Exact Free Energy Functional for a Driven Diffusive Open Stationary Nonequilibrium System," Phys. Rev. Lett. **89**, 030601 (2002) (cit. on p. 12).

[21]B. Derrida, J. L. Lebowitz, and E. R. Speer, "Exact Large Deviation Functional of a Stationary Open Driven Diffusive System: The Asymmetric Exclusion Process," J. Stat. Phys. **110**, 775–810 (2003) (cit. on p. 12).

[22]R. Chetrite and H. Touchette, "Nonequilibrium Markov Processes Conditioned on Large Deviations," Ann. Henri Poincaré **16**, 2005–2057 (2015) (cit. on p. 13).

[23]P. Chleboun, S. Grosskinsky, and A. Pizzoferrato, "Current large deviations for partially asymmetric particle systems on a ring," J. Phys. A: Math. Theor. **51**, 405001 (2018) (cit. on p. 13).

[24]B. Derrida, B. Douçot, and P.-E. Roche, "Current Fluctuations in the One-Dimensional Symmetric Exclusion Process with Open Boundaries," J. Stat. Phys. **115**, 717–748 (2004) (cit. on p. 13).

[25]T. Bodineau and B. Derrida, "Current Fluctuations in Nonequilibrium Diffusive Systems: An Additivity Principle," Phys. Rev. Lett. **92**, 180601 (2004) (cit. on pp. 13, 14, 17).

[26]T. Bodineau and B. Derrida, "Cumulants and large deviations of the current through non-equilibrium steady states," C. R. Phys. **8**, 540–555 (2007) (cit. on p. 14).

[27]P. I. Hurtado and P. L. Garrido, "Test of the Additivity Principle for Current Fluctuations in a Model of Heat Conduction," Phys. Rev. Lett. **102**, 250601 (2009) (cit. on p. 14).

[28]P. I. Hurtado and P. L. Garrido, "Large fluctuations of the macroscopic current in diffusive systems: A numerical test of the additivity principle," Phys. Rev. E **81**, 041102 (2010) (cit. on p. 14).

[29]T. Bodineau and B. Derrida, "Distribution of current in nonequilibrium diffusive systems and phase transitions," Phys. Rev. E **72**, 066110 (2005) (cit. on p. 14).

[30]P. I. Hurtado and P. L. Garrido, "Spontaneous Symmetry Breaking at the Fluctuating Level," Phys. Rev. Lett. **107**, 180601 (2011) (cit. on p. 14).

[31]N. Tizón-Escamilla, C. Pérez-Espigares, P. L. Garrido, and P. I. Hurtado, "Order and Symmetry Breaking in the Fluctuations of Driven Systems," Phys. Rev. Lett. **119**, 090602 (2017) (cit. on p. 14).

[32]C. P. Espigares, P. L. Garrido, and P. I. Hurtado, "Dynamical phase transition for current statistics in a simple driven diffusive system," Phys. Rev. E **87**, 032115 (2013) (cit. on p. 14).

[33]L. Zarfaty and B. Meerson, "Statistics of large currents in the Kipnis–Marchioro–Presutti model in a ring geometry," J. Stat. Mech.: Theory Exp. **2016**, 033304 (2016) (cit. on p. 14).

[34]P. L. Garrido, "Notes about the macroscopic fluctuating theory," Journal of Statistical Mechanics: Theory and Experiment **2021**, 024001 (2021) (cit. on p. 15).

[35]A. Das, S. Chatterjee, P. Pradhan, and P. K. Mohanty, "Additivity property and emergence of power laws in nonequilibrium steady states," Phys. Rev. E **92**, 052107 (2015) (cit. on p. 16).

[36]A. Das, S. Chatterjee, and P. Pradhan, "Spatial correlations, additivity, and fluctuations in conserved-mass transport processes," Phys. Rev. E **93**, 062135 (2016) (cit. on p. 16).

[37]A. Das, A. Kundu, and P. Pradhan, "Einstein relation and hydrodynamics of nonequilibrium mass transport processes," Phys. Rev. E **95**, 062128 (2017) (cit. on p. 16).

[38]S. Chatterjee, A. Das, and P. Pradhan, "Hydrodynamics, density fluctuations, and universality in conserved stochastic sandpiles," Physical Review E **97**, 10.1103/physreve.97.062142 (2018) (cit. on pp. 16, 26, 28, 30, 35, 37, 47, 51, 53, 60–62, 65, 68, 70, 105).

[39]L. Bertini, A. D. Sole, D. Gabrielli, G. Jona-Lasinio, and C. Landim, "Non equilibrium current fluctuations in stochastic lattice gases," Journal of Statistical Physics **123**, 237–276 (2006) (cit. on p. 17).

[40]A. Imparato, V. Lecomte, and F. van Wijland, "Equilibriumlike fluctuations in some boundary-driven open diffusive systems," Phys. Rev. E **80**, 011131 (2009) (cit. on p. 17).

[41]Y. Baek, Y. Kafri, and V. Lecomte, "Extreme current fluctuations of boundary-driven systems in the large-N limit," J. Stat. Mech.: Theory Exp. **2016**, 053203 (2016) (cit. on p. 17).

[42]Y. Baek, Y. Kafri, and V. Lecomte, "Dynamical Symmetry Breaking and Phase Transitions in Driven Diffusive Systems," Phys. Rev. Lett. **118**, 030604 (2017) (cit. on p. 17).

[43]O. Shpielberg and E. Akkermans, "Le Chatelier Principle for Out-of-Equilibrium and Boundary-Driven Systems: Application to Dynamical Phase Transitions," Phys. Rev. Lett. **116**, 240603 (2016) (cit. on p. 17).

[44]O. Shpielberg, Y. Don, and E. Akkermans, "Numerical study of continuous and discontinuous dynamical phase transitions for boundary-driven systems," Phys. Rev. E **95**, 032137 (2017) (cit. on p. 17).

[45]P. Bak, C. Tang, and K. Wiesenfeld, "Self-organized criticality: an explanation of the 1/fnoise," Physical Review Letters **59**, 381–384 (1987) (cit. on pp. 18–20, 23).

[46]P. Bak, *How nature works: the science of self-organized criticality* (Oxford University Press, 1997) (cit. on pp. 18, 19).

[47]S. R. Nagel, "Instabilities in a sandpile," Reviews of Modern Physics **64**, 321–325 (1992) (cit. on p. 18).

[48]P. Bak, C. Tang, and K. Wiesenfeld, "Self-organized criticality," Physical Review A **38**, 364–374 (1988) (cit. on pp. 19, 20).

[49]B. B. Mandelbrot, *The fractal geometry of nature*, 3rd ed. (W. H. Freeman and Comp., 1983) (cit. on p. 19).

[50]L. Palmieri and H. J. Jensen, "The forest fire model: the subtleties of criticality and scale invariance," Frontiers in Physics **8**, 10.3389/fphy.2020.00257 (2020) (cit. on p. 19).

[51]E. Novikov, A. Novikov, D. Shannahoff-Khalsa, B. Schwartz, and J. Wright, "Scale-similar activity in the brain," Physical Review E **56**, R2387–R2389 (1997) (cit. on p. 19).

[52]J. Hesse and T. Gross, "Self-organized criticality as a fundamental property of neural systems," Frontiers in Systems Neuroscience **8**, 10.3389/fnsys.2014.00166 (2014) (cit. on p. 19).

[53]A. N. Burkitt, "A review of the integrate-and-fire neuron model: I. Homogeneous synaptic input," Biol. Cybern. **95**, 1–19 (2006), eprint: 16622699 (cit. on p. 19).

[54]A. N. Burkitt, "A review of the integrate-and-fire neuron model: II. Inhomogeneous synaptic input and network properties," Biol. Cybern. **95**, 97–112 (2006), eprint: 16821035 (cit. on p. 19).

[55]F. Frontera and F. Fuligni, "Shot-noise character of hard x-ray emission in a solar flare," The Astrophysical Journal **232**, 590 (1979) (cit. on p. 19).

[56]M. J. Aschwanden and et al, "25 years of self-organized criticality: solar and astrophysics," Space Science Reviews **198**, 47–166 (2014) (cit. on p. 19).

[57]C. Tebaldi, "Self-organized criticality in economic fluctuations: the age of maturity," Frontiers in Physics **8**, 10.3389/fphy.2020.616408 (2021) (cit. on p. 19).

[58]R. F. Voss and J. Clarke, "Flicker ($\frac{1}{f}$) noise: Equilibrium temperature and resistance fluctuations," Physical Review B **13**, 556–573 (1976) (cit. on p. 19).

[59]H. J. Jensen, *Self-organized criticality* (Cambridge University Press, 1998) (cit. on p. 19).

[60]H. M. Jaeger, C.-h. Liu, and S. R. Nagel, "Relaxation at the angle of repose," Physical Review Letters **62**, 40–43 (1989) (cit. on pp. 19, 131).

[61]V. Frette, K. Christensen, A. Malthe-Sørenssen, J. Feder, T. Jøssang, and P. Meakin, "Avalanche dynamics in a pile of rice," Nature **379**, 49–52 (1996) (cit. on pp. 20, 27, 131).

[62]S. S. Manna, "Two-state model of self-organized criticality," Journal of Physics A: Mathematical and General **24**, L363–L369 (1991) (cit. on pp. 21, 28, 34, 35, 102).

[63]R. Dickman, M. Alava, M. A. Muñoz, J. Peltola, A. Vespignani, and S. Zapperi, "Critical behavior of a one-dimensional fixed-energy stochastic sandpile," Physical Review E **64**, 10.1103/physreve.64.056104 (2001) (cit. on pp. 21, 22, 26, 28, 35, 36, 46, 47, 70).

[64]K. Christensen, Á. Corral, V. Frette, J. Feder, and T. Jøssang, "Tracer Dispersion in a Self-Organized Critical System," Phys. Rev. Lett. **77**, 107–110 (1996) (cit. on pp. 21, 27, 131).

[65]P. Grassberger, D. Dhar, and P. K. Mohanty, "Oslo model, hyperuniformity, and the quenched edwards-wilkinson model," Physical Review E **94**, 10.1103/physreve.94.042314 (2016) (cit. on pp. 21, 22, 27, 28, 131, 132, 151).

[66]L. T. Rolla, "Activated random walks on $\mathbb{Z}^d$," Probability Surveys **17**, 478–544 (2020) (cit. on pp. 21, 22, 28, 102, 103).

[67]L. T. Rolla and V. Sidoravicius, "Absorbing-state phase transition for driven-dissipative stochastic dynamics on $\mathbb{Z}$," Invent. Math. **188**, 127–150 (2012) (cit. on pp. 22, 102).

[68]A. Vespignani, R. Dickman, M. A. Muñoz, and S. Zapperi, "Absorbing-state phase transitions in fixed-energy sandpiles," Physical Review E **62**, 4564–4582 (2000) (cit. on p. 22).

[69]A. Vespignani and S. Zapperi, "How self-organized criticality works: a unified mean-field picture," Physical Review E **57**, 6345–6362 (1998) (cit. on p. 22).

[70]H. Hinrichsen, "Non-equilibrium critical phenomena and phase transitions into absorbing states," Adv. Phys. **49**, 815–958 (2000) (cit. on p. 22).

[71]A. Fey, L. Levine, and D. B. Wilson, "Driving sandpiles to criticality and beyond," Physical Review Letters **104**, 10.1103/physrevlett.104.145703 (2010) (cit. on p. 22).

[72]R. Dickman, M. A. Muñoz, A. Vespignani, and S. Zapperi, "Paths to self-organized criticality," Brazilian Journal of Physics **30**, 27–41 (2000) (cit. on p. 22).

[73]D. Dhar and R. Ramaswamy, "Exactly solved model of self-organized critical phenomena," Physical Review Letters **63**, 1659–1662 (1989) (cit. on p. 22).

[74]D. Dhar, "Self-organized critical state of sandpile automaton models," Physical Review Letters **64**, 1613–1616 (1990) (cit. on p. 22).

[75]V. B. Priezzhev, D. Dhar, A. Dhar, and S. Krishnamurthy, "Eulerian walkers as a model of self-organized criticality," Physical Review Letters **77**, 5079–5082 (1996) (cit. on p. 22).

[76]S. Majumdar and D. Dhar, "Equivalence between the abelian sandpile model and the q→0 limit of the potts model," Physica A: Statistical Mechanics and its Applications **185**, 129–145 (1992) (cit. on p. 22).

[77]M. Podder and L. T. Rolla, "Uniform threshold for fixation of the stochastic sandpile model on the line," Journal of Statistical Physics **182**, 10.1007/s10955-021-02731-3 (2021) (cit. on p. 22).

[78]A. Cipriani, R. S. Hazra, and W. M. Ruszel, "Scaling limit of the odometer in divisible sandpiles," Probability Theory and Related Fields **172**, 829–868 (2017) (cit. on p. 22).

[79]R. Dickman, A. Vespignani, and S. Zapperi, "Self-organized criticality as an absorbing-state phase transition," Physical Review E **57**, 5095–5105 (1998) (cit. on p. 22).

[80]A. Vespignani, R. Dickman, M. A. Muñoz, and S. Zapperi, "Driving, conservation, and absorbing states in sandpiles," Physical Review Letters **81**, 5676–5679 (1998) (cit. on p. 22).

[81]P. Le Doussal and K. J. Wiese, "Exact mapping of the stochastic field theory for manna sandpiles to interfaces in random media," Physical Review Letters **114**, 10.1103/physrevlett.114.110601 (2015) (cit. on p. 22).

[82]J. J. Ramasco, M. A. Muñoz, and C. A. da Silva Santos, "Numerical study of the langevin theory for fixed-energy sandpiles," Physical Review E **69**, 10.1103/physreve.69.045105 (2004) (cit. on p. 22).

[83]R. Dickman, "n-site approximations and coherent-anomaly-method analysis for a stochastic sandpile," Physical Review E **66**, 10.1103/physreve.66.036122 (2002) (cit. on p. 22).

[84]S. D. da Cunha, R. R. Vidigal, L. R. da Silva, and R. Dickman, "Diffusion in stochastic sandpiles," The European Physical Journal B **72**, 441–449 (2009) (cit. on pp. 22, 27, 30, 35, 54, 58, 68).

[85]D. Dhar, "Theoretical studies of self-organized criticality," Physica A: Statistical Mechanics and its Applications **369**, 29–70 (2006) (cit. on p. 22).

[86]F. Redig, "Mathematical aspects of the abelian sandpile model," Les Houches, Session LXXXIII 2005, 657–729 (2006) (cit. on p. 22).

[87]P. Pradhan, "Time-dependent properties of sandpiles," Frontiers in Physics **9**, 10.3389/fphy.2021.641233 (2021) (cit. on pp. 22, 24–26, 70, 91).

[88]A. A. Ali, "Self-organized criticality in a sandpile model with threshold dissipation," Physical Review E **52**, R4595–R4598 (1995) (cit. on p. 22).

[89]J Kertesz and L. B. Kiss, "The noise spectrum in the model of self-organised criticality," Journal of Physics A: Mathematical and General **23**, L433–L440 (1990) (cit. on p. 23).

[90]L. Laurson, M. J. Alava, and S. Zapperi, "Power spectra of self-organized critical sandpiles," Journal of Statistical Mechanics: Theory and Experiment **2005**, L11001–L11001 (2005) (cit. on p. 23).

[91]H. J. Jensen, K. Christensen, and H. C. Fogedby, "$1/f$ Noise, distribution of lifetimes, and a pile of sand," Physical Review B **40**, 7425–7427 (1989) (cit. on p. 23).

[92]T. Hwa and M. Kardar, "Dissipative transport in open systems: an investigation of self-organized criticality," Physical Review Letters **62**, 1813–1816 (1989) (cit. on pp. 23, 24, 68).

[93]G. Grinstein and D.-H. Lee, "Generic scale invariance and roughening in noisy model sandpiles and other driven interfaces," Phys. Rev. Lett. **66**, 177–180 (1991) (cit. on p. 24).

[94]R. Garcia-Millan, G. Pruessner, L. Pickering, and K. Christensen, "Correlations and hyperuniformity in the avalanche size of the oslo model," EPL (Europhysics Letters) **122**, 50003 (2018) (cit. on pp. 25, 47, 68).

[95]A. C. Yadav, R. Ramaswamy, and D. Dhar, "Power spectrum of mass and activity fluctuations in a sandpile," Physical Review E **85**, 10.1103/physreve.85.061114 (2012) (cit. on p. 25).

[96]S. Maslov, C. Tang, and Y.-C. Zhang, "$1/f$ Noise in bak-tang-wiesenfeld models on narrow stripes," Physical Review Letters **83**, 2449–2452 (1999) (cit. on p. 25).

[97]M Baiesi and C Maes, "Realistic time correlations in sandpiles," Europhysics Letters (EPL) **75**, 413–419 (2006) (cit. on p. 25).

[98]A. Giometto and H. J. Jensen, "Connecting the microdynamics to the emergent macrovariables: self-organized criticality and absorbing phase transitions in the deterministic lattice gas," Physical Review E **85**, 10.1103/physreve.85.011128 (2012) (cit. on p. 25).

[99]J. M. Carlson, J. T. Chayes, E. R. Grannan, and G. H. Swindle, "Self-orgainzed criticality and singular diffusion," Physical Review Letters **65**, 2547–2550 (1990) (cit. on p. 25).

[100]J. M. Carlson, E. R. Grannan, and G. H. Swindle, "Self-organizing systems at finite driving rates," Physical Review E **47**, 93–105 (1993) (cit. on p. 25).

[101]J. M. Carlson, E. R. Grannan, G. H. Swindle, and J. Tour, "Singular diffusion limits of a class of reversible self-organizing particle systems," The Annals of Probability **21**, 1372–1393 (1993) (cit. on p. 25).

[102]D. Tapader, P. Pradhan, and D. Dhar, "Density relaxation in conserved manna sandpiles," Physical Review E **103**, 10.1103/physreve.103.032122 (2021) (cit. on pp. 26, 28, 35, 37, 47, 60, 67, 68).

[103]D. Dhar and P. Pradhan, "Probability distribution of residence times of grains in sand-pile models," Journal of Statistical Mechanics: Theory and Experiment **2004**, P05002 (2004) (cit. on p. 27).

[104]P. Pradhan and D. Dhar, "Probability distribution of residence times of grains in models of rice piles," Physical Review E **73**, 10.1103/physreve.73.021303 (2006) (cit. on p. 27).

[105]P. Pradhan and D. Dhar, "Sampling rare fluctuations of height in the Oslo ricepile model," J. Phys. A: Math. Theor. **40**, 2639 (2007) (cit. on p. 27).

[106]P. Pradhan and D. Dhar, "Probability distribution of residence times of grains in models of rice piles," Phys. Rev. E **73**, 021303 (2006) (cit. on p. 27).

[107]D. Dhar and P. Pradhan, "Probability distribution of residence times of grains in sand-pile models," J. Stat. Mech.: Theory Exp. **2004**, P05002 (2004) (cit. on p. 27).

[108]A. Mukherjee and P. Pradhan, "Dynamic correlations in the conserved manna sandpile," Phys. Rev. E **107**, 024109 (2023) (cit. on pp. 27, 77, 83, 87, 90, 93, 96, 108, 110, 133, 137, 150).

[109]D. Hexner and D. Levine, "Hyperuniformity of critical absorbing states," Physical Review Letters **114**, 10.1103/physrevlett.114.110602 (2015) (cit. on pp. 27, 28, 47, 68).

[110]D. Hexner and D. Levine, "Noise, diffusion, and hyperuniformity," Physical Review Letters **118**, 10.1103/physrevlett.118.020601 (2017) (cit. on pp. 27, 28).

[111]S. Torquato and F. H. Stillinger, "Local density fluctuations, hyperuniformity, and order metrics," Physical Review E **68**, 10.1103/physreve.68.041113 (2003) (cit. on pp. 27, 28, 47, 151).

[112]S. Torquato, "Hyperuniformity and its generalizations," Physical Review E **94**, 10.1103/physreve.94.022122 (2016) (cit. on pp. 27, 151).

[113]U. S. Nizam, G. Makey, M. Barbier, S. S. Kahraman, E. Demir, E. E. Shafigh, S. Galioglu, D. Vahabli, S. Husnugil, M. H. Guneş, E. Yelesti, and S. Ilday, "Dynamic evolution of hyperuniformity in a driven dissipative colloidal system," Journal of Physics: Condensed Matter **33**, 304002 (2021) (cit. on p. 28).

[114]R. Dandekar and D. Dhar, "A class of exactly solved assisted-hopping models of active-inactive state transition on a line," EPL (Europhysics Letters) **104**, 26003 (2013) (cit. on p. 28).

[115]R. Dandekar, "Exact hyperuniformity exponents and entropy cusps in models of active-absorbing transition," Europhysics Letters **132**, 10008 (2020) (cit. on p. 28).

[116]T. Sadhu and B. Derrida, "Correlations of the density and of the current in non-equilibrium diffusive systems," Journal of Statistical Mechanics: Theory and Experiment **2016**, 113202 (2016) (cit. on pp. 38, 41, 47, 51, 60, 67, 87).

[117]T. Sadhu and D. Dhar, "Steady state of stochastic sandpile models," Journal of Statistical Physics **134**, 427–441 (2009) (cit. on p. 41).

[118]A. De Masi and P. A. Ferrari, Journal of Statistical Physics **107**, 677–683 (2002) (cit. on pp. 47, 60, 94).

[119]K. Jain, "Simple sandpile model of active-absorbing state transitions," Physical Review E **72**, 10.1103/physreve.72.017105 (2005) (cit. on pp. 50, 70).

[120]The details of the results will be presented elsewhere (cit. on p. 51).

[121]U MARCONI, A PUGLISI, L RONDONI, and A VULPIANI, "Fluctuation–dissipation: response theory in statistical physics," Physics Reports **461**, 111–195 (2008) (cit. on p. 53).

[122]D. K. C. MacDonald, *Noise and fluctuations*, Dover Books on Physics (Dover Publications, Mineola, NY, June 2006) (cit. on pp. 55, 88, 144).

[123]D. Hexner, P. M. Chaikin, and D. Levine, "Enhanced hyperuniformity from random reorganization," Proceedings of the National Academy of Sciences **114**, 4294–4299 (2017) (cit. on pp. 62, 69).

[124]L. Corte, P. M. Chaikin, J. P. Gollub, and D. J. Pine, "Random organization in periodically driven systems," Nature Physics **4**, 420–424 (2008) (cit. on p. 69).

[125]M. R. Evans and T Hanney, "Nonequilibrium statistical mechanics of the zero-range process and related models," Journal of Physics A: Mathematical and General **38**, R195 (2005) (cit. on p. 71).

[126]R. Dickman, L. T. Rolla, and V. Sidoravicius, "Activated random walkers: facts, conjectures and challenges," Journal of Statistical Physics **138**, 126–142 (2010) (cit. on pp. 102, 103).

[127]S. Katz, J. L. Lebowitz, and H. Spohn, "Nonequilibrium steady states of stochastic lattice gas models of fast ionic conductors," Journal of Statistical Physics **34**, 497–537 (1984) (cit. on p. 121).

[128]G. Pruessner and H. J. Jensen, "Anisotropy and Universality: The Oslo Model, the Rice Pile Experiment, and the Quenched Edwards-Wilkinson Equation," Phys. Rev. Lett. **91**, 244303 (2003) (cit. on p. 131).

[129]J. A. Bonachela and M. A. Muñoz, "Confirming and extending the hypothesis of universality in sandpiles," Phys. Rev. E **78**, 041102 (2008) (cit. on pp. 160, 161).

[130]M. Basu, U. Basu, S. Bondyopadhyay, P. K. Mohanty, and H. Hinrichsen, "Fixed-Energy Sandpiles Belong Generically to Directed Percolation," Phys. Rev. Lett. **109**, 015702 (2012) (cit. on pp. 160, 161).

[131]S. B. Lee, "Universality class of the conserved Manna model in one dimension," Phys. Rev. E **89**, 060101 (2014) (cit. on pp. 160, 161).

[132]G. Gasper and M. Rahman, *Basic hypergeometric series* (Cambridge University Press, 2004) (cit. on p. 165).